

1 Introduction

Medical progress has been increasingly influenced in recent years by the adoption, development and deployment of intervention treatments based on the availability of novel biomaterials via tissue engineering (1) (TE). Biomaterials are now considered to be viable elements of many clinical procedures providing transient or permanent treatments for damaged or diseased tissues in diverse and critical body systems. The potential widespread deployment of biomaterials within many dissimilar *in vivo* environments has highlighted the importance of confirming suitability for their intended application prior to clinical use (2, 3). Confirmation of suitability is a complex task, as many factors contribute to the selection of a biomaterial to fulfil a projected role, further complicated by the fact that biomaterials may be sourced or fabricated through a number of alternative materials.

There are two primary research approaches; the preparation of scaffolds from biological sources (Section 2.1.2) or the creation of new synthetic polymer derived scaffolds (Section 2.1.3) (4). Natural polymers are constrained by issues including; purification complications, potential immunogenic host reactions, timeliness of enzymatic degradation, and confirming sterility of the polymer. Synthetic, polymer derived biomaterials represent a major advancement in TE and regenerative medicine since they take advantage of the well-established tunable physical properties of polymers and their ability to be quickly produced

and are widely accessible. Furthermore, biodegradable polymers have shown great promise whilst being explored as potential biomaterials. Researched thermoplastic biopolymers for TE applications include poly glycolic acid (PGA) (5), poly(lactic-co-glycolic acid) (PLA) (6) and poly(glycerol sebacate) (PGS) (7).

Over the last twenty years PGS in particular has especially attracted extensive interest by researchers (Section 2.1.3.3). Among its attractions is that PGS is sourced from the non-toxic and low-cost monomers, sebacic acid and glycerol. The elastomeric mechanical properties of PGS can easily be constructed to enhance its cytocompatibility and degradation *in vivo* (7). The ability to tailor the density of crosslinking has optimised porous PGS for a range of soft tissue bioengineering applications including; blood vessels, cardiac tissue (8, 9) and cartilage (10).

In contrast to the positive advantages of PGS as a tailorable biomaterial, PGS does have limitations introduced through its processing demands. The high temperatures required to form precise geometries is a significant obstacle and impedes the direct incorporation of cells or temperature sensitive molecules in PGS. However, a novel photocurable form of PGS (PGS-M) has been produced by functionalisation with methacrylate units and has been shown in a contemporary study to address many of these limitations (11). The availability of PGS-M has made feasible many potential new and exciting opportunities for future clinical deployments of polymer based biomaterials and has therefore been adopted as the focus biomaterial for this thesis.

However, despite PGS-M's promise the success of biodegradable materials in general lies in the researcher's capability to produce polymers which achieve required degradation, biocompatibility, and physical properties to elicit positive biological responses. To ensure the effective functioning of any implanted biomaterial, preservation of the material's surface chemistry and mechanical properties within the body is essential [1] (Figure 1 (A)). Figure 1 (B) displays an overview of the cell - surface interaction process. The interactions between the polymer biomaterials and elements of the biological system arise at the polymers surface interface (>10 nm) (Section 2.1.5). The adsorbed protein layer (12) in addition to surface topography (13) and surface chemistry (functional group surface distribution) (14). All of which occur on the nanoscale surface of the material.

To fully realise the potential of biomaterials, polymer surface related research needs to be the focus of development efforts, especially the field of surface modification (Figure 1 (C)). Advancements in surface functionalisation have demonstrated progress in the ability to modify a biomaterials surface through patterning techniques. The impact of incorporating surface chemical functional groups, such as amine ($-NH_2$), carboxyls ($-COOH$), hydroxyls ($-OH$), and methyls ($-CH_3$), have on a polymer's capacity to promote cellular growth have also been evaluated in previous studies (15, 16). Research studies have also shown that $-OH$ surface functionality presents a neutral, hydrophilic surface upon which cellular growth is related to an increase in surface functionalities containing oxygen (17). The requirement for bioengineering to produce biomaterials with specific surfaces suited to cellular growth is crucial. Understanding how and

why a surfaces topography and surface chemistry improves or limits a cells ability to grow on a material is the first step in developing the next generation of cell specific biomaterials (15, 16, 17).

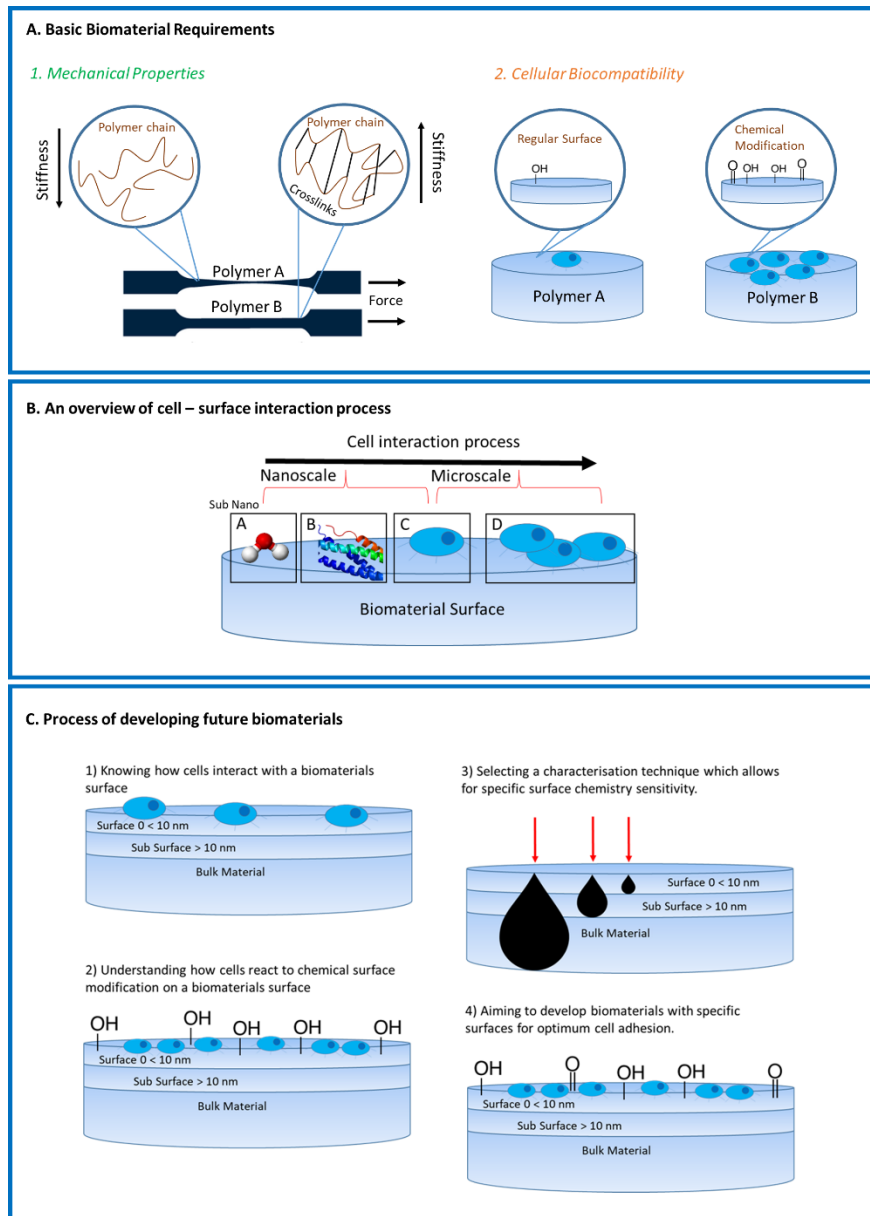


Figure 1: Section A. Two key requirements for biomaterials. 1) Tuneable mechanical properties and 2) Cellular biocompatibility. Section B. An overview of cell – surface interaction process. A) Water – surface interaction. B) Protein adsorption to biomaterial. C) Cell attachment. D) Cell differentiation. Section C. The overview of the goal of developing future biomaterials.

As highlighted in selecting an appropriate characterisation technique is integral in the process of developing future biomaterials (Figure 1 C.3). Polymeric biomaterial characterisation is a multifaceted undertaking where a range of complementary characterisation approaches can each provide a contribution. An ideal characterisation technique will without changing either the chemical composition or structures architecture, provide comprehensive multiscale information pertaining to the materials nanostructure. Including a biomaterials mechanical structural properties, surface topography and surface functional group distribution (28).

There are many existing characterisation approaches that possess capabilities which have the potential to contribute to the characterisation of biomaterials but currently they all exhibit limitations which preclude them from completely satisfying these requirements (Section 2.2); Energy Dispersive X-ray Spectroscopy (EDX) can characterise the elemental composition of materials (20), however, some elements do have overlapping EDX peaks and EDX does not provide an insight into the topography of nanoscale structures. Electron Energy Loss Spectroscopy (EELS) is capable of identifying the elemental components, the sensitive response to a samples configuration and composition and EELS high energy based resolution make it very effective and powerful tool. Yet EELS is limited in that it does not provide information on topographical structure and the high energies used can damage beam sensitive biomaterials (21). Raman Spectroscopy is fast and reliable in generating a materials chemical spectra but has limitations stemming from poor lateral resolution with only micron scale analysis (22). X-ray photoelectron spectroscopy (XPS) is able to characterise

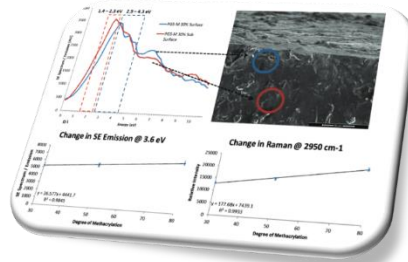
sample materials through element and chemical composition identification (23). XPS is also highly sensitivity technique when applied to inorganic and organic materials (23, 24), but it is not capable of undertaking chemical surface mapping at nanoscale resolutions. Lastly, Phase-contrast Atomic Force Microscopy (AFM) can deduce 3-dimensional material morphology, distinguish between different materials, providing spatial distribution information and does not require a vacuum (25). However, AFM has signal to noise ratio issues as well as management of tip sample forces required.

As indicated in Figure 1 (3.4) enhanced material characterisation capabilities including; novel surface chemical spectroscopy and imaging methods on nano- and micro-scale levels are considered necessary to provide the fundamental analysis steps needed to support future biomaterial surface development. For biomaterial characterisation only a small number of existing characterisation techniques provide the capability to undertake surface analysis at the nanoscale. Of these none provide the ability to undertake multiscale chemically mapping of beam sensitive biomaterials. Therefore, the requirement for a high resolution, multiscale, chemical mapping capability for characterisation of synthetic polymer derived biomaterials is yet to be satisfied.

This thesis exploits the recently developed technique of Secondary Electron Hyperspectral Imaging (SEHI). SEHI captures and analyses spectral information from material samples providing a means of mapping chemical bonding within polymer derived biomaterials at surface depths of >10 nm (Section 2.4.6). Collection of Secondary Electron (SE) emission spectra (SES) by means of the

Scanning Electron Microscope (SEM) provides the foundation for the SEHI technique. SEHI accomplishes this by constructing a series of images based on the target area of the material sample, where a selected SE energy band forms each image. The process of collecting SE spectra wholly relies on the probe electron – material interactions. SES calculates electron emission energies post inelastic collisions. SES benefits from employing a low KeV (between 0.5-2 keV) primary electron beam which makes it possible for the SES to collect the spectra of beam sensitive materials. Although, SEs are produced throughout the primary beam interaction depth, only SEs emitted within the SE escape depth can be detected as SEs emitted at a greater depth will be absorbed by the bulk of the sample material. The SE shallow escape depth raises the issue of surface contamination affecting the spectra results, a problem faced by other surface analysis techniques. However, SES has been shown to have operational characteristics that allow it to overcome substantial surface contamination to produce accurate spectra that are reproducible and reveal characteristics of the underlying material (26, 27). Previous research work had established that the SE spectra for certain hydrocarbon materials are substantially affected by excitation of intramolecular vibrations (18, 19). Although the SEHI technique can provide extensive chemical and synchronised structural characterisation information, this thesis showed that SEHI is capable of multiscale, chemically mapping, which critically can be employed on beam sensitive biomaterials. Chapters 3, 4 and 5 in this thesis all shows SEHI has the requirement for multiscale, high resolution, chemical mapping.

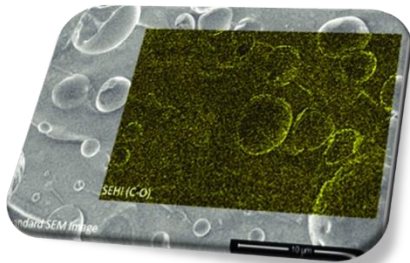
Chapter 3: "Characterizing Cross-Linking Within Polymeric Biomaterials in the SEM by Secondary Electron Hyperspectral Imaging"



Chapter 3: SEHI provided spatially-resolved cross-linking analysis allowing for insights into the stiffness properties of PGS-M.

1. Understanding the mechanical properties of polymers

Chapter 5: Identifying and mapping chemical bonding within Phenolic Resin using Secondary Electron Hyperspectral Imaging"

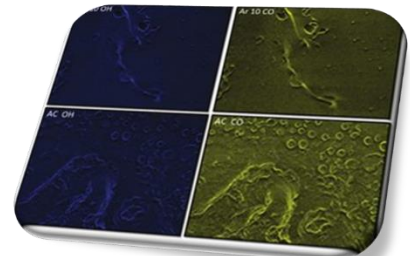


Chapter 5: SEHI exhibited the ability to map localised chemical bonding within phenolic resin. SEHI results provided predicted localised stiffness variation which was subsequently validated using novel nano indentation mapping.

Chapter 3 SEHI identified CHx functional group emission within PGS-M.

2. Understanding the biocompatibility of polymers

Chapter 4: "Understanding Surface Modifications Induced via Argon Plasma Treatment through Secondary Electron Hyperspectral Imaging"



Chapter 4: SEHI maps were employed for the first time to highlight the lateral distributions of diverse functional groups. Understanding functional group distribution allowed for insights into PGS-M cellular biocompatibility.

Figure 2: Thesis structure. Chapters 4 and 5 build upon the data provided in Chapter 3. The publication in chapter 3 titled "Characterising cross-linking within polymeric biomaterials in the SEM by Secondary Electron Hyperspectral Imaging." introduced SEHI as a novel SEM-based analysis tool for beam sensitive biomaterials. Secondary electrons emanating from polymer derived materials within the SEM for hyperspectral imaging were for the first time exploited to identify CH functional groups allowing spatially-resolved cross-linking analysis. This included; molecular order/orientation and cross linking density. As shown

in Figure 2, the findings presented in Chapter 3 are built upon by Chapters 4 and 5.

Chapter 4 furthers on this initial paper discussing the publication titled “Understanding surface modifications induced via Argon Plasma treatment through Secondary Electron Hyperspectral Imaging”. Here SEHI maps were employed to highlight the lateral distributions of diverse functional groups that were impacted by the sterilisation treatments. This evidence combined with the results from a number of established surface analysis techniques and a cellular metabolic activity assay constructed a strong argument as to why low-pressure Argon glow discharge should be considered for future optimisation as a prospective terminal sterilisation method. This chapter included modification of a biomaterial`s surface and introduced the possibility of mapping functional groups on a biomaterials surface using SEHI. Lastly the publication presented in chapter 5 entitled “Identifying and mapping chemical bonding within Phenolic Resin using Secondary Electron Hyperspectral Imaging” presents a detailed investigation of phenolic resin surface structures by means of SEHI analysis. SEHI made possible novel insights into the phenolic resin secondary electron emission variations and relate these to localised differences in chemical bonding.

Chapter 5 builds on the work published in Chapter 3, by presenting SEHI`s ability to map chemical crosslinks locally across a materials surface. In this instance to map both methylene and ether bridge distribution within phenolic resin. SEHI results was then used to predict localised stiffness variation which was

subsequently validated using novel nano-indentation mapping. The results obtained confirmed that SEHI is a significant advance in high resolution chemical imaging capability. Having the ability to understanding localised stiffness is essential for not just understanding the structural integrity of a polymer-derived biomaterial network, but also how cells respond to differing localised crosslinking.

The analysis presented in this thesis makes a persuasive argument for establishing SEHI as a viable and effective toolset for polymer characterisation in the context of TE. It is anticipated that the research findings published during the completion of this thesis will assist researchers in the development of novel and practical biomaterials through the ability of SEHI to offer new insights into the composition and structure of polymer material systems. The author is also confident that the advanced characterisation approach promoted by SEHI will be of high value to researchers from many disciplines involved in the multiscale characterisation of polymers and complex chemical macromolecular structures beyond tissue engineering. It is observed that the development of advanced polymeric materials can only be efficiently achieved with the development of correspondingly advanced material characterisation techniques.

While it has been shown that the SEHI technique can provide extensive chemical and synchronised structural characterisation information, two key questions remain over its future use for the characterisation of polymer derived biomaterials. 1) Can SEHI deliver insights into the mechanical properties of a material? 2) Is the captured SE spectra able to identify functional groups that

play a key role in biomaterials engineering TE, and if so, can SEHI map these functional groups at the nanoscale? This thesis will focus on providing evidence to determine the answers to these questions.

1.1 References

1. W. He, R. Benson: *4 - Polymeric Biomaterials In Plastics Design Library, Handbook of Polymer Applications in Medicine and Medical Devices*. William Andrew Publishing, 55-76, ISBN 9780323228053. (2014). <https://doi.org/10.1016/B978-0-323-22805-3.00004-9>.
2. E. Rabkin, F. Schoen: *Cardiovascular tissue engineering*. Cardiovascular Pathology. **11**, 305-317. (2002).
3. S. Jockenhoevel, K. Chalabi, J. Sachweh, H. Groesdonk, L. Demircan, M. Grossmann, G. Zünd, B. Messmer: *Tissue engineering: complete autologous valve conduit- a new moulding technique*. Thoracic and Cardiovascular Surgery. **49**, 287-290. (2001).
4. L.A. Loureiro dos Santos: *Natural Polymeric Biomaterials: Processing and Properties, Reference Module in Materials Science and Materials Engineering*. Elsevier. (2017). <https://doi.org/10.1016/B978-0-12-803581-8.02253-0>.
5. S. Terasaka, Y. Iwasaki, N. Shinya, T. Uchida: *Fibrin glue and polyglycolic Acid nonwoven fabric as a biocompatible dural substitute*. Neurosurgery. **58**. 134-139. (2006).
6. G. Zünd, T. Breuer, T. Shinoka, P. Ma, R. Langer, J. Mayer, J. Vacanti: *The in vitro construction of a tissue engineered bioprosthetic heart valve*. European Journal of Cardiovascular and Thoracic Surgery. **11**. 493-497. (1997).
7. Y. Wang, G.A. Ameer, B.J. Sheppard, R. Langer: *A tough biodegradable elastomer*. Nat Biotechnol. **20**. 602-6 (2002). doi: 10.1038/nbt0602-602.
8. M. Radisic, H. Park, T.P. Martens, J.E. Salazar-Lazaro, W. Geng, Y. Wang: *Pre-treatment of synthetic elastomeric scaffolds by cardiac fibroblasts improves engineered heart tissue*. J Biomed Mater Res A. **86**. 713-24. (2008) doi: 10.1002/jbm.a.31578.
9. W. Wu, R.A. Allen, Y. Wang: *Fast-degrading elastomer enables rapid remodeling of a cell-free synthetic graft into a neoartery*. Nat Med. **18**. 1148-53. (2012). doi: 10.1038/nm.2821.
10. C.G. Jeong, S.J. Hollister: *A comparison of the influence of material on in vitro cartilage tissue engineering with PCL, PGS, and POC 3D scaffold architecture seeded with chondrocytes*. Biomaterials. **31**. 4304-12. (2010) doi: 10.1016/j.biomaterials.2010.01.145.
11. S. Pashneh-Tala, R. Owen, H. Bahmaee, S. Rekštyte, M. Malinauskas, F. Claeysens, Front. Phys., **6**. 41. (2018).
12. D.D. Deligianni, N. Katsala, S. Ladas, D. Sotiropoulou, J. Amedee, Y.F. Missirlis: *Effect of surface roughness of the titanium alloy Ti-6Al-4V on human bone marrow cell response and on protein adsorption*. Biomaterials. **22**. 1241-1251. (2001).
13. L.C. Hsu, J. Fang, D.A. Borca-Tasciuc, R.W. Worobo, C.I. Moraru: *Effect of micro- and nanoscale topography on the adhesion of bacterial cells to solid surfaces*. Appl. Environ. Microbiol. **79**. 2703-2712. (2013).

14. K.R. Milner, A.J. Snyder, C.A. Siedlecki: *Sub-micron texturing for reducing platelet adhesion to polyurethane biomaterials*, J. Biomed. Mater. Res. A **76**. 561–570. (2006).
15. B.G. Keselowsky, D.M. Collard, A.J. García: *Surface chemistry modulates focal adhesion composition and signaling through changes in integrin binding*. Biomaterials. **28**. 5947–54. (2004). doi: 10.1016/j.biomaterials.2004.01.062.
16. M.A. Lan, C.A. Gersbach, K.E. Michael, B.G. Keselowsky, A. García: *Myoblast proliferation and differentiation on fibronectin-coated self-assembled monolayers presenting different surface chemistries*. Biomaterials. **22**. 4523–31. (2005).
17. C.D. Tidwell, S.I. Ertel, B.D. Ratner, B.J. Tarasevich, S. Atre, D.L. Allara: *Endothelial cell growth and protein adsorption on terminally functionalized, self-assembled monolayers of alkanethiolates on gold*. Langmuir. **13**. 3404–3413. (1997).
18. N.A. Stehling, R. Masters, Y. Zhou, R. O'Connell, C. Holland, H. Zhang, C. Rodenburg: *New perspectives on nano-engineering by secondary electron spectroscopy in the helium ion and scanning electron microscope*. MRS Commun. **8**. 226. (2018).
19. R.C. Masters, N. Stehling, K. Abrams, V. Kumar, A. Schäfer, D. Lidzey, C. Rodenburg: *Mapping polymer molecular order in the SEM with secondary electron hyperspectral imaging*. Adv Sci. **6**. 5. (2019).
20. M.S.I Khan, S.W. Oh, Y.L. Kim: *Power of Scanning Electron Microscopy and Energy Dispersive X-Ray Analysis in Rapid Microbial Detection and Identification at the Single Cell Level*. Sci Rep **10**. 2368 (2020).
21. O.L. Krivanek, T.C. Lovejoy, N. Dellby, T. Aoki, R.W. Carpenter, P. Rez, E. Soignard, J. Zhu, P.E. Batson, M.J. Lagos: *Vibrational spectroscopy in the electron microscope*. Nature **514**, 209–212 (2014).
22. H.J. Butler, L. Ashton, B. Bird, G. Cinque, K. Curtis, J. Dorney, K. Esmonde-White, N.J. Fullwood, B. Gardner, P.L. MartinHirsch, M.J Walsh, M.R. McAinsh, N. Stone, F.L. Martin: *Using Raman Spectroscopy to Characterize Biological Materials*. Nat. Protoc. **11**. (4). 664–687. (2016).
23. N.Farr, J. Thanarak, J. Schäfer, A Quade, F. Claeysens, N. Green, C. Rodenburg: *Understanding Surface Modifications Induced via Argon Plasma Treatment through Secondary Electron Hyperspectral Imaging*. Adv. Sci. 2020, 2003762
24. O. Bondarchuk, A.P. LaGrow, A. Kvasha, T. Thieu, E. Ayerbe, I. Urdampilleta: *On the X-ray photoelectron spectroscopy analysis of LiNixMnyCozO2 material and electrodes*. Applied Surface Science. **535**. 147699. (2021)
25. M. Farré, D. Barceló. *Analysis and Risk of Nanomaterials in Environmental and Food Samples in Comprehensive Analytical Chemistry*. **59**. 2–361 (2012).
26. D.C. Joy. M.S, Prasad. and H.M Meyer, III: *Experimental secondary electron spectra under SEM conditions*. Journal of Microscopy, **215**. 77–85. (2004).
27. A. Khursheed. *Secondary Electron Energy Spectroscopy in the Scanning Electron Microscope*. World Scientific Publishing Co Pte Ltd. ISBN: 9789811227028.
28. M. Rahmati. E.A. Silva. J. E. Reseland, C.A. Heyward. H.J. Haugen. *Biological responses to physicochemical properties of biomaterial surface*. Chem. Soc. Rev. **49**, 5178. (2020).

2. Literature Review

2.1 Tissue engineering of Biomaterials

Tissue engineering (TE) is a biomedical engineering discipline which combines biology with engineering (1). The goal of TE research is the creation of replacement human organs or tissue structures. Maintenance, restoration or improvement of tissue function, through TE, is expected to allow the more effective treatment of medical disorders than is possible using current medical practices. TE, as its name implies, is a field of research that requires a multidisciplinary approach. Although research is principally driven from a biology and engineering discipline perspective, other disciplines including polymer chemistry also have valuable contributions to make. The future importance of TE can be judged by the fact that it has been estimated that in the region of 7.5 million patients require artificial biological implants each year in the United States alone (2). Difficulties with current clinical practices, including *in vivo* compatibility and donor availability, have driven the demand for a radical alternative approach such that TE offers.

Biomaterials are considered to offer an essential contribution to the improvement of human health and associated quality of life (3). The scope of potential TE products encompasses a diverse and widespread range of clinical replacements including, but not limited to, skin, blood vessels, cardiac tissue, nerve conduits and structural cartilage and bone applications. Significant

challenges still need to be overcome prior to the universal deployment of viable human compatible biomaterials. Four key processes have been identified during the *in vivo* or *in vitro* phases of tissue development and growth (4):

1. Cellular differentiation and proliferation
2. Extracellular matrix (ECM) production
3. Degradation of the scaffold
4. Remodelling and potential growth of the tissue.

For a TE product to be a truly viable replacement for natural tissue, it is essential that the replacement's physical and biological properties provide for these processes to occur. Synthetic materials incorporated within the TE replacement must be accepted by the host without adverse side effects and also often eventually degrade as new host tissue develops and remodels. A matrix framework, usually called a scaffold, is the core of a TE product which is seeded with cells either *in vitro* or *in vivo*. The TE matrix scaffold may be sourced or constructed through a number of alternative materials. However, there are two principal research approaches; the preparation of biological scaffolds and the creation of new synthetic polymer derived scaffolds. Polymeric biomaterials (biopolymers) can be used for the substitution of a range of tissues over short or long time periods within physiological environments (5).

2.1.1 Polymer derived biomaterials

Polymer materials exhibit a range of chemical, mechanical and physical properties. These properties have encouraged extensive research and development into potential applications of polymeric biomaterials. The field of biomedical applications has made significant advances over recent years in the development of polymeric materials that are biodegradable and biocompatible (3). Within the range of synthetic and hybrid materials being employed in medicine, polymeric biomaterials are the most widely used (6).

Developments of biodegradable polymeric materials, which exhibit a nominal immunogenicity, are currently being assessed for their suitability for deployment as biomaterials. These materials hold the promise of being excellent choices for developing therapeutic devices. Candidate applications include controlled/sustained release drug delivery vehicles, temporary prostheses and permeable structures. Polymer derived biomaterials may be divided into two subgroups based on the mechanism by which they degrade within the host. For use in biomedical products a number of synthetic and natural polymers are being assessed that are capable of degradation by hydrolytic or enzymatic mechanisms.

Natural and synthetic polymers each have different strengths; natural polymers are similar to the constituents found in extracellular matrices, synthetic polymers are comparatively versatile, adaptable and suitable for chemical modification (7).

2.1.2 Natural polymers biomaterials

Naturally occurring polymers generally display an enzymatically degradable mechanism and have a respectable clinical record as biodegradable biomaterials (8). In contrast to some synthetically produced polymers, natural polymers are comparable to biological tissues (9) as they display bioactivity (10, 11), offer cells with receptor-binding ligands and exhibit proteolytic degradation (12). Disadvantages of natural polymers include purification complications, possible immunogenic host response, reproducibility, timeliness of enzymatic degradation, and ensuring sterility of the material.

2.1.3 Synthetic polymer biomaterials

Hydrolytically degradable polymers are synthetically produced constructed by means of hydrolytically labile chemical bonds. There are many functional groups susceptible to hydrolysis which frequently includes orthoesters, esters, amides, anhydrides and urethanes (13). Synthetic organic chemistry research together with novel bioprocesses is driving the development of polymeric materials that have the future potential to be viable biomaterials.

The mechanical, chemical and physical properties of polymeric biomaterials may be tailored by chemical modification or synthesis of its functional groups in response to the regeneration potential of any tissue (14). The ability to polymerise and synthesise reactive monomers using a range of chemical processes, in situ, has provided options for many injectable polymers, both permanent and biodegradable (6). The success of biodegradable materials lies

in the capacity to produce biomaterials which achieve suitable biocompatibility, physical properties and degradation to provoke favourable cellular responses.

Commonly researched biodegradable polymers include poly(α -hydroxy esters), poly glycolic acid (PGA), together with their copolymers poly(glycerol sebacate) (PGS) and poly(lactic-co-glycolic acid) (PLA). Hydrolysis of ester bonds and bulk erosion are these polymers degradation mechanism. By modifying the copolymer ratio, the crystallinity and the molecular weight, the rate of degradation may be tailored as required (14).

2.1.3.1 Polyglycolic acid (PGA)

One of the first biodegradable synthetic polymers explored for potential use as a biomedical material is Polyglycolide acid (PGA). PGA is formed through either polycondensation of glycolic acid or ring-opening polymerisation of glycolide and has a crystallinity of ~60% (see figure 1). The high crystallinity of PGA confers it with a high tensile modulus and beneficial mechanical properties (15, 16).

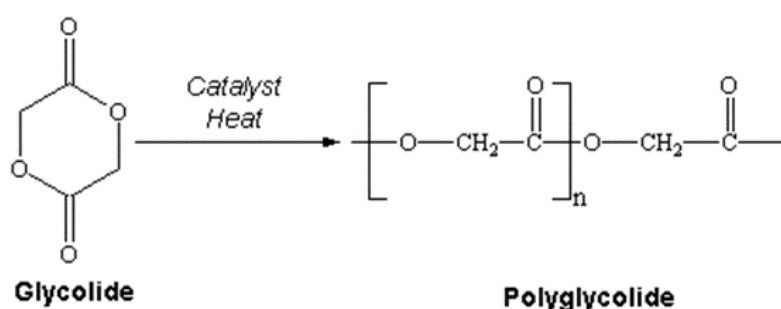


Figure 1: Ring-opening polymerization of glycolide to polyglycolide.

PGA was first researched due to its excellent skin closing performance as biocompatible glue (16). Although PGA demonstrates an ability to assist in the regeneration of damaged tissue, in vivo degradation may lead to toxic by-products (16, 17). The high rate of PGA degradation has limited a wider role for the material in biomedical applications. Non-specific scission of its ester backbone is the mechanism by which PGA degrades and may lead within 1-2 months to substantial loss of strength in vivo (18).

2.1.3.2 Polylactic acid (PLA)

Ring-opening polymerisation of lactide acid is the usual method of creating PLA (See figure 2). Two optically active forms of PLA exist, termed d-lactide and l-lactide. Formation of semi-crystalline PLA is the result of polymerisation of these monomers. Production of PGA is by the same mechanism of polymerisation.

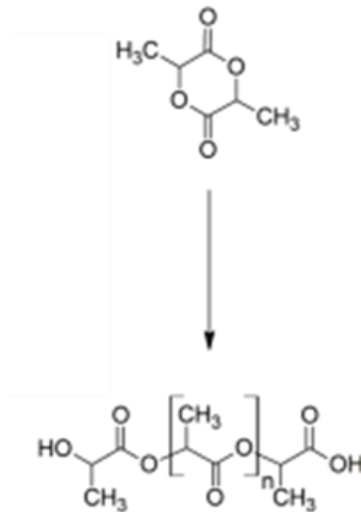


Figure 2: The ring-opening polymerisation of lactide acid to produce Poly(lactide acid) (PLA).

PLA polymer exhibits high tensile strength and PGA degrades gradually. These characteristics make the PLA polymer appropriate for situations where a biomaterial replacement will be subject to load bearing including orthopaedic repair. Research has combined PLA and PGA together in a copolymer to form a biomaterial scaffold which was then seeded with fibroblasts and endothelial cells. Published data reported that the PGA/PLA scaffolds were formed after 14 days and were closely comparable to native tissue (19). A study using a PGA/PLA sandwich scaffold implanted into a lamb model (20, 21) reported initial polymer stiffness issues with the scaffold being susceptible to structural problems. Both PGA and PLA have strengths and weaknesses when used separately or together in biomaterials but are not at the time of publication considered a viable alternative to native tissue due to concerns of the polymers *in vivo* structural integrity (20, 21).

2.1.3.3 Poly(glycerol sebacate) (PGS) and PGS-M Scaffolds

The synthetic polymer Poly(glycerol sebacate) (PGS) has attracted much interest by researchers over the last twenty years. PGS is sourced from the non-toxic and inexpensive monomers, sebacic acid and glycerol. The elastomeric mechanical properties of PGS can be configured to optimise its degradation *in vivo* and cytocompatibility (22). This capability is the result of being able to fine-tune the polycondensation reactions by which PGS is produced. Tailoring the density of crosslinking has optimised porous PGS for several bioengineering applications such as; cardiac tissue (23), blood vessels (24), and cartilage (25). The use of PGS as a biomaterial for cell transport to damaged tissues has also led to applications in heart (26) and retina (27) research. An interesting application of PGS as a biomaterial is as nerve guidance tubes for peripheral nerve repair (28).

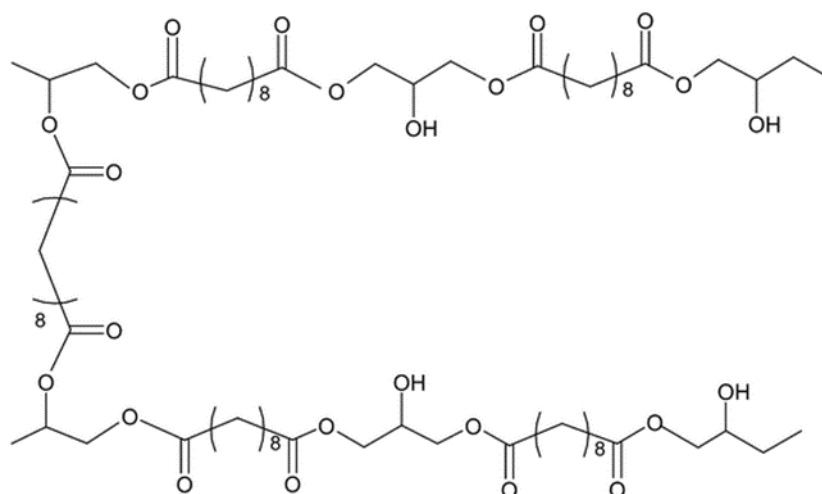


Figure 3: Crosslinking of PGS.

The processing capabilities of PGS have limitations that are in contrast to the positive advantages of PGS as a tailorable biomaterial. Through a polycondensation reaction, PGS as a soluble prepolymer is uncomplicated to manufacture, although high temperatures (>110°C) within a vacuum to thermally cure the polymer is needed to crosslink PGS (See figure 3). This complication makes the construction of accurate geometries challenging and impedes PGS in directly incorporating cells or temperature sensitive molecules.

However, an alternative form of photocurable PGS produced by functionalisation with methacrylate units (29) has in a contemporary study addressed some of these limitations. Without the high temperatures previously needed the study found that PGS is able to crosslink through the addition of methacrylate units and a photoinitiator molecule. Methacrylation has been regularly used as functionalisation method to make photocurable biomaterials (29). PGS-methacrylate (PGS-M) crosslinks by the way of free-radical polymerisation and its synthesis is straightforward. The distinctive properties of PGS-M are likely to be the result of the configuration of crosslinking and the hydrogen-bonding interactions between the hydroxyl groups. Good biocompatibility of PGS-M has been observed through in vitro studies (29). The ability to configure the nanoscale features of the polymer has raised expectations that PGS-M may lead to a new generation of biomaterials.

2.1.4 Cell - Surface interactions

All biomaterials derived from biological and polymer origins, synthetic and natural, have both strengths and weaknesses in their suitability as medical replacements. For successful clinical applications, polymer-derived biomaterials are required to endure the biological environment of an implantation site and also promote a desired cell interaction. This interaction is dependent on the molecular and structural properties of the material (30). Crucially, the interactions between elements of the biological system and polymer biomaterials occur at the surface interface. Despite synthetic polymers often providing appropriate degradation mechanisms and physical infrastructure to form a viable biomaterial, their ability to replicate a natural environment in which cells proliferate and grow raises concerns (31). Figure 4 shows the cell – surface interaction process and at what length scale each interaction occurs. Biological environments invariably are characterised by the presence of water which attempts to penetrate the surface of biomaterials through molecular adsorption according to the specifics of the biomaterial surface structure and nanoscale chemistry.

A surface can either be classified as hydrophilic or hydrophobic dependent to what extent a surface promotes water adsorption. The behaviour of water/biomaterial surface interaction has long been under investigation as it forms the basis of the biological response of the biomaterial when placed within a biological environment. Studies have previously shown that increased hydrophilicity results in enhanced cell adhesion (32) making the requirement for a hydrophilic surface a prerequisite for successful biomaterials.

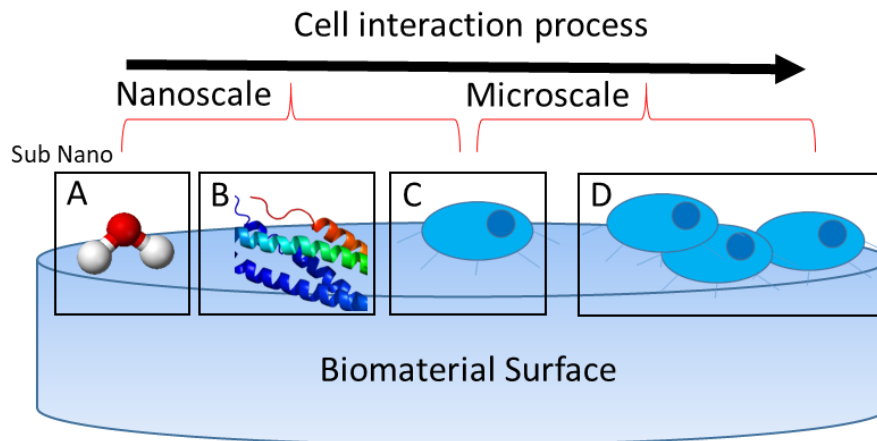


Figure 4: An overview of cell – surface interaction process. A) Water – surface interaction. B) Protein adsorption to biomaterial. C) Cell attachment. D) Cell differentiation.

As consequence of a biomaterial coming into contact with a biological environment a monolayer of protein adsorbs into the biomaterials surface within minutes. It is expected that adsorption from the biomaterial surface will initially start with proteins due to them being immediately available for attachment. Prior to their substitution by larger proteins which have a stronger attraction to the surface (33). The three major proteins which support cellular adhesion are albumin, IgG, and fibrinogen. Investigations into the mechanisms by which polymers surfaces adsorb these proteins has been long an area of interest for biomaterial researchers (34). Displaying the ability to absorb proteins gives a potential biomaterial a promising advantage to sustain cellular growth (35).

As Figure 5 indicates the first two stages of the cell-surface interaction process interact at the nano-scale. Consequently, both the water and protein absorption

which happen on the biomaterials surface is directly reliant on the nano-structural chemistry of the material. The third stage involves cells attaching to the surface as part of the biological response. This stage is slightly more complexed as to which length scale it falls under, although cells are micron sized they attach and are influenced by the nano-structural chemistry of the material. Initial cell attachment is influenced by the adsorbed protein film (36) as well as surface topography (37) and surface chemistry (38, 39). It is essential that the biomaterial surface will have undergone protein and water adsorption creating a modified surface layer prior to the arrival of any cells. Cell spreading and differentiation forms the final stage of the process and is effected by the roughness and wettability of the microscale surface features.

Both improved cell growth and increased biocompatibility are recognised benefits of biomaterial surfaces exhibiting moderate hydrophilicity (40). Having an understanding of these processes is the key to developing future biomaterials with surfaces optimised to supporting cellular growth.

2.1.5 Nano-structural requirements of Biomaterials

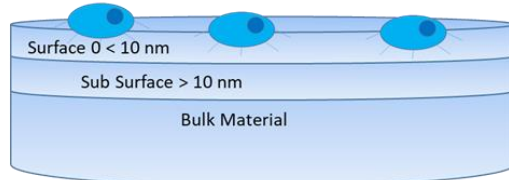
As previously discussed the interactions between elements of the biological system and polymer biomaterials occur at the surface interface. The requirement for bioengineering to produce biomaterials with specific surfaces suited to cellular growth is crucial. Understanding how and why a surface's topography and surface chemistry improves or limits a cells ability to grow on a material is the first step to developing the next generation of cell specific

biomaterials. Therefore, surface related research needs to be at the forefront of development efforts in order to achieve the progress required to fully realise the potential of biomaterials, especially in the fields of surface characterisation and surface modification (41). Substantial research effort has been focused on understanding the influence of polymer surface functionality in the observed cellular response (42). Chemical functional groups present in the polymer's surface can directly influence cell growth (43).

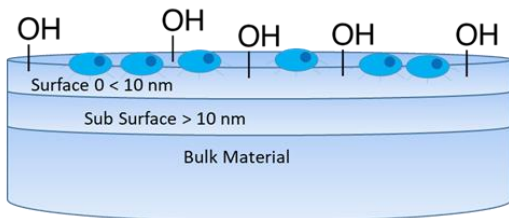
Characterising the chemical functional groups in a biomaterial's surface is considered integral to understanding its cellular response. Previous studies have evaluated the impact surface chemical functional groups, such as Carboxyls (-COOH), Hydroxyls (-OH), Amine (-NH₂) and Methyls (-CH₃), have on a polymers ability to sustain cellular growth (44, 45). Protein adsorption studies have revealed that albumin and fibronectin are readily eluted from surfaces coated with -COOH (46). Similarly, research has proposed that -OH surface functionality represents a neutral, hydrophilic surface on which cellular growth is proportional with an increase in oxygen containing surface functionalities (43). Studies highlighted above often assume that functional group distribution across a polymers surface is uniform. However, advancements in surface functionalisation have shown great success in being able to modify a biomaterials surface by patterning techniques (47, 48). A number of studies have shown that cellular behaviour is directly influenced by the configuration of the surface morphology at the micro and nanoscale related to the surface's texture and chemical distribution (49). This finding provides an opportunity to regulate cell function by tailoring the chemical surface patterning and

topography of a biomaterial (50, 51). In particular, the adhesion of bacteria (52), leukocytes (53) and platelets (54) can all be influenced by means of surface chemistry in both micron and nanoscale structures.

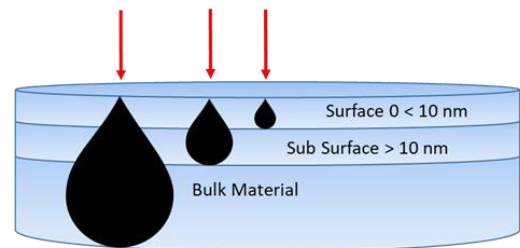
1) Knowing how cells interact with a biomaterials surface



2) Understanding how cells react to chemical surface modification on a biomaterials surface



3) Selecting a characterisation technique which allows for specific surface chemistry sensitivity.



4) Aiming to develop biomaterials with specific surfaces for optimum cell adhesion.

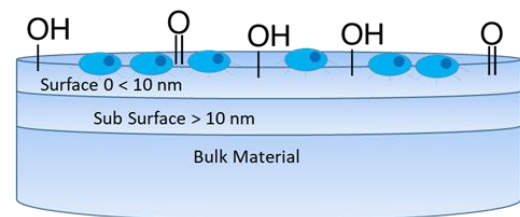


Figure 5: The overview of the goal of developing future biomaterials.

The development of a polymer with a nanostructure which is optimised to facilitate a positive cellular response should be a goal of materials scientists. Figure 5 displays the process by which bioengineering requires the use of biomaterial surface characterisation methods to help create the next generation of biomaterials. If this can be achieved, then polymer derived biomaterials have the potential of being the first choice as TE replacement options. Establishing a detailed understanding of what are the essential surface chemical characteristics a biomaterial must possess in order to promote cellular proliferation and growth is a crucial first step.

2.2 Nanoscale surface characterisation methods

The structure of a biomaterial capable of promoting cell growth and remodelling is by nature usually relatively fragile and lacking in robustness. The characterisation of polymeric biomaterials is a complex undertaking where a number of complementary characterisation techniques can each make a contribution (55). An ideal characterisation technique will provide detailed multiscale information relating to the materials nanostructure without changing either the structures architecture or chemical composition. Many current characterisation techniques possess valuable capabilities that may contribute to biomaterial characterisation but all have limitations which prevent them from fully satisfying these requirements. As figure 5 illustrates consideration must be given to the scale/depth each characterisation method allows information to be taken from. For biomaterials there is a clear requirement to give true surface analysis for reasons discussed in 2.1.4. To drive the development of improved polymer based biomaterials it is essential that characterisation techniques are available which provide materials scientists with the appropriate information to guide the production of suitable polymer chemical patterned surface structures. Analysis of the chemical and structural composition of a biomaterial's surface at the nanoscale is required allowing for chemical and structural information to be obtained (56, 57).

Commonly applied analysis techniques for polymer characterisation include: electron energy loss spectroscopy (EELS), energy dispersive X-ray spectroscopy (EDX), Raman spectroscopy, X-ray photoelectron spectroscopy

(XPS) and atomic force microscopy (AFM) (58). Each offers an ability to characterise biomaterials but each have their own unique benefits and also limitations for use in characterising polymeric biomaterials. As described in previous sections the length scale and physical depth of analysis of the material is of critical importance. Section 2.14. discussed that cell – biomaterial surface interactions happen primarily within the surface layer (< 10nm) of biomaterials and between nano-micron length scales. Crucial water, protein and initial cell interactions occur in response to the nano structure features of the biomaterial surface. Figure 6 shows the length scale of analysis and the lateral and depth resolution for each of the common characterisation techniques highlighted. Despite some techniques not allowing for nanoscale or true surface analysis, these have been included for discussion as they are routinely used characterisation methods for biomaterials.

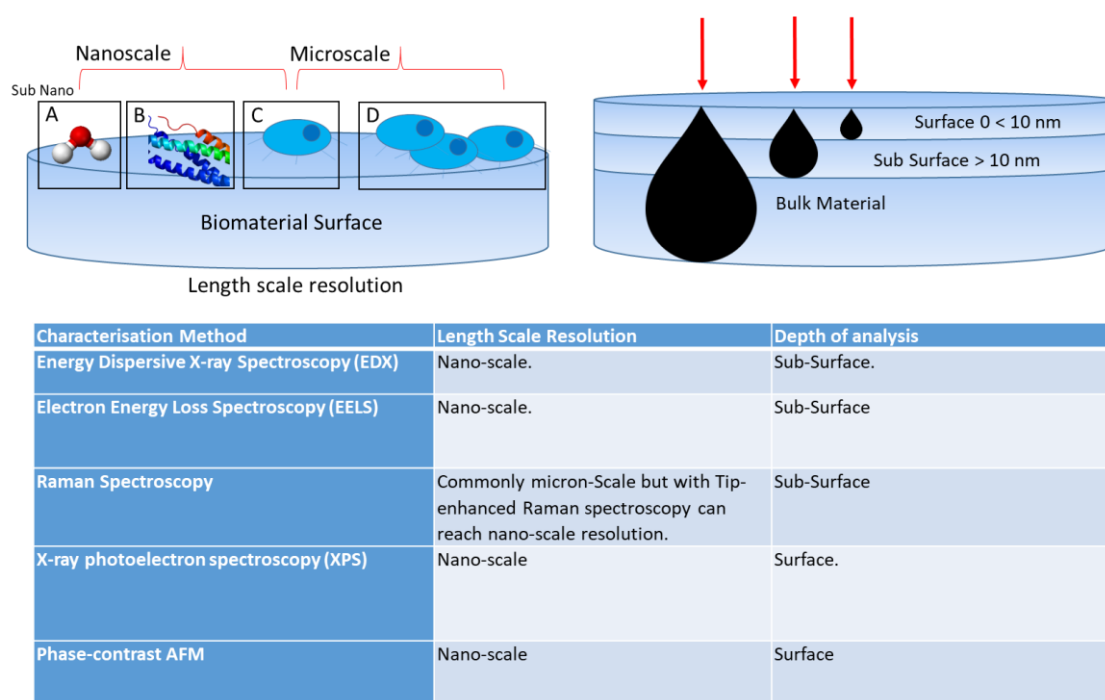


Figure 6: A comparison of the length scale resolution and depth analysis of common biomaterial characterisation techniques.

2.2.1 Energy Dispersive X-ray Spectroscopy (EDX)

Energy-dispersive X-ray spectroscopy (EDX) is an analytical technique extensively applied in the elemental characterisation of target samples. EDX exploits the characteristic X-ray spectrum emitted by a sample once bombarded by a beam of electrons to acquire chemical information. These x-rays emissions are a result of inelastic interaction (specifically ionisation) with inner shell electrons. EDX can characterise the elemental composition of the analysed volume, with features or phases able to be analysed.

Unfortunately, EDX peaks for low atomic number elements (H to Be) are weak and the detection limits are relatively high (59, 60). Some elements also have overlapping EDX peaks which makes the correct interpretation of the data dependent on the operator. The ability to correctly identify low atomic number elements such as C, N, O, is very important for the characterisation of polymer derived biomaterials which use these elements commonly in their underlying chemistry. An alternative method of measuring characteristic x-rays overcoming some of these peak identification issues is wavelength-dispersive X-ray spectroscopy (WDS). WDS is a characterisation technique with the ability to give elemental information for a range of materials with a better resolution to that of EDX. However, WDS is very expensive and therefore not often available.

Usually, EDX is supplied with electron microscopes to facilitate the chemical analysis of sample features being observed in a digital monitor (61). In

conjunction with electron microscopes, the EDX technique has the ability to construct elemental distribution maps called 'dot maps', an example of which is shown in Figure 7. Figure 7 shows an example where EDX has been used to characterise bone healing (62). Detection using EDX in this study successfully identified Ca and P in the interface to the bone implant corroborating new bone formation along the implant surface. EDX also identified Ca at interface of the bone cartilage which correlated with local nanomechanical properties (63). However, despite studies showing EDX's ability to map elements, the X-ray emissions are being formed by large emission interaction volumes with the elemental mapping not being truly surface sensitive.

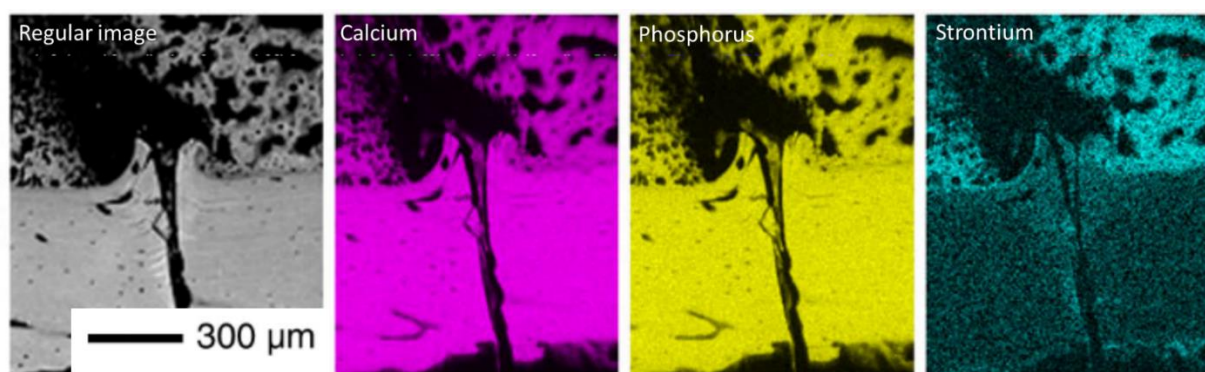


Figure 7: BSE image and Ca (magenta), P (yellow), and Sr (cyan) elemental maps demonstrate Sr incorporation into the fracture callus after therapeutic administration. Adapted with permission from Springer Nature (62).

Quantitative analysis of heterogeneous materials frequently results in inaccurate data as EDX is a comparatively insensitive method (64). EDX can be seen to be a valuable tool to analyse a target sample's chemical composition but it does not provide an insight into the topography of nanoscale structures that directly impact cellular growth. For chemical analysis EDX has a role in biomaterial

research but its lack of surface specific analysis information is a significant limitation.

2.2.2 Electron Energy Loss Spectroscopy (EELS)

Electron Energy Loss Spectroscopy (EELS) provides a capability to identify the elemental components of a target sample. EELS is a technique used in electron microscopes, however, EELS measures the ionisation losses suffered by the primary electron beam. The EELS technique is centred on the inelastic interaction of the primary beam electrons with the electrons present within the sample material. Electrons in the primary beam lose energy in ionization events. This energy loss is dependent on the identity of the atoms that are ionised. Large energy losses come from ionisation events, small energy losses are from collective excitation (e.g. Plasmon's etc.) and allow for information regarding bonding present within a material.

An EELS spectrum is generated by measuring the transmitted primary electrons sorted by energy. An example EELS spectrum is shown in Figure 8 (65). Figure 8 shows typical EELS spectra from biological compounds. The two different EELS spectra presented show (a) the low loss region which give information regarding the bonding present. As little energy is needed to interact with valence electrons as they are weakly bound, the low loss region therefore gives less information regarding the elements and more about bonding present. (b) is the loss due to core shell ionisation, this is similar to EDX, but also the shape of the ionisation edges provides some bonding information. For the purpose of

characterising the surface of biomaterials the low loss region is of specific interest.

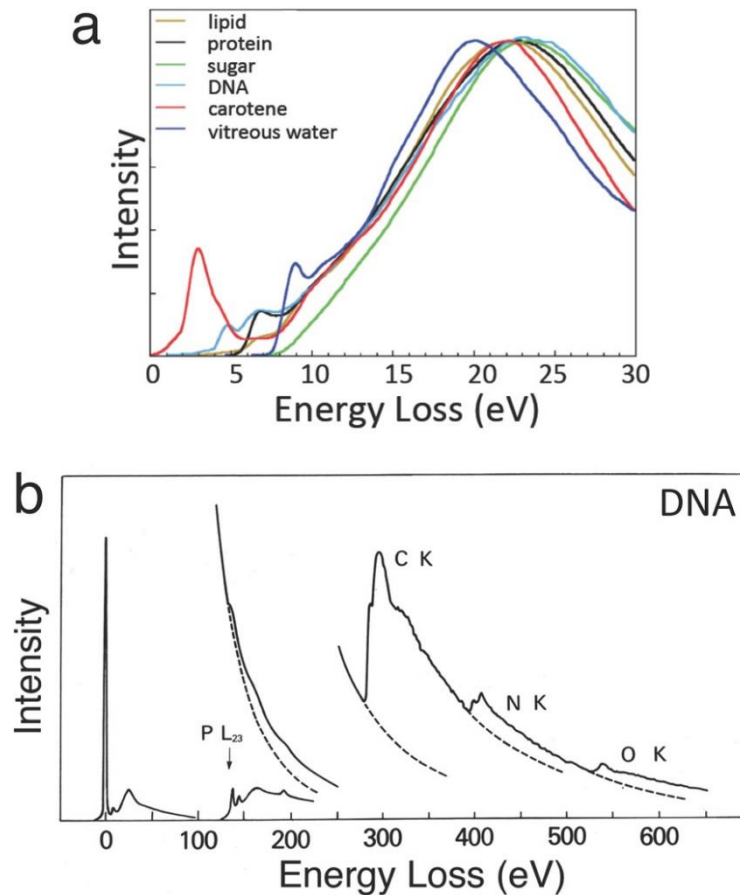


Figure 8: Image obtained from (65) “Typical electron energy loss spectra (EELS) from biological compounds. (a) Low-loss spectra up to energy loss of 30 eV from major cellular components after processing to remove plural inelastic scattering. (b) EELS up to energy loss of 650 eV from DNA deposited on a thin carbon film, showing core edges of phosphorus, carbon, nitrogen and oxygen.”

The sensitivity and high energy based resolution by EELS to a samples configuration and composition make it very effective analysis toolset. For light elements the sensitivity of EELS is superior to that of EDXS. However, EELS shares with EDX the limitation that it does not provide information on the topographical structure of a biomaterial directly. EELS requires that thin samples must be used (< 100 nm), the preparation of sufficiently thin sections from biomaterials is a significant challenge and limitation as it rules EELS out

as a surface analysis technique. In many instances the surface of biomaterials is often rough as a result of surface oxidation or a product of the polymerisation process, such surface irregularities can considerably alter the EELS vibrational spectra.

The ability of EELS to detect vibrational spectra within the primary beam induced electronic transitions has been achieved through technique advancements where energy resolution can now be greater than 40 meV. The development is also applicable to biomaterials (66), although with cautious monitoring for prospective beam damage (67). To apply EELS in studies of beam sensitive materials a primary beam is frequently used to control the exposure and provide an EELS spectrum. EELS often requires a primary beam of electrons to be accelerated to energies usually between 100 keV and 1 MeV (68) prior to impacting the samples, some beam sensitive materials are not capable of withstanding this volume of electron bombardment without damage. At even considerable lower energies (4 KeV) materials have been shown to undergo sputtering damage, and alter the EELS spectra as a consequence of beam exposure (69).

2.2.3 Raman Spectroscopy

Raman spectroscopy is a routinely applied technique for biomaterial characterisation. The basis for Raman spectroscopy is the interaction of an incident light beam comprising of monochromatic light, UV range or near-infrared, producing a scattering effect when focused on the vibrating molecules within the target sample (70). Elastic scattering, known as Rayleigh scattering,

occurs at a radiation frequency comparable to that of the incident light beam where the beam strikes the sample. Alternatively, after the incident beam interacts with vibrational modes associated with the chemical bonding present within the material, the resulting inelastic scattered radiation has a different frequency when likened to that of the incident beam (71). This inelastic scattering is known as Raman scattering (72). Capturing these emissions allows Raman spectroscopy to provide that every molecule has an associated characteristic vibrational mode due to its unique profile of chemical bonds, this is known as a 'molecular footprint'. Therefore, Raman is widely deployed in the analysis of synthetic biomaterials as it is a fast and reliable means of sampling the vibrational modes in the material allowing a material's Raman profile to be calculated (70).

Great interest has been shown in the recent development of Raman microspectroscopy and its potential to extend the application of the Raman technique. Here, a Raman spectrometer is integrated within an optical/electron microscope, hence facilitating both visual and spectroscopic characterisation of the sample (70). Raman mapping capability can be integrated into SEMs to obtain both local chemical information and microstructural information often simultaneously. However, poor lateral resolution is a feature of Raman profile. Recent advances have predicted that Raman combined with the Scanning Electron Microscopy instrumentation could achieve a 1.5 μm depth resolution and a sub-micron lateral resolution (73). Another exciting advancement has come with Tip-enhanced Raman spectroscopy (TERS) which aims for molecular mapping at the nanoscale. A distinctive aspect of TERS is its sensitivity and

increased spatial resolution when compared to that of conventional Raman making it appropriate for analysing interactions and the structure of polymers with nano-structures (74). Making Raman with <100 nm spatial resolution is possible using TERS (75). TERS application hinges on correct tip condition and structure being key for the ability to produce an improved Raman signal. Further research is still required to fabricate reliable tips which allow for a reduced signal to noise ratio. SEM-Raman and TERS ownership is considered expensive and consequently is a capability that is not widely available.

Raman in general has an interaction escape volume greater than $\sim 1.5 \mu\text{m}$ (dependent on the wavelength and the material) which means that for biomaterial analysis, which demands information at nanoscale depths, Raman fails to provide the required surface sensitivity. Raman profiles are currently only able to provide material characteristics on the micron scale where information is based on taking averages across the materials surface (first monolayer) /subsurface. Despite these limitations Raman is still considered a valuable tool for characterising the sub-surface chemical composition of biomaterials.

2.2.4 X-ray photoelectron spectroscopy (XPS)

X-ray photoelectron spectroscopy (XPS) is a spectroscopy technique that exploits the *photoelectron effect* where the exposure of a material to electromagnetic radiation results in the consequent emission of electrons, identified as photoelectrons, from the material. Emitted photoelectrons are captured by detectors which enable measurement of the energy of the

photoelectron emissions. Measuring the energies of the photoelectrons provides insights into the chemical elements of the material by calculating the energy emitted due to the work function and binding energy of an element. Calculating the binding energy of the emitted electron allows the XPS technique to characterise sample materials through element identification, chemical composition and distributions (76). XPS can be used to qualitatively display the change in chemical bonding as a consequence of a shift in binding energy. An example XPS spectrum is given in Figure 9. This XPS spectrum shows elemental measurements of non-treated and plasma treated polypropylene (PP) modified for use as a potential biomaterial (77). Plasma treated PP exhibiting a shape change of its XPS peak compared to that of untreated PP. The visible shoulders on the high bonding energy side of treated PP suggests that more O containing (and COOH/COOR @ 289.2 eV) functional groups are introduced by the plasma treatment of PP.

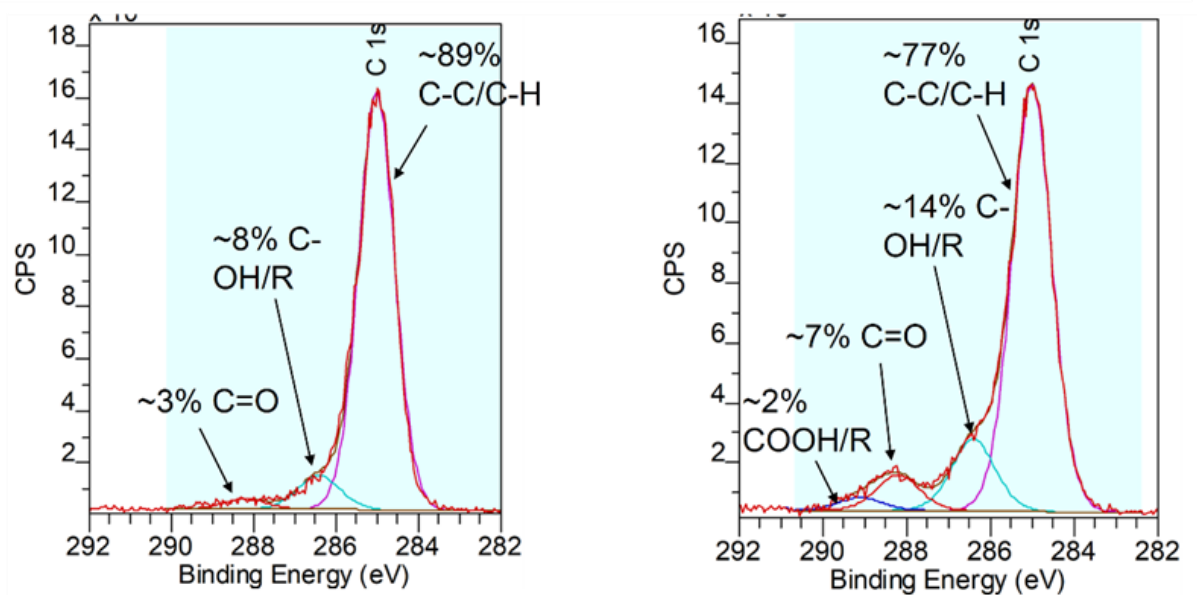


Figure 9: X ray photoelectron spectrometer (XPS) peak fits of the non-treated and plasma treated polypropylene (77).

XPS has been shown to be a highly sensitivity technique for inorganic and organic materials (78) capable of characterising the surface of sample materials (79). XPS uses monochromatic X-rays to bombard the sampling volume, resulting in the emission of photoelectrons whose energies are representative to the chemical bonding present. XPS uses such X-rays as the electromagnetic radiation source usually at an energy of <1.5 KeV. This relatively low energy beam consequently results in the typical photoelectron emission escape depth being between 1-10 nm of the materials surface (76). The shallow escape depth of the photoelectrons makes XPS a valuable technique in the analysis of the chemical characterisation of biomaterial surfaces (80, 81).

XPS has many strengths as a polymer characterisation capability but it also has limitations. Significantly, XPS is capable of undertaking chemical surface mapping but it does not possess the ability to capture nanoscale resolution of a material's surface (82). Therefore, it is considered that XPS alone would not provide a full scope characterisation capability without other complimentary surface imaging techniques at an appropriate image resolution. Additionally, the physical size limit of an XPS target sample at < 2.5 cm introduces restrictions for materials where cutting of the samples to fit the apparatus may lead to deformity or contamination of the material surface.

2.2.5 Atomic force microscopy (AFM)

For the characterisation of polymer materials, the AFM technique has a number of attractive features particularly the absence of the need for the sample to undergo any pre-analysis treatment or be subject to a vacuum during analysis.

Avoidance of the need to apply treatments to subject samples does allow the technique to be applied to a range of materials that are sensitive to harsher test environments, including polymer derived biomaterials.

AFM employs a cantilever to which is attached a sharp tip of approximately 20 nm in diameter. The AFM tip, usually comprising of Si, moves in reaction to tip-surface interactions (as shown in Figure 8). Measurements of tip movement are taken by using a photodiode to focus a laser beam (83). Tip geometry may be selected according to the characteristics of the samples surface topology, the image line for tips with both large and small opening angles can be seen in Figure 10 (84). Appropriate tip selection is essential as, a larger diameter tip can describe a significantly different image line depending on the topology characteristics of the sample. AFM instruments typically have horizontal resolutions of around 1 nm and vertical resolutions of less than 0.1 nm (85). For characterising biomaterials AFM has a number of advantages. It is feasible to measure the scale of the nano-structures quantitatively due to AFM images being represented in 3D (85).

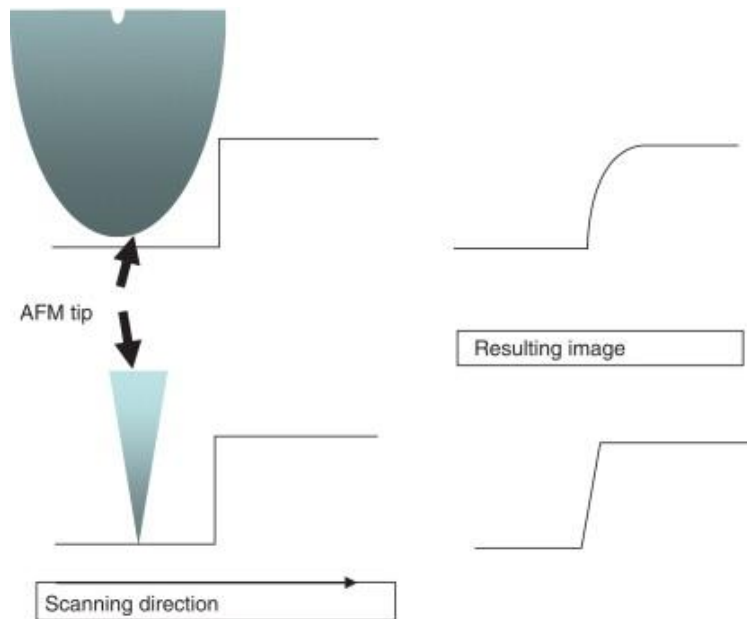


Figure 10: Image taken from (84) “Influence of the tip geometry on the resulting image line for a tip with large opening angle (above) and small opening angle (bottom). In the case of a large angle, the convolution leads to a significant change in the slope of the measured image line.”

However, despite the successes of AFM it does come with disadvantages for use in characterising biomaterials. A significant restriction on the overall effectiveness of the AFM toolset for polymer characterisation is its limited magnification capability, denying it a true multiscale analysis range unlike the electron microscope linked techniques described above. Another limitation is that a scanning electron microscope typically has an image size for a signal scan in the millimetre range whereas AFM is limited to scans of approximately 150 square micrometres (83). Thermal drift linked with a relatively slow scan rate also has the potential to induce thermal derogation within sensitive polymer derived biomaterials. A prerequisite for material samples to be produced with a ‘flat surface’, possible through cryomicrotoming, to permit surface imaging makes AFM a poor choice for imaging polymer derived biomaterials as this pre-treatment will eliminate or modify key individual

surface topology features. The surface features of biomaterials as previously discussed play an essential role in the attachment of cells through their chemical and topographical properties. Without a flat surface AFM suffers from tip wear which makes it very difficult to accurately reproduce results.

2.3 Perspective on current state of biomaterial characterisation and the potential of the scanning electron microscope.

As summarised in Table 1, to date there is unquestionably an extensive range of biomaterial characterisation techniques. These methodologies together allow for a detailed overview of biopolymer chemistry and morphology at various length scales. Imaging techniques, perhaps, give the most detailed overview of surface information and offer accurate material identification at the nanometre scale. However, TEM in common with other imaging techniques does not possess the ability to characterise molecular scale properties including bulk averaged polymer crystallinity or orientation. This prevents most researchers having access to high quality morphology characterisation data without cutting edge apparatus and associated proficiency. Included in Table 1 but yet to be discussed is a conventional SEM analysis. In this thesis, it is proposed that novel techniques integrated with the capabilities of a scanning electron microscope (SEM) has the potential to offer a viable solution to this problem.

Each of the methods evaluated have their advantages and disadvantages as discussed. For biomaterial characterisation use, only a select few allow crucial surface analysis to be performed at the nanoscale (AFM, XPS, EELS). Of these

only two allow for chemical analysis conclusions to be drawn (XPS and AFM). Unfortunately, XPS does not allow nanoscale resolution for chemical mapping and AFM does not allow multiscale analysis and suffers with tip wear related issues. With that said, there is to date no analysis method capable of multiscale (micron – nano), chemically mapping, which can be employed on beam sensitive biomaterials. The requirement for multiscale, high resolution, chemical mapping is yet to be satisfied.

Table 1: Comparison of the strengths and weaknesses of biomaterial characterisation methods.

Characterisation Method	Strengths	Weaknesses
Energy Dispersive X-ray Spectroscopy (EDX)	<ul style="list-style-type: none"> -Can characterise the elemental composition -In conjunction with TEM and SEM microscopes, EDX technique is capable of producing elemental distribution maps -Elemental depth information of a sample is possible 	<ul style="list-style-type: none"> -Some elements do have overlapping EDX peaks so that interpreting the data sometimes requires experience -Low atomic number elements (H to Be) cannot be detected. Which is important for polymers consisting of C, N, or O. -Does not provide an insight into the topography of nanoscale structures
Electron Energy Loss Spectroscopy (EELS)	<ul style="list-style-type: none"> -Capable of identifying the elemental components of a target sample - The sensitive response and high energy based resolution to a samples configuration and composition make it very effective and powerful tool. -For light elements the sensitivity of EELS is superior to that of EDXS 	<ul style="list-style-type: none"> -Limited in that it does not provide information on the topographical structure -High energies could damage beam sensitive biomaterials -Analysis requires that 'thin' samples must be used
Raman Spectroscopy	<ul style="list-style-type: none"> -Fast and reliable in generating a materials chemical spectra -SEM-Raman could attain a sub micron lateral resolution and 1.5 μm depth resolution - Raman mapping can be incorporated into SEMs to obtain both local chemical and microstructural data concurrently. 	<ul style="list-style-type: none"> -Issues stem from its poor lateral resolution -Difficult to interpret data -Only able to give bulk material characteristics on the micron scale

Characterisation Method	Strengths	Weaknesses
X-ray photoelectron spectroscopy (XPS)	<ul style="list-style-type: none"> -Technique is able to characterise sample materials element identification, chemical composition. -Highly sensitivity technique for inorganic and organic materials -The shallow escape depth of the photoelectrons makes XPS a valuable technique in the analysis of the chemical characterisation of surfaces 	<ul style="list-style-type: none"> -Not capable of undertaking chemical surface mapping at nanoscale resolutions -Expensive
Phase-contrast AFM	<ul style="list-style-type: none"> -Can deduce 3-dimensional material morphology -No need for the sample to undergo any pre-analysis treatment -Can distinguish between different materials, providing spatial distribution information - Does not need vacuum 	<ul style="list-style-type: none"> -Limited magnification capability denying it a true multiscale analysis range -Signal to noise ratio issues -Management of tip sample forces required
Conventional SEM	<ul style="list-style-type: none"> -Recent SEM`s have now have a lateral resolution competitive to that of TEM - High productivity, minimal sample preparation 	<ul style="list-style-type: none"> -Data can be difficult to reliably analyse, open to interpretation

As noted in Table 1, SEMs are already commonly accessible in universities and industry throughout the world. Scientific advancements over recent decades have enhanced the spatial resolution achievable in an SEM to a level competitive to that of a TEM (86). For high-resolution biomaterial characterisation, conventional secondary electron (SE) based SEM techniques are not optimal. Different polymer structures found in biomaterials display similar topography which can result in the generation of contrast images which are problematic to interpret. EDX and backscattered electron (BSE) imaging are two commonplace techniques for material identification using the SEM, conventional arrangements of these methods are deficient in the spatial resolution essential to evaluate the nanoscale features which are widely considered as key for the analysis of biomaterials. This thesis is focused on the evaluation of a novel, SEM based surface sensitive imaging technique, capable of overcoming current conventional analysis shortfalls by providing nanoscale chemical mapping.

Prelude – For section 2.4 of the literature review some of the sections provided have been reproduced from (N.T.H. Farr, S.F. Hamad, E. Gray, C.M. Magazzeni, F. Longman, D.E.J. Armstrong, J.P. Foreman, F. Claeysens, N.H. Green, C. Rodenburg: Identifying and mapping chemical bonding within Phenolic Resin using Secondary Electron Hyperspectral Imaging. *Polym. Chem.*, 2021,12, 177–182). Sections which include wording from this publication are clearly stated before the section. This is an open access article under the terms of the Creative Commons Attribution License, which permits use, distribution and reproduction in any medium, provided the original work is properly cited. I, Nicholas Farr am the first author of this publication and wrote the manuscript, including the sections included in this thesis.

2.4 Scanning Electron Microscopy

Release, acceleration and focusing of electrons from an electron gun to form a narrow beam which is scanned over a target sample (See figure 11) are the core operating principles of a Scanning electron microscope (SEM) (87). Continuing developments in ease of use, sample preparation techniques, beam control, improved detectors and the ability to capture scanning results within a digital database for post-scan processing have all contributed to the improvement of SEM capabilities over recent decades since its first applications (88, 89).

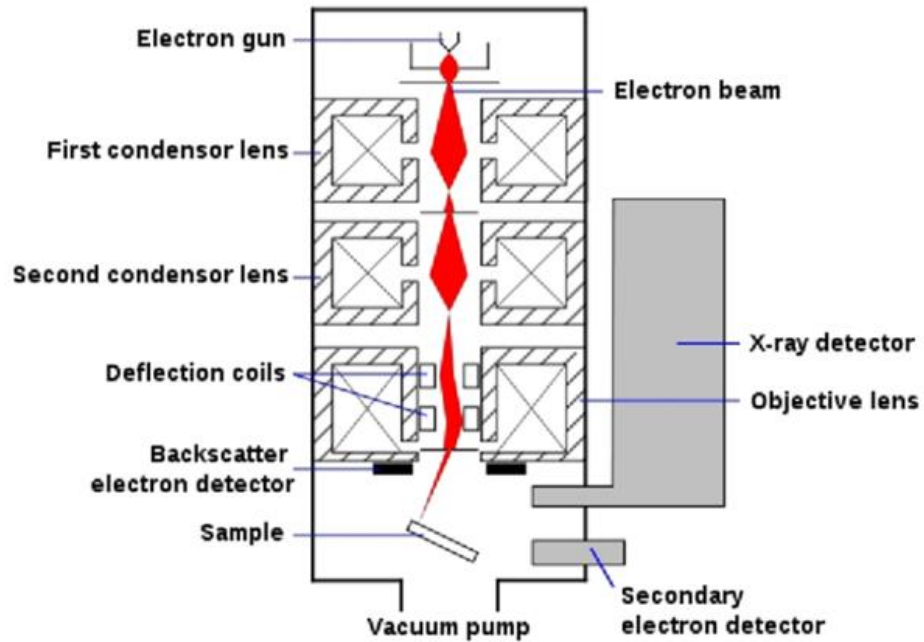


Figure 11: Basic representation of an SEM. Image amended from (90)

Inclusion of electromagnetic lenses focuses the incident e beam and ensures that electrons leaving the sample can reach the detectors without undergoing further scattering. Usually, the electron beam is thermionically emitted from an electron gun fitted with either a tungsten or lanthanum hexaboride cathode (91). Some SEMs have a field-emission electron gun (FEG) as the beam source with the electron beam either cold-cathode or thermionically emitted using single crystal tungsten wire. This single crystal tungsten wire is shaped to a fine point less than 100 nm and commonly coated with a thin layer of Zirconium Dioxide emitter (ZrO_2) (92). This layer is applied to decrease the surface work function as set in the 'Schottky' type emitter design. Within the column a series of electromagnetic lenses focus the primary electron beam in the direction of the target sample (92). Magnetic fields within the lenses are employed to accurately focus the electron beam. To control the current reaching the target sample an objective lens aperture and a pair of condenser lenses are installed. Through

varying the current flowing through the objective lens coil the electron beam can be focused on to the target sample (93).

Scanning the surface of a target sample is completed using a raster based approach with distinct steps of the electron probe which correspond to a single pixel in an SEM image (94). The electron signal produced from the sample at each step can be captured by a range of possible detectors (See section 3.4). The SEM image is constructed by repeating the steps until all the selected surface area is scanned. The resolution of the image obtained for a given probe size is given by the target material and primary beam energy. The electron beam probe only interacts with a limited interaction volume due to the effect of electron interactions (More information given in Section 2.4.3). This volume is determined by the primary beam energy. The greater the primary beam energy is the larger volume of sample interaction. This incident beam interaction volume is demonstrated in Figure 12 with a characteristic 'waterdrop' shape.

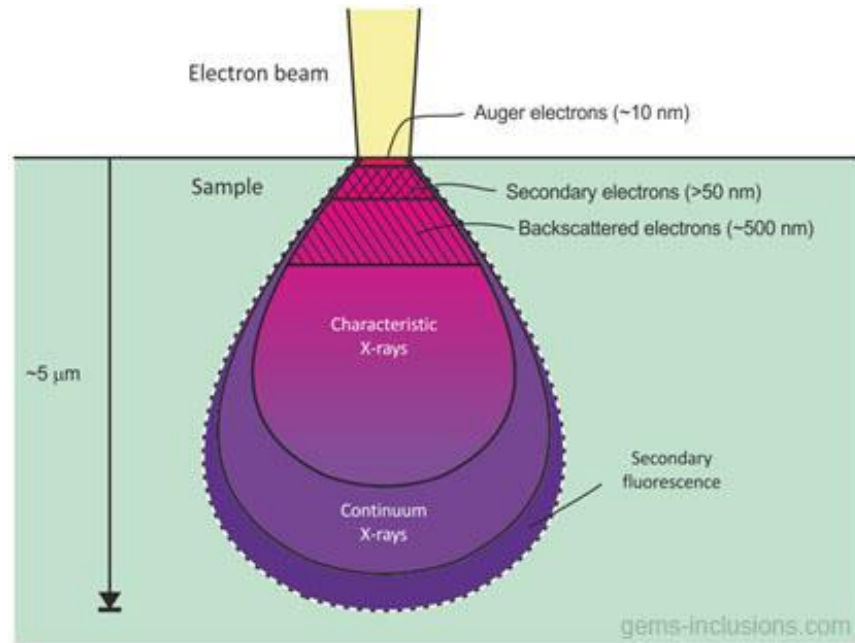


Figure 12: An electron beam interaction diagram. Obtained and amended from (95).

Carefully chosen SEM operating techniques combined with innovative post processing of captured data forms the basis for an approach called secondary electron hyper spectral imaging (SEHI). The evaluation of this technique is the main objective of this thesis and section 2.4.6 introduces SEHI's development. But first a comprehensive understanding of the characteristics and application techniques of SEMs is an essential prerequisite for researchers to fully exploit the potential of the SEM in their work. In addition to competence in the basic operation of the equipment, a comprehensive understanding of images and spectra obtained in the SEM requires in-depth knowledge of electron beam specimen interaction and the equipment (in particular detectors) (96).

2.4.1 Electron Detectors with an SEM (Section published in Farr et al Polym. Chem., 2021,12, 177–182)

Both SE and BSE emissions can each be exploited to extract complementary sets of information from a target sample within an SEM. Modern SEMs are configured to utilise detectors which have the ability to distinguish between these two types of emissions and are capable of filtering either SEs or BSEs from an intermixed sample image signal. As previously highlighted the ability to research surface effects in polymers at the nanoscale level relies primarily on the capture of target images built from SE1 emissions. The most common detector employed in SE imaging is the Everhart-Thornley detector (ETD). ETDs mix SE1, SE2 and SE3 emissions, this approach provides limited resolution with SE images being hard to interpret in respect to their specific SE emissions. Alternatively, the other commonly used SE detector is the Through-lens detector (TLD). The TLD suppresses SE2 and SE3 emissions to collect mainly SE1 emissions (92). By virtue of collecting SE1 emissions the TLD can provide high resolution surface images, suited perfectly for the use of chemically mapping the nanoscale surface of polymers.

2.4.1.1 Everhart-Thornley detector (ETD)

The electron detector installed within the majority of current SEMs is the ETD. ETD detectors possess the ability to detect both BSE and SE emissions. ETD detectors are composed of a scintillator mounted within a Faraday cage located in the specimen chamber (97). When it is stimulated by target emitted electrons a luminescence signal is generated by the scintillator. The Faraday cage works

to reduce the unwanted background electromagnetic resonance that may distort the detectors signal. For applications supporting biomaterial research the ETD is primarily employed for its SE detection capability rather than BSE. The luminescence signal generated by the scintillator releases photons which travel to a photomultiplier via a light guide and photocathode (97). Prior to arriving at a collector the photomultiplier amplifies the signal (see figure 13).

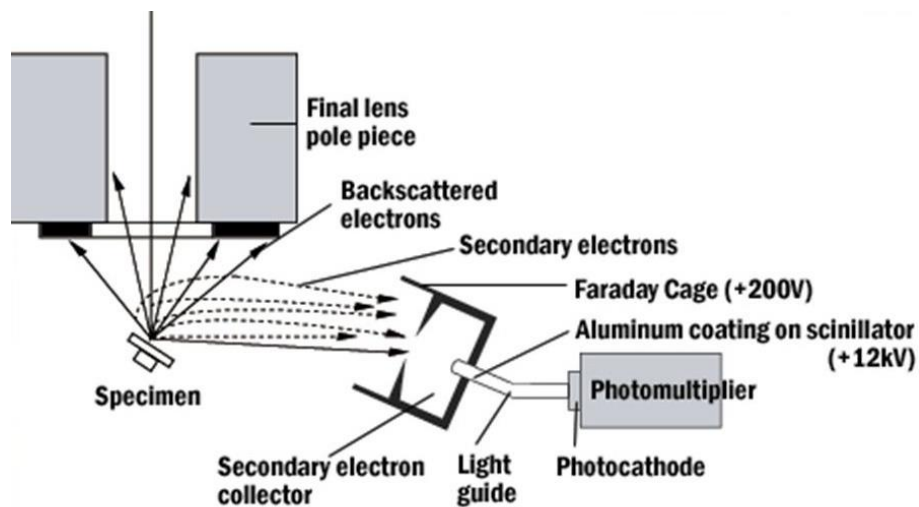


Figure 13: Everhart-Thornley detector schematic. Obtained and amended from (98).

Creating a voltage bias in the Faraday cage component of the ETD enables the ETD to be selective as to which electrons can reach the detector based on the electrons energy. This technique allows low energy electrons to be detected regardless of their emission energy. Figure 13 illustrates an example ETD set up. To capture an image signal composed of mainly SEs an ETD bias of approximately +250 V will be required to swamp the low number of BSEs likely to arrive at the detector (91, 97). Consequently, switching the ETD to a negative bias would cause low energy SEs to be repelled from the ETD and therefore the high energy BSEs would dominate the image signal. For polymer derived

biomaterial research where the configuration of the SEM is optimised to support topographical nanoscale analysis, an ETD detector biased to approximately +250 V is considered appropriate to deliver superior SE detection.

2.4.1.2 Through-lens detector (TLD) (Section published in Farr et al Polym. Chem., 2021,12, 177-182)

The detector of choice in this thesis and all subsequent section was the TLD. The TLD selected is depicted in figure 14. This TLD arrangement utilises electrostatic deflectors to enable the detection of SEs when set to a high-resolution immersion mode where target samples are immersed in a magnetic field and the TLD is positioned above the objective lens of the electron column (99).

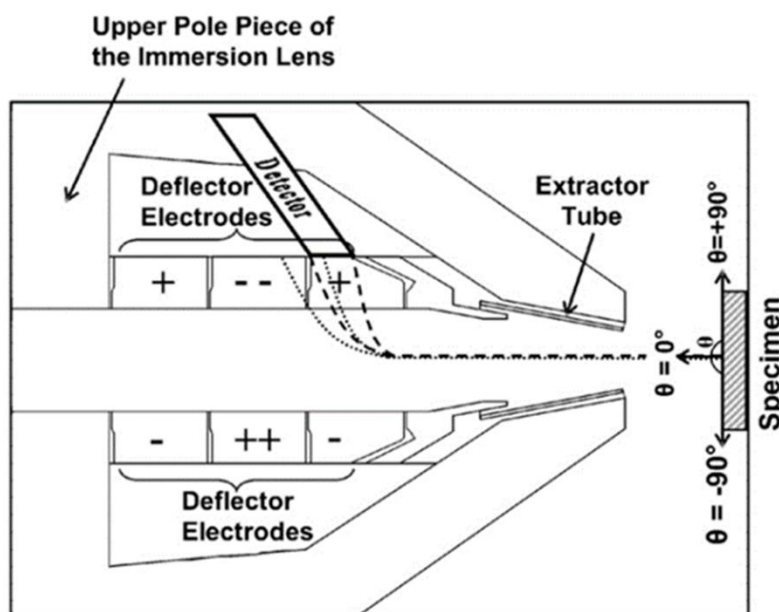


Figure 14: Schematics of TLD arrangements in SEMs manufactured by FEI Co. XL-30 design TLD. Adapted from (99) with permission from Elsevier.

Configuration of TLD detectors varies according to both the manufacture and the actual SEM model. Figure SI 3 illustrates a FEI XL-30 design which is a widely used SEM having a TLD integrated into the incident electron probe consisting of a scintillator detector and a 'deflector' electrode (99). The deflector is installed as a guide to drive SEs towards the detector and is set to a bias of -60V. This bias can be adjusted to collect *SE1* emissions from energy ranges of interest. Additionally, the SEM's pole-piece incorporates a positively biased electrode whose purpose is to help attract SEs within the specimen chamber towards the detector. TLDs predominantly detect *SE1s* which provide the highest spatial resolution information as they are emitted by the target sample through direct interaction with the primary electron beam.

2.4.2 Imaging polymer derived biomaterial in a SEM

Three key challenges that need to be addressed by researchers to effectively use an SEM in the analysis of polymer based biomaterials are:

- 1) The development of SEM techniques that are capable of producing chemical contrast images at higher lateral image resolution.
- 2) A reduction of polymer charging whilst imaging. Often due to the non-conductor nature of polymers.
- 3) The reduction of radiation damage to the polymer sample through beam interaction

Innovations in the development of the low-voltage scanning electron microscope (LVSEM) have made significant steps towards addressing these

challenge. An LVSEM is essentially an SEM operating with primary beam energy values of between 1 and 2 keV. Key advancements in electron optics and developments of the FEG gun have enabled LVSEMs to operate at nanometre resolution with low beam voltages (100). It was not feasible for previous generations of SEM designs to operate satisfactorily at these low beam voltages (100). Polymer material analysis was limited by only having access to low quality images due to the low energies with the beam resulting in lack of resolution prior to these developments (100).

2.4.2.1 Issues with resolution and contrast

Previous work has made clear that the existing SEM apparatus lacked the spatial resolution needed for analysis of organic polymer samples (101). To enable LVSEMs to produce high resolution images at low beam energies (between 1-2 KeV) significant developments in the capability of electron optics has been necessary, particularly in the field of beam focus and detection techniques (101, 102, 103).

One common approach adopted is setting the target sample to a negative bias voltage, the electron beam exiting the column can then be decelerated prior to interacting with the sample (see figure 15).

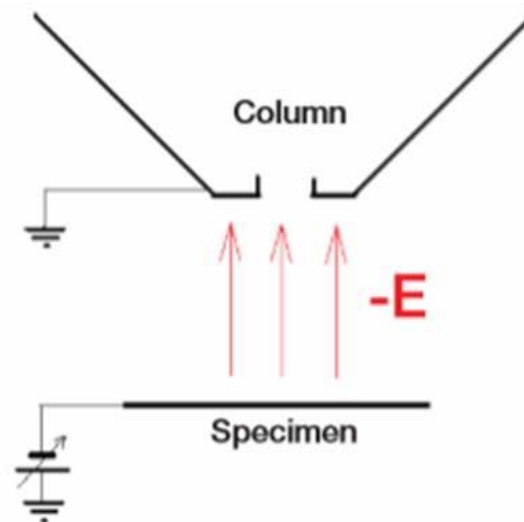


Figure 15: The process of electron beam deceleration

The practical disadvantage of using such techniques is that to achieve a high quality electron beam the electron column must generate a relatively high energy beam, however, by applying these beam decelerating techniques the electron beam voltage can be reduced prior to interacting with the sample without loss of beam quality. For most biomaterials that typically display complex geometries or have high insulating properties beam deceleration techniques are not always successful. Although through many developments the capabilities of the SEM have been constantly improved, the quality of the sample employed is still as important as the quality of the instrument (102). Sample preparation is still one of the most challenging components in achieving optimal resolution. For polymer-derived biomaterials which require analysis of the true surface of the material, this means there is a requirement not to use conductive coating of the samples prior to imaging. Conductive coatings are employed to reduce the accumulation of surface electrons, in particular for beam energies in the range of 5-20 keV, this effect can prevent electron

emissions from the target sample (102, 103). This formation of electrons on the surface creates what is observed as “glaring” on SEM images. Literature has indicated the use of freezing methods in preparation of polymer and biological samples can improve SEM image resolution (104). However, complications arise from not freezing the material quickly enough allowing the formation of damaging ice crystals within the material as a consequence of the preparation process. To overcome these issues polymer samples can instead be placed on carbon conductive tabs and imaged at lower ~1 KeV beam energies. Additionally, the dimensions of the polymer can be optimised by imaging thinner sections of the sample and using carbon conductive paint to electrically ground the samples onto the carbon mounting tabs.

2.4.2.2 Reduction of sample charging

As previously highlighted, the build-up on the target sample of negative charge is a common occurrence when using an SEM at conventional voltages (5 – 20 keV) for polymers analysis (103). During the raster scanning process any negative charge that builds up on the polymer sample triggers the polymer to repel the electron beam. Distortion or obscuration of SEM images may occur through hydrocarbon contamination in conditions such as the presence of ambient hydrocarbons (105). An unwanted charge can build on the polymer when the incident electron beam probe delivers electrons at a faster rate than the sample surface can emit electrons after surface interactions. LVSEMs reduce the likelihood of this charge build-up by operating at lower beam acceleration voltages (100, 105).

The deployment of innovative beam scanning patterns, such as frame integration, is also an effective strategy to mitigate the consequences of charge build up. Frame integration scanning patterns use short dwell times (100ns) to capture within a sample area a number of frame sequences, thereby reducing polymer charging prior to integration of the frame pixels within the final image (106). The rationale for short dwell times is to facilitate the dissipation of any charge accumulated during each capture frame before the scan pattern advances onto the next frame. If charge accumulation issues are still apparent, then orientating the polymer target to a high angle relative to the electron beam has been shown to establish a geometry that promotes the escape of SEs. Coating of the polymer sample prior to imaging is also regarded as a feasible option. However, sample coating requires that the nano-structure of the polymer be enveloped with a conductive 'splutter coat' layer, such a layering approach does raise questions of whether the captured images are actually true representations of the samples surface topology.

2.4.2.3 Reducing polymer damage in SEM

Where the electron beam interacts with the target sample a proportion of the energy from the beam is transformed into heat relative to the acceleration voltage selected (105). The effects of this heating are dependent on the characteristic of the sample material but at typical SEM accelerating voltages possible deterioration in the form of; cracking, sublimation, decomposition and deformation may take place.

Heat can build up within the sample as a direct result of the collisions involved in the inelastic scattering of primary beam electrons. Inelastic collisions are capable of causing effects such as crosslinking and chain scission through energy transfer to the target sample. Studies have shown at primary beam energies of 20 – 30 KeV surface temperatures are as high as 53°C (107). Such surface temperatures is problematic when considered that biopolymers have been shown to undergo initial heat induced crystallisation at ~45°C (108). The ability of a sample to withstand this heat is dependent on the samples dimensions, the beam current conditions and the likelihood of radial conduction heat loss due to the samples thermal conductivity.

The poor thermal conductivity of organic polymer materials results in a higher propensity for the heating effects of beam currents to inflict thermal damage to the samples through only small increases in temperature (105). However, with LVSEM technology using lower acceleration voltages than typical SEM practice, sample damage is expected to be also be correspondingly less. LVSEMs using acceleration voltages of 2 KeV or less are considered to be capable of minimal target sample damage (107).

2.4.3 Background of the interpretation of Secondary electrons (Section published in Farr et al Polym. Chem., 2021,12, 177-182)

The primary electron beam interacts with atoms within the material by causing electrons to be emitted. These emissions are as a result of a range of physical interactions (93). Figure 13 shows the interaction volume of a primary electron beam and a range of association emissions.

Elastic interactions are those which change the path of the incident electrons in the primary electron beam probe whilst having a negligible effect on their kinetic energy. Inelastic interactions in contrast are those which result in a loss of kinetic energy of the incident electrons (94). High energy electrons that are emitted by an elastic interaction of an incident electron with the nucleus of the material samples' atoms, are designated as back scattered electrons (BSE). The energy of BSEs is comparable to that of the beam probe's incident electrons. Electrons emitted from the sample at lower energy are categorised as secondary electrons (SE). SEs typically display energy voltage of less than 50 eV. SEs result from inelastic scattering and are the consequence of either collisions within the electron cloud or by interaction with loosely bound electrons in the material's structure.

As stated previously the electron beam probe will only interact within a finite interaction volume due to the effect of inelastic interactions. This volume is depended on the primary beam energy. The greater the primary beam energy is, the greater volume of sample interaction. This incident beam interaction volume is represented in figure 16 with a characteristic 'waterdrop' shape.

SEs are the sample's emissions that are associated with SEM images (109). SEs may be emitted from the materials at relatively low kinetic energies, < 10 eV, as a result of potential interaction with electron clouds. The low kinetic energy places a significant limit on the actual escape depth of SEs emitted from a sample, which can often be < 10 nm, and as a consequence SE derived images are inherently surface specific. To interpret the images generated by an SEM it

is essential to understand how the SE contrast is captured. Selection of an appropriate detector by the user is also dependent on this knowledge.

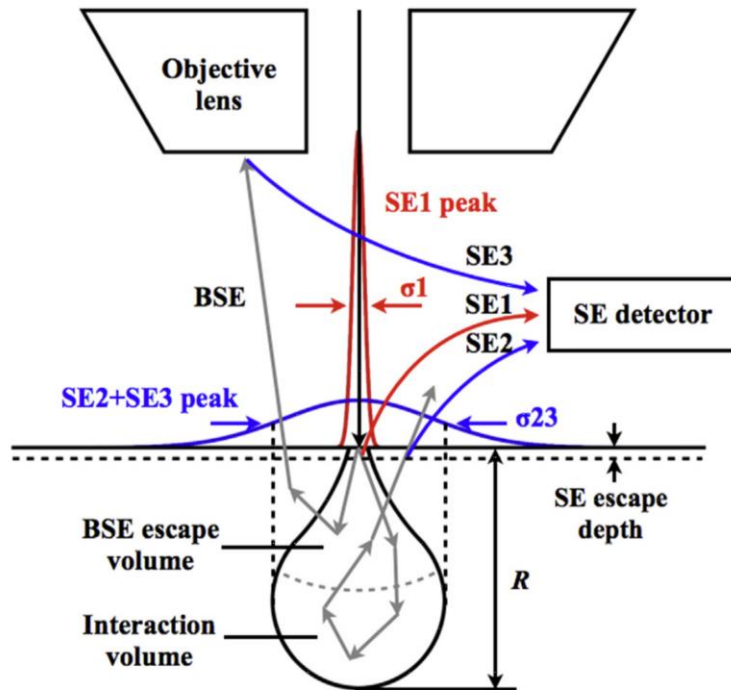


Figure 16: Diagram shows the relative escape depths of SEs and BSEs and their interaction paths prior to detection. Image adapted from (110) with permission from Elsevier. “Schematic of the electrons emitted from a range, R , below the surface of the sample. SE1 is generated from impacted electrons (IE) right after incidence, SE1 have spatially localised information (s_1). Then, IE spread to interaction volume with a size of range R .”

There are a number of different ways that SEs are detected in an SEM (See figure 16). The majority of SEs detected originate as a result of inelastic interactions between the probe incident electrons and the sample (110), this is in addition to collisions between BSEs and the SEM chamber components after emission from the target sample surface. (This process is depicted in figure 16) These different sources of SEs are termed *SE1*, *SE2* and *SE3* retrospectively. SEs from each of these difference sources exhibit dissimilar signals types for both resolution and contrast. When undertaking SEM analysis of a polymer`s

topographical nanostructure, it is essential to configure the apparatus with a detector which can isolate *SE1* from *SE2* and *SE3*. Despite both *SE1* and *SE2* emissions providing topographical contrast due to their angular distribution and their short escape depth (as shown in Figure 17). *SE1* emission differs from that of *SE2* as a result of their interaction paths, *SE2*s emissions are generated from BSEs when they pass through the surface, when exiting the sample, unlike *SE1* which are generated from impacted electrons directly after beam incidence. *SE1* emissions therefore possess spatially localised information and are suitable for processing into high resolution surface images.

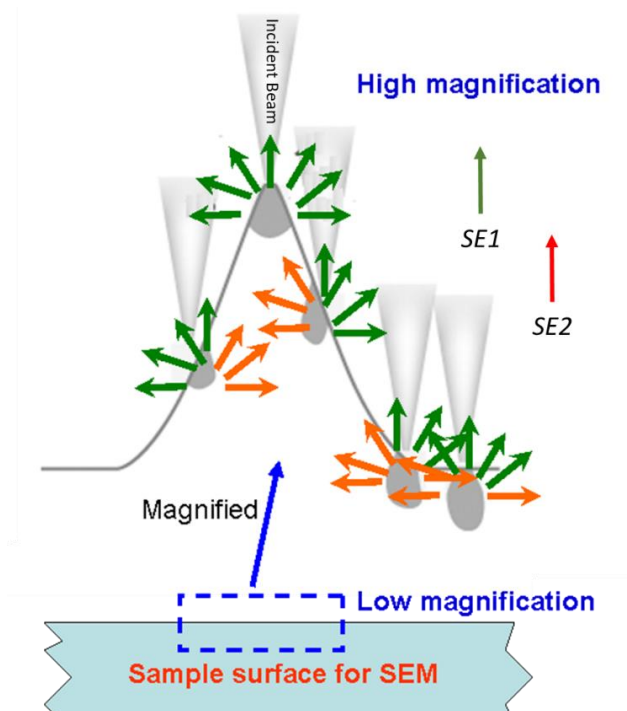


Figure 17: Diagram showing the topographic effect on SEM contrast of *SE1* and *SE2* emissions. Figure amended from (111)

2.4.4 Information contained in secondary electron spectra (SES) (Section published in Farr et al Polym. Chem., 2021,12, 177-182)

Electrons emitted from a target sample through probe electron/material interactions within the SES can be detected and displayed by way of spectra constructed according to their measured energy ranges. From the resultant spectra, conclusions can be drawn regarding the samples chemical composition and structure. SES is not a recent development for material characterisation, SES has been investigated since 1947 (112). Over the last few decades, SES has only recently started to flourish through innovations in instrumentation, signal processing and imaging proficiency (113, 114, 115).

The process of developing SE spectra wholly relies on the probe electron – material interactions. SES measures electron emission energies post inelastic sample collisions. SES benefits from employing a low KeV (between 0.5-2 keV) primary electron beam which makes it possible for the SES to collect the spectra of beam sensitive materials. Although, SEs are produced throughout the primary beam interaction depth, only SEs emitted within the SE escape depth can be detected, as SEs emitted at a greater depth will be absorbed by the bulk of the sample material. The SE shallow escape depth raises the issue of surface contamination affecting the spectra results, a problem faced by other surface analysis techniques. However, SES has been shown to have operational characteristics that allow it to overcome substantial surface contamination to produce accurate spectra that are reproducible and reveal characteristics of the underlying material (113, 115). In contrast EELS provides an average measurement over the material samples thickness and does not allow for high

resolution surface characterisation. For polymers which require a tailored surface, such as polymer derived biomaterials, the SES form of detailed surface analysis is considered to be an essential perspective due to the fact that established cells react to a biomaterial's surface on the nanoscale level.

Although, SES, EELS and XPS all have strengths as material characterisation methods, the singular ability of SES to support the secondary electron hyperspectral imaging (SEHI) technique is considered particularly advantageous for the analysis of a range of material types. As distinctive SE energy spectra have been collected for many decades (114, 115) it is often wrongly assumed that SE images show only topographical contrast. However, with recent progress in SE spectra analysis and energy-filtering detection, advances in capability now enable the capture of spectral images from selected distinct SE energy ranges, which studies have shown to carry chemical and functional information (116, 117, 118). Both SE and BSE emitted at low primary beam energy ranges contain chemical information. Lower energy SEs contains information about valence bands and higher energy SEs (*SE2*) have been associated to the atomic number of the elements from which they are emitted (116). BSE imaging has demonstrated a capacity to provide chemical contrast images of materials where topographical features are negligible, however, SEHI can provide comparable images of materials at significantly enhanced image resolutions (117). Standard SEM images are compiled from all surface emitted SEs without discrimination of their energy ranges. In contrast, SEHI compiles a series of images based on the specific energy ranges of emitted SEs. SEHI

software processes capture this series of energy range images to construct an inclusive SE spectrum for the material.

SE emission has also been used to assess structural changes through topographical changes. Previously published work has shown that surface morphology effects are particularly meaningful in higher energy emissions (117, 118, 128, 131). However, if a user wished to avoid topographical SE emissions and reduce the possibility of surface morphology effects, attention should be given to emissions below 6 eV. With previous work showing that these energy ranges are suitable to functional group emissions and not surface morphology effects emissions (116, 117).

Figure SI 12 (graphical abstract) displays the process by which information contained in the SEHI spectrum provides the basis for mapping chemical changes within the surface of materials. This capability is predicted to provide new opportunities for researchers to characterise novel polymer materials. The value of the SEHI characterisation technique has successfully been demonstrated in range of applications varying between; the analysis of molecular orientation within organic electronic devices, semi-crystalline polymers chemical mapping and exposing variations in nanostructures that form natural materials (116, 117, 118, 119). SEHI can be summarised as a technique that is responsive to surfaces and is capable on beam sensitive materials of resolving chemical, compositional and structural differences at the nanoscale level. It is proposed that an effective microanalysis tool for nanostructured polymers results from the integration of the capabilities of a low voltage SEM and those of secondary electron microscopy.

2.4.5 Modelling secondary electron spectroscopy (SES) (Section published in Farr et al Polym. Chem., 2021,12, 177-182)

SE emissions captured in electron microscopes has been the subject of an increasing number of studies using a modelling approach that simulates the production of secondary electron emission from sample materials. Many of these studies have adopted the Monte Carlo approach to simulation modelling. Within a Monte Carlo simulation a statistical probability is assigned to every event, with the probability figure based on first principles and available experimental results. Multiple events are simulated until the process yields a statistically relevant result. Monte Carlo simulation, based on a conductive polymer using experimental data, has revealed that a material's local crystallinity and electron affinity directly influence the SE energy spectrum (120, 121).

In addition to polymer analysis, further insightful work has been directed at carbon species analysis. The characteristic SE spectra of sp^3 hybridised, sp^2 hybridised, or hydrocarbon contamination moieties captured using a combination of experimental studies and Monte Carlo based simulation has been published (118, 120, 122). This result has enabled carbon based contamination and deposition induced by the electron beam within a SEM to be identified and mitigated. Through applied modelling simulations, significant advances in the appreciation of time dependence both in secondary electron emission (123) and in the charge dynamics of insulators (124) have been made.

2.4.6 Introducing Secondary Electron Hyperspectral Imaging (SEHI)

As previously mentioned, an ideal characterisation technique will without changing either the chemical composition or structures architecture, provide comprehensive multiscale information pertaining to the materials nanostructure. Many of the existing characterisation techniques evaluated have a role in the characterisation of biomaterials but are unable to fulfil all the requirements due to inherent limitations. Enhanced material characterisation capabilities including; novel surface chemical spectroscopy and imaging methods on nano- and micro-scale levels are considered necessary to provide the fundamental analysis steps needed to support biomaterial deployment. Only a subset of existing characterisation techniques discussed can perform surface analysis at the nanoscale. Of these, none can chemically map of beam sensitive biomaterials at multiscale.

This thesis explores the recently developed technique of SEHI with the aim to evaluate its ability to fulfil the requirement for as a high resolution, multiscale, chemical mapping characterisation method applicable to polymer based biomaterials. SEHI captures and analyses spectral information from material samples providing a chemical fingerprint of polymer derived biomaterials at surface depths of >10 nm. Figure 18 shows a Venn diagram of how SEHI development has been made achievable by the SEM advancements previously discussed. Combining both SE imaging and the collection of SE emission spectra by means of the SEM provides the foundation for the SEHI and has been extensively discussed (125, 126, 127, 128). Briefly, SEHI constructs a series of images based on the target area of the material sample, where a selected SE energy band forms each image. Figure 19 shows an example of a range of image

slices taken at different energies which make up a SEHI image stack. In order to allow chemical information to be resolved on both nanometre and sub-nanometre scales by SEHI, an LV-SEM instrument with a probe diameter appropriate to these scales is required (129). The ability of SEHI to compose spectral images that suppress topographic contrast whilst containing functional and chemical information has been dependent on modern advances in data analysis and energy filtered SE detection (125).

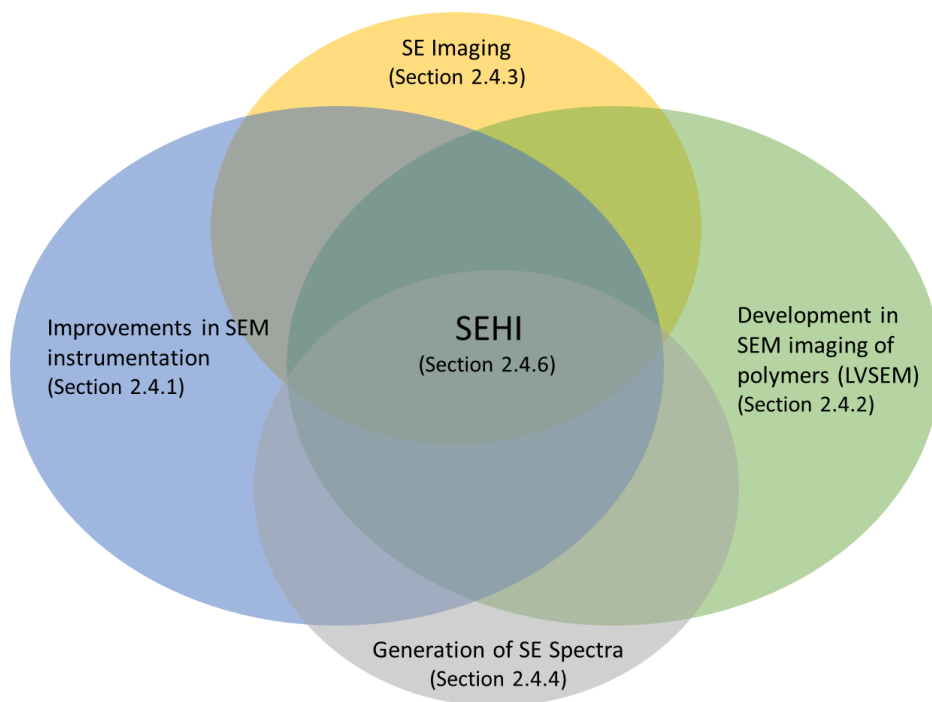


Figure 18: Venn diagram of the development of secondary electron hyperspectral imaging (SEHI).

Determining crystallinity in polymer samples using SEHI has made swift advances (120, 121, 126). Previous research work had established that the SE spectra for certain hydrocarbon materials are substantially affected by excitation of intramolecular vibrations (118, 121). The successful results of these

studies has increased confidence that deployment of SEHI could enable a unique characterisation method to be established that will support the evaluation, at a nanoscale level, the mechanics of cellular response within a biomaterial formed environment. Effective deployment of SEHI is anticipated therefore to ideally play a major role in the development of functional tissue scaffolds built from novel biomaterials.

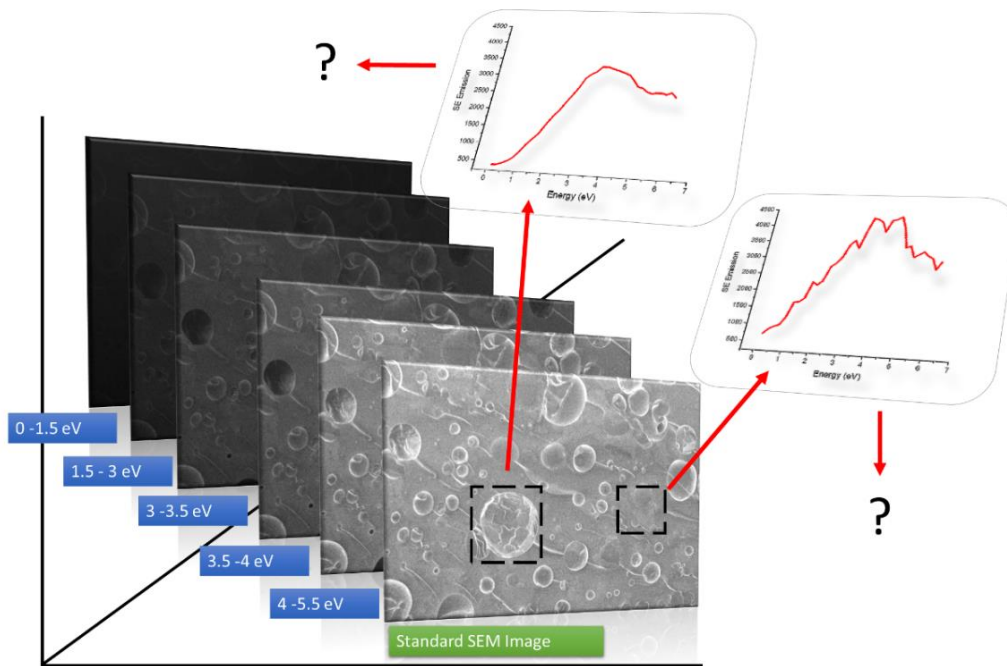


Figure 19: An overview of the process of secondary electron hyperspectral imaging (SEHI) Amended from (130).

Although it has been shown that the SEHI technique can provide extensive chemical and synchronised structural characterisation information, two key questions remain over its future use for the characterisation of polymer derived biomaterials. 1) Can SEHI deliver insights into the mechanical properties of a material? 2) Is the captured SE spectra able to identify functional groups that play a key role in biomaterials engineering /TE? And if so can SEHI map these

functional groups at the nanoscale? This thesis will focus on providing evidence to determine the answers to these questions.

References for Section 2.1.

1. A. Gefen: *Introduction to Biomedical Engineering Second edition*. Edited by: Enderle J, Blanchard S, Bronzino. *BioMed Eng OnLine* **4**. 44 (2005). <https://doi.org/10.1186/1475-925X-4-44>
2. O. C. S. Cassell, S.O.P. Hofer, W. Morrison, K.R. Knight: *Vascularisation of tissue-engineered grafts: the regulation of angiogenesis in reconstructive surgery and in disease states*. *British Journal of Plastic Surgery*. **55**. 603-610. (2002).
3. W. He, R. Benson: *4 - Polymeric Biomaterials In Plastics Design Library, Handbook of Polymer Applications in Medicine and Medical Devices*. William Andrew Publishing, 55-76, ISBN 9780323228053. (2014). <https://doi.org/10.1016/B978-0-323-22805-3.00004-9>.
4. E. Rabkin, F. Schoen: Cardiovascular tissue engineering. *Cardiovascular Pathology*. **11**. 305-317. (2002).
5. L.A. Loureiro dos Santos: *Natural Polymeric Biomaterials: Processing and Properties, Reference Module in Materials Science and Materials Engineering*. Elsevier. (2017). <https://doi.org/10.1016/B978-0-12-803581-8.02253-0>.
6. B. Love: *Chapter 9 - Polymeric Biomaterials*. Academic Press. 205-238. (2017).
7. X. Tang, S.K. Thankappan, P. Lee, S. E. Fard, M. D. Harmon, K. Tran, X. Yu: *Chapter 21 - Polymeric Biomaterials in Tissue Engineering and Regenerative Medicine, Natural and Synthetic Biomedical Polymers*, Elsevier. 351-371. (2014).
8. S. Jockenhoevel, K. Chalabi, J. Sachweh, H. Groesdonk, L. Demircan, M. Grossmann, G. Zünd, B. Messmer: *Tissue engineering: complete autologous valve conduit- a new moulding technique*. *Thoracic and Cardiovascular Surgery*. **49**. 287-290. (2001).
9. H. Lodish, A. Berk, S. Zipursky: *Molecular Cell Biology*. New York: W. H. Freeman. (2000).
10. M. Rothenburger, P. Vischer, W. Völker, B. Glasmacher, E. Berendes, H. Scheld, M. Deiwick: *In vitro modelling of tissue using isolated vascular cells on a synthetic collagen matrix as a substitute for heart valves*. *Thoracic and Cardiovascular Surgery*. **49**. 204-209. (2001).
11. M. Rothenburger, W. Völker, P. Vischer, E. Berendes, B. Glasmacher, H. Scheld, M. Deiwick: *Tissue engineering of heart valves: formation of a three-dimensional tissue using heart valve cells*. *ASAIO Journal*. **48**. 586-591. (2002).
12. P Taylor, S. Allen, S. Dreger, M. Yacoub: *Human cardiac valve interstitial cells in collagen sponge: A biological three-dimensional matrix for tissue engineering*. *Journal of Heart Valve Disease*. **11**. 298-307. (2002).
13. S. Li: *Hydrolytic degradation characteristics of aliphatic polyesters derived from lactic and glycolic acid*. *J Biomed Mater Res*, **48**. 342-353. (1999)
14. T. Sabu, B. Preetha, M.S. Sreekala: *In Woodhead Publishing Series in Biomaterials, Fundamental Biomaterials: Ceramics*, Woodhead Publishing. 1-46. (2018).
15. P. Tormala: *Biodegradable self-reinforced composite materials: Manufacturing structure and mechanical properties* *Clin Mater*, **10**. 29-34. 1992.

16. S. Terasaka, Y. Iwasaki, N. Shinya, T. Uchida: *Fibrin glue and polyglycolic Acid nonwoven fabric as a biocompatible dural substitute*. *Neurosurgery*. **58**. 134-139. (2006).
17. Q. Ye, G. Zünd, S. Jockenhoevel, S. Hoerstrup, A. Shoerberlein, J. Grunenfelder, J. M. Turina: *Tissue engineering in cardiovascular surgery: new approach to develop completely human autologous tissue*. *European Journal of Cardiothoracic Surgery*. **17**. 449-454. (2000).
18. P.B. Maurus, C.C. Kaeding: *Bioabsorbable implant material review*. *Oper Tech Sport Med*, **12**. 158-160. (2004).
19. G. Zünd, T. Breuer, T. Shinoka, P. Ma, R. Langer, J. Mayer, J. Vacanti: *The in vitro construction of a tissue engineered bioprosthetic heart valve*. *European Journal of Cardiovascular and Thoracic Surgery*. **11**. 493-497. (1997).
20. T. Shinoka, D. Shum-Tim, P. Ma, R. Tanel, R. Langer, J. Vacanti, J. Mayer: *Tissue-engineered heart valve leaflets: Does cell origin affect outcome*. *Circulation*, **96**. Suppl. II, II102-II107. (1997).
21. T. Shinoka, D. Shum-Tim, P. Ma, R. Tanel, N. Isogai, R. Langer, J. Vacanti, J. Mayer: *Creation of viable pulmonary artery autografts through tissue engineering*. *Journal of Thoracic and Cardiovascular Surgery*. **115**, 536-546 (1998).
22. Y. Wang, G.A. Ameer, B.J. Sheppard, R. Langer: *A tough biodegradable elastomer*. *Nat Biotechnol*. **20**. 602-6 (2002). doi: 10.1038/nbt0602-602.
23. M. Radisic, H. Park, T.P. Martens, J.E. Salazar-Lazaro, W. Geng, Y. Wang: *Pre-treatment of synthetic elastomeric scaffolds by cardiac fibroblasts improves engineered heart tissue*. *J Biomed Mater Res A*. **86**. 713-24. (2008) doi: 10.1002/jbm.a.31578.
24. W. Wu, R.A. Allen, Y. Wang: *Fast-degrading elastomer enables rapid remodeling of a cell-free synthetic graft into a neoartery*. *Nat Med*. **18**. 1148-53. (2012). doi: 10.1038/nm.2821.
25. C.G. Jeong, S.J. Hollister: *A comparison of the influence of material on in vitro cartilage tissue engineering with PCL, PGS, and POC 3D scaffold architecture seeded with chondrocytes*. *Biomaterials*. **31**. 4304-12. (2010) doi: 10.1016/j.biomaterials.2010.01.145.
26. Q. Chen, H. Ishii, G.A. Thouas, A.R. Lyon, J.S. Wright, J.J. Blaker. JJ: *An elastomeric patch derived from poly(glycerol sebacate) for delivery of embryonic stem cells to the heart*. *Biomaterials*. **31**. 3885-93. doi: 10.1016/j.biomaterials.2010.01.108. (2010).
27. C.D. Pritchard, K.M. Arnér, R.S. Langer, F.K. Ghosh: *Retinal transplantation using surface modified poly(glycerol-co-sebacic acid) membranes*. *Biomaterials* **31**. 7978-84. (2010).
28. C.A. Sundback, J.Y. Shyu, Y. Wang, W.C. Faquin R.S. Langer, J.P. Vacanti JP: *Biocompatibility analysis of poly(glycerol sebacate) as a nerve guide material*. *Biomaterials* **26**. 5454-64. (2005).
29. S. Pashneh-Tala, R. Owen, H. Bahmaee, S. Rekštyte, M. Malinauskas, F. Claeysens, *Front. Phys.*, **6**. 41. (2018).
30. Y. Wang, J. Nie, B. Chang, Y. Sun, W. Yang: *Poly (vinylcaprolactam)-based Biodegradable Multiresponsive Microgels for Drug delivery*. *Biomacromolecules*. **14**. 3034-3046. (2013).
31. X. Zhang, S. Lü, C. Gao, C. Chen, X. Zhang, M. Liu: *Highly Stable and Degradable Multifunctional Microgel for Self-regulated Insulin Delivery under Physiological Conditions*. *Nanoscale*. **5** (14), 6498-6506. (2013).
32. B.G. Keselowsky, D.M. Collard, A.J. García: *Surface chemistry modulates focal adhesion composition and signaling through changes in integrin binding*. *Biomaterials*. **28**. 5947-54. (2004). doi: 10.1016/j.biomaterials.2004.01.062.

33. P. Roach, D. Englin, K. Rohde and C. C. Perry: *Modern bio-materials: a review - bulk properties and implications of surface modifications*. Journal of material science: Materials in medicine **18**. 1263. (2007)
34. M. Malmsten, D. Muller B. Lassen: *Sequential Adsorption of Human Serum Albumin (HSA), Immunoglobulin G (IgG), and Fibrinogen (Fgn) at HMDSO Plasma Polymer Surfaces*. J Colloid Interface Sci. **93**(1) 88-95. 1997).
35. X. Jiang, G. M. Whitesides: *Principles of Tissue Engineering (Third Edition)* (2007).
36. D.D. Deligianni, N. Katsala, S. Ladas, D. Sotiropoulou, J. Amedee, Y.F. Missirlis: *Effect of surface roughness of the titanium alloy Ti-6Al-4V on human bone marrow cell response and on protein adsorption*. Biomaterials. **22**. 1241-1251. (2001).
37. L.C. Hsu, J. Fang, D.A. Borca-Tasciuc, R.W. Worobo, C.I. Moraru: *Effect of micro- and nanoscale topography on the adhesion of bacterial cells to solid surfaces*. Appl. Environ. Microbiol. **79**. 2703-2712. (2013).
38. K.R. Milner, A.J. Snyder, C.A. Siedlecki: *Sub-micron texturing for reducing platelet adhesion to polyurethane biomaterials*, J. Biomed. Mater. Res. A **76**. 561-570. (2006).
39. J. Tan, H. Shen, K.L. Carter, W.M. Saltzman: *Controlling human polymorphonuclear leukocytes motility using microfabrication technology*, J. Biomed. Mater. Res. **51**. 694-702. (2000).
40. R.E. Baier: *Surface behavior of biomaterials: the theta surface for biocompatibility*. Journal of material science: Materials in medicine **17**. 1057. (2006).
41. W. He, R. Benson: *4 - Polymeric Biomaterials In Plastics Design Library, Handbook of Polymer Applications in Medicine and Medical Devices*. William Andrew Publishing, 55-76, ISBN 9780323228053. (2014). <https://doi.org/10.1016/B978-0-323-22805-3.00004-9>.
42. Y. Ohya. H. Matsunami, T. Ouchi: *Cell growth on the porous sponges prepared from poly(depsipeptide-co-lactide) having various functional groups*. J Biomater Sci Polym Ed. **15**. 111-233. (2004).
43. C.D. Tidwell, S.I. Ertel, B.D. Ratner, B.J. Tarasevich, S. Atre, D.L. Allara: *Endothelial cell growth and protein adsorption on terminally functionalized, self-assembled monolayers of alkanethiolates on gold*. Langmuir. **13**. 3404-3413. (1997).
44. B.G. Keselowsky, D.M. Collard, A.J. Garcia: *Surface chemistry modulates focal adhesion composition and signaling through changes in integrin binding*. Biomaterials. **28**. 5947-54. (2004). doi: 10.1016/j.biomaterials.2004.01.062.
45. M.A. Lan, C.A. Gersbach, K.E. Michael, B.G. Keselowsky, A. Garcia: *Myoblast proliferation and differentiation on fibronectin-coated self-assembled monolayers presenting different surface chemistries*. Biomaterials. **22**. 4523-31. (2005).
46. L. Liu, S. Chen, C.M. Giachelli, B.D Ratner, S. Jiang: *Controlling osteopontin orientation on surfaces to modulate endothelial cell adhesion*. J Biomed Mater Res A. **74**. 23 31. (2005).
47. H. Alemohammad, E. Toyserkani: *Bio-Instructive Scaffolds for Musculoskeletal Tissue Engineering and Regenerative Medicine*. (2017)
49. D.D. Deligianni, N. Katsala, S. Ladas, D. Sotiropoulou, J. Amedee, Y.F. Missirlis: *Effect of surface roughness of the titanium alloy Ti-6Al-4V on human bone marrow cell response and on protein adsorption*. Biomaterials. **22**. 1241-1251. (2001).
50. M. C. Tanzi, G. Candiani: *Foundations of Biomaterials Engineering*. Academic Press. (2019).
51. X. Jiang, G. M. Whitesides: *Principles of Tissue Engineering (Third Edition)*.

- Academic Press. (2007).
52. L.C. Hsu, J. Fang, D.A. Borca-Tasciuc, R.W. Worobo, C.I. Moraru: *Effect of micro- and nanoscale topography on the adhesion of bacterial cells to solid surfaces*. *Appl. Environ. Microbiol.* **79**. 2703–2712. (2013).
53. J. Tan, H. Shen, K.L. Carter, W.M. Saltzman: *Controlling human polymorphonuclear leukocytes motility using microfabrication technology*, *J. Biomed. Mater. Res.* **51**. 694–702. (2000).
54. K.R. Milner, A.J. Snyder, C.A. Siedlecki: *Sub-micron texturing for reducing platelet adhesion to polyurethane biomaterials*, *J. Biomed. Mater. Res. A* **76**. 561–570. (2006).

References for Section 2.2 and 2.3.

55. S.I. Ertel, B.D. Ratner, T.A. Horbett: *Radiofrequency plasma deposition of oxygen-containing films on polystyrene and poly(ethylene terephthalate) substrates improves endothelial cell growth*. *J Biomed Mater Res.* **24**(12) 1637–59. (1990).
56. D.G. Castner: *Biomedical surface analysis: Evolution and future directions (Review)*. *Biointerphases.* **12** (2). (2017). doi:10.1116/1.4982169.
57. K. Merrett, R.M Cornelius, W.G. McClung, L.D Unsworth, H. Sheardown: *Surface analysis methods for characterizing polymeric biomaterials*. *J Biomater Sci Polym Ed.* **13**(6). 593–621. (2002).
58. Y. Leng: *Materials Characterization: Introduction to Microscopic and Spectroscopic Methods*. John Wiley & Sons, (2013). DOI:10.1002/9783527670772.
59. M.S.I Khan, S.W. Oh, Y.L. Kim: *Power of Scanning Electron Microscopy and Energy Dispersive X-Ray Analysis in Rapid Microbial Detection and Identification at the Single Cell Level*. *Sci Rep* **10**. 2368 (2020).
60. S.P. Lynch: *Gaseous Hydrogen Embrittlement of Materials in Energy Technologies: The Problem, its Characterisation and Effects on Particular Alloy Classes*. Woodhead Publishing. (2012).
61. S. Nasrazadani, S. Hassani: *Handbook of Materials Failure Analysis with Case Studies from the Oil and Gas Industry*. (Butterworth-Heinemann). (2016). <https://doi.org/10.1016/C2014-0-01712-1>
62. A. Brüel: *Strontium is incorporated into the fracture callus but does not influence the mechanical strength of healing rat fractures*. *Calcif. Tissue Int.* **88**. 142–152 (2011).
63. A. Palmquist, L. Emanuelsson, R. Brånemark, P. Thomsen: *Biomechanical, histological and ultrastructural analyses of laser micro- and nano-structured titanium implant after 6 months in rabbit*. *J. Biomed. Mater Res B.* **97**. 289–298. (2011).
64. W.J. Wolfgang: *Handbook of Materials Failure Analysis with Case Studies from the Aerospace and Automotive Industries*. Butterworth-Heinemann. (2016).
65. M.A. Aronova, R D Leapman: *Development of Electron Energy Loss Spectroscopy in the Biological Sciences*. *MRS bulletin.* **37**. (1). 53–62. (2012). doi:10.1557/mrs.2011.329.
66. F.S. Hage, R.J. Nicholls, J.R. Yates, D.G. McCulloch, T.C. Lovejoy, N. Dellby, O.L. Krivanek, K. Refson, Q.M. Ramasse: *Nanoscale momentum-resolved vibrational spectroscopy*. *Sci. Adv.* **4**. 7495 (2018).

67. O.L. Krivanek, T.C. Lovejoy, N. Dellby, T. Aoki, R.W. Carpenter, P. Rez, E. Soignard, J. Zhu, P.E. Batson, M.J. Lagos: *Vibrational spectroscopy in the electron microscope*. *Nature* **514**, 209–212 (2014).
68. J. Verbeeck, D. Schryvers: *Encyclopedia of Analytical Science* (Second Edition). Elsevier. (2005). <https://doi.org/10.1021/ed082p1313.2>.
69. B.E. Kahn, S.A. Chaffins, J.Y. Gui, F. Lu, D.A. Stern, Ar.T. Hubbard: *Surface vibrational spectroscopy. A comparison of the EELS spectra of organic adsorbates at Pt(111) with IR and Raman spectra of the unadsorbed organics*. *Chemical Physics*. **141** (1). 21–39. (1990). [https://doi.org/10.1016/0301-0104\(90\)80016-Q](https://doi.org/10.1016/0301-0104(90)80016-Q).
70. H.J. Butler, L. Ashton, B. Bird, G. Cinque, K. Curtis, J. Dorney, K. Esmonde-White, N.J. Fullwood, B. Gardner, P.L. Martin-Hirsch, M.J Walsh, M.R. McAinsh, N. Stone, F.L. Martin: *Using Raman Spectroscopy to Characterize Biological Materials*. *Nat. Protoc.* **11**. (4). 664–687. (2016).
71. G. Agrawal, S.K. Samal: *Raman Spectroscopy for Advanced Polymeric Biomaterials*. *ACS Biomater. Sci. Eng.* **4** (4). 1285–1299. (2018). DOI: 10.1021/acsbiomaterials.8b00258.
72. C.C Moura, R.S Tare, R.O.C Oreffo, S. Mahajan: *Raman Spectroscopy and Coherent Anti-Stokes Raman Scattering Imaging: Prospective Tools for Monitoring Skeletal Cells and Skeletal Regeneration*. *J. R. Soc. Interface.* **13** (118), DOI: 10.1098/rsif.2016.0182. (2016).
73. O Hollricher, U. Schmidt. S. Breuninger: *RISE microscopy: correlative Raman-SEM imaging*. *Micros. Today* **22**. 36–39 (2014).
74. X. Yan, H. Sato, Y. Ozaki: *Chapter 4 - Raman and tip-enhanced Raman scattering spectroscopy studies of polymer nanocomposites*. *Spectroscopy of Polymer Nanocomposites*. William Andrew Publishing. 88–111. (2016).
75. S. Rabha, B.K. Saikia: *18 - Advanced micro- and nanoscale characterization techniques for carbonaceous aerosols*. Editor(s): Chaudhery Mustansar Hussain. *Handbook of Nanomaterials in Analytical Chemistry*. Elsevier. 449–472. (2020).
76. A.G. Shard: *Characterization of Nanoparticles. Measurement Processes for Nanoparticles. Micro and Nano Technologies*. Elsevier. 349–371. (2020). <https://doi.org/10.1016/C2017-0-00312-9>
77. N.Farr, J. Thanarak, J. Schäfer, A Quade, F. Claeysens, N. Green, C. Rodenburg: *Understanding Surface Modifications Induced via Argon Plasma Treatment through Secondary Electron Hyperspectral Imaging*. *Adv. Sci.* **2020**, 2003762. <https://doi.org/10.1002/adv.202003762>
78. O. Bondarchuk, A.P. LaGrow, A. Kvasha, T. Thieu, E. Ayerbe, I. Urdampilleta: *On the X-ray photoelectron spectroscopy analysis of LiNixMnyCozO2 material and electrodes*. *Applied Surface Science*. **535**. 147699. (2021).
79. Z. Rafiee, M. Nejatian, S. Bodbodak, S.M. Jafari: *Chapter Eight - Surface composition of nanoencapsulated food ingredients by X-ray photoelectron spectroscopy (XPS), in Nanoencapsulation in the Food Industry, Characterization of Nanoencapsulated Food Ingredients*. Academic Press. **4**. 243–268. (2020).
80. L. Sabbatini, P.G. Zamboni: *XPS and SIMS surface chemical analysis of some important classes of polymeric biomaterials*. *Journal of Electron Spectroscopy and Related Phenomena*. **81**. 3. 285–301. (1996).
81. S.L. McArthur, G. Mishra C.D. Easton C.D: *Applications of XPS in Biology and Biointerface Analysis*. In: Smentkowski V. (eds) *Surface Analysis and Techniques in Biology*. Springer, Cham. (2014). https://doi.org/10.1007/978-3-319-01360-2_2.

82. G.J. Vancso, H. Hillborg, H. Hillborg, H. Schönherr: *Chemical Composition of Polymer Surfaces Imaged by Atomic Force Microscopy and Complementary Approaches*. *Advances in polymer science*, **182**, 55-129. (2005).
83. S.S. Ray: *Environmentally Friendly Polymer Nanocomposites*. Woodhead Publishing Ltd. (2013).
84. R. Hiesgen, J. Haiber: *Encyclopedia of Electrochemical Power Sources*. Elsevier Science. (2009).
85. M. Farré, D. Barceló: *Analysis and Risk of Nanomaterials in Environmental and Food Samples in Comprehensive Analytical Chemistry*. **59**. 2-361 (2012).
86. D. C. Joy: *Scanning electron microscopy: Second best no more*. *Nat. Mater.* **8** (10). 776-777. (2009).

References for Section 2.4

87. C.W. Oatley: *The early history of the scanning electron microscope*. *J. Appl. Phys.* 7532, R1-R13. (1982).
88. J.B. Pawley: *LVSEM for biology*. In: Schatten, H., Pawley, J. (Eds.), *Biological Low-Voltage Scanning Electron Microscopy*. Springer. 27-106. (2008).
89. D. Newbury: *Developments in instrumentation for microanalysis in low-voltage scanning electron microscopy*. In: Schatten, H., Pawley, J. (Eds.), *Biological Low-Voltage Scanning Electron Microscopy*. Springer. 263-304. (2008).
90. O. Choudhary, P. Choudhary: *Scanning electron microscope: Advantages and disadvantages in imaging components*. *Int. J. Curr. Microbiol. Appl. Sci.* **6**. 1877-1882. (2017).
91. C.E. Lyman: *Scanning electron microscopy, X-ray microanalysis, and analytical electron microscopy: a laboratory workbook*. New York: Plenum Press. (1990).
92. J. Goldstein, D.E. Newbury, D.C. Joy, C.E. Lyman, P. Echlin, E. Lifshin, L. Sawyer, J.R. Michael: *Scanning Electron Microscopy and X-Ray Microanalysis*. 3rd Edition. Springer. (2003).
93. Z. Wang: *Elastic and Inelastic Scattering in Electron Diffraction and Imaging*. Plenum Press. (1995).
94. W. Zhou, R.P. Apkarian, Z.L. Wang, and D.C. Joy: *Fundamentals of Scanning Electron Microscopy in Scanning Microscopy for Nanotechnology*. Springer New York. 1-40. (2006).
95. <https://www.gems-inclusions.com/inclusions-studies/analytical-methods/sem-eds-wds-analysis> (Online - obtained and amended - 25/01/2021).
96. M.T. Postek, A.E. Vladár: *Does Your SEM Really Tell the Truth? How Would You Know? Part 2*. *Scanning*. **36**. (3). 347-355. (2014).
97. T. Everhart, R.F.M. Thornley: *Wide-band detector for micro-microampere low energy electron currents*. *J. Sci. Instrum.* **37**. (7). 246-248. (1960).
98. <https://cmrf.research.uiowa.edu/scanning-electron-microscopy> (Online - obtained and amended 25/01/2021).
99. P. Kazemian, S. A. M. Mentink, C. Rodenburg and C. J. Humphreys: *Quantitative secondary electron energy filtering in a scanning electron microscope and its applications*. *Ultramicroscopy*. **107**. 2-3. 140-150. (2007).

100. J. Butler, D.C. Joy, G. Bradley, S. Krause: Low-voltage scanning electron microscopy of polymers. *Polymer (Guildf)*. **36**. (9). 1781–1790. (1995).
101. J.B. Pawley: *Practical aspects of high-resolution LVSEM*. *Scanning*. **12**. 247–252. (1990). <https://doi.org/10.1002/sca.4950120502>
102. H. Schatten: *Low voltage high-resolution SEM (LVHRSEM) for biological structural and molecular analysis*. *Micron*. **42**. 2. 175–185. (2011)
103. J.B Pawley: *LVSEM for biology*. In: Schatten, H., Pawley, J. (Eds.), *Biological Low-Voltage Scanning Electron Microscopy*. Springer. 27–106. (2008).
104. J. B. Pawley, H. Ris: *Structure of the cytoplasmic filament system in freeze-dried whole mounts viewed by HVEM*, *J. Microsc.*, **13**. 319–332. (1987).
105. R.F. Egerton, P. Li, M. Malac: *Radiation damage in the TEM and SEM*, *Micron*. **35**. (6). 99–409. (2004).
106. D.L. Vezie, E.L. Thomas, W.W. Adams: *Low-voltage, high-resolution scanning electron microscopy: a new characterization technique for polymer morphology*. *Polymer (Guildf)*. **36**. (9). 1761–1779. (1995).
107. J.L. Holmes, K.N Bachus, R.D. Bloebaum: *Thermal effects of the electron beam and implications of surface damage in the analysis of bone tissue*. *Scanning*. **22**. 243–248. (2000). <https://doi.org/10.1002/sca.4950220403>
108. V. Speranza, A. Sorrentino, F. De Santis, R. Pantani: *Characterization of the Polycaprolactone Melt Crystallization: Complementary Optical Microscopy, DSC, and AFM Studies*. 720157. (2014). <https://doi.org/10.1155/2014/720157>
109. Q. Wan: *Angle selective backscattered electron contrast in the low-voltage scanning electron microscope: Simulation and experiment for polymers*. *Ultramicroscopy*, **171**, 126–138. (2016).
110. M. Suga, S. Asahina, Y. Sakuda, H. Kazumori, H. Nishiyama, T. Nokuo, V. Alfredsson, T. Kjellman, S. M. Stevens, H. S. Cho, M. Cho, L. Han, S. Che, M. W. Anderson, F. Schüth, H. Deng, O. M. Yaghi, Z. Liu, H. Y. Jeong, A. Stein, K. Sakamoto, R. Ryoo, O. Terasaki: *Recent progress in scanning electron microscopy for the characterization of fine structural details of nano materials*. *Progress in Solid State Chemistry*. **42**. 1–2. (2014).
111. L. Yougui: *Practical Electron Microscopy and Database*. (2006) www.globalsino.com/EM/
112. V.R. Kollafh: *Zur Energieverteilung der Sekundarelektronen*. *Mepergebnisse und Diskussion*. (1947).
113. D.C. Joy. M.S, Prasad. and H.M Meyer, III: *Experimental secondary electron spectra under SEM conditions*. *Journal of Microscopy*, **215**. 77–85. (2004).
114. J. A. Venables, D. R. Batchelor, M. Hanbucken, C. J. Harland, G. W. Jones: *Surface Microscopy with Scanned Electron Beams*. *Philosophical Transactions of the Royal Society of London. Series A, Mathematical and Physical Sciences*. **318**, 1541. (1986).
115. A. Khursheed. *Secondary Electron Energy Spectroscopy in the Scanning Electron Microscope*. World Scientific Publishing Co Pte Ltd. ISBN: 9789811227028.
116. Q. Wan, K. J. Abrams, R. C. Masters, A. C. S. Talari, I. U. Rehman, F. Claeysens, C. Holland, C. Rodenburg, *Adv. Mater.* **29**, 1703510. (2017).
117. V. Kumar, W.L. Schmidt, G. Schileo, R.C. Masters, M. Wong-Stringer, D.C. Sinclair, I.M. Reaney, D. Lidzey and C. Rodenburg: *Nanoscale Mapping of Bromide Segregation on the Cross Sections of Complex Hybrid Perovskite*

- Photovoltaic Films Using Secondary Electron Hyperspectral Imaging in a Scanning Electron Microscope*. ACS Omega **2**, 2126–2133 (2017).
118. K.J. Abrams, M. Dapor, N. Stehling, M. Azzolini, S.J. Kyle, J.S. Schäfer, A. Quade, F. Mika, S. Kratky and Z. Pokorna: *Making Sense of Complex Carbon and Metal/Carbon Systems by Secondary Electron Hyperspectral Imaging*. Adv. Sci. 1900719 (2019).
119. R. C. Masters, A. J. Pearson, T. S. Glen, F.-C. M. Sasam, L. Dapor, Li. A. M. Donald, D. G. Lidzey, C. Rodenburg: *Sub-nanometre resolution imaging of polymer–fullerene photovoltaic blends using energy-filtered scanning electron microscopy*. Nat. Commun. **6**, 6928. (2015).
120. M. Dapor, R.C. Masters, I. Ross, D.G. Lidzey, A. Pearson, I. Abril, R. Garcia-Molina, J. Sharp, M. Unčovský, T. Vystavel, F. Mika and C. Rodenburg: *Secondary electron spectra of semicrystalline polymers – A novel polymer characterisation tool?*. J. Electron Spectros. Relat. Phenomena **222**, 95–105 (2018). doi:10.1016/j.elspec.2017.08.001.
121. R.C. Masters, N.A. Stehling, K.J. Abrams, V. Kumar, M. Azzolini, N.M. Pugno, M. Dapor, A. Huber, P. Schäfer, D.G. Lidzey and C. Rodenburg: *Mapping Polymer Molecular Order in the SEM with Secondary Electron Hyperspectral Imaging*. Adv. Sci. (2019).
122. M. Azzolini, T. Morresi, K. Abrams, R. Masters, N. Stehling, C. Rodenburg, N.M. Pugno, S. Taioli, M. Dapor: *An Anisotropic Approach for Simulating Electron Transport in Layered Materials: Computational and Experimental Study of Highly Oriented Pyrolytic Graphite*, (2018). doi:10.1021/acs.jpcc.8b02256.
123. C. Li, S.F. Mao and Z.J. Ding: Time-dependent characteristics of secondary electron emission. J. Appl. Phys. **125**, 24902 (2019), doi:10.1063/1.5080264.
124. C. Li, S.F. Mao, Y.B. Zou, Y.G. Li, P. Zhang, H.M. Li and Z.J. Ding: A Monte Carlo modeling on charging effect for structures with arbitrary geometries. J. Phys. D. Appl. Phys. **51** 165301 (2018), doi:10.1088/1361-6463/aab2cf.
125. N. Stehling, R. Masters, Y. Zhou Y, R. O'Connell, C. Holland, H. Zhang, C. Rodenburg: *New perspectives on nano-engineering by secondary electron spectroscopy in the helium ion and scanning electron microscope*. MRS Commun. **23** (6). 226–240. (2018).
126. Q. Wan, K.J. Abrams, Masters RC, A.C.S. Talari, I.U. Rehman, F. Claeysens, C. Holland, C. Rodenburg: *Mapping nanostructural variations in silk by secondary electron hyperspectral imaging*. Adv Mater. **29**. 1703510. (2017).
127. J.F. Nohl: *Secondary electron hyperspectral imaging: nanostructure and chemical analysis for the LV-SEM, Materials Science and Technology*, **36**. (5). 527–539. (2020).
128. N.A. Stehling: Scanning Electron Microscopy for Nano-morphology Characterisation of Complex Hierarchical Polymer Structures. PhD thesis, University of Sheffield. (2019).
129. C. Schönjahn, C.J. Humphreys, M. Glick: *Energy-filtered imaging in a field-emission scanning electron microscope for dopant mapping in semiconductors*. J Appl Phys. **92**. (12). 7667–7671. (2002).
130. N.T.H. Farr, S.F. Hamad, E. Gray, C.M. Magazzeni, F. Longman, D.E.J. Armstrong, J.P. Foreman, F. Claeysens, N.H. Green, C. Rodenburg: *Identifying and mapping chemical bonding within phenolic resin using secondary electron hyperspectral imaging*. Polym. Chem. **12**. 177–182. (2021).

131. Q. Wan: Scanning electron microscopy investigation of bio-polymer composites morphology. PhD Thesis, University of Sheffield. (2017).

3. Characterising cross-linking within polymeric biomaterials in the SEM by Secondary Electron Hyperspectral Imaging

Macromolecular Rapid Communications
Volume 41, Issue 3
December 2019,
DOI: 10.1002/marc.201900484

Nicholas Farr, *¹ Samand Pashneh-Tala,¹ Nicola Stehling,¹ Frederik Claeysens,¹ Nicola Green,¹ and Cornelia Rodenburg¹

¹ University of Sheffield Faculty of Engineering, Material Science and Engineering, Sheffield, S1 3JD, UK

Received 6 September 2019; accepted 29 October 2019

3.1 Prelude

A biomaterial's mechanical properties are defined by its underlying chemical composition and structural relationships whose local variations determine cell growth propensity. For this reason, novel surface chemical spectroscopy and imaging methods on nano- and micro-scale levels are needed. In particular, crosslinking density and local variations in molecular order are major contributors to a biomaterial's mechanical properties (local stiffness) and consequently the biocompatibility of the material [1]. Established averaging methods for the estimation of molecular order and crosslinking density do not provide information of spatial distributions within the biomaterials. Chapter 3 presents the publication titled "Characterising cross-linking within polymeric biomaterials in the SEM by Secondary Electron Hyperspectral Imaging." This publication

shows SEHI can provide the necessary spectral information and that the captured spectra can also be exploited for SE imaging.

3.1.1 Thesis Question 1 Can SEHI deliver insights into the mechanical properties of a biomaterial?

Chapter 3 tackled this question by evaluating the efficacy of SES to reveal new insights into the mechanical properties of PGS-M morphology. Chapter 3 was the first publication to show secondary electron spectroscopy (SES) being used to characterise crosslinking in polymer derived biomaterials. Characterisation of three different forms of PGS-M each with different crosslinking structures was successfully conducted. Here SES provided a cross-linking characterisation toolset with crosslinking density and variation information captured at a multi-scale level. Prior to this publication the magnitude of crosslinking within a biomaterial could only be inferred through limited analytical techniques undertaken with traditional approaches for measuring the extent of crosslinking based on bulk mechanical averaging techniques.

SES showed the capacity to overcome these limitations by providing the means to identify the bonding (CHx) associated with crosslinking within PGS-M together with its unique ability to distinguish spatial distributions of this bonding across the polymers surface. The publication presented in this chapter shows that changes in Raman intensity (Green 514.5 nm laser) (at 2950 cm^{-1} (C-H vibrations [2-6]) closely correlates with the SE intensity changes at 3.6 eV. Both intensity peaks are similarly affected by CH bonding and consequently the cross-linking process of PGS-M. This result was the first time SES had been shown to be capable of predicting and evaluating indirectly the mechanical properties of a polymer. Selecting potential biomaterials for tissue

engineering applications is dependent on mechanical properties such as surface stiffness and roughness.

3.1.2 Thesis Question 2: Is the captured SE spectra able to identify specific functional groups that play a key role in biomaterials engineering TE and if so can SEHI map these functional groups at the nanoscale?

Chapter 3 was the first publication to identify the SE emissions of a chemical functional group. SES provided the means to identify the bonding (CH_x) associated with crosslinking within PGS-M together with the ability to distinguish spatial distributions of this bonding across the polymers surface.

3.1.3 Brief Summary

This study demonstrated that by using SEHI it is possible to map a biomaterial's CH variation with ease in the scanning electron microscope. SEHI images show that cross-linking and thus hardness is also likely to change locally observed as variation in CH vibrations. This work therefore proposes an innovative surface approach to providing researchers with effective tools to visualise and characterise novel biomaterials in the SEM.

3.2 Contributions

NF performed the majority of the experimental work and data analysis and wrote the manuscript. SPT synthesised PGS-M and conducted the mechanical testing. NG, FC and CR contributed to the experimental design, project supervision, and the writing of the manuscript. Please see overleaf for the paper. Published by WILEY-VCH Verlag GmbH & Co. KGaA, Weinheim. This is an open access article under the terms of the Creative Commons Attribution License, which permits use, distribution and re-

production in any medium, provided the original work is properly cited. For more information see (<https://creativecommons.org/licenses/by/4.0/>)

3.3 References

1. M. Rahmati. E.A. Silva. J.E. Reseland. C.A. Heyward. H.J. Haugen. *Biological responses to physicochemical properties of biomaterial surface*. Chem. Soc. Rev. 49, 5178 (2020).
2. E. Andreassen. *Infrared and Raman spectroscopy of polypropylene*. In: Karger-Kocsis J. (eds) Polypropylene. Polymer Science and Technology Series. Springer, Dordrecht. (1999).
3. NK. Howell. G. Arteaga. Nakai, S. Li-Chan, E.C.Y. *Raman Spectral Analysis in the C–H Stretching Region of Proteins and Amino Acids for Investigation of Hydrophobic Interactions*. Journal of Agricultural and Food Chemistry. 47 (3), 924-933. (1999).
4. A. Baranowska-Korczyn. A. Warowicka. M. Jasiurkowska-Delaporte. B. Grześkowiak. M. Jarek. B. Maciejewska. J. Jurga-Stopa. S. Jurga. *Antimicrobial electrospun poly ϵ -caprolactone scaffolds for gingival fibroblast growth*. RSC Advances. 6. 10.1039/C6RA02486F. (2016).
5. Accessed and obtained 11/05/2021- <https://www.renishaw.com/en/raman-bands-explained--25808>
6. Accessed and obtained 11/05/2021 - https://static.horiba.com/fileadmin/Horiba/Technology/Measurement_Techniques/Molecular_Spectroscopy/Raman_Spectroscopy/Raman_Academy/Raman_Tutorial/Raman_bands.pdf
7. H.I. Chang. Y. Wang. *Regenerative medicine and tissue engineering-cells and biomaterials*. InTechOpen, (2011).
8. A. Ranella. M. Barberoglou. S. Bakogianni. C. Fotakis. E. Stratakis. *Tuning cell adhesion by controlling the roughness and wettability of 3D micro/nano silicon structures*. Acta Biomaterialia. 6. 2711. (2010).



Characterizing Cross-Linking Within Polymeric Biomaterials in the SEM by Secondary Electron Hyperspectral Imaging

Nicholas Farr,* Samand Pashneh-Tala, Nicola Stehling, Frederik Claeysens, Nicola Green, and Cornelia Rodenburg

A novel capability built upon secondary electron (SE) spectroscopy provides an enhanced cross-linking characterization toolset for polymeric biomaterials, with cross-linking density and variation captured at a multiscale level. The potential of SE spectroscopy for material characterization has been investigated since 1947. The absence of suitable instrumentation and signal processing proved insurmountable barriers to applying SE spectroscopy to biomaterials, and consequently, capturing SE spectra containing cross-linking information is a new concept. To date, cross-linking extent is inferred from analytical techniques such as nuclear magnetic resonance (NMR), differential scanning calorimetry, and Raman spectroscopy (RS). NMR provides extremely localized information on the atomic scale and molecular scale, while RS information volume is on the microscale. Other methods for the indirect study of cross-linking are bulk mechanical averaging methods, such as tensile and compression modulus testing. However, these established averaging methods for the estimation of polymer cross-linking density are incomplete because they fail to provide information of spatial distributions within the biomaterial morphology across all relevant length scales. The efficacy of the SE spectroscopy capability is demonstrated in this paper by the analysis of poly(glycerol sebacate)-methacrylate (PGS-M) at different degrees of methacrylation delivering new insights into PGS-M morphology.

signal processing, and imaging capability that SE spectroscopy can be exploited to open up a new realm of opportunities for novel material characterization of polymers in the scanning electron microscope (SEM) by SE hyperspectral imaging (SEHI). While in a standard SEM an image is formed from all detected SEs that are emitted from a surface regardless of their energy, in SEHI a series of images is collected, each of which is created using SEs from a defined energy band. Such SEHI image series can then be used to extract a SE spectrum. In the last 5 years, SEHI has been deployed in a wide variety of applications, but in particular, for the mapping of semi-crystalline polymers, exploring the molecular orientation of organic electronic devices, and recently revealing nanostructure variations within natural materials.^[2,3] Here we show that the SEHI approach can be also utilized as a novel characterization tool to map cross-link densities in beam sensitive biomaterials.

Polymer cross-links are the covalent bonds which are irreversibly formed between molecular chains of the

The potential of secondary electron (SE) spectroscopy for material characterization has been investigated as far back as 1947.^[1] However, it is only with recent advancements in instrumentation,

polymer. Increasing the density of cross-links decreases the ability of polymer chains to slide over each other and accordingly increases the relative mechanical tensile strength of the polymer and its brittle fracture resilience.^[4]

Therefore, a polymer-based biomaterial's cross-linking density is a major contributor to its mechanical properties.^[5] For a polymer to be considered as a viable biomaterial, promotion of cell growth is essential. The ability of the biomaterial to promote cell growth is highly influenced by local surface variations that arise as a consequence of these mechanical properties. Localized variations in cross-linking density are important for the biocompatibility of the material and as yet there is no imaging tool available to assess such variations. This might seem surprising as it has been shown that cross-linking density is also associated with the biodegradation rate of biomaterial scaffolds and can be utilized as an effective control of biodegradation.^[6]

Additionally, cross-linking has demonstrated an ability to suppress the immunogenicity of an implanted scaffold.^[7] Thus the ability to quantify the extent and density of cross-linking is considered to be a key capability to promote the efficient development of effective biomaterials. The behavior and kinetics of the

N. Farr, Dr. S. Pashneh-Tala, Dr. N. Stehling, Dr. F. Claeysens, Dr. N. Green, Dr. C. Rodenburg
Department of Materials Science and Engineering
Sir Robert Hadfield Building
Mappin Street, Sheffield S1 3JD, UK
E-mail: nfarr1@sheffield.ac.uk

Dr. N. Green
INSIGNEO Institute for In Silico Medicine
The Pam Liversidge Building
Sir Robert Hadfield Building
Mappin Street, Sheffield S1 3JD, UK

The ORCID identification number(s) for the author(s) of this article can be found under <https://doi.org/10.1002/marc.201900484>.

© 2019 The Authors. Published by WILEY-VCH Verlag GmbH & Co. KGaA, Weinheim. This is an open access article under the terms of the Creative Commons Attribution License, which permits use, distribution and reproduction in any medium, provided the original work is properly cited.

DOI: 10.1002/marc.201900484

cross-linking processes of polymer-derived biomaterials have been previously surveyed by applying diverse analytical techniques such as nuclear magnetic resonance (NMR), differential scanning calorimetry, and Raman spectroscopy (RS). While NMR can provide extremely localized information on both the atomic scale and molecular scale, the RS information volume is typically on the microscale. Other available methods for the indirect study of the cross-linking structures of soft polymers are bulk mechanical averaging methods, such as tensile and compression modulus testing. However, these established averaging methods for the estimation of polymer cross-linking density are incomplete as they fail to provide information on spatial distributions within the biomaterial morphology across all relevant length scales.

To develop a comprehensive understanding of the key relationships between the biocompatibility of different polymer structures, the capability to reveal both nano- and microscale levels of structural detail is essential. Here we demonstrate that SEHI can provide structural detail information using poly(glycerol sebacate)-methacrylate (PGS-M) as an example.

PGS-M is an elastomeric degradable polymer and a functionalized form of the well-studied poly(glycerol sebacate) (PGS). PGS being a non-toxic tuneable polymer,^[8,9] has become an interesting potential biomaterial in various promising applications such as supporting the growth of cardiac tissue,^[10] blood vessels,^[11,12] and cartilage.^[13,14] PGS-M differs from PGS as a result of functionalization with methacrylate groups which causes the polymer to be photocurable. The photocurable capability of PGS-M enhances the existing strengths of PGS by allowing the material to be cross-linked at lower temperatures and pressures. This enables the precise fabrication of highly detailed microscale structures and the potential direct incorporation of cells or temperature sensitive molecules.^[15] The ease with which PGS-M can be synthesized together with the adaptability of its physical properties and suitability for use with different cell types, makes PGS-M an attractive candidate for an extensively deployed biomaterial.^[15] The adaptability relies on user-defined cross-linking as PGS-M can be photocured at various degrees of methacrylation and the degree of methacrylate (DM) used in its production has a direct relationship to the density of cross-linking. The greater the DM, the greater the average cross-linking density. Tensile testing has previously revealed that the mechanical properties of PGS-M varied in accordance with its morphology, both Young's modulus and UTS increased significantly with increasing levels of DM.^[15,16] Further validation is required to confirm this relationship but PGS-M is generating much interest as a biomaterial. PGS-M is therefore considered an ideal model polymer to assess SEHI as a viable biomaterial cross-linking characterization technique.

In this study, SEHI will be applied to characterize the increasing cross-linking densities of PGS-M at three different DM levels: 30%, 50%, and 80%. Argon plasma treatment has been included in the study to initiate supplementary cross-linking variation within a single set of PGS-M samples.

Plasma modification of a polymeric biomaterial's surface layer is often carried out in order to: generate functional groups on its surface, change free surface energy, increase surface hydrophilicity or achieve hydrophobicity, change cross-linking of surfaces, change surface morphology, or remove impurities. Previous studies on PGS, which has a similar structure to PGS-M, have

observed that plasma treatment^[17] intensified hydrophilicity, increased the capability of stimulating cell proliferation, and extracellular matrix production. Such studies have also indicated that plasma treatment has induced surface cross-linking within the chemically similar PGS, but as yet no technique has been able to map their existence^[17] using traditional characterization methods, presumably due to a lack in surface sensitivity.

During plasma treatment inert gases are used to eliminate some of the atomic species from the polymer's surface, thereby producing reactive surface radicals. These radicals subsequently react within the surface structure forming chemical bonds, a process that has the potential to result in a cross-linked surface.^[18] Argon plasma treatment is active in sputtering several nanometers of material from the sample surface, thus making surface modifications on a nanometer scale, which may be beneficial to the deployment of PGS-M as a biomaterial.^[19] The purpose of the introduction of argon plasma treatment within the study will be to treat the surface of PGS-M and analyze the resulting cross-linking density on cross-sections of the material as a further illustration of lateral and depth mapping of cross-linking using SEHI.

Nanoindentation results displayed in **Figure 1**, showed a relationship between the increase in the degree of methacrylation and a subsequent increase in hardness and stiffness of the polymer. Alongside previous work this result corroborates the proposition that increasing the percentage of the degree of methacrylate (DM) used in the production of PGS-M has a direct relationship to the density of cross-linking observed.^[15,16] The results also provide evidence that increasing DM does directly increase the hardness of the material and has a strong influence on its elastic modulus.

Figure 2A presents the results of Raman spectroscopy applied to the PGS-M samples with three different DM. The expected position of the first peak of interest is at 2200 cm^{-1} and relates to C=C bonding.^[20] The weaker bonding energies of double bonds and acrylate groups are a common starting point for radical reactions like polymerization or cross-linking processes. Therefore, the absence of this peak in the observed results is a strong indication of the successful process of cross-linking and shows that polymerization is complete. The most prominent differences observed between PGS-M 30%, 50%, and 80% DM were in the spectral range around 2950 cm^{-1} . PGS-M photocured polymers show an increase of CH vibrations, specifically C-H alkyl, which is associated with the cross-linking of PGS-M after photo-polymerization. The asymmetric and symmetric stretching vibration of a methyl group usually occurs at about 2965 and 2880 cm^{-1} , respectively. Peaks in the data within this range consist of C-H vibrations with the intensity ratios having previously been related to composition and cross-linking.^[21] Formation of the polymer network after successful photocuring of PGS-M can therefore be confirmed by identifying an increase in alkyl groups. This is a product of the elimination of acrylate groups,^[22] which are observed through a corresponding increase in C-H vibrations. Furthermore, due to the small height of PGS-M samples, the observed signal included components detected at $<1500\text{ cm}^{-1}$ which were generated by the underlying borosilicate glass. This is not an uncommon occurrence and has previously been documented to produce pronounced peaks in the fingerprint region.^[15]

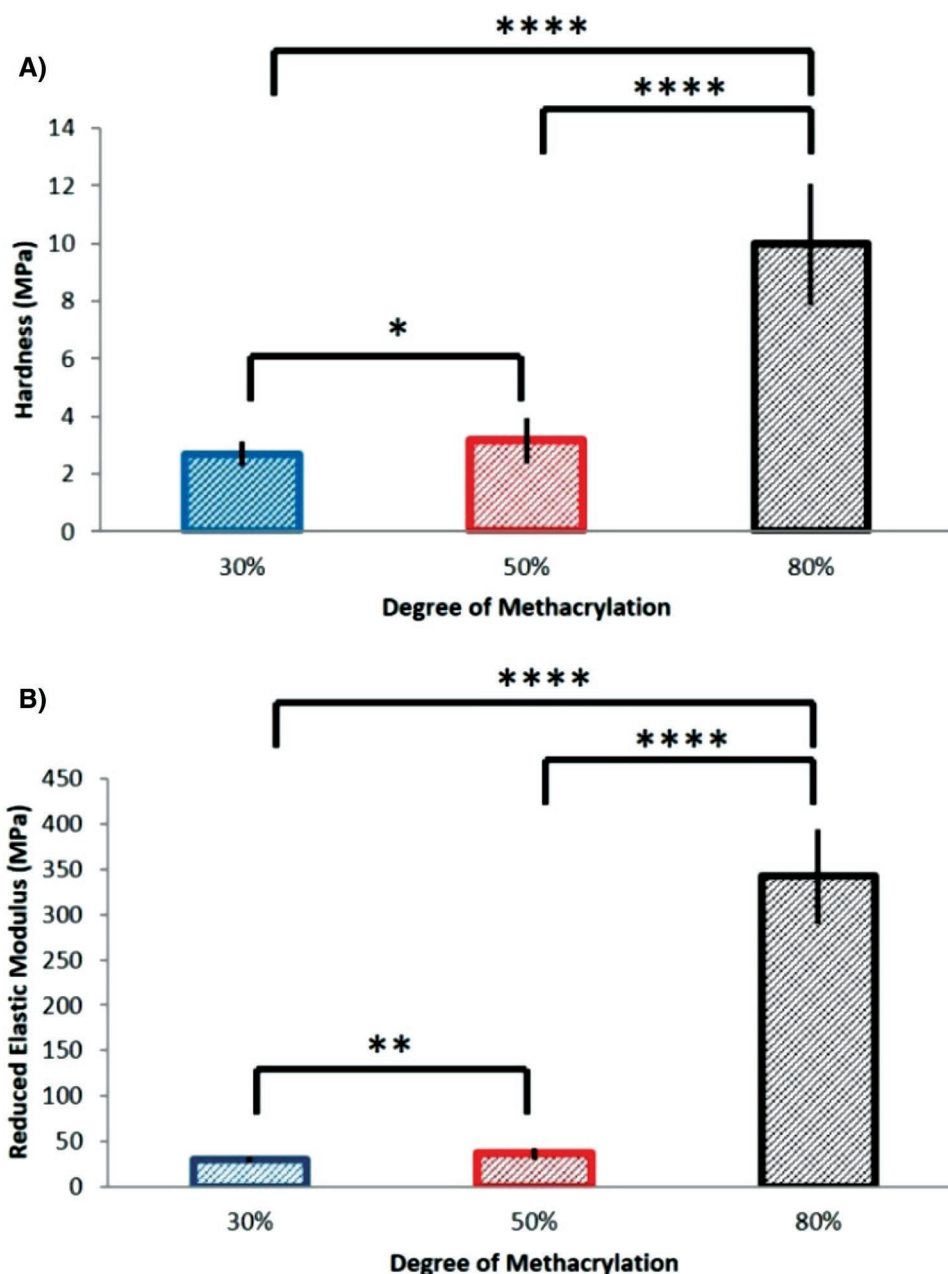


Figure 1. A) Outlines the hardness (MPa) and B) reduced elastic modulus (MPa) obtained from nanoindentation for varying degrees of methacrylation of PGS-M (mean \pm STD error bars). The degree of significance is indicated as **** p < 0.0001, *** p < 0.001, ** p < 0.01, and * p < 0.05.

The SE spectra captured from the surfaces of PGS-M for the three specimens with different cross-linking densities are displayed in Figure 2B. It can be observed that the dominant peak intensity values rise as the DM-driven cross-linking density increases. This effect is prominent within the energy window of 2.9–4.3 eV for PGS-M. It has been recently established that SE emission 3.3–4.7 eV are attributable to hydrogenated carbon bonding. Abrams et al.^[23] have shown by the results of an electron beam contamination study that amorphous contamination (hydrogenated carbon) deposits on carbon-based samples can be identified through energy peaks within the 3.3–4.7 eV range.

The peaks associated with hydrogenated carbon correlate with the observed C–H vibrations peak given in the captured Raman spectrum as predicted by these results. Figure 2C,D shows the change in the Raman data at 2950 cm^{-1} and SE emission change at 3.6 eV respectively, for PGS-M samples. The changes in Raman intensity at 2950 cm^{-1} (C–H vibrations) closely correlates with the SE intensity changes at 3.6 eV. Both peaks are similarly affected by CH bonding and consequently the cross-linking process of PGS-M. The correlation also holds for the relative integrated intensity for both Raman and SE emissions representing the wider to C–H vibrations windows

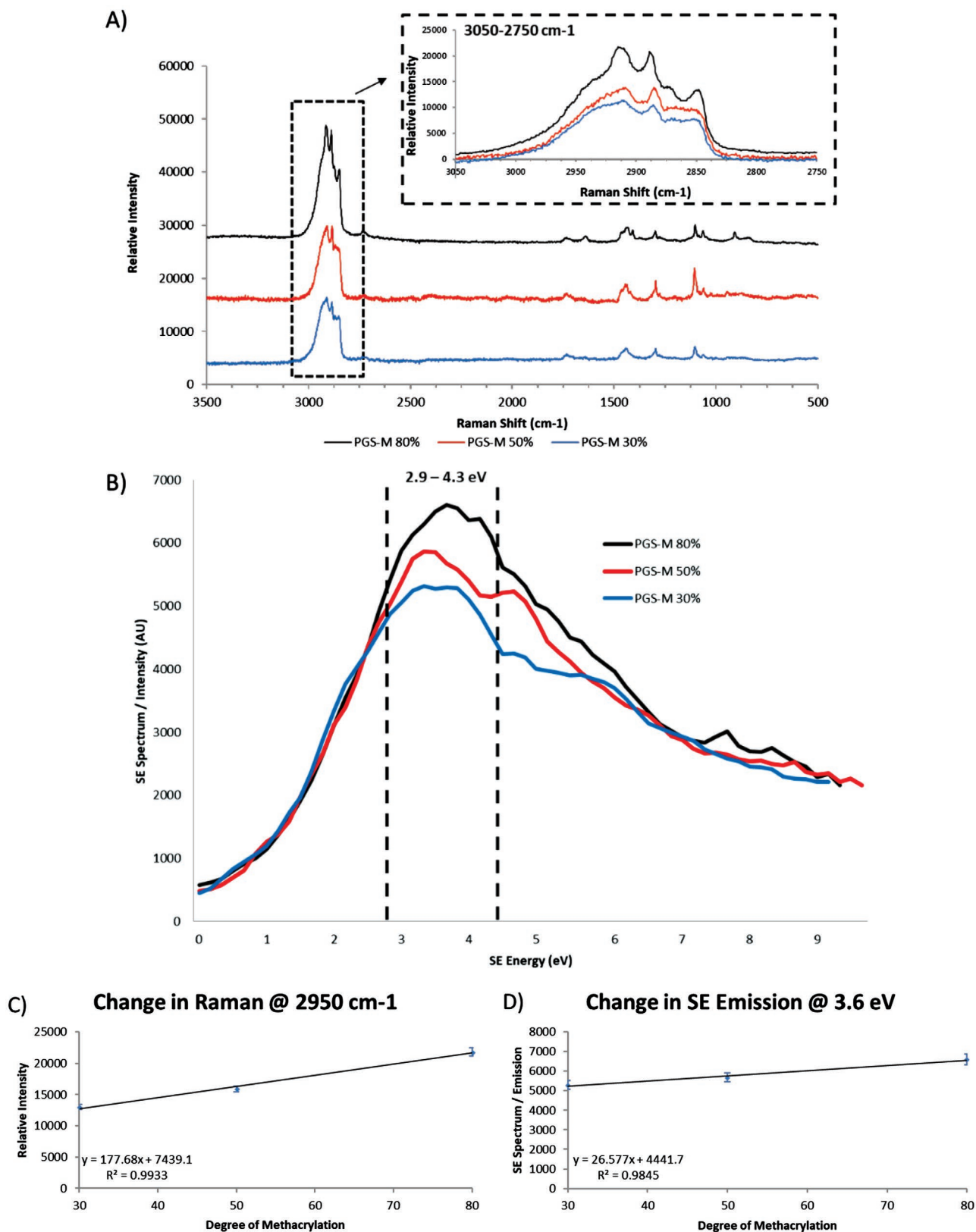


Figure 2. A) Offset Raman spectra for 30%, 50%, and 80% low-molecular-weight PGS-M. B) Secondary electron spectra for 30%, 50%, and 80% low-molecular-weight PGS-M. C) Raman peak values for 30%, 50%, and 80% low-molecular-weight PGS-M ($n = 4$) at 2950 cm^{-1} (mean \pm STD error bars). D) Secondary emission values for 30%, 50%, and 80% low-molecular-weight PGS-M ($n = 4$) at 3.6 eV (mean \pm STD error bars).

(Raman: 3000–2790 cm^{-1} and SE energy region: 2.9–4.3 eV) as shown in Figure S4, Supporting Information. The consistency of SEHI results when compared to those of the Raman spectrum provides a strong argument that both the techniques possess the ability to detect cross-linking in PGS-M through CH bonding changes. However, SEHI displays the additional benefits of a multiscale imaging capability and thus the ability to capture spatial variations.

The SE spectrum also provides a new insight into a previously unknown link between DM and the heterogeneous/homogeneous structure of the PGS-M polymer. **Figure 3A** displays the standard deviation of the cross-linking variation between samples of PGS-M at 80% and 30% DM. The results reveal that PGS-M 30% DM displays a significantly greater variation than that of PGS-M at 80%. The evident increase in the variation in SE spectra values that represents cross-linking density across the polymer samples appears to correlate to a lower DM percentage. This is not unexpected as the chemical composition between samples will exhibit production variability. However, the variation detail observed in the SEHI data across the range of DM% provides an insight not available previously.

The ability of SEHI to isolate compositional chemical changes in both the micro- and nanoscale is expected to provide a novel capability for future work directed at analyzing cellular behavior within seeded biomaterials. As previously affirmed, other techniques that have been historically applied to quantifying cross-linking lack the ability for spatial mapping of the variation of the cross-linking within a sample across these length scales. This makes SEHI an especially useful technique to characterize cross-linking variations within a multiscale approach that provides the ability to map nanoscale variations in particular, if component analysis is used (see Figures S2, S3, and S5, Supporting Information).

In order to isolate cross-linking density as the major contributor to the peak intensity of SE emissions observed in the SEHI spectra, the potential contribution from PGS-M molecular weight was investigated. Comparison results of SEHI spectra of low- and high-molecular-weight forms of 30% PGS-M are displayed in Figure 3B. These results show that molecular weight has no direct impact on the relative intensity of the previously dominant (3.6 eV) peak. However, a new dominant peak around 2.1 eV was observed within the spectrum for the high-molecular-weight form (Figure 3B). Whilst all the spectra have broadly the same profile, some notable differences can be observed that are the consequence of variations in molecular ordering. Conspicuously, around 2.1 eV, the high-molecular-weight PGS-M sample is seen to display a clear peak whereas in the low-molecular-weight PGS-M sample a lesser peak is observable, resulting in only a slight change within the spectrum gradient around 2 eV. These differences can be attributed to the crystalline phases in the semi-crystalline PGS-M sample. This spectral association with increased molecular weight has not been previously observed. The region of these peaks are consistent with previously published work,^[24] which show the shift to higher or lower energies is related to differences in the molecular order of the material. In this instance, the addition of a peak around 1.4–2.3 eV for high-molecular-weight PGS-M is considered a

marker of a more crystalline state in high-molecular-weight when compared to that of low-molecular-weight PGS-M. The ability to observe and, ideally in a future capability, to quantify molecular weight ordering within polymer-derived biomaterials is considered to be an important development, particularly as molecular weight has been shown to have a strong influence on cellular growth.^[25] Figure S2, Supporting Information, displays component analysis of captured SEHI image stacks that indicate 30% low-molecular-weight PGS-M possesses a measurably greater variation of lateral molecular weight composition than that observed for the 80% low-molecular-weight PGS-M sample. These variations are considered to be the consequence of different regions of the PGS-M samples containing dissimilar ratios of high-molecular-weight and low-molecular-weight structures as a result of an expected inconsistency in polymer curing. The approach of SEHI to construct spectra from a stack of images, captured from different deflector voltages, enables the option to further validate this hypothesis by examining each of the individual SEM images. The source SEM images shown in Figure 3B provide supporting evidence that a greater variation of structures is present on the high-molecular-weight PGS surface. It can therefore be seen that the elements of the SEHI approach are complementary and facilitate biomaterial characterization through multiple perspectives and has the ability to carry out depth analysis by using SEHI on cross-sections.

Figure 4A shows that there are variations in the PGS-M sample within the thickness of the sample. While there is only a slight intensity difference between surface and subsurface spectra in the region responding to cross-linking, the appearance of a dominant low energy peak around 2.2 eV within the subsurface PGS-M SE spectrum is indicative of variations in molecular weight. Some surface fragmentation, perhaps hydrolysis-driven surface degradation, would affect the ratio of crystalline and amorphous phases. The subsurface of PGS-M is assumed to be protected from such environmental factors and consequently exhibits a more ordered and crystalline structure. The observation of this low energy peak is consistent with previously documented changes in SE electron emission profiles in response to molecular ordering dissimilarities.^[24] This proposed rationale for surface fragmentation is further supported by the slight reduction in cross-linking recorded in the intensity of the C–H bonding SE peak.

Figure 4B presents the SE spectrum of PGS-M after undergoing 100 W argon plasma surface treatment for 3 min. An SEM image of argon plasma treated cross-section of PGS-M distinctly shows morphology differences between an upper surface “crust” and the polymer’s internal structure. Both surface and subsurface spectrums exhibit small molecular weight peaks at 2 and 1.6 eV respectively, slightly changing the gradient of each spectrum. However, in contrast to non-treated PGS-M samples, the 2.9–4.3 eV peaks associated with C–H vibrations are dominant. The fragmentation of molecular chains is expected to occur deeper than 50 μm .^[26] This has resulted in the reduction of the molecular weight peak observable within the spectrum of subsurface argon plasma treated PGS-M in comparison to that of untreated subsurface PGS-M. The spectrum of the near surface of PGS-M collected post argon treatment indicates a clear increase in dominant

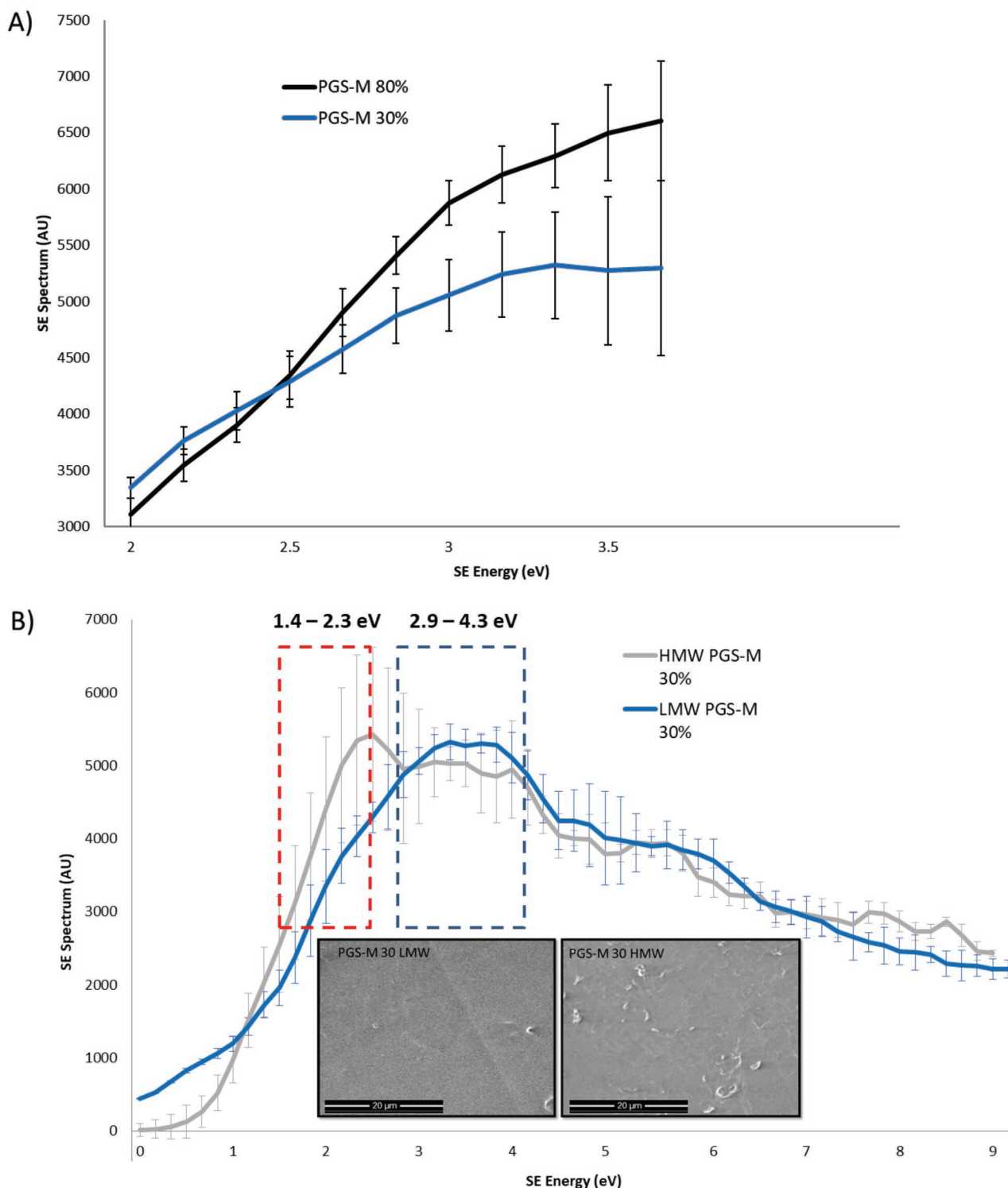


Figure 3. A) Secondary electron spectra for 30% ($n = 4$) and 80% ($n = 4$) low-molecular-weight PGS-M isolating SD variation between 2–3.6 eV (mean \pm STD error bars). B) Secondary electron spectra for 30% low- ($n = 4$) and high-molecular-weight ($n = 4$) (mean \pm STD error bars). Inset SEM images show sub-micron variation visually between high- and low-molecular-weight PGS-M.

peak intensity compared to that of the subsurface spectrum. This indicates an increase of cross-linking within the surface of argon plasma treated PGS-M. It has long been established

that argon plasma has sufficient energy to produce radicals by breaking the C–H bonds. The recombination of these radicals leads to cross-linking of the molecular chains at the

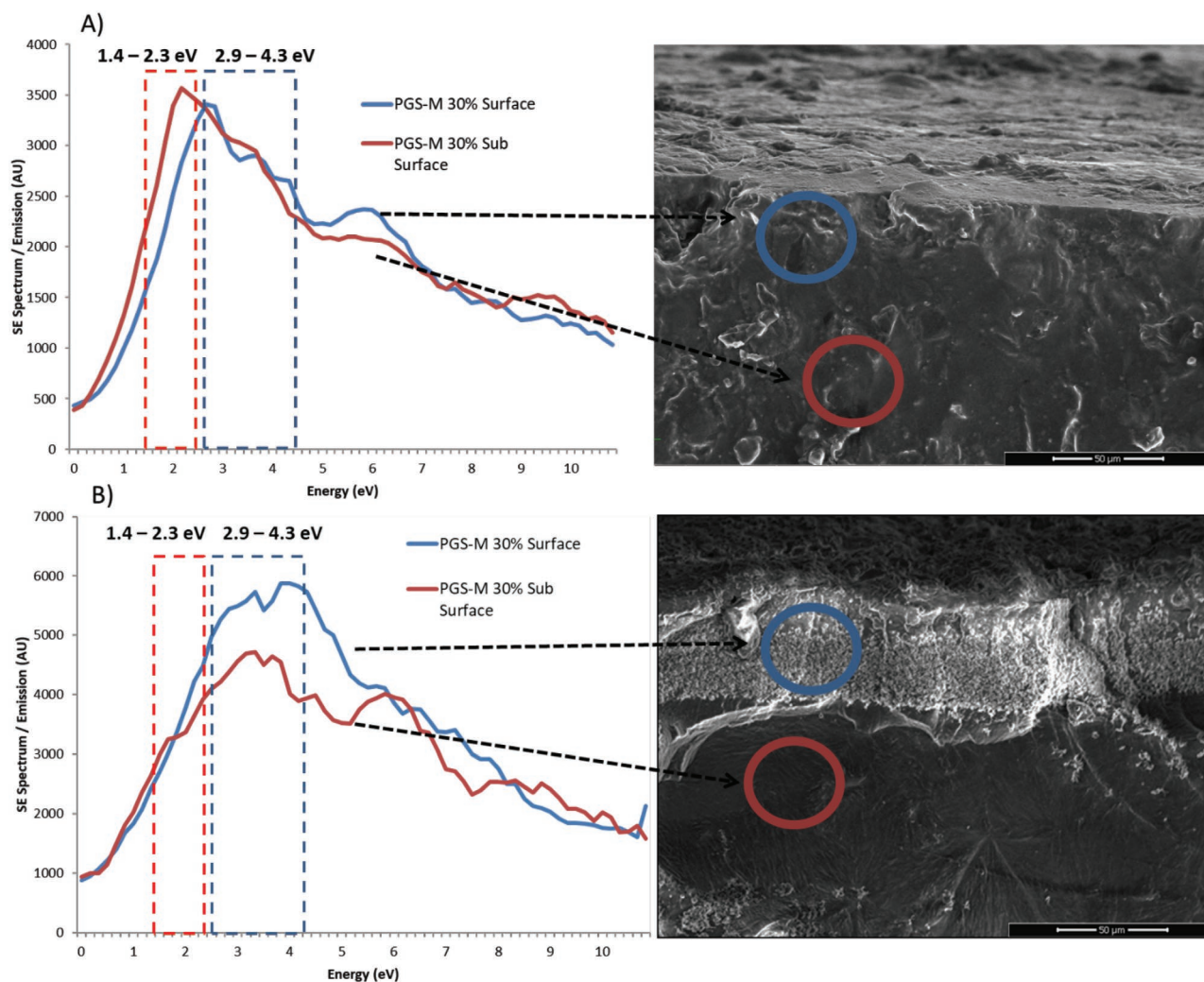


Figure 4. A) Secondary electron spectra and SEM image for and of surface and subsurface 30% low-molecular-weight PGS-M. B) Secondary electron spectra and SEM image for and of surface and subsurface 30% low-molecular-weight argon plasma-treated PGS-M.

polymer surface. SEHI spectra displayed in Figure 4B has for the first time highlighted that post plasma treatment, there is an increase of cross-linking on the surface when compared to subsurface layers of PGS-M.

This future potential application of SEHI as a characterization tool for polymer-derived biomaterials is of interest as most polymer surfaces, especially hydrocarbon surfaces; are chemically inert, have low surface energies, and also exhibit low adhesion properties, all of which are disadvantageous for many bio- material practical applications.

In conclusion, this study provides evidence that SEHI enables the mapping of cross-linking distribution at a multiscale level within a polymer (PGS-M). The SEHI capability to provide both nano- and microscale levels of detail of the morphology of biomaterials is considered to be a valuable tool, especially for polymer-based biomaterials. Here, cross-linking density and local variations in molecular order are major contributors to a biomaterial's mechanical properties and accordingly the consequential biocompatibility of the material. SEHI not only provides an alternative to contemporary

analysis tools, but also provides researchers with a novel and enhanced nanostructure analysis capability for characterizing cross-linking and its spatial variation in beam sensitive biomaterials.

Supporting Information

Supporting Information is available from the Wiley Online Library or from the author.

Acknowledgements

The authors thank EPSRC for funding under SEE MORE: Secondary Electron Emission-Microscopy for Organics with Reliable Engineering Properties (EP/N008065/1), and studentships for N.F. (EP/R513313/1) and N.S. (1816190) S.P.-T. and F.C. under the EPSRC (Award 1624504 and Doctoral Prize Fellowship). Electron microscopy and analysis was performed in the Sorby Centre for Electron Microscopy at the University of Sheffield. All data are accessible through <https://doi.org/10.15131/shef.data.11303525>.

Conflict of Interest

The authors declare no conflict of interest.

Keywords

cross-linking characterization, polymeric biomaterials, secondary electron emission, secondary electron hyperspectral imaging, secondary electron spectroscopy, tissue engineering

Received: September 6, 2019

Revised: October 29, 2019

Published online: December 20, 2019

-
- [1] V. R. Kollaflh, *Zur Energieverteilung der Sekundarelektronen I: Mepergebnisse und Diskussion. Annalen der Physik* **1947**, *1*, 357.
- [2] Q. Wan, K. J. Abrams, R. C. Masters, A. C. S. Talari, I. U. Rehman, F. Claeysens, C. Holland, C. Rodenburg, *Adv. Mater.* **2017**, *29*, 1703510.
- [3] R. C. Masters, A. J. Pearson, T. S. Glen, F.-C. M. Sasam, L. Li, M. Dapor, A. M. Donald, D. G. Lidzey, C. Rodenburg, *Nat. Commun.* **2015**, *6*, 6928.
- [4] A. W. Martinez, J. M. Caves, S. Ravi, W. Li, E. L. Chaikof, *Acta Biomater.* **2014**, *10*, 26.
- [5] N. Reddy, R. Reddy, Q. Jiang, *Trends Biotechnol.* **2015**, *33*, 362.
- [6] M. Bing, W. Xiaoya, W. Chengtie, C. Jiang, *Regener. Biomater.* **2014**, *1*, 81.
- [7] Y. Wang, J. Bao, X. Wu, Q. Wu, Y. Li, Y. Zhou, L. Li, H. Bu, *Sci. Rep.* **2016**, *6*, 24779.
- [8] Y. Wang, G. A. Ameer, B. J. Sheppard, R. Langer, *Nat. Biotechnol.* **2002**, *20*, 602.
- [9] L. X. Jun, A. A. Karim, C. Owh, *J. Mater. Chem. B.* **2015**, *3*, 7641.
- [10] M. Kharaziha, M. Nikkhah, S.-R. Shin, N. Annabi, N. Masoumi, A. K. Gaharwar, G. Camci-Unal, A. Khademhosseini, *Biomaterials* **2013**, *34*, 6355.
- [11] K. W. Lee, D. B. Stolz, Y. Wang, *Proc. Natl. Acad. Sci. USA* **2011**, *108*, 2705.
- [12] W. Wu, R. A. Allen, Y. Wang, *Nat. Med.* **2012**, *18*, 1148.
- [13] C. K. Hagandora, J. Gao, Y. Wang, A. J. Almarza, *Tissue Eng., Part A.* **2013**, *19*, 729.
- [14] J. M. Kempainen, S. J. Hollister, *J. Biomed. Mater. Res., Part A.* **2010**, *94A*, 9.
- [15] S. Pashneh-Tala, R. Owen, H. Bahmaee, S. Reksytyte, M. Malinauskas, F. Claeysens, *Front. Phys.* **2018**, *6*, 41.
- [16] A. Singh, S. Asikainen, A. K. Teotia, P. A. Shiekh, E. Huutilainen, I. Qayoom, J. Partanen, J. Seppälä, J. V. Kumar, *ACS Appl. Mater. Interfaces.* **2018**, *8*, 11677.
- [17] T. Theerathanagorn, J. Klangjorhor, M. Sakulsombat, P. Pothacharoen, D. Pruksakorn, P. Kongtawelert, W. Janvikul, *J. Biomater. Sci., Polym. Ed.* **2015**, *26*, 1386.
- [18] S. Makoto, I. Taku, K. Masaru, N. Nobuyuki, T. Yasuhiko, Y. Hiroshi, *J. Micro/Nanolithogr., MEMS, MOEMS*, **2013**, *12*, 041309.
- [19] Nordson MARCH, *AZoNano*, <https://www.azonano.com/article.aspx?ArticleID=5207> (accessed: May 2019).
- [20] R. M. Silverstein, G. C. Bassler, *J. Chem. Educ.* **1962**, *39*, 546.
- [21] K. B. R. Devi, R. Madivanane, *Eng. Sci. Technol.*, **2012**, *2*, 795.
- [22] C. L. E. Nijst, J. P. Bruggeman, J. M. Karp, L. Ferreira, A. Zumbuehl, C. J. Bettinger, R. Langer, *Biomacromolecules* **2007**, *8*, 3067.
- [23] K. J. Abrams, M. Dapor, N. Stehling, M. Azzolini, S. J. Kyle, J. S. Schäfer, A. Quade, F. Mika, S. Kratky, Z. Pokorna, I. Konvalina, D. Mehta, K. Black, C. Rodenburg, *Adv. Sci.* **2019**, *6*, 1900719.
- [24] R. C. Masters, N. Stehling, K. Abrams, V. Kumar, M. Azzoloni, N. M. Pugno, M. Dapor, A. Huber, P. Schäfer, D. G. Lidzey, C. Rodenburg, *Adv. Sci.* **2019**, *6*, 1801752.
- [25] C. C. Yeh, C. N. Chen, Y. T. Li, C. W. Chang, M. Y. Cheng, H. I. Chang, *Cell. Polym.* **2011**, *30*, 261.
- [26] A. V. Shyichuk, J. R. White, I. H. Craig, I. D. Syrotynska, *Polym. Degrad. Stab.* **2005**, *88*, 415.



Supporting Information

for *Macromol. Rapid Commun.*, DOI: 10.1002/marc.201900484

**Characterizing Cross-Linking Within Polymeric Biomaterials
in the SEM by Secondary Electron Hyperspectral Imaging**

**Nicholas Farr,* Samand Pashneh-Tala, Nicola Stehling,
Frederik Claeysens, Nicola Green, and Cornelia Rodenburg**

Supporting Information

Characterising cross-linking within polymeric biomaterials in the SEM with Secondary Electron Hyperspectral Imaging

Nicholas Farr^a, Samand Pashneh-Tala^a, Nicola Stehling^a, Frederik Claeysens^a, Nicola Green^a, and Cornelia Rodenburg^a

^a*Department of Materials Science and Engineering, Kroto Research Institute, University of Sheffield, Sheffield, United Kingdom*

Materials and Methods

For the following methods, all chemical reagents were obtained from Sigma Aldrich, UK, unless otherwise stated.

Synthesis of PGS Prepolymer

The melt-polycondensation reaction of equimolar amounts of sebacic acid and glycerol was employed to produce the PGS prepolymer (Fisher Scientific, UK). For 24 h in a nitrogen gas atmosphere at 120°C, the constituents were intermixed and stirred. To extract water from the mixture a vacuum was applied. The reaction was then sustained for 24, or 48 h as required.

Synthesis of PGS-M Prepolymer

PGS-M prepolymer was synthesised as described previously (1). PGS prepolymer free hydroxyl groups were methacrylated to manufacture a photocurable prepolymer. It was presumed that two of the three hydroxyl groups present in glycerol reacted with sebacic acid. This reaction leaving 3.9 mmol of hydroxyl groups per gram of PGS prepolymer available for methacrylation (2, 3). PGS prepolymer was methacrylated at two distinct molecular weights. PGS prepolymer at low and high molecular weight (referred to as Low Mw and High Mw PGS) was created by polycondensation reactions, respectively of 48 and 72 h duration. Gel permeation chromatography (GPC) (ViscotekGPCMaxVE 2001 with PLgel 5µm Mixed C column) determined the number average molecular weight (Mw) of the PGS prepolymer to be 2,230 ± 40, 2,770 ± 100, and 3,360 ± 50 g/mol and the weight average molecular weight (Mw) to be 5,420 ± 430, 8,960 ± 840, and 17,340 ± 760 g/mol for reaction lengths of 48, 60, and 72 h, respectively. PGS prepolymer was synthesized by the polycondensation reaction of glycerol with sebacic acid at 120°C.

Dichloromethane was used to dissolve the prepolymers (Fisher Scientific, UK) 1:4 (w/v) then methacrylic anhydride and an equimolar quantity of trimethylamine was added gradually. To achieve PGS-M polymers of 30%, 50% and 80% DM, methacrylic anhydride at three concentrations (0.3, 0.5, and 0.8 mol/mol of PGS prepolymer hydroxyl groups) was employed in the reaction. 4-methoxyphenol was also added to the PGS prepolymer at 1 mg/g. After the reaction was instigated at 0°C the temperature was raised over a 24h period to room temperature. 30 mM hydrochloric acid (Fisher scientific, UK) at 1:1 (v/v) was used to wash the solution which was then dried with calcium chloride (Fisher scientific, UK). Rotary evaporation was then used to remove the dichloromethane under vacuum.

Synthesis of Photocured PGS-M

PGS-M prepolymers were mixed at 1% (w/w) with the photoinitiator diphenyl(2,4,6-trimethylbenzoyl)phosphine oxide/2-hydroxy-2-methylpropiophenone (50/50 blend) (further denoted as photoinitiator blend), cast in silicone moulds and exposed to UV light for 10 min (100 W, OmniCure Series 1000 curing lamp) to photocure. Photocured PGS-M samples were washed in methanol to remove residual photoinitiator blend and unreacted prepolymer and then dried (1).

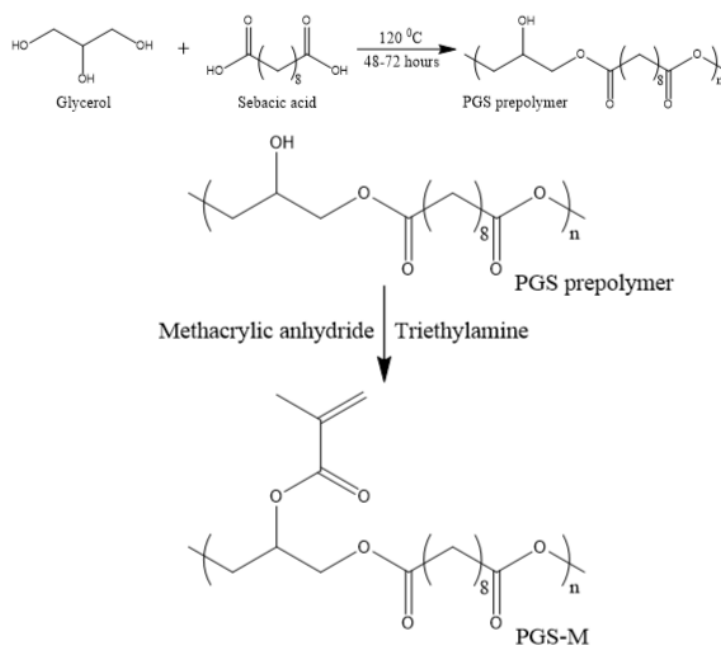


Figure S1 - Displays PGS-M chemical synthesis from monomers, to PGS pre-polymer and finally produced of PGS-M.

PGS-M Cross-linking Characterisation

1. SEM and Image Data Processing

Imaging

Observation of the surface morphology of the PGS-M samples was performed using a Scanning Electron Microscope (FEI Nova Nano 450 SEM). The PGS-M samples were not subject to deposition of conductive coating, in contrast to usual polymers SEM analysis practice. To avoid surface charging and consequent damage to the sample a low accelerating voltage (1 KV) with typical vacuum pressure of 10^{-5} mbar at a working distance of 3mm was applied. An Everhart-Thornley Detector (ETD) for low magnification images and a Through Lens Detector (TLD) for high magnification images were used for the collection of SE images.

SEHI Acquisition and Image Processing

The FEI Nova Nano 450 SEM is provided with a through lens detector which includes a voltage controlled deflector electrode. The deflector electrode channels the signal into the SE detector. The deflector electrode is set to a predetermined number of deflector voltages and an image is generated for each deflector voltage. Spectra and hyperspectral images are acquired through post-processing of such image series. Stage bias has been performed to allow energy calibration of this process through experiments (4, 5). Fiji software was utilised to perform image processing (6). Histogram and spectral off-set normalisation (7) has been applied retrospectively to optimise all images for brightness and contrast, and to limit the effects of differing sample work functions. Once S curves have then been obtained they are differentiated to produce the SE curves which are reported in the main manuscript. Component analysis was then performed to image stacks utilising non negative matrix factorization (nmf) to isolate components of interest.

PGS-M Cross-linking Validation

Raman Spectroscopy

Raman spectroscopy (Renishaw inVia micro-Raman) was employed to analyse the chemical structure of the PGS-M Low Mw 30%, 50% and 80% placed on borosilicate glass. Using a 50x objective the laser power was 20 mW with a $1\ \mu\text{m}$ spot size. A Peltier-cooled multichannel CCD detector was used for data recording with a 2,400 lines/mm diffraction grating at a slit opening of $65\ \mu\text{m}$ and a spectral resolution of in the order of $1\ \text{cm}^{-1}$.

Nanoindentation

Nanoindentation measurement was performed on wax embedded PGS-M disks. The PGS-M was embedded at 42°C and sectioned smooth. A Bruker's Hysitron TI Premier nanoindenter, attached to a Berkovich tip was used for nanoindentation studies. A matrix of 12 indentations was applied, spaced $60\ \mu\text{m}$ apart. The polymer sample was loaded for 5 s, held for 80 s, and

unloaded for 3 s. The hold period was added to allow any effects from creep in the polymer to be minimised. A peak force of 200 μN was applied with a lift height of 20 nm. The Oliver Pharr method was utilised to analyse each of the unloading segments of the polymer indentation. This provided a reduced modulus (E_r) value as well as sample hardness (H).

Low Temperature Plasma Treatment

PGS-M samples were exposed to low-pressure Argon gas in a Diener Electronic Zepto plasma cleaner at 40 kHz, 100 W, and 0.3 mbar air for 3 minutes. 3 minutes of exposure was chosen as a maximum limit to exclude any effects of sample heating which have been shown to lead to surface modification of a different kind (8). SEHI spectra were then collected from the plasma treated surface and sub surface of cross-sectioned PGS-M 30%. An Argon plasma source was selected as a consequence of its main mechanism being physical sputtering by Argon ions, this process has previously been linked to causing highly crosslinked surfaces. As the molecular structure of PGS-M includes oxygen atoms this enhances the treatment, whereby carbon atoms in polymers are easily volatilised when oxygen atoms are present.

Additional Results

Figure S2 displays component analysis of 80% and 30% Low Mw PGS-M. In this instance non-negative matrix factorization (nmf) isolated two components between 0 – 5 eV, one being a peak around 3.2 eV, highlighted in the text as CH vibrations, and another with peaks observed around 1.4 – 2.3 eV. This is in the energy range that we attributed to molecular weight in the main manuscript. The graphs reveal some variation between 80% and 30% PGS in both components but this particularly pronounced for the molecular weight component (component 2) of the 30% PGS-M sample. Images displayed in figure S3 of the supporting information reflect the spatial variation in component 2 for both 80% and 30% PGS-M. These images provide further support for the view that the variation observed in component 2 in the 30% PGS-M sample is caused by spatial variations.

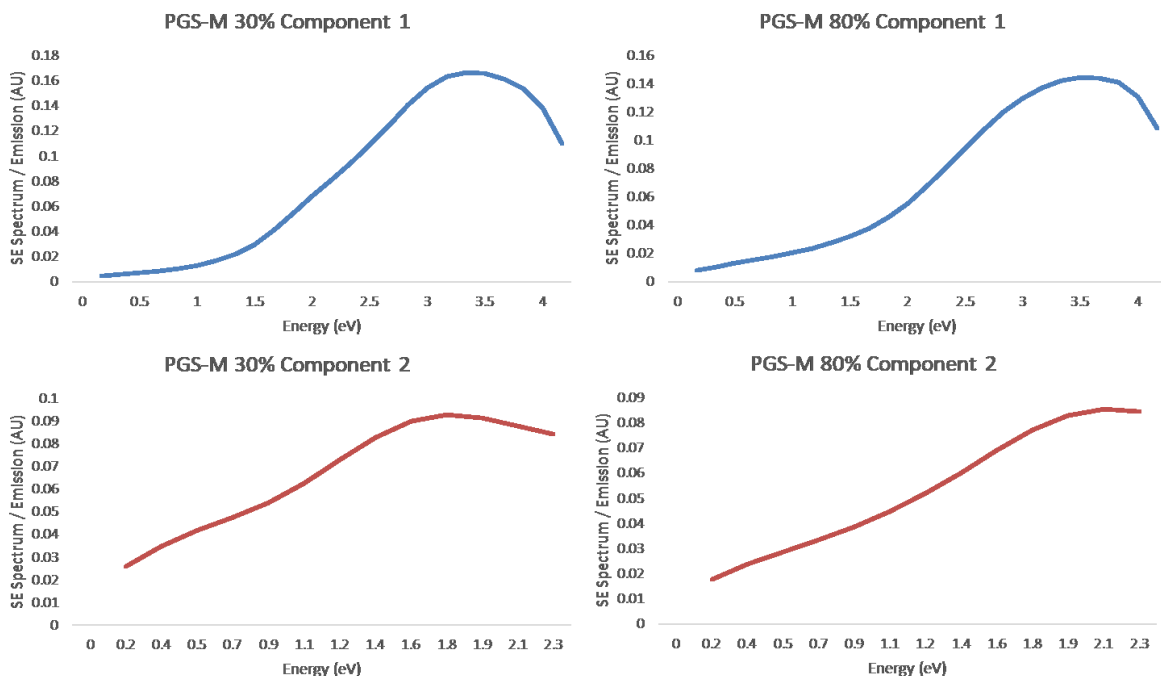


Figure S2 - Non negative matrix factorization (nnmf) multivariate analysis of 30% ($n=4$) and 80% ($n=4$) PGS-M. Isolating two components: component 1 is associated with CH Vibrations and component 2 is associated with Molecular Weight.

30% PGS-M Component 2 80% PGS-M Component 2

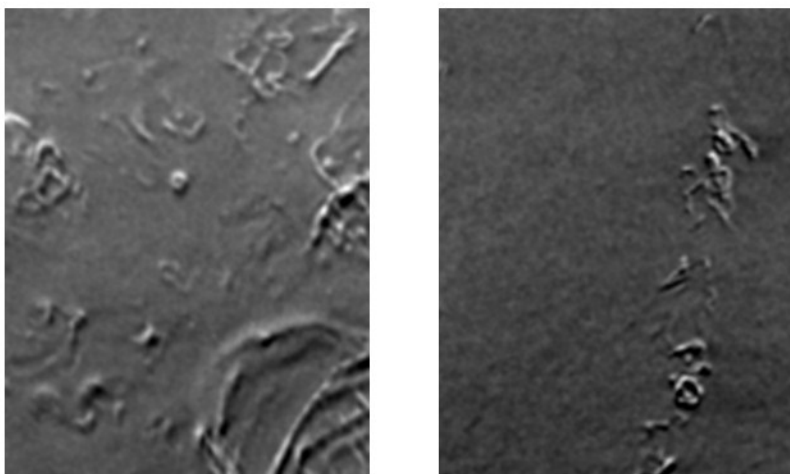


Figure S3 Resulting images of component 2 of 30% and 80% PGS-M from non negative matrix factorization (nnmf) component analysis.

The peaks associated with hydrogenated carbon correlate with the observed CH vibrations peak given in the captured Raman spectrum. Figure 4A/B shows the relative intensity change in the Raman data between $3000 - 2790 \text{ cm}^{-1}$ and SE relative intensity emission change between $2.9 - 4.3 \text{ eV}$ respectively for PGS-M samples. The changes in Raman intensity around this region (CH

vibrations) closely correlates with the SE intensity changes identified. Both peaks are similarly affected by CH bonding and consequently the cross-linking process of PGS-M.

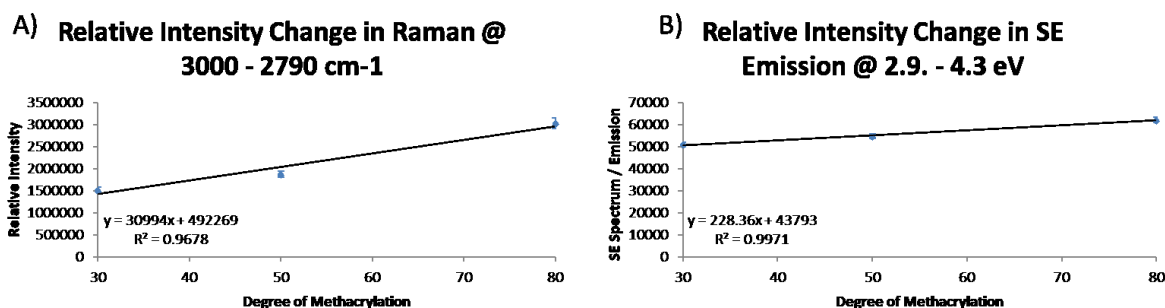


Figure S4 A) Relative Intensity Raman peak values for 30%, 50% and 80% Low Mw PGS-M ($n=4$) at 2950 cm^{-1} (mean \pm STD error bars). B) Relative Intensity Secondary emission values for 30%, 50% and 80% Low Mw PGS-M ($n=4$) at 3.6 eV (mean \pm STD error bars).

Figure S5 displays component analysis of subsurface 30% Low Mw PGS-M post Argon plasma treatment. In this case non-negative matrix factorization (nnmf) isolated two components between 0 – 4 eV, the first being a peak observed around 2.9 eV, highlighted in the manuscript text as CH vibrations, and the second a peak observed around 1.8 eV. This occurs in the energy range that we have attributed the molecular weight component in the main manuscript. Images in the figure provide further support for our assertion that the two components have different visual distributions within the material.

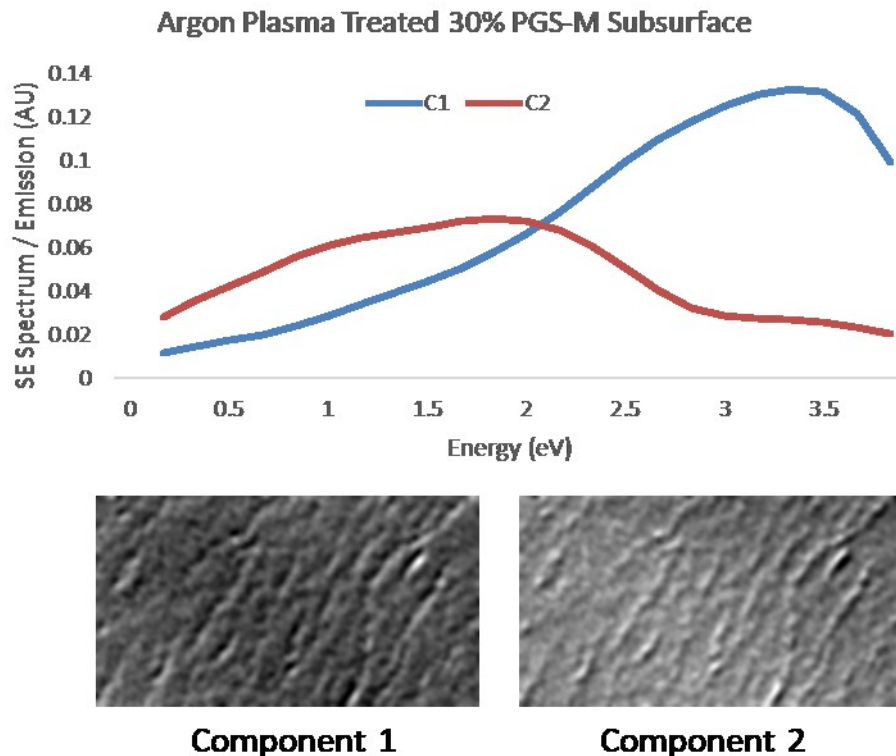


Figure 5 - Non negative matrix factorization (nmf) including component images of the subsurface of 30% PGS-M post Argon plasma treatment. Isolating two components: component 1 is associated with CH Vibrations and component 2 is associated with Molecular Weight.

References

1. S. Pashneh-Tala, R. Owen, H. Bahmaee, S. Rekštyte, M. Malinauskas, F. Claeysens, Synthesis, characterization and 3D micro-structuring via 2-photon polymerization of poly(glycerol sebacate)-methacrylate-an elastomeric degradable polymer. *Frontiers in Physics*. 2018 **6**, 41.
2. C.L.E. Nijst, J.P. Bruggeman, J.M. Karp, L. Ferreira, A. Zumbuehl, C.J. Bettinger, Synthesis and Characterization of Photocurable Elastomers from Poly(glycerol-co-sebacate). *Biomacromolecules*. 2007. **8**, 3067–73.
3. J.L. Ifkovits, R.F. Padera, J.A. Burdick, Biodegradable and radically polymerized elastomers with enhanced processing capabilities. *Biomed Mater*. 2008. **3**, 34104.
4. P.S. Kazemian, A.M. Mentink, C. Rodenburg. C.J. Humphreys. Quantitative secondary electron energy filtering in a scanning electron microscope and its applications. *Ultramicroscopy*. 2007. **107**, 140–150.
5. Q. Wan, K.J. Abrams, R.C. Masters, A.C.S. Talari, I.U. Rehman. Mapping Nanostructural Variations in Silk by Secondary Electron Hyperspectral Imaging. Claeysens F. Holland C. Rodenburg, C. *Adv. Mater*. 2017 **29**, 1703510.

6. J. Schindelin, I. Arganda-Carreras, E. Frise, V. Kaynig, M. Longair, T. Pietzsch, S. Preibisch, C. Rueden, S. Saalfeld, B. Schmid, J.Y. Tinevez, D.J. White, V. Hartenstein, K. Eliceiri, P. Tomancak, A. Cardona. Fiji: an open-source platform for biological-image analysis. *Nat. Methods*. 2012. **9**, 676.
7. N.A. Stehling, R. Masters, Y. Zhou, R. O'Connell, C. Holland, H. Zhang, C. Rodenburg, New perspectives on nano-engineering by secondary electron spectroscopy in the helium ion and scanning electron microscope. *MRS Commun.* 2018. **8**, 226–240.
8. J. Yip, K. Chan, K.M. Sin, K.S. Lau, Study of plasmaetched and laser-irradiated polyamide materials. *Mater. Res. Innov.* 2002. **6**, 44–50.

4. Understanding Argon Plasma Sterilisation through Secondary Electron Hyperspectral Imaging

Advanced Science
Early View
January 2021,
DOI: 10.1002/adv.202003762

Nicholas Farr, ^{*1,3} Jeerawan Thanarak, ^{1,3} Jan Schäfer, ² Antje Quade, ² Frederik
Claeyssens, ^{1,3} Nicola Green, ^{1,3} and Cornelia Rodenburg¹

¹ University of Sheffield Faculty of Engineering, Material Science and Engineering, Sheffield, S1 3JD, UK

² Leibniz Institute for Plasma Science and Technology (INP e.V.), Felix-Hausdorff-Str. 2, 17489 Greifswald, Germany.

³ Insigneo Institute for in silico Medicine, The Pam Liversidge Building, Sir Robert Hadfield Building, Mappin Street, Sheffield, UK

Received 2 October 2020; accepted 10 November 2020

4.1 Prelude

This chapter presents the article titled “Understanding Argon Plasma Sterilisation through Secondary Electron Hyperspectral Imaging”. The work presents a detailed investigation of biomaterial surface structures by means of SEHI. SEHI allows key insights into a samples secondary emission properties and in turn their chemical functional groups which results in high resolution chemical imaging. Such imaging provides key insights into the biocompatibility of biomaterials. Specifically, by applying SEHI the energy distribution of emitted secondary electrons (SEs) is used to map various sample properties. SEHI maps were developed to evaluate the application of Argon Plasma Sterilisation in combination with a novel gas permeable packaging method. Thus opened up a new route to achieving biomaterial terminal sterilisation.

Terminal sterilisation is the process of destroying all microorganisms within a final stage of a packaging process. Prior to being selected for an invasive surgical procedure it is standard practice for all non-biological materials to be sterilised. Prior to this study PGS-M was sterilised using a high temperature autoclave procedure. This process limits the advantages of PGS-M over PGS as the high temperatures required to sterilise the material prevents heat sensitive biomolecules being included during the production of PGS-M. Aside from autoclaving a range of sterilisation techniques, such as gamma (γ) radiation, are deployed in the medical device industry but their suitability for being applied to polymeric biomaterials have at this time has not yet been established. A widely employed and effective non-thermal option for tissue sterilisation has been Gamma radiation. However, gamma radiation has been shown to cause polymer chain-scission and an alternative non-thermal sterilisation is required to suit the requirements of poly-derived biomaterials.

4.1.1 Thesis Question 1 Can SEHI deliver insights into the mechanical properties of a biomaterial?

Chapter 4 further progressed the work presented in chapter 3 by modifying the surface of PGS-M using Ar plasma treatment. SEHI data and nanoindentation measurements identified that Ar plasma treatment significantly increased the stiffness of PGS-M samples due to crosslinking. SEHI produced maps of CO bonding that for the first time suggested the surface structures of PGS-M varied locally and can be changed depending on Ar treatment time. SES provided a toolset that delivered crosslinking density and functional group variation data at the nanoscale.

4.1.2 Thesis Question 2: Is the captured SE spectra able to identify specific functional groups that play a key role in biomaterials engineering TE and if so can SEHI map these functional groups at the nanoscale?

Furthering chapter 3, the SEHI technique facilitated the capture of a number of key insights into the sample's electron emission properties leading to the identification of their chemical functional groups (C-H, C-O, C-C, O-H). This consequently resulted in the creation of high resolution chemical images. The publication showed for the first time such chemical imaging was capable of being produced using SEHI and also provided evidence of its potential to reveal key insights into the biocompatibility of the biomaterials analysed.

The publication focused on characterising the effects on the biomaterial samples of different conditions of Argon Plasma treatment when compared to the known industry standard Autoclave sterilisation technique. The experimental process followed during this work exploited a range of analysis techniques, including the pioneering use of SEHI. This was an exciting development for SEHI as it delivered the ability to isolate functional groups on the surface of biomaterials, in addition to its novel capacity to map them at the nanoscale. The publication presented in chapter 4 also analysed a range of polymers with different functional group distributions. These included; PGS-M, PCL, PCL-M, Nylon 6 and polypropylene. All the materials apart from polypropylene were imaged as a rough surface and SES/SEHI demonstrated its capability of imaging or mapping their surfaces chemically. Analysis of the polypropylene was the first time SES/SEHI mapping had been conducted on a fibre shaped material with differing surface angles. Despite this challenge, SES analysis was successfully performed and reliable mapping data of Polypropylene's surface functional groups distributions was collected.

Aside from identifying oxygen containing functional groups this study also furthered previously published work from the Rodenburg group that has shown that surface morphology effects are particularly meaningful in higher SE emissions (1,2,3). This publication aimed to reduce the possibility of surface morphology effects by focusing on emissions below 6 eV. Previous work has shown that these SE energy ranges are appropriate to functional group emissions and not surface morphology emissions effects (4,5). To clarify this point an experimental section was added to the supporting information (page 14/15). As the manuscript indicates we do observe a rougher surface after AC compared to that of Argon treatment. This relationship is similarly observed within the SE spectra taken at higher energies (Figure S12 of the SI). S13 allows a comparison to be drawn from SEHI functional group emission and > 6 eV topographical SEM images.

4.1.3 Brief Summary

In summary this work focuses on characterising the effects on the biomaterial samples of different conditions of Argon Plasma treatment comparable to the known industry standard of Autoclave sterilisation. In the process of doing so this work exploits a range of analysis techniques including the pioneering use of SEHI, which for the first time has been able to characterise various surface functional groups. This is an exciting development as SEHI delivers the ability to isolate functional groups on the surface of biomaterials, in addition to its novel capacity to map them at the nanoscale.

4.2 Contributions

NF performed the majority of the experimental work and data analysis and wrote the manuscript. JT synthesised PGS-M and conducted the cell culture/contact angle measurements. JS and AQ conducted the XPS analysis. NG, FC and CR contributed to

the experimental design, project supervision, and the writing of the manuscript. Please see overleaf for the paper. Advanced Science published by Wiley-VCH GmbH. This is an open access article under the terms of the Creative Commons Attribution License, which permits use, distribution and reproduction in any medium, provided the original For more information see (<https://creativecommons.org/licenses/by/4.0/>).

4.3 References

1. V. Kumar, W.L. Schmidt, G. Schileo, R.C. Masters, M. Wong-Stringer, D.C. Sinclair, I.M. Reaney, D. Lidzey and C. Rodenburg: *Nanoscale Mapping of Bromide Segregation on the Cross Sections of Complex Hybrid Perovskite Photovoltaic Films Using Secondary Electron Hyperspectral Imaging in a Scanning Electron Microscope*. ACS Omega **2**, 2126 2133 (2017).
2. Q.Wan: Scanning electron microscopy investigation of bio-polymer composites morphology. PhD Thesis, University of Sheffield. (2017).
3. Q. Wan, K. J. Abrams, R. C. Masters, A. C. S. Talari, I. U. Rehman, F. Claeysens, C. Holland, C. Rodenburg, Adv. Mater. **29**, 1703510. (2017).
4. K.J. Abrams, M. Dapor, N. Stehling, M. Azzolini, S.J. Kyle, J.S. Schäfer, A. Quade, F. Mika, S. Kratky and Z. Pokorna: *Making Sense of Complex Carbon and Metal/Carbon Systems by Secondary Electron Hyperspectral Imaging*. Adv. Sci. 1900719 (2019).
5. N.A. Stehling: Scanning Electron Microscopy for Nano-morphology Characterisation of Complex Hierarchical Polymer Structures. PhD thesis, University of Sheffield. (2019).



Understanding Surface Modifications Induced via Argon Plasma Treatment through Secondary Electron Hyperspectral Imaging

Nicholas Farr,* Jeerawan Thanarak, Jan Schäfer, Antje Quade, Frederik Claeysens, Nicola Green, and Cornelia Rodenburg

Understanding the effects that sterilization methods have on the surface of a biomaterial is a prerequisite for clinical deployment. Sterilization causes alterations in a material's surface chemistry and surface structures that can result in significant changes to its cellular response. Here we compare surfaces resulting from the application of the industry standard autoclave sterilisation to that of surfaces resulting from the use of low-pressure Argon glow discharge within a novel gas permeable packaging method in order to explore a potential new biomaterial sterilisation method. Material surfaces are assessed by applying secondary electron hyperspectral imaging (SEHI). SEHI is a novel low-voltage scanning electron microscopy based characterization technique that, in addition to capturing topographical images, also provides nanoscale resolution chemical maps by utilizing the energy distribution of emitted secondary electrons. Here, SEHI maps are exploited to assess the lateral distributions of diverse functional groups that are effected by the sterilization treatments. This information combined with a range of conventional surface analysis techniques and a cellular metabolic activity assay reveals persuasive reasons as to why low-pressure argon glow discharge should be considered for further optimization as a potential terminal sterilization method for PGS-M, a functionalized form of poly(glycerol sebacate) (PGS).

Biomaterials are rapidly expanding their contribution to today's medical progress, particularly in the role of a permanent or transient alternative for damaged or diseased tissues. It is essential that all biomaterials are sterilized prior to implantation within the patient. Additionally, the preservation of the mechanical properties and surface chemistry of a biomaterial poststerilization is essential for the correct function of the material within the body.^[1] However, commonly deployed sterilization techniques such as autoclaving (AC), irradiation, or chemical treatment have been shown to alter the surface and/or the mechanical structure of polymer-based biomaterials.^[2] In comparison, plasma technology has demonstrated a promising potential for surface treatment of biomaterials.^[3] A recent review suggests that argon (Ar) plasma can be employed as a viable alternative sterilization procedure for biomaterials.^[4] However, several challenges have to be overcome in order to establish plasma sterilization as a standardized ISO method including the characterization of

N. Farr, J. Thanarak, Dr. F. Claeysens, Dr. N. Green, Dr. C. Rodenburg
Department of Materials Science and Engineering
Sir Robert Hadfield Building
University of Sheffield
Mappin Street, Sheffield S1 3JD, UK
E-mail: nfarr1@sheffield.ac.uk

N. Farr, J. Thanarak, Dr. F. Claeysens, Dr. N. Green
Insigneo Institute for In Silico Medicine
The Pam Liversidge Building
Sir Robert Hadfield Building
University of Sheffield
Mappin Street Sheffield S1 3JD, UK

Dr. J. Schäfer, Dr. A. Quade
Leibniz Institute for Plasma Science and Technology (INP e.V.)
Felix-Hausdorff-Str. 2 Greifswald 17489, Germany

The ORCID identification number(s) for the author(s) of this article can be found under <https://doi.org/10.1002/adv.202003762>

© 2020 The Authors. *Advanced Science* published by Wiley-VCH GmbH. This is an open access article under the terms of the Creative Commons Attribution License, which permits use, distribution and reproduction in any medium, provided the original work is properly cited.

DOI: 10.1002/adv.202003762

bioactive species of plasma,^[5] understanding of microbiological interactions,^[6] and achieving standardization of the plasma sterilization method. In particular, ISO standardization requires separate time consuming analyses of surface properties for each specified sterilization condition. Here, Ar plasma treatment is combined with the deployment of semi gas-permeable packaging in order to form a model treatment of potential sterilization method for future use with polymer-based biomaterials. Moreover, secondary electron hyperspectral imaging (SEHI) is applied to reveal any localized changes in key functional groups (CH, OH, and CO) on the surface of a biomaterial induced as a result of Ar treatment.

The foundation of SEHI is the collection of secondary electron (SE) emission spectra by means of the scanning electron microscope (SEM). The SE spectra for some hydrocarbon materials were found to be strongly influenced by excitation of intramolecular vibrations.^[7] Thus, SEHI can be successfully applied to the characterization of polymers,^[8] including novel polymeric biomaterials, and has already revealed the changes in molecular weight and CH vibrations that occur as a consequence of Ar

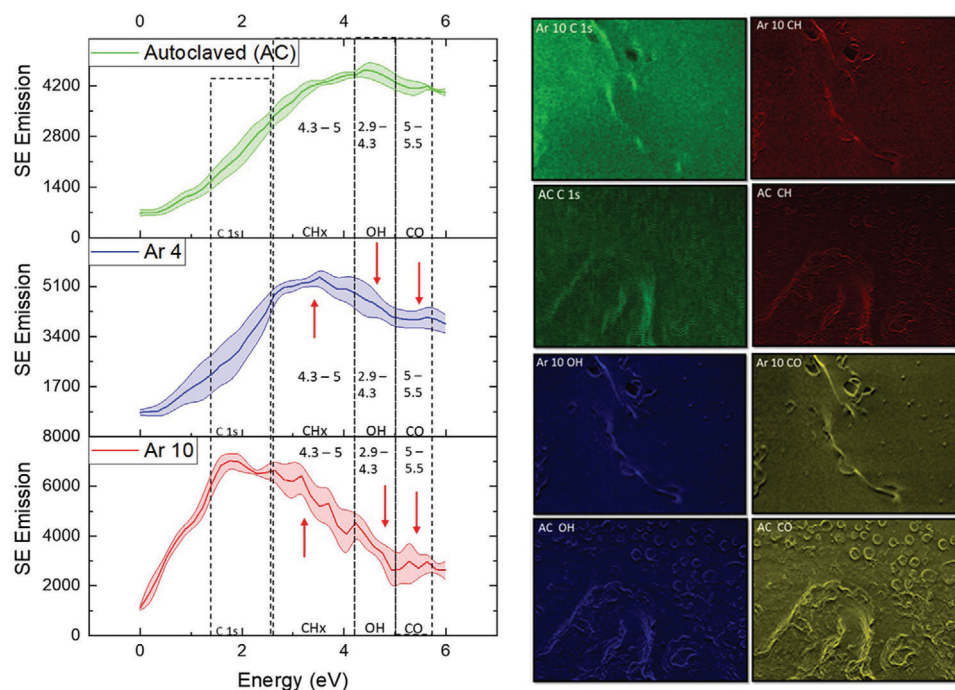


Figure 1. A) Secondary electron spectra for AC, Ar 4, and Ar 10 treated PGS-M highlighting the regions identified as associated with functional group emissions. B) SEHI images generated from the component analysis of Ar 10 and AC. Mapping C 1s, CH, OH, and CO bonding.

plasma treatment.^[9] As SEHI is carried out in the SEM, local variation in chemical changes and sample topography can be assessed in one step.^[10] To do this, SEHI constructs a series of images of the sample area, where each image is formed from a selected SE energy band. While innovative synchronized structural and chemical characterization of materials by SEHI has many uses, this study focuses on revealing and mapping the spatial variation of functional groups that are affected by Ar plasma treatment through identifying specific energy bands for CH-, OH-, and CO- groups. In order to identify suitable energy bands for mapping such variations, a number of reference materials are used to evaluate the effects that Ar plasma treatment exhibits on local surface chemistry of sterilized biomaterials. This is important as a biomaterial's functional groups are closely coupled to its ability to promote cell growth through the local surface variations that result from the differing polymer side chains.^[11,12,13] Detrimental surface hydrophobic characteristics of some biomaterials developed from synthetic polymers are manifested as a lack of cell adhesion,^[14] resulting in the implanted biomaterial presenting poor tissue infiltration and integration outcomes. Thus a range of material characterization techniques in addition to SEHI are utilized here to further evaluate the effects of Ar plasma treatment of the surface topology of a polymer-based biomaterial, in this instance PGS-M.

PGS-M is a functionalized form of poly(glycerol sebacate) (PGS)^[15,16] The PGS-M polymer, formed by rendering PGS (an elastomeric degradable and nontoxic tunable polymer^[15]) photocurable through the process of methacrylation, displays characteristics that are perceived as advantageous for biomaterial applications.^[17,18] It has been observed that PGS-M is likely to include small quantities of unreacted methacrylate side chains after polymerization by UV, removal of the unreacted methacry-

late, and creating OH- groups on the surface has the potential to aid cellular growth and further the materials biocompatibility. Previous studies have indicated that plasma treatment can remove unreacted methacrylate.^[19] In this study, low-pressure argon glow discharge has been applied for surface treatment of PGS-M samples. Plasma treated samples exhibit different functional group densities than those of nontreated PGS-M control samples. Changes include CO bonding and an increase of polar hydroxyl groups established through SEHI. These changes explain the varying ability of PGS-M to support cellular adhesion after AC or Ar plasma treatment as demonstrated by contact angle measurements and cell metabolic activity assays.

The PGS-M materials were enclosed in a gas semipermeable bag, which was exposed to low-pressure Ar glow discharge. Use of the semipermeable bag ensures that any sterilization effect will not be compromised between the Ar plasma treatment and cell growth experiments. In order to assess the chemical changes taking place during this Ar plasma treatment, and compare this to the effects of AC sterilization, SE spectra were collected and presented in **Figure 1**. This figure shows the SE spectra of AC PGS-M, 10 min argon plasma treated PGS-M (Ar 10), and 4 min argon plasma treated PGS-M (Ar 4) (nontreated PGS-M spectra can be found in the Supporting Information). For all treatments a peak is observable within the 1.4–2.3 eV range, however, differences arise in intensities of the peaks found within this range. Previous studies have isolated the energy range of 1.4–2.3 eV to the molecular order of carbon (C 1) polymers^[6] with a higher order yield intensity in this energy region. Ar 10 clearly exhibits a greater carbon peak (M_w) compared to that of Ar 4 and AC. This can be understood as follows: argon plasma treatment causes a high levels of free radicals to create crosslinking sites post-treatment, which directly affect the molecular order of the material. Argon

plasma treated surfaces also exhibit a greater SE emission in the energy range that is associated with CH vibrations, with all samples expressing CH₂ and CH₃ peaks (Rationale in Figure S2 in the Supporting Information). Furthermore, the intensity is increased by prolonged Ar plasma exposure. The peak intensity in this energy region has been previously shown to have a direct relationship with the crosslinking density of PGS-M.^[9] Therefore, the SE spectrum of Ar 10 suggests a highly crosslinked surface layer. Reactions within the surface structure by argon plasma induced radicals form crosslinks, which have the potential to enhance the crosslinking density between the surface molecular chains.^[20,21]

Further, differences in the SE spectra for argon plasma treated and AC samples are observed within the region of 5–5.5 eV, related to C=O bonding (Figure S2, Supporting Information). The spectrum shows that post-argon plasma treatment emissions in the 5–5.5 eV range are greatly diminished. Argon plasma treatment is understood to cleave away C–O–C bonds attached to the methacrylate within PGS-M (Figure S6, Supporting Information). By cleaving away this bond, removal of methacrylate greatly decreases the amount of C=O bonds present within the polymer. It is worth noting that the decrease in C=O bonding is most noticeable in the Ar 10 rather than Ar 4 samples, which indicates that the cleavage of methacrylate units is time and area dependent. As more methacrylate is removed, surface crosslinking recombination increases, resulting in an increase in surface crosslinking of Ar 10. Once methacrylate units are removed, an OH containing hydroxyl group remains, signified by Ar 10 and Ar 4 showing emissions within 4.3–5 eV.

While the SE spectra provide an insight into the average chemical changes at the surface, which could also be obtained by other surface sensitive methods such as x-ray photoelectron spectroscopy (XPS) (Figures S3–S5, Supporting Information), using the above specific energy ranges to form images in the SEM is only possible with SEHI. In order to obtain images from the corresponding spectral components, a non-negative matrix factorization (nmf) was used to isolate various components between 0 and 6 eV (Figure S7, Supporting Information). Figure 1B displays images generated of these components from the Ar 10 and AC surfaces that can be matched to the peak allocation described in the Supporting Information (SEHI images and nmf of nontreated PGS-M are displayed in Figure S13 in the Supporting Information). When viewing SEHI images, the brighter the primary color, the greater the SE emissions associated with that component. Consequently, the brighter the emission color, the greater the functional group prevalence,^[9] where all analyzed materials are used to determine the upper and lowest emission values. It is expected that at the length scale of micro/nanometers, structures will include emission from multiple functional groups. To establish the distribution of functional groups, one should consider the brightness of specific emissions. Figure 1B shows the distribution of C 1, C–H, O–H, and C=O bonding within Ar 10 and AC samples.

It is notable that the topography of Ar 10 plasma treated samples differs greatly from AC samples, an observation consistent with previous reports.^[4] SEHI images show micrometer-sized spherical features are clearly present within AC, with strong SE emission signatures of C=O bonding. The C=O bonding related emissions of these structures indicate that they contain excess methacrylate groups. C=O bonding across the matrix of Ar 10 on

the whole is diminished seemingly as a result of the cleaving of methacrylate post-Ar plasma treatment. SEHI images displayed in Figure 1B do show spherical nanofeatures within Ar 10, which exhibit emission of C=O bonding. It is proposed that remnants of methacrylate, which have not yet been cleaved away from the surface of PGS-M by Ar plasma treatment, are still traceable. Additionally, the micrometer spherical features within AC samples emitted a far weaker CH bonding signature than the Ar plasma treated samples, indicating that less crosslinking occurs around these larger regions. **Figure 2** displays SEHI images that further confirm the breakdown of the micrometer spherical features in AC PGS-M with high SE emission in relation to CO bonding into the nanodot structures present in the Ar 10 surface.

From SEHI images alone it is obvious from the reduction of area with strong SE emission in the CO– bonding related energy range that excess methacrylate has been removed from the sample as a consequence of the Ar plasma treatment. Furthermore, the increase in OH groups and CH related crosslinking has clearly become more abundant across the surface matrix post-Ar plasma treatment. As previously stated, the removal of unreacted methacrylate together with the introduction of surface OH groups is recognized to aid cell growth through the enhanced cellular response expected in materials that exhibit greater crosslinking, and it is expected that cells would adhere and proliferate better on Ar plasma treated surfaces.

To test the expectations based on SEHI functional group mapping and for the purpose of using argon plasma as a terminal sterilant, it is important to understand how the SEHI results link to those obtained through commonly practiced characterization methodologies. This is achieved by investigating how the argon plasma treatment has affected the mechanical properties of PGS-M. **Figure 3A** shows the results of nanoindentation. As forecasted by the SEHI analysis above, Ar 10 displayed an increase in hardness compared to Ar 4 or AC samples. The trend in the nanoindentation data substantiates the SEHI map of CH vibrations and opens up the potential of SEHI as a nondestructive alternative to time consuming nanoindentation measurements. Furthermore, SEHI has the advantage of allowing for crosslinking information to be obtained at a scale smaller than that available with nanoindentation, using CH-bonding maps.

While CH-bonding maps offer a potential substitute for nanomechanical testing, we speculate that OH-bonding maps could substitute for contact angle measurements since cleavage of excess methacrylate units from PGS-M allows the formation of hydroxyl groups, leading to an increased hydrophilicity. SEHI bonding maps allow for spatially detailed information unlike that from a contact angle, which just gives bulk samples data. XPS data (Figure S3, Supporting Information) and SE spectra (Figure 1A) both show the average content of OH– groups increase as a result of Ar treatment. What SEHI offers is a greater spatial understanding of how the micrometer–nanoscale structures emit high traces of OH– groups in the AC samples. SEHI images in Figure S9 in the Supporting Information show that the Ar plasma treated PGS-M displayed a greater signature of OH-groups around nanoscale structures, which are polar and therefore increase hydrophilicity.^[22] Indeed, contact angle results (Figure 3C) showed that argon plasma treatment increased the hydrophilicity, which is consistent with previous studies that demonstrated that plasma has the capacity to change the surface

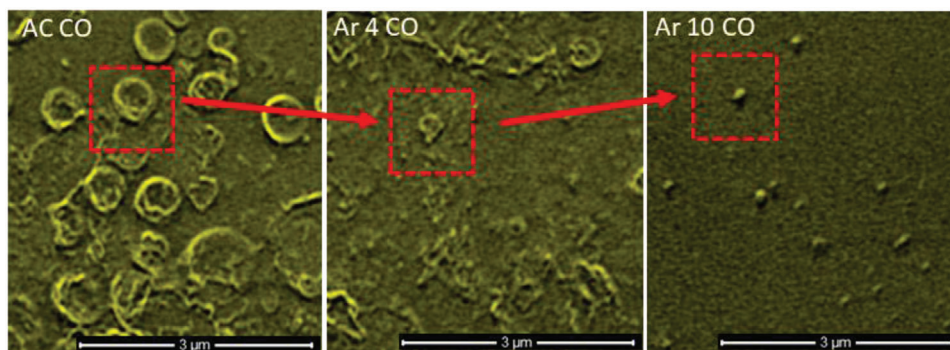


Figure 2. SEHI images generated from the component analysis of AC, Ar 4, and Ar 10 mapping CO bonding. Red insets highlight the reduction of micrometer–nanoscale features high in CO bonding.

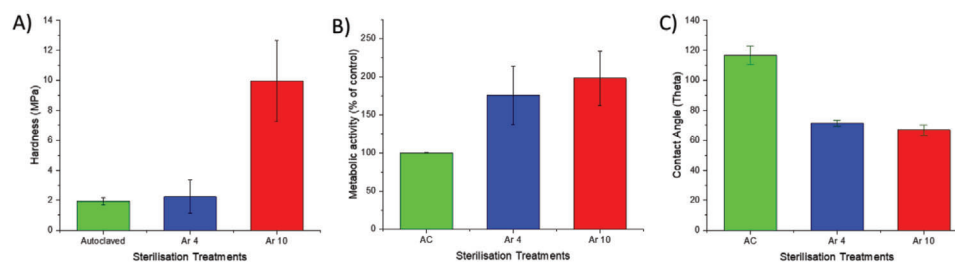


Figure 3. A) The hardness (MPa) obtained from nanoindentation for varying degrees of AC, Ar 4, and Ar 10 treated PGS-M (mean \pm STD error bars). B) The cell metabolic rate increase (Resazurin assay) of cells cultured on argon treated PGS-M with relative increase given compared to that of AC scaffolds C) The contact angle (theta) obtained for varying degrees of AC, Ar 4, and Ar 10 treated PGS-M (mean \pm STD error bars).

chemistry, generating increased hydrophilicity and resulting in enhanced cell adhesion.^[23] However, it is noted that there can be contributions from topography changes, which can effect contact angle measurements as surface alterations are visible. Previous research has also shown that an increase in OH containing functionalities is proportional to improved cellular growth.^[24] Based on this and SEHI results, one expects improved cellular growth even though the sample materials were not directly exposed to the plasma but were enclosed within a gas-permeable bag ensuring that the surfaces remain sterile after plasma treatment until future use.

Here, we assess the sample materials potential to support cellular growth using a cellular metabolic activity assay (Resazurin assay). Figure 3B displays metabolic activity of cells growing on the argon plasma treated PGS-M samples and also the AC PGS-M samples. The results show greater cellular metabolic activity on the argon plasma treated sample surfaces, indicative of an increase in cell adherence and proliferation above that of the AC samples. Although a large disparity in cellular metabolic activity was observed between the argon plasma treated samples, it is considered that this was due to variation in plasma conditions within the actual plasma chamber at different sample positions due to the Ar inlet being located at the rear of the plasma chamber. These disparities emphasize the importance of minimizing variations in the plasma conditions, a more consistent plasma environment may be achievable using more advanced plasma sources.

The observed data confirms that argon plasma treatment shows a positive relationship to cellular growth. However, SEHI

data and nanoindentation also identified that Ar plasma treatment significantly increased the stiffness of PGS-M samples due to crosslinking. SEHI maps of CO bonding suggest that surface structures vary locally and can be changed from ≈ 500 nm size (4 min Ar) to ≈ 50 nm size (10 min Ar) depending on Ar treatment time. Therefore, future work is recommended to optimize the Ar plasma intensity and duration in order to produce a sterilized bio-material while controlling the local variation of mechanical properties to surface patterns that promote cellular growth. Further to this work, a large scale sterilization study is required to determine the efficacy of the model argon plasma treatments with regards to sterilization at various conditions with a view to providing evidence of its capacity to achieve the recommended sterility assurance levels (SALs) to be termed a sterilization method under ISO requirements^[25,26] SEHI offers an efficient way to achieve this due to its ability to map functional groups with the required image resolution together with an ability to map at multilength scales. This ability is vital to attaining a comprehensive understanding of cell behavior on Ar plasma treated surfaces. This future work, in combination with the use of gas semipermeable bags as demonstrated in this study, would pave the way for the wider deployment of argon plasma as a terminal biomaterial sterilization process.

Supporting Information

Supporting Information is available from the Wiley Online Library or from the author.

Acknowledgements

The authors thank EPSRC for funding under SEE MORE: Secondary Electron Emission-Microscopy for Organics with Reliable Engineering Properties (EP/N008065/1), and studentship for N.F. (EP/R513313/1). J.T. would like to thank the Royal Thai Government for their studentship. Electron microscopy and analysis was performed in the Sorby Centre for Electron Microscopy at the University of Sheffield. J.S. thanks the Leibniz Association under Grant SAW-2017-IPHT-1. All data are accessible through "10.15131/shef.data.13217636".

Conflict of Interest

The authors declare no conflict of interest.

Keywords

argon plasma treatment, polymer characterization, polymeric biomaterials, secondary electron emission, secondary electron hyperspectral imaging

Received: October 2, 2020
Revised: November 10, 2020
Published online:

-
- [1] I. Chiulan, A. N. Frone, C. Brandabur, D. M. Panaitescu, *Bioengineering* **2017**, *24*, 5.
- [2] M. Ahmed, G. Punshon, A. Darbyshire, A. M. Seifalian, *J. Biomed. Mater. Res., Part B* **2013**, *101*, 1182.
- [3] K. Schröder, A. Meyer-Plath, D. Keller, A. Oehl, *Plasmas Polym.* **2002**, *7*, 103.
- [4] M. Griffin, N. Naderi, D. M. Kalaskar, E. Malins, R. Becer, C. A. Thornton, I. S. Whitaker, A. Mosahebi, P. E. M. Butler, A. M. Seifalian, *Int. J. Biomater.* **2018**, *2018*, 6565783.
- [5] X. Lu, G. V. Naidis, M. Laroussi, S. Reuter, D. B. Graves, K. Ostrikov, *Phys. Rep.* **2016**, *630*, 1.
- [6] P. Bourke, D. Ziuzina, L. Han, P. J. Cullen, B. F. Gilmore, *J. Appl. Microbiol.* **2017**, *123*, 308.
- [7] N. A. Stehling, R. Masters, Y. Zhou, R. O'Connell, C. Holland, H. Zhang, C. Rodenburg, *MRS Commun.* **2018**, *8*, 226.
- [8] R. C. Masters, N. Stehling, K. Abrams, V. Kumar, A. Schäfer, D. Lidzey, C. Rodenburg, *Adv. Sci.* **2019**, *6*, 1801752.
- [9] N. Farr, S. Pashneh-Tala, N. Stehling, F. Claeysens, N. Green, C. Rodenburg, *Macromol. Rapid Commun.* **2019**, *41*, 3.
- [10] K. J. Abrams, M. Dapor, N. Stehling, M. Azzolini, S. J. Kyle, J. S. Schäfer, A. Quade, F. Mika, S. Kratky, Z. Pokorna, I. Konvalina, D. Mehta, K. Black, C. Rodenburg, *Adv. Sci.* **2019**, *6*, 1900719.
- [11] J. N. Barbosa, P. Madureira, M. A. Barbosa, A. P. Aguas, *Biomaterials* **2005**, *26*, 3021.
- [12] S. N. Rodrigues, I. C. Gonçalves, M. C. Martins, M. A. Barbosa, B. D. Ratner, *Biomaterials* **2006**, *27*, 5357.
- [13] Y. Arima, H. Iwata, *Biomaterials* **2007**, *28*, 3074.
- [14] J. N. Lee, X. Jiang, D. Ryan, G. M. Whitesides, *Langmuir* **2004**, *20*, 11684.
- [15] Y. Wang, G. A. Ameer, B. J. Sheppard, R. Langer, *Nat. Biotechnol.* **2002**, *20*, 602.
- [16] S. Pashneh-Tala, R. Owen, H. Bahmaee, S. Rekštyte, M. Malinauskas, F. Claeysens, *Front. Phys.* **2018**, *6*, 41.
- [17] M. Kharaziha, M. Nikkhah, S. R. Shin, N. Annabi, N. Masoumi, A. K. Gaharwar, G. Camci-Unal, A. Khademhosseini, *Biomaterials* **2013**, *34*, 6355.
- [18] K.-W. Lee, D. B. Stolz, Y. Wang, *Proc. Natl. Acad. Sci. USA* **2011**, *108*, 2705.
- [19] C. Liu, N.-Y. Cui, S. Osbeck, H. Liang, *Appl. Surf. Sci.* **2012**, *259*, 840.
- [20] F. Ayhan, H. Ayhan, E. Piskin, *J. Bioact. Compat. Polym.* **1998**, *13*, 65.
- [21] S. Makoto, I. Taku, K. Masaru, N. Nobuyuki, T. Yasuhiko, Y. Hiroshi, *J. Micro/Nanolithogr.* **2013**, *12*, 41309.
- [22] B. G. Keselowsky, D. M. Collard, A. J. García, *Biomaterials* **2004**, *25*, 5947.
- [23] Y. Tamada, Y. Ikada, *Polymer* **1993**, *34*, 2208.
- [24] S. I. Ertel, B. D. Ratner, T. A. Horbett, *J. Biomed. Mater. Res.* **1990**, *24*, 1637.
- [25] ANSI/AAMI ST67:2003, Sterilization of health care products - Requirements for products labeled "STERILE".
- [26] ANSI/AAMI/ISO 11137:2006, Sterilization of health care products".



Supporting Information

for *Adv. Sci.*, DOI: 10.1002/advs.202003762

Understanding surface modifications

induced via Argon Plasma treatment

through Secondary Electron Hyperspectral Imaging

Nicholas Farr, Jeerawan Thanarak, Jan Schäfer, Antje Quade, Frederik Claeysens, Nicola Green, and Cornelia Rodenburg*

Supplementary Information

Understanding surface modifications induced via Argon Plasma treatment through Secondary Electron Hyperspectral Imaging

Nicholas T.H Farr, *^{1,3} Jeerawan Thanarak, ^{1,3} Jan S. Schäfer, ² Antje Quade, ² Frederik Claeysens, ¹ Nicola H. Green, ^{1,3} and Cornelia Rodenburg¹

1 Department of Materials Science and Engineering, Sir Robert Hadfield Building, Mappin Street, University of Sheffield, UK.

2. Leibniz Institute for Plasma Science and Technology. (INP Greifswald e.V.) Felix-Hausdorff-Str. 2, 17489 Greifswald, Germany.

3. Insigneo Institute for *in silico* Medicine, The Pam Liversidge Building, Sir Robert Hadfield Building, Mappin Street, Sheffield, UK

Materials and Methods

For the following methods, all chemical reagents were obtained from Sigma Aldrich, UK, unless otherwise stated.

Synthesis of polyglycerol (sebacate)-methacrylate (PGS-M)

The low molecular weight PGS-M polymer was fabricated following the protocol from Pashneh-Tala et al [1]. In brief, the PGS prepolymer was synthesised by mixing 1:1 (mol/mol) glycerol and sebacic acid, using a hot plate at 120°C, 300 rpm for 48 hours. Nitrogen gas was applied in the first 24 hours, then a vacuum was applied to the system for another 24 hours to remove the water from condensation. To methacrylate the PGS prepolymer, 1:4 (w/v) dichloromethane (DCM) was used to dissolve the prepolymer. Subsequently, the system was changed to 0°C in dark condition at 300 rpm. 1:1 (mol/mol of PGS hydroxyl groups) of Triethylamine (TEA) and 1 mg/g PGS hydroxyl group of 4-Methoxyphenol (MeHQ) were added into the system. Methacrylate anhydride (MAA) was used to control the percentage of methacrylation, in this case, 0.5 mol of MAA was added per mol PGS hydroxyl groups. After 24 hours of methacrylation, 30mM hydrochloric acid was used to wash the PGS-M polymer. The water from reaction was then removed by using CaCl₂. Lastly, DCM was removed by rotary evaporation.

To synthesis PGS-M scaffolds, residual DCM was taken out from PGS-M polymer using vacuum. 70% PGS-M in DCM was blended with 1:1 (w/w) toluene, 10% Hypermer™ B246 and 25% diphenyl(2,4,6-trimethylbenzoyl) phosphine oxide/ 2-hydroxy 2-methylpropiophenone and blended (photoinitiator) at 350 rpm. After 5 minutes of blending, 4 ml dH₂O was added dropwise to the emulsion. The emulsion was then photocured for 5 minutes each side and washed with methanol for 4 days and dH₂O for 4 days.

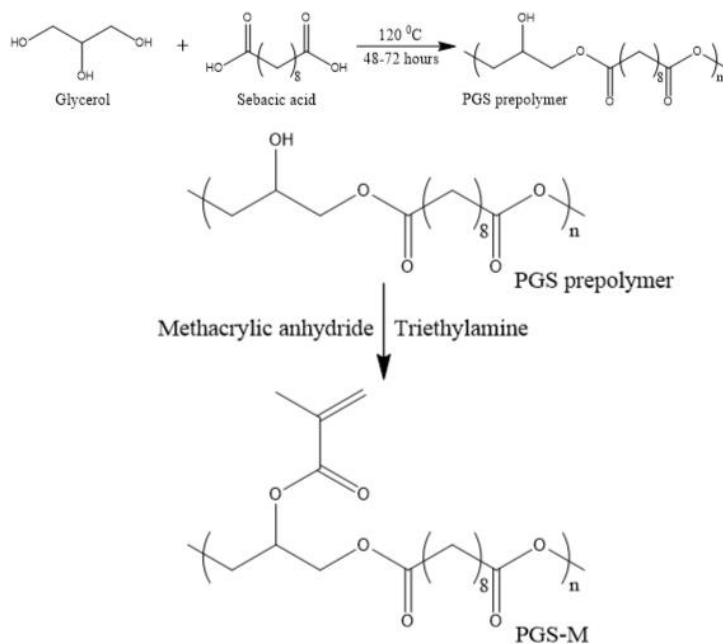


Figure S1 - PGS-M chemical synthesis from monomers, to PGS pre-polymer and finally produced of PGS-M.

Low Temperature Plasma Sterilisation Treatment

PGS-M samples were prepared by exposing them to low-pressure argon glow discharge in a Diener Electronic Zepto plasma cleaner at 40 kHz, 100 W, and 0.3 mbar air for 4 minutes and 10 minutes in Tyrex gas semi-permeable packaging. 10 minutes of exposure was chosen as a maximum limit to exclude any effects of sample heating which have been shown to lead to additional surface modifications [2].

Autoclave sterilisation

To sterilise PGS-M samples by steam sterilisation an autoclave method was performed. This required the samples to be immersed in dH₂O within a hot-steam environment at approximately 121°C for 20 minutes. The autoclaved PGS-M samples were then stored in the sterile dH₂O.

PGS-M Characterisation

1. SEM and Image Data Processing

Imaging

Observation of the surface morphology of the PGS-M samples was performed using a Scanning Electron Microscope (FEI Nova Nano 450 SEM). The PGS-M samples were not subject to deposition of conductive coating, in contrast to usual polymers SEM analysis practice. To avoid surface charging and consequent damage to the sample a low accelerating voltage (1 KV) with typical vacuum pressure of 10^{-5} mbar at a working distance of 3mm was applied. An Everhart-Thornley Detector (ETD) for low magnification images and a Through Lens Detector (TLD) for high magnification images were used for the collection of SE images.

SEHI Acquisition and Image Processing

The FEI Nova Nano 450 SEM is provided with a through lens detector which includes a voltage controlled deflector electrode. The deflector electrode channels the signal into the SE detector. The deflector electrode is set to a predetermined number of deflector voltages and an image is generated for each deflector voltage. Spectra and hyperspectral images are acquired through post-processing of such image series. A short dwell time of 100 ns and the inclusion of 16 frame integrations is applied to reduce beam exposure and sample damage. Stage bias has been performed to allow energy calibration of this process through experiments [3, 4]. Fiji software was utilised to perform image processing [5]. Histogram and spectral off-set normalisation [6] has been applied retrospectively to optimise all images for brightness and contrast, and to limit the effects of differing sample work functions. Once S curves have then been obtained they are differentiated to produce the SE curves which are reported in the main manuscript. Component analysis was then performed to image stacks utilising non negative matrix factorization (nnmf) to isolate components of interest.

Raman Spectroscopy

Raman spectroscopy (Renishaw inVia micro-Raman) was employed to analyse the chemical structure of the PGS-M placed on borosilicate glass. Using a 50x objective the laser power was 20 mW with a 1 μm spot size. A Peltier-cooled multichannel CCD detector was used for data recording with a 2,400 lines/mm diffraction grating at a slit opening of 65 μm and a spectral resolution of in the order of 1 cm^{-1} .

Nanoindentation

Nanoindentation measurement was performed on wax embedded PGS-M disks. The PGS-M was embedded at 42°C and sectioned smooth. A Bruker's Hysitron TI Premier nanoindenter, attached to a Berkovich tip was used for nanoindentation of PGS-M. A matrix of 12 indentations was applied, spaced 60 μm apart. The polymer sample was loaded for 5 s, held for

80 s, and unloaded for 3 s. The hold period was added to allow any effects from creep in the polymer to be minimised. A peak force of 200 μN was applied with a lift height of 20 nm. The Oliver Pharr method was utilised to analyse each of the unloading segments of the polymer indentation. This provided a reduced modulus (E_r) value as well as sample hardness (H).

Water contact angle

Before measuring water contact angle, PGS-M samples were air dried inside a class II biological cabinet. The wettability of a surface of the samples was measured by dropping 5 μl of water onto the dried surface. A blunt cannule was pointed vertically to the model and placed above the surface of the samples for approximately 1-2 mm before injecting the water droplet. The needle and the water droplet were monitored by the build-in camera. The horizontal line was specified at the upper surface of the sample. Once the water droplet was injected, the angle data and the image of the droplet were obtained within 30 seconds.

Cell Culture

Human dermal fibroblasts were isolated from donor skin obtained with informed consent and ethical approval (15/YH/0177). Fibroblasts were cultured in Dulbecco's Modified Eagle Medium (DMEM) with 10% (v/v) Fetal Calf Serum (FCS), 2×10^{-3} M glutamine, 10% (v/v) Penicillin-Streptomycin and 0.625 $\mu\text{g}/\text{ml}$ amphotericin B. 1×10^5 . Cells were then seeded in a 12 well-plate and allowed to attach on the samples overnight before moving to a fresh 12 well-plate. The cells were then grown for one week at 37°C, 5% CO_2 in an incubator. A control was also prepared by seeding the cells onto tissue culture plastic surface. After one week of experiment, the samples were stained with resazurin assay to quantify the cell metabolic rate.

Metabolic activity assay

The reduction of resazurin to its fluorescent product resorufin was used to measure the metabolic activity of the cells on the scaffolds. Resazurin sodium salt solution (10 mg ml^{-1} in PBS) was diluted 1:50 ratio in fresh culture media. The cell seeded samples were then immersed in 2 ml of this solution for 4 hours in an incubator. The plate was placed on a rocker throughout the incubation time. Aliquots of the solution were then removed and fluorescent absorbance was measured using the Biotek FLx 800 fluorescence plate reader (λ_{ex} 530 nm, λ_{em} 590 nm).

Statistical Analysis

SE spectra for all materials were processed through an in-house MATLAB script to organise and process the spectrum image stack in to the spectra given in Figure 1 and SI 2. Each materials SE spectra was formed by calculating a mean and

standard deviation of $n=4$ independent SE spectra measurements. An in-house Non-Negative Matrix Factorization (NNMF) method was applied to determine the spectrum distribution of the SE components within each material. NNMF retains the spatial information of extracted components that corresponds to the structural differences in the components. NNMF achieves this by allowing only positive correlated combinations which enables an intuitive representation of the data. NNMF spectra output is then presented graphically with no further statistical analysis.

Hardness measurements presented are set from the raw MPa hardness values provided by the Bruker's Hysitron TI Premier nanoindenter. To present these results in a graph, as shown in Figure 3, a mean and standard deviation was calculated from the $n=12$ raw indent measurements (captured for each material). For the cell metabolic assay, fluorescent absorbance was measured using the Biotek FLx 800 fluorescence plate reader. A mean and standard deviation of these values was then calculated and presented in figure 3. Contact angle (Theta) raw values was obtained and captured by the built-in camera. From the raw values captured a mean and standard division was calculated and presented in figure 3 for the three materials ($n=3$).

Additional Results

Analysis of Reference Samples

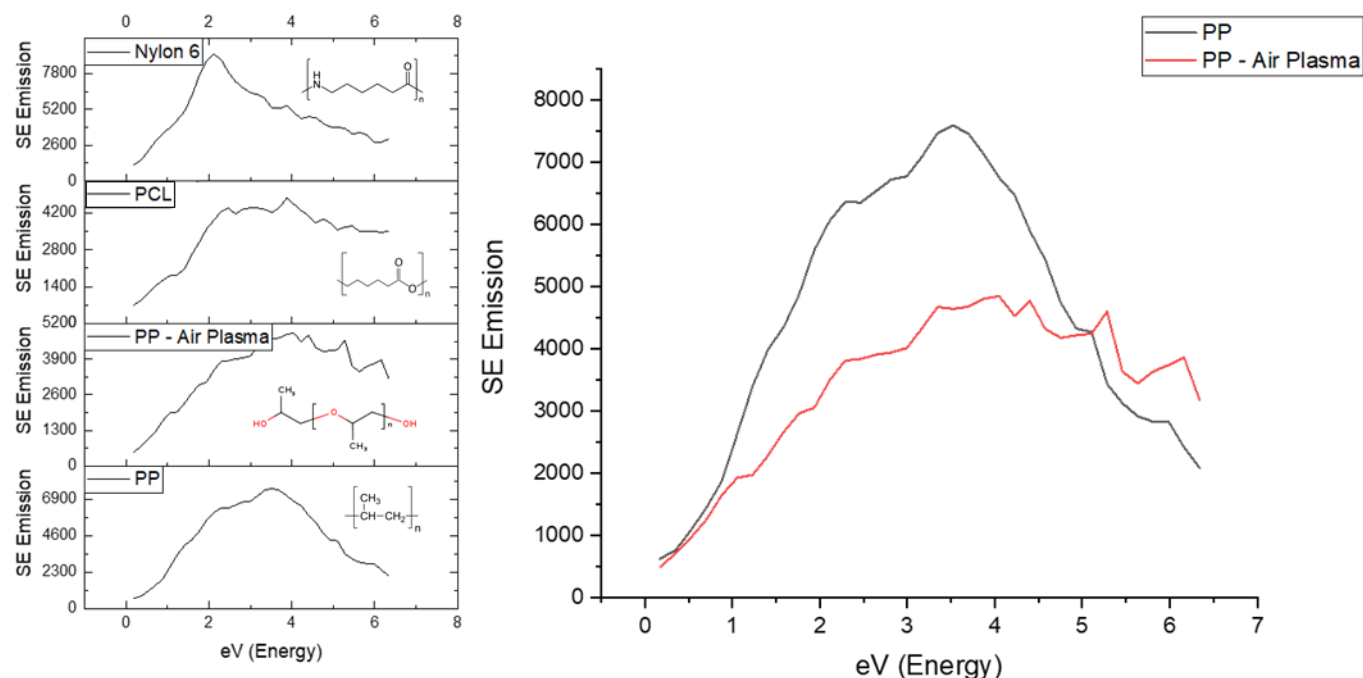


Figure S2 - Secondary electron spectra for Nylon 6, Polycaprolactone, Polypropylene and Air Plasma treated Polypropylene.

Figure S2 displays the SE spectrums of Polypropylene (PP), Air Plasma treated PP, Nylon 6 and Polycaprolactone (PCL). Previous studies have isolated the energy range of 1.4 – 2.3 eV to the molecular order of the materials [7], for polymers, isolating the molecular weight of the material, thought to be associated with C-C backbone bonding [8]. For all reference materials (PP, PCL and Nylon 6) a peak is observable within the 1.4 – 2.3 eV range. Preceding studies have also characterised multiple peaks in this energy range of 2.9 - 4.3 eV as emissions attributed to CH vibrations [9]. In this instance two peaks occur within the data set. Firstly, a peak around 2.3 eV which is visible in all reference sample spectra, and secondly a peak around 3.2 eV which is expressed in all but Nylon 6. It is therefore considered that due to the chemical structure of these materials the 2.3 eV peak is related to CH₂ bonding whereas the 3.2 eV peak is related to CH₃ bonding. This hypothesis explains why the 3.2 eV peak is absent in Nylon as this material does not possess the CH₃ functional group.

Previously captured SE spectra of HOPG have shown that emission peaks around 4.5 – 5 eV are observed within aged HOPG [9]. It is now proposed that this is at least partially a consequence of oxidation on the material surface resulting in –OH hydroxyl groups forming. This process of oxidation to change the surface structure of a PP material was used in this study. The PP was air plasma treated to allow hydroxyl groups to form on the surface of the sample. During the air plasma

oxidation process polar groups such as carboxylic acids, ketones and ester groups will also develop at the polymer surface [10]. Figure S2 displays the SE spectra of air plasma treated PP and non-treated PP. It is notable that the molecular weight peak of air plasma treated PP is greatly reduced. This is attributed to surface melting occurring due to the slight surface heating associated with the action of the chemical etching breaking crosslinks, this may possibly also explain the reduction in CH vibrations observed. The air plasma treatment of PP is shown to have caused an increase in SE emissions within two peaks around 5 eV and 6 eV when compared to non-treated PP. The previously described 5 eV peaks in aged HOPG leads to an assumption that observations in this energy range are associated with an increase in OH groups on the surface of PP post aging oxidation. An additional peak of interest occurs around 6 eV, this peak is proposed to be the result of CO bonding ensuing from carboxylic acid groups that were formed post treatment.

To provide supporting evidence for this proposal, Nylon 6 and PCL-M were used as reference materials. Nylon 6 contains an amide CO, but does not possess a hydroxyl group. This is confirmed in its observed SE spectrum and further contributes to the proposal by showing emission peaks around 5 – 6 eV. However, there are minimal emission peaks present around 4.5 - 5 eV. PCL-M has emission peaks present at both 4.3-5 eV that are associated with OH and also at 5 – 6 eV which are considered to be associated with C=O (see figure 1D). This result is expected as PCL-M contains both of these functional groups.

X-ray photoelectron spectrometer (XPS) measurements of the samples were taken and applied to corroborate the SE spectra results. XPS is an effective technique for the identification of chemical composition and oxidation state. Subtle changes in peak positions and shape can yield information on changes in surface chemistry. Figure S3 shows all samples contained carbon, oxygen and nitrogen elements. The results indicated that all the samples surfaces showed evidence of impurities such as: (N), Si, Na, Ca, Cl and S. The samples also followed the same trends identified by SEHI in relation to O composition within their structures. Post plasma treatment the PP-surface showed a higher concentration of O in comparison to the original PP non-treated surface. The PP O/C ratio on treated sample surfaces was observed to increase after application of plasma treatment in air, a result that further points to plasma treatment establishing oxygen rich functional groups.

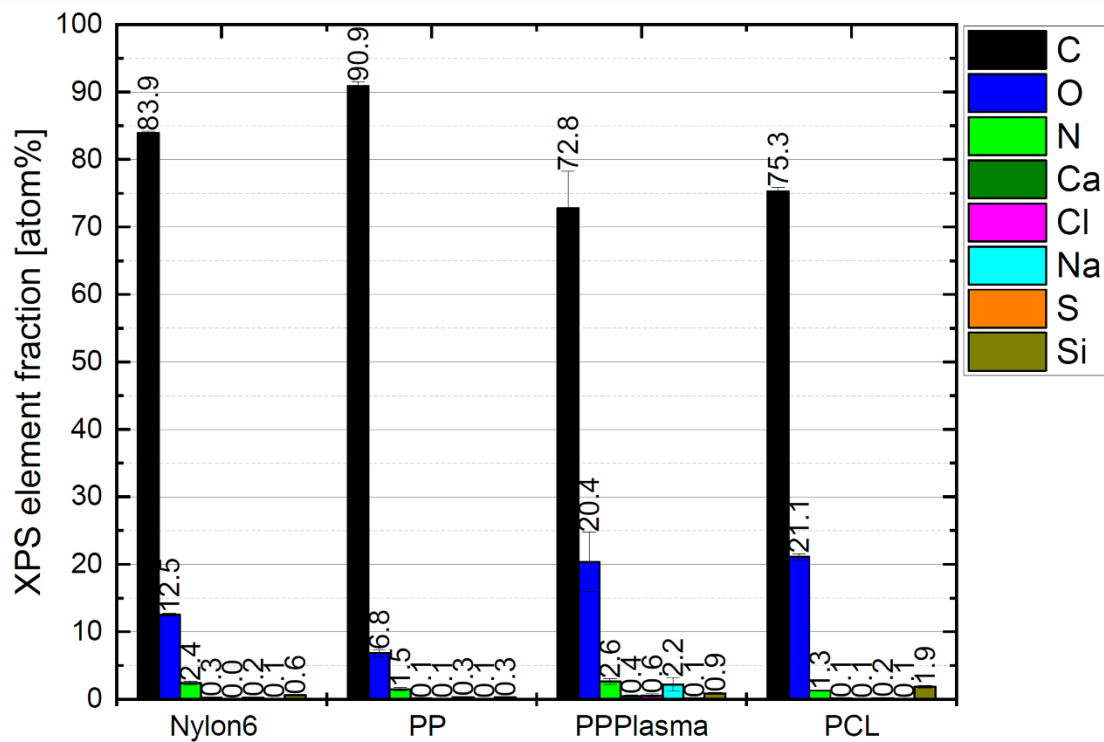


Figure S 3 - X ray photoelectron spectrometer (XPS) measurements of Nylon 6, PCL-M , Polypropylene and Air Plasma treated Polypropylene.

Survey scans of the non-treated and plasma treated polypropylene are shown in Figure S4. This figure displays that contaminants, such as: Na, N, Cl and Si were detectable, particularly after plasma treatment. Small peaks are noticeable within the accompanying SE spectra but further analysis is required before these can be reliably detected and characterised. The source of this contamination is expected to be the consequence of the multi sample use of the plasma chamber. Thus for sterilisation applications a dedicated plasma treatment chamber should be used.

Figure S5 depicts that plasma treated PP exhibiting a shape change of its XPS peak compared to that of untreated PP. The observable shoulders on the high bonding energy side of treated PP suggests that more O containing (and COOH/COOR @ 289.2 eV) functional groups were introduced by the plasma treatment of PP.

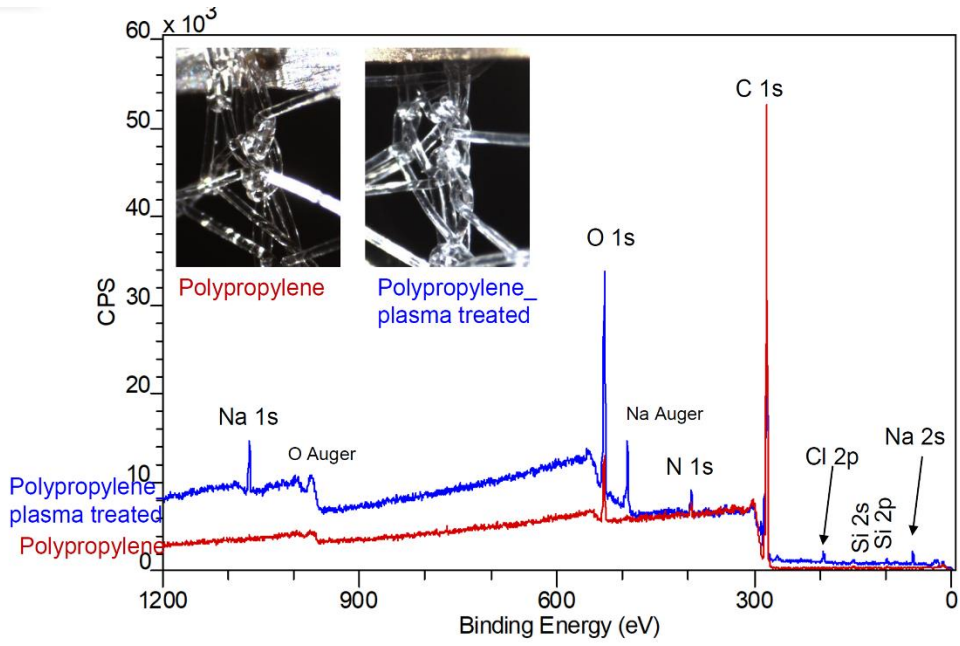


Figure S 4 - X ray photoelectron spectrometer (XPS) Survey scans of the non-treated and plasma treated polypropylene

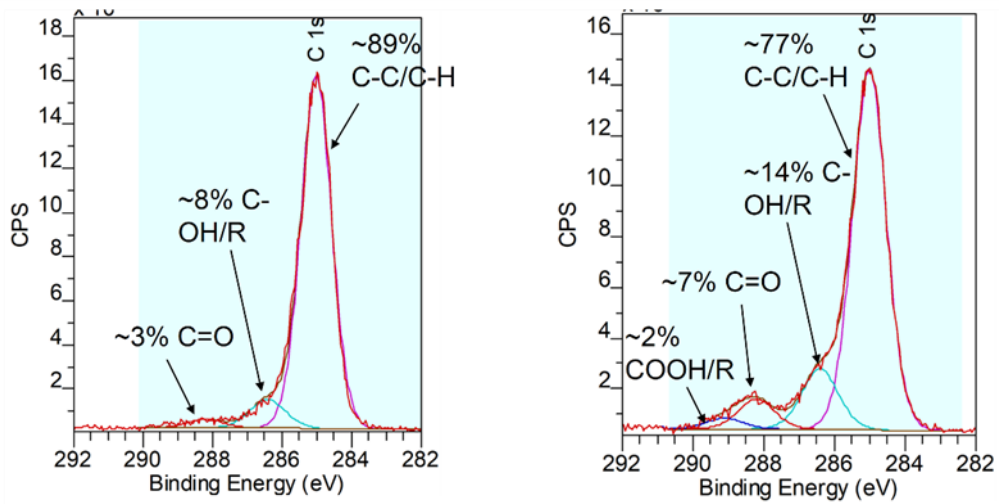


Figure S 5 - X ray photoelectron spectrometer (XPS) peak fits of the non-treated and plasma treated polypropylene

Further analysis of Argon Treated PGS-M

To support the premise that Argon plasma cleaves methacrylate from the surface of treated PGS-M, Raman spectra were captured from the samples (S6). Figure S6a shows the Raman fingerprint region in the range of 500 – 2000 cm^{-1} . A notable difference between Argon plasma treated and AC samples is observed within a peak at 1045 cm^{-1} , which is associated with C-O-C bonding in PLA [11]. SE analysis correlates with the observed CH vibrations (2750 – 3200 cm^{-1}) peak present in the Raman spectra as predicted by these results. The changes in Raman intensity at 2950 cm^{-1} (CH vibrations) closely correlates with the SE intensity changes within the 2.9 – 4.3 eV range. Both peaks are similarly affected by CH bonding and consequently the cross-linking process of PGS-M. The consistency of both SE and Raman spectra provides a robust argument that both techniques can detect cross-linking in PGS-M through CH bonding changes. However, SE displays the additional benefits of a multiscale imaging capability and thus the ability to capture spatial variations.

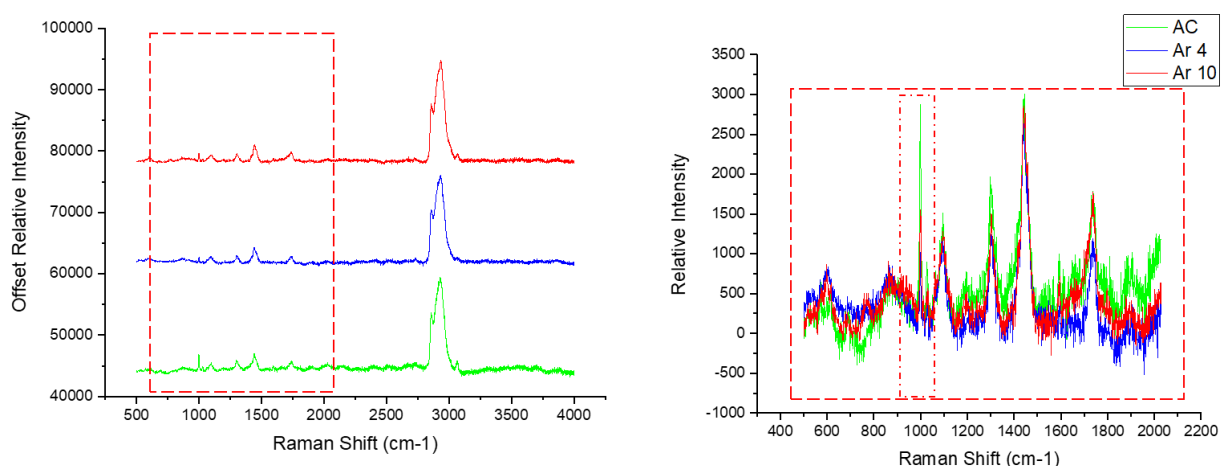
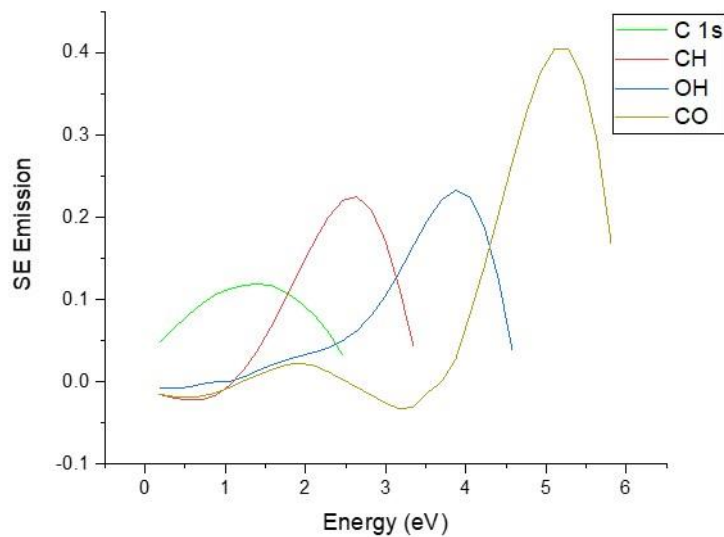


Figure S 6 - A) Off set full Raman spectrums for AC, AR 4 and Ar 10 treated PGS-M. B) Raman fingerprint region spectrums for AC, AR 4 and Ar 10 treated PGS-M.

From the combined results of Raman and SE analysis there is a strong argument that unreacted methacrylate has been removed by Argon plasma treatment. A slight reduction of C=O was identified by Raman (700 cm^{-1}). However, as the escape depth of Raman is greater it is likely Raman is giving reference to the aggregate sample whereas SEHI is closely focused at the surface of PGS-M with an escape depth of 10 nm.

In order to obtain images from the corresponding spectral components a non-negative matrix factorisation (nnmf) was used to isolate various components between 0 – 6 eV. Figure 1B displays images generated these components from the Ar 10 and AC surfaces that can be matched to the peak allocation described above. Of specific interest, one component

consisted of a peak ~ 3 eV highlighted that was previously identified as CH vibrations. Additionally, a component at 4.5 eV associated with OH is observable, together with a peak evident around 5.6 eV related to C=O bonding. Here SEHI demonstrates that it is possible to map functional groups on the surface of PGS-M using the components generated from nnmf.



Figures S 7 - Non negative matrix factorisation (nnmf) multivariate analysis of AC, Ar 4 and Ar 10 treated PGS-M. Isolating four components.

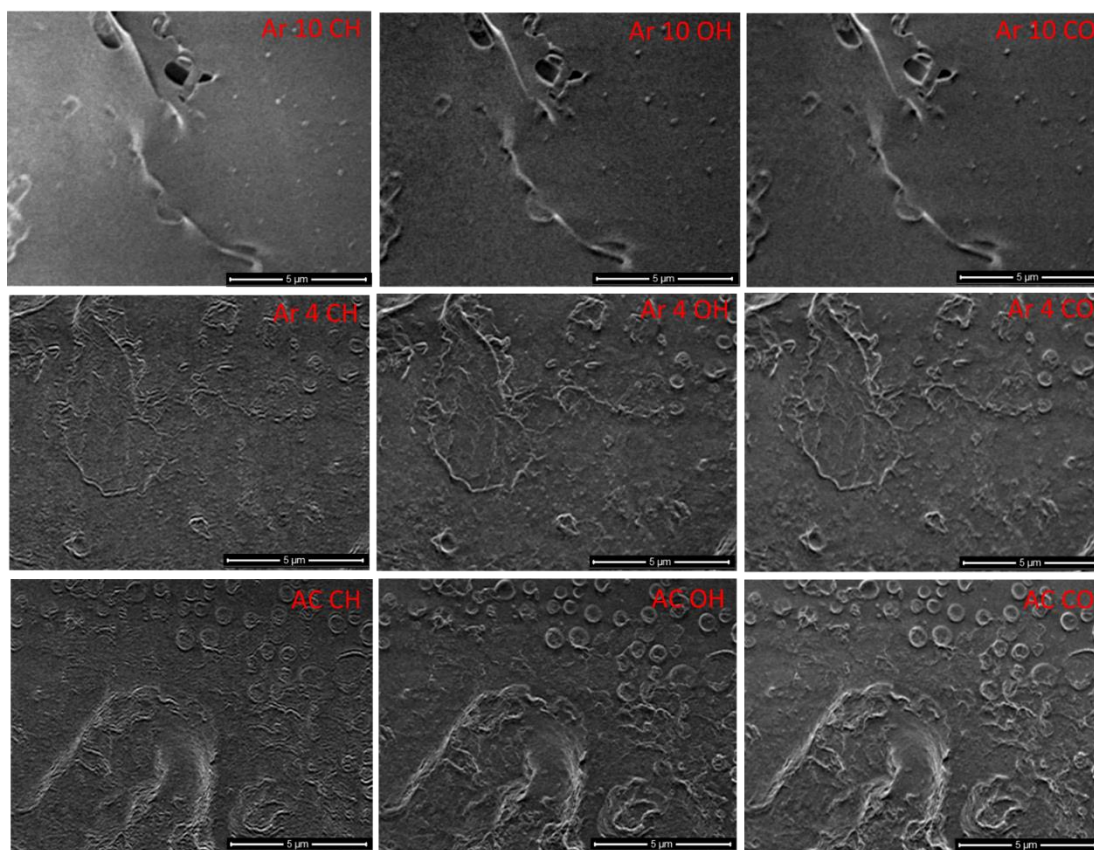


Figure S 8 - Resulting SEI images of AC, Ar 4 and Ar 10 treated PGS-M. Isolating functional group components from non negative matrix factorisation (nnmf) component analysis.

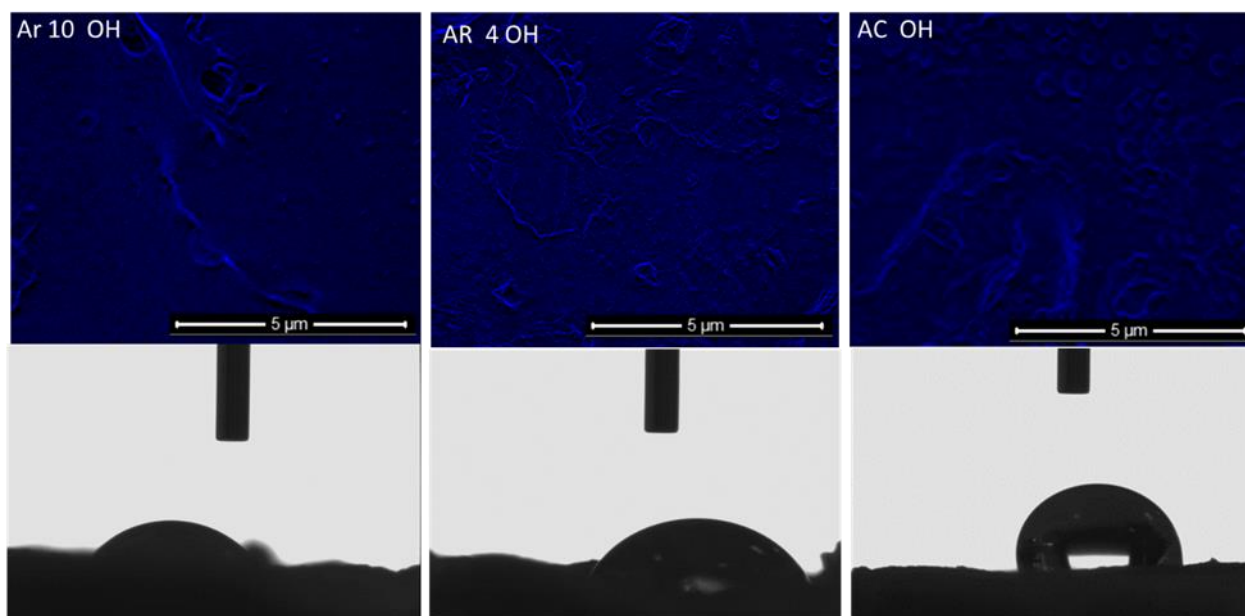


Figure S 9 - Resulting SEI images of AC, Ar 4 and Ar 10 treated PGS-M. Isolating one component (OH) from non-negative matrix factorisation (nnmf) component analysis.

Analysis of Autoclaved PGS-M vs Non Sterile (Non treated) PGS-M

This publication focuses on PGS-M as a biomaterial source, therefore, there are no circumstances that can be conceived where it could possibly be implanted without first being subject to sterilisation. However, SE emission data was collected on non-treated non-sterile PGS-M as a comparison study with autoclaved PGS-M and is presented in Figure S10. Previous group publications (1) have discussed the development of PGS-M and the practicalities of the inclusion of methacrylate to render the polymer photo-curable. Producing this photocurable form of PGS gives the material a host of production benefits including the speed and simplicity of the single step photocuring process and the potential ability to attach bioactive molecules on the remnant acrylate groups without the fear of denaturing as a result of heat polymerisation, However, as a non-heat sterilisation method was yet to be evaluated this previous work included autoclaving as a terminal sterilant.

As it is known PGS/PGS-M can be cross-linked with high temperatures (120°C for 48 hours) (12). The process of autoclaving is performed with the material being hydrated. The consequence of hydrating PGS-M was that the polymer would not crosslink in response to heat, as high pressures in heat polymerisation are required to remove water from the material. If the polymer is still hydrated this process cannot be completed. Therefore, the only crosslinking within the material would be in response to the UV photocuring step. Subsequent to the established process step of including dH₂O to stop the mechanism of autoclaving causing cross-linking, SE spectra was collected before and after autoclaving. It was established that this process resulted in autoclaving inducing no extra crosslinking. Instead a slight decrease of CH vibrations (2.9 – 4.3 eV) previously linked to crosslinking density of the material (8) was observed. This was also coupled with a very slight overall emission decrease in molecular order (1.4 – 2.3 eV) of the polymer.

This decrease in cross-linking and molecular order associated emission was expected in response to hydrolysis degradation, both through the hydrolysis of anhydride, stopping further cross-linking, and the hydrolysis of the PGS-M backbone ethers (Figure S11). It is the design intent of PGS/PGS-M to degrade by ether hydrolysis within the body over time. This is common with thermally cured PGS which showed degradation in PBS, reducing in mass by 10% in 31 days (13). However, this process was advanced when high autoclave temperatures were used. Hydrolysing cross-linked PGS-M reduces CH vibrations as well as produce amorphous regions within the polymer surface. SE emission associated with OH/CO is increased as the formation of OH/CO containing functional side chains are formed through the ether hydrolysis reaction (Figure S11).

Figure 2 in the main manuscript displays how functional group distribution influences local plasma etching behaviour thus leading to topography and surface chemistry changes. As mentioned in the manuscript this isn't a novel finding for organic compounds as it is known plasma treatment of Polytetrafluoroethylene (PTFE) strips the fluorine molecules from the

carbon backbone of the polymer. Topographically, plasma treatment changes the surface morphology of PTFE with different morphologies resulting from different plasma gases used (14). The inset in S10 is a further indication of this process for PGS-M as it is clear non-treated PGS-M samples show micron-scale structures which appear to diminish after Ar plasma treatment (Figure 2). This is an expected effect of OH/CO containing sidechains from PGS-M being stripped away by Ar plasma changing the surface morphology and chemistry.

To allow a comparison to be drawn using SEHI images analysis, nnmf component analysis was performed on both AC PGS-M and non-treated PGS-M. The SE spectra components of both materials given from nnmf are shown in figure S12. Here we see components highlighted with peaks around 3.5 eV, 4.5 eV, and 5.5 eV. These peak positions fit into the ranges previously highlighted as CH, OH and CO functional groups emissions. Figure S13 allows the comparison of SEHI images produced from nnmf. SEHI images show that CH emission (given in red) has a slightly greater overall intensity within AC PGS-M than Non treated PGS-M. Whereas for CO and OH emissions, non-treated PGS-M has a greater emission than that of AC PGS-M.. These SEHI images corroborate the SE spectrums shown in S10. Figure S13 also includes an overlay of OH and CH SEHI maps for AC PGS-M. This overlay shows emission intensities from OH and CH differing across the materials surface. Future work should look to introduce colour mapping for SEHI images to allow multiple overlays without losing the high image resolution

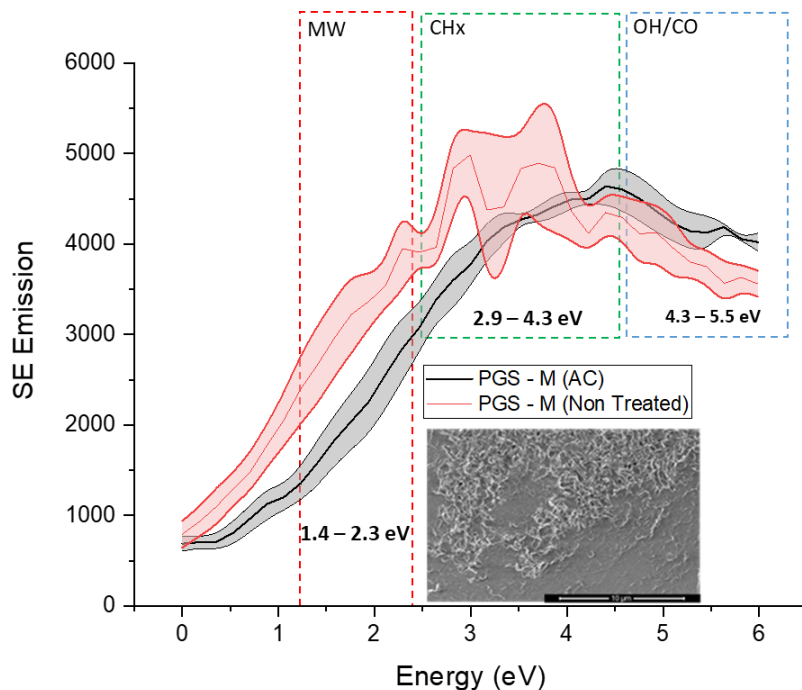


Figure S10 - Secondary electron spectra for PGS – M (non-sterile) and PGS-M after autoclave (AC) sterilisation. Inset shows an SEM image (HFW 15 μ m) of non-sterile PGS-M.

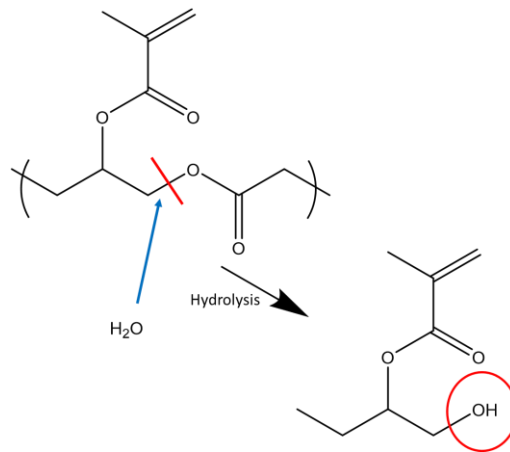


Figure S11 – Hydrolysis reaction of PGS-M.

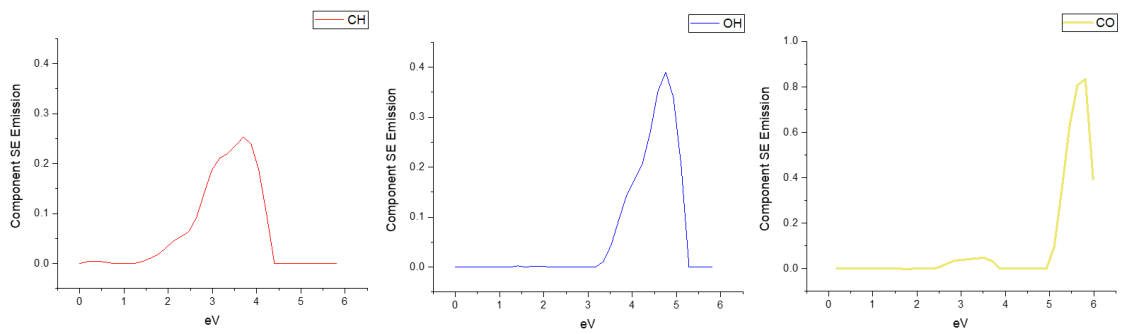


Figure S12 - Non negative matrix factorisation (nmf) multivariate analysis of non-treated and AC PGS-M. Isolating three components.

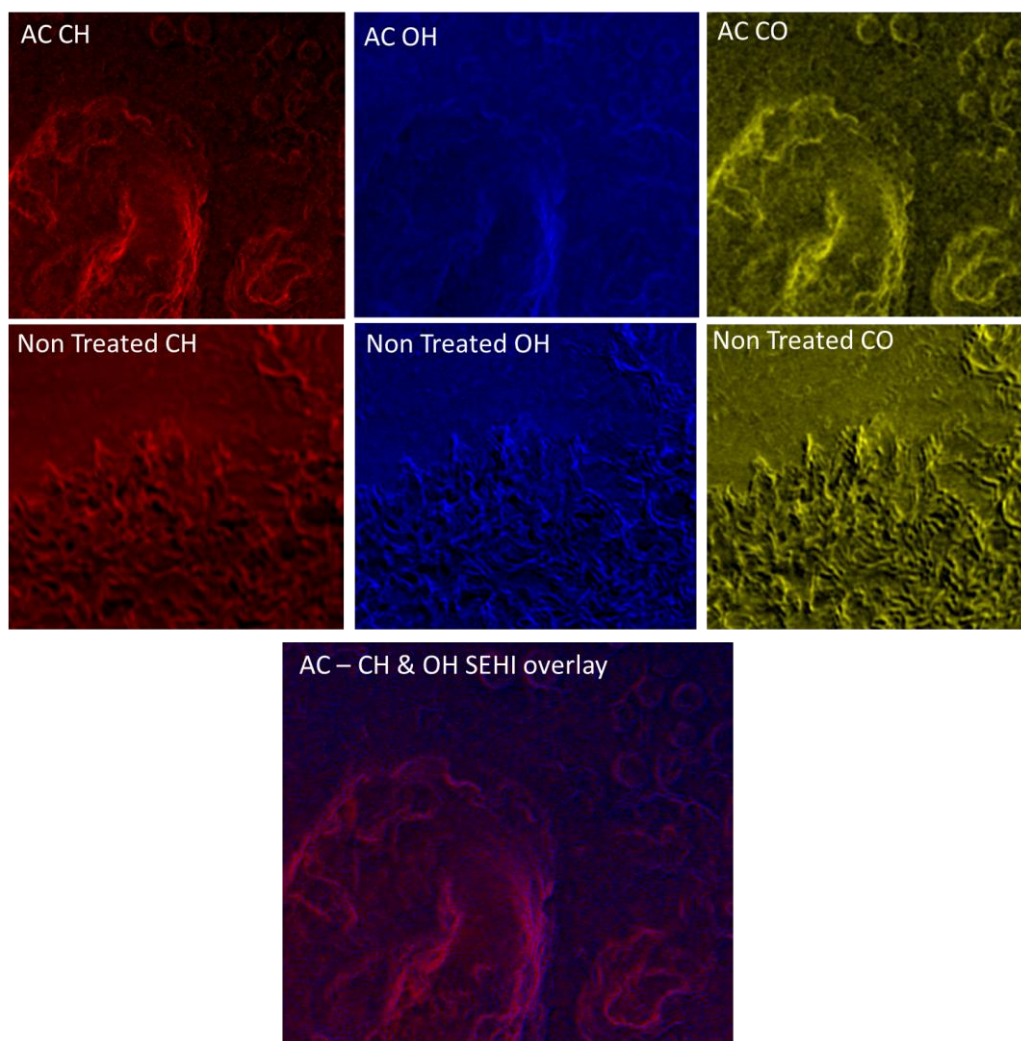


Figure S13 - Resulting SEHI images of non-treated and AC PGS-M. Isolating three components from non negative matrix factorisation (nmmf) component analysis. SEM images showing topography emission (>6 eV) are also included. HFW for all images shown is 4 μ m. SEHI emission intensities for AC images differ slightly to that in the main manuscript. This is as a result of nmmf analysing just the two conditions (non treated and AC) than that of all treatment groups.

Using Secondary Electron Spectroscopy to assess structural changes through topographical changes

Figure 1B shows SEHI images of PGS-M after Ar 10, Ar 4 and AC treatments. These images indicate that AC PGS-M surface has an irregular topography compared to that of Ar 10 and Ar 4. In the main text of this publication we focus on emissions below 6 eV which are appropriate to functional group emissions and not surface morphology related SE emissions (9)(16) . However, it is known that analysing higher level SE energy emission can provide information regarding the topography of the material (15). Figure S14 corroborates SEHI images in Figure 1B by indicating a stronger SE emission in higher energies regimes of AC PGS-M compared to that of Argon plasma treatment samples. Future work to better understand this emission range would be beneficial but it is apparent that surface roughness can exhibit higher SE emission yields in higher energies. Figure S13 shows SEHI functional group component images accompanied with SEM images showing topography emissions greater than 6 eV. The previous section has discussed how functional group distribution influences local plasma

etching behaviour and as a consequence leads to topography changes. In figure S13 we see that topographical images show a depth perception and greater surface edge resolution compared to those of SEI images. A caveat on this form of analysis is that different materials are expected to show chemical and topographical information at different energies as this information is dependent on the emission angle of the material (16).

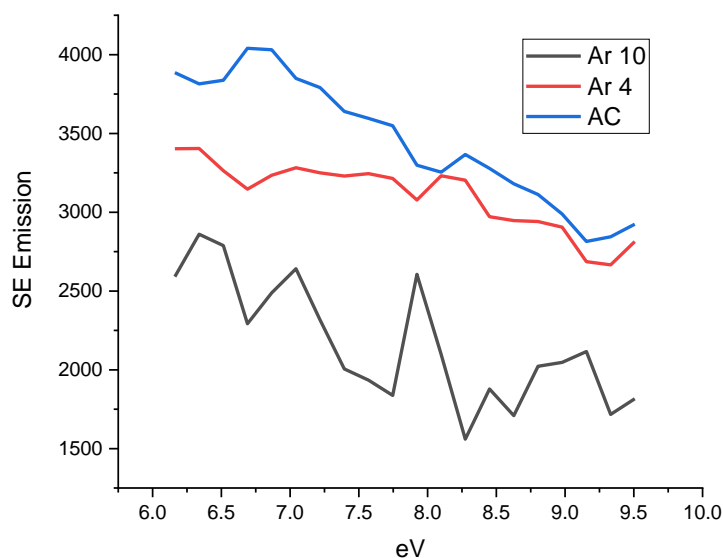


Figure S14 – Higher energies secondary electron spectra for PGS – M after undergoing AC, Ar 4 and Ar 10 plasma treatment.

References

1. S. Pashneh-Tala, R. Owen, H. Bahmaee, S. Rekštyte, M. Malinauskas, F. Claeysens. *Front. Phys.* **2018**. 6. 41.
2. J. Yip, K. Chan, K.M. Sin, K.S. Lau, *Mater. Res. Innov.* **2002**. 6, 44. 4.
3. P.S. Kazemian, A.M. Mentink, C. Rodenburg. CJ. Humphreys. Quantitative secondary electron energy filtering in a scanning electron microscope and its applications. *Ultramicroscopy*. 2007. 107, 140–150.

4. Q. Wan, K.J. Abrams, R.C. Masters, A.C.S. Talari, I.U. Rehman, F. Claeysens, C. Holland, C. Rodenburg, *Adv. Mater.* **2017**. 29, 1703510.
5. J. Schindelin, I. Arganda-Carreras, E. Frise, V. Kaynig, M. Longair, T. Pietzsch, S. Preibisch, C. Rueden, S. Saalfeld, B. Schmid, J.Y. Tinevez, D.J. White, V. Hartenstein, K. Eliceiri, P. Tomancak, A. Cardona, *Nat. Methods.* **2012**. 9, 676.
6. N.A. Stehling, R. Masters, Y. Zhou, R. O'Connell, C. Holland, H. Zhang, C. Rodenburg, *MRS Commun.* **2018**. 8, 226.
7. R.C. Masters, N. Stehling, K. Abrams, V. Kumar, A. Schäfer, D. Lidzey, C. Rodenburg, *Adv Sci.* 2019. 6, 5.
8. N. Farr, S. Pashneh-Tala, N. Stehling, F. Claeysens, N. Green, C. Rodenburg. *Macromolecular Rapid Communications.* 2019. 41. 3
9. K.J. Abrams, M. Dapor, N. Stehling, M. Azzolini, S.J. Kyle, J.S. Schäfer, A. Quade, F. Mika, S. Kratky, Z. Pokorna, I. Konvalina, D. Mehta, K. Black, and C. Rodenburg. *Adv Sci.* **2019**. 6, 19.
10. M. Abdouss, N. Sharifi-Sanjani, P. Bataille, *Journal of Applied Polymer Science.* **1999**. 74. 3417
11. K. Yuniarto, YA. Purwanto, S. Purwanto, BA. Welt, HK. Purwadaria, T. Candra Sunarti. *AIP Conference Proceedings*, **2016**. 1725, 020101
12. Y. Wang, GA. Ameer, BJ. Sheppard, R. Langer. A tough biodegradable elastomer. *Nat Biotechnol.* **2002**. 20:602–6.
13. M, Frydrych. B. Chen. Large three-dimensional poly(glycerol sebacate)-based scaffolds – a freeze-drying preparation approach. *J Mater Chem B* (2013) 1:6650–61. doi: 10.1039/C3TB20842G
14. R Kim-Sung. *Journal of Applied Polymer Science.* **2002**. 77: 1913–1920

15. V. Kumar, Vikas. W. Schmidt, G. Schileo, R. Masters, M Stringer, D. Sinclair, I. Reaney, D. Lidzey, C. Rodenburg, ACS Omega. **2017**. 2. 2126-2133.
16. Q. Wan, R. Masters, D. Lidzey, K. Abrams, M. Dapor, R. Plenderleith, S. Rimmser, F. Claeysens, C. Rodenburg, Ultramicroscopy. **2016**. 171.

5. Identifying and mapping chemical bonding within Phenolic Resin using Secondary Electron Hyperspectral Imaging

Polymer Chemistry
Volume: 12 Issue: 2
December 2020,
DOI: 10.1039/D0PY01220C

Nicholas T.H. Farr, ^{*1,2} Sameer F. Hamad,¹ Euan Gray,¹ Christopher M. Magazzeni,³ Fodio Longman,¹ David E. J. Armstrong,³ Joel P. Foreman,¹ Frederik Claeysens,^{1,3} Nicola Green,^{1,3} and Cornelia Rodenburg¹

¹ University of Sheffield Faculty of Engineering, Material Science and Engineering, Sheffield, S1 3JD, UK

² Insigneo Institute for in silico Medicine, The Pam Liversidge Building, Sir Robert Hadfield Building, Mappin Street, Sheffield, UK

³ Department of Materials, University of Oxford, Parks Road, Oxford, UK

Received 27 August 2020; accepted 14 December 2020

5.1 Prelude

Chapter 5 presents the article titled "Identifying and mapping chemical bonding within Phenolic Resin using Secondary Electron Hyperspectral Imaging". The work presents a detailed evaluation of phenolic resin surface using the SEHI technique which is based on the collection of secondary electron emission spectra in an SEM. This unique approach allows key insights into a samples SE emission properties and in turn their chemical bonding which results in high resolution chemical imaging. Such imaging provides key insights into the mechanical properties of phenolic resin.

Prior to this publication the author of this thesis co-authored the publication "S. Hamad, N. Farr, T. Fei, N.F. Shukor, J.S. Dean, S.A. Hayes, J.P. Foreman, C. Rodenburg: Optimizing size and distribution of voids in phenolic resins through the choice of catalyst types. *Journal of Applied Polymer Science* 136(47):48249. (See appendix 2)" This publication laid the groundwork for the development of the fast acting resin investigated within this chapter. In Hamad et al investigation of the bonding present within the newly developed phenolic resin was conducted by bulk chemical averaging methods and did not provide information of the chemical bonding variation existing within the material.

Hamad et al identified that the mechanical properties of cured phenolic resins are affected by the incidence of microvoids. Producing resins that are void free is usually accomplished through the employment of long heated cure cycles (3 > 4 days). This long cure period incurs excessive energy consumption and time costs for industry. To address this issue an ability to modify the distribution and void size was developed based on a short cure cycle (4 hrs) enabled through a fast action acid catalyst to improve the balance between the resin's mechanical properties and the curing time necessary.

5.1.1 Thesis Question 1 Can SEHI deliver insights into the mechanical properties of a biomaterial?

SEHI spectra captured in this chapter revealed local variations in crosslinking and molecular order across phenolic resin. This was the first time SES or SEHI was applied to analysis of thermoset, highly crosslinked polymer networks.

Presented SEHI analysis and related SE spectra provided compelling evidence that a greater prevalence of CO bonding exists in close proximity (~50 nm) to void sites than

the typical distribution observed within the matrix. This result can be explained to be the consequence of an increased incidence of ether bridges observed at such void sites. Based on the demonstrated capability, SEHI is considered to be an ideal analysis tool with the capacity to isolate local variations in chemical bonding which have a direct relation to the mechanical properties of phenolic resin.

5.1.2 Thesis Question 2: Is the captured SE spectra able to identify specific functional groups that play a key role in biomaterials engineering TE and if so can SEHI map these functional groups at the nanoscale?

Chapter 5 applies the findings from chapters 3 and 4 to a different materials system for further evaluation. SEHI images overlaid on standard SEM images showed for the first time the distribution of CO bonding within Phenolic resin. In this publication SEHI mapped CHx CO and OH functional groups providing a better understanding of the functional group distribution that exists around phenolic resin void sites.

Selection of a suitable component analysis method is a key requirement to generate SES functional group SE components without user bias. Component Analysis is used to determine the spectrum distribution of components in the material. This chapter includes an evaluation of the application of Non-Negative Matrix Factorization (NNMF) being applied to generate spectral components. An example data set analysing phenolic resin was used to illustrate the selection of the component analysis methodology. In this instance a 5 component analysis was selected for review. In Fig SI 10, the spectrum plot of five (5) components is shown. Two methods are utilised to compare their performances in the component analysis process. Firstly, the Principal Component Analysis (PCA) that aims to reduce the dimensionality of the data (stack of hyperspectral SEHI images) in an interpretable (components) way. It achieves this by

preserving the information of the data within the components and clustering positive and negative correlated components together. PCA assumes that the components are a linear combination of features and therefore, concentrates these features within the first component of the data. The orthogonality assumption of PCA therefore implies that spectrum is only concentrated in the first component of the analysis. On the other hand, the NMF method preserves the spatial information of extracted components that corresponds to the structural differences in the components, hence retaining the global structure of the material. It achieves this by allowing only additive (positive) correlated combinations this enables an intuitive representation of the data since each component forms a part of the data (see Fig SI 10). The above analysis shows that the NMF performs better when dealing with SEHI image stacks due to its ability to efficiently extract features that are only positively correlated which ensures that both spatial and structural information are retained. Additionally, this non-negativity nature of NMF improves result interpretation and precision.

5.1.3 Brief Summary

The publication presented in this chapter showed for the first time that characterising and gaining a better understanding of the effects of differing chemical bonding mechanisms together with mapping any lateral distributions on the mechanical properties of phenolic resin can be accomplished using SEHI. In the process of doing so this work exploits a range of analysis techniques which for the first time has been able to characterise various surface chemical bonding. This is an exciting development as SEHI delivers the ability to isolate chemical bonding on the surface of polymer, in addition to its novel capacity to map them at the nanoscale.

5.2 Contributions

NF performed the majority of the experimental work and data analysis and wrote the manuscript. SH synthesised the phenolic resin and CM conducted the nano-indentation analysis. NG, FC and CR contributed to the experimental design, project supervision, and the writing of the manuscript. Please see overleaf for the paper. This is an open access article under the terms of the Creative Commons Attribution License, which permits use, distribution and reproduction in any medium, provided the original work is properly cited. See <https://creativecommons.org/licenses/by/3.0/> for more information.






Cite this: *Polym. Chem.*, 2021, **12**, 177

Received 27th August 2020,
Accepted 14th December 2020

DOI: 10.1039/d0py01220c

rsc.li/polymers

Identifying and mapping chemical bonding within phenolic resin using secondary electron hyperspectral imaging†

Nicholas T. H. Farr,  *^{a,b} Sameer F. Hamad,^a Euan Gray,^a Christopher M. Magazzeni,^c Fodio Longman,^a David E. J. Armstrong,^c Joel P. Foreman,^a Frederik Claeysens,^a Nicola H. Green ^{a,b} and Cornelia Rodenburg ^a

The distributions of methylene and ether bridges have been shown to impact the mechanical properties of phenolic resin. This work demonstrates the ability of the novel SEM based technique, secondary electron hyperspectral imaging (SEHI), to characterise and map methylene and ether bridges within phenolic resin at the nanoscale.

Phenolic resins are a group of the most versatile polymers ever formulated. Although they were first produced around 1907 and were consequently one of the first polymers commercially available, they have been in constant development and use ever since and are widely used in various applications.¹ A recent review article highlighted the deployment prospects of phenolic resin and evaluated where future research should focus to further increase and improve the potential of phenolic resins for future industrial applications.² The article highlighted that improving phenolic resin's heat resistance and reducing brittleness are key enablers to future deployment opportunities. Demands from the aerospace industry and other industries with challenging environmental conditions raise the requirement to improve the long-term high-temperature oxidation resistance of phenolic resin.³ Historical studies have long establishing how novel synthesis interventions can augment the material's properties by altering the macromolecular structure of phenolic resin.^{4,5}

Research focused on increasing phenolic resin's thermal stability with the aim of producing 'tougher' forms of phenolic resin has shown success by optimising the distribution of voids in the resins.⁶ Alternative approaches to addressing known 'brittleness issues' within phenolic resin,^{7,8} have also

shown success through the inclusion of substances such as, rubber, glass fibres and thermoplastic resins.^{9–11}

Further work towards delivering 'tougher' phenolic resins has investigated altering the polymer network of the resin by changing the bonding ratios of methylene and ether bridges.^{12,13} This work has identified improvements to the efficiency of the resin's production process which also mitigate environmental concerns of current practice. It has been observed that the quantity of ether bridges forming within the resin increases when the F:P (formaldehyde:phenol) ratio increases and, depending on processing conditions, high numbers of ether linkages¹⁴ reduce the strength of the cured resin.¹⁵

Despite the improved functionality of such resin more efficient and potentially greener ways of improving toughness of phenolic resin have come from studies targeted at altering the polymer network of phenolic resin by changing the bonding ratios of methylene and ether bridges have also delivered tougher materials.^{12,13} The proportion of ether bridges rises with increases in the F:P (formaldehyde:phenol) ratio, with an excessive amount of ether linkages¹⁴ reducing the strength of the cured resin.¹⁵ It is important to note that processing conditions are also influential on the final strength of the cured resin.

Fast acting catalysts reduce the resin's curing time and impart "void like" structures.⁶ This is in contrast to phenolic resins that are required to be produced free from voids which typically require intensive curing processes using multiple heating cycles.

Such processes carry the disadvantage of slower curing cycles that create extra formaldehyde emissions. Future optimisation of phenolic resin properties requires an understanding of how these processes affect the material's structure at the nanoscale. The ability to map chemical bonding changes at the nanoscale would enable polymer scientists to better construct and optimise processes designed to alter the bonding ratios of methylene and ether bridges observed in phenolic resin.

^aDepartment of Materials Science and Engineering, Sir Robert Hadfield Building, Mappin Street, University of Sheffield, UK. E-mail: nfarr1@sheffield.ac.uk

^bInsigneo Institute for in Silico Medicine, The Pam Liversidge Building, Sir Robert Hadfield Building, Mappin Street, Sheffield, UK

^cDepartment of Materials, University of Oxford, Parks Road, Oxford, UK

†Electronic supplementary information (ESI) available. See DOI: 10.1039/d0py01220c



Secondary electron hyperspectral imaging (SEHI) is a novel technique built on SE spectroscopy and has been used for characterising the surface chemistry of innovative polymeric biomaterials.¹⁶ A scanning electron microscope's (SEM) ability to detect secondary electrons (SEs) emissions from a material sample is the basis for SEHI. A series of images collected from selected SE energy bands is constructed to form the SEHI images stacks. This is in contrast to a standard SEM which assembles a single image with SEs of all energies contributing to it. SEHI delivers novel characterisation insights by creating a wide-ranging SE spectral representation of the sample material. A number of research studies have demonstrated SEHI's effectiveness including; molecular orientation of organic electronic devices,¹⁷ semi-crystalline polymer mapping and natural materials nanostructure variations¹⁸ but has not yet been applied to the mapping of ether or methylene bridges.

This study focuses on analysing the chemical bonding structure of a form of phenolic resin, PR382. PR382 has recently been produced⁶ with the design aim of minimising losses in desirable mechanical properties which occur as a consequence of using typical current resin production processes. This is achieved by substituting a new faster curing, more cost effective and environmentally friendlier fast curing cycle based production process. Analysis of phenolic resin requires the ability to map the chemical bonding distribution within the resin through the application of the SEHI technique. The emphasis of this study is mapping and showing sensitivity to specific bonding mechanisms that are present within the phenolic resin sample post synthetic intervention, as an example of how the SEHI technique can provide an enhanced understanding of micron – nano scale structures. This work establishes that the voids created as the phenolic resin cures in response to a slow acting acid catalyst, are a focus for a high level of CO bonding attributable to ether bridge formation around the voids sites.

Materials and methods

Materials

In this study, the resole commercial phenolic resin Cellobond J2027X pre-polymer was used (supplied by Caleb Technical Products Ltd, UK). This kind of resin is usually available as a water-based controlled-viscosity resin, which can be cured either with the application of heat only using long cure cycle (3–4 days) or with the use of a strong acid catalyst, short cure cycle (3 h) at low temperature (~60 °C). It is suitable for the fabrication of fibre composites by hand layup and resin transfer molding. Catalyst (Cellobond Phencat 382), supplied by the same company (Caleb Technical Products Ltd, UK), was used in this study. Phencat 382 is a relatively slow action acid catalyst (working life ~4 h), which is activated at low temperature, typically 60–80 °C. It is an acid-based catalyst consisting of, C3–9-alkyl esters (75–90%) and phosphoric acid (10–25%) by weight. A short cure cycle was selected where the resole phenolic resin was initially mixed with slow action acid catalyst

(Phencat 382) then decanted into the PTFE mold to be placed in an autoclave for polymerisation. The catalyst ratio was 5 wt% of the resin. Phenolic resin samples were fractured to allow for analysis of the cross-section of the material.

Methods

Imaging. Phenolic resin samples were fractured and placed on a carbon tab on an aluminium stub ready for SEM imaging. Observation of the fracture surface morphology of the flexural strength samples (PR382) was performed using a Scanning Electron Microscope (FEI Nova Nano 450 SEM). The PR382 samples were not subject to deposition of conductive coating, in contrast to usual polymers SEM analysis practice. To avoid surface charging and consequent damage to the sample a low accelerating voltage (1 kV) with typical vacuum pressure of 10⁻⁵ mbar at a working distance of 3 mm was applied. An Everhart–Thornley Detector (ETD) for low magnification images and a Through Lens Detector (TLD) for high magnification images were used for the collection of SE images.

SEHI acquisition and image processing. The FEI Nova Nano 450 SEM is provided with a through lens detector which includes a voltage controlled deflector electrode. The deflector electrode channels the signal into the SE detector. The deflector electrode is set to a predetermined deflector voltages and an image is generated for each deflector voltage (more detailed information provided in ESI†). Spectra and hyperspectral images are acquired through post-processing of such image series. Stage bias experiments have been performed to allow energy calibration of this process through experiments.^{17,19} Fiji software was utilised to perform image processing.²⁰ Histogram and spectral off-set normalisation²¹ has been applied retrospectively to optimise all images for brightness and contrast, and to limit the effects of differing sample work functions. The work function of a material is the minimum energy required to remove an electron from the solid to outside the solids surface within a vacuum. Once S-curves have then been obtained they are differentiated to produce the SE curves. Component analysis was then performed to image stacks utilising non negative matrix factorization (nnmf) to isolate components of interest.

Theoretical grounds of secondary electron spectroscopy (SES). A typical SE spectra is a plot of the number of electrons detected within a specific energy range. Each chemical functional group produces a set of characteristic peaks in the SE spectra (SES).¹⁶ Based on knowledge of functional groups, material properties can also be inferred from the measurement of the kinetic energy and the number of the emitted SEs in some circumstances. SEHI can be summarised as a technique that is responsive to surfaces and is capable of imaging beam sensitive materials by resolving chemical, compositional and structural properties at the nanoscale level – depending on the energy range used for imaging. SEHI is proposed as an effective microanalysis tool for nanostructured polymers with the ability of mapping chemical functional groups of particular interest. More information on the theoretical grounds for probe-sample analysis and SES are given in the ESI.†



Results and discussion

To illustrate the chemical bonding variations within PR382, SE spectra given in Fig. 1 represent spectra captured from three different areas (1, 2 and 3) across the cross-sectioned material. Each area's SEM field of view is included to show the exact region of analysis. Area 3 differs by virtue of its increased magnification which allows analysis of a single void site of interest.

Previous studies have isolated the energy range of 1.4–2.3 eV to the molecular order of polymers.²² An increase in peak intensity in this range indicates an increased molecular order, indicative of the material being more crystalline. Areas 1 & 2 show a higher intensity level when compared to area 3. Area 3 is therefore disordered, as we do not observe any sharp peaks within 1.4–2.3 eV range. These observed differences are due to areas 1 and 2 both encompassing a greater density of cured cross-linked networks than that of area 3 which focuses on a singular void site.

SE spectra analysis can provide for comparisons to be drawn regarding crosslinking networks. The SE emission captured in this study for areas 1 and 2 exhibited a greater SE emission in the energy range associated with CH vibrations and –OH groups^{16,23,24} when compared to that of area 3. The

increase of CH₂ and –OH formation in this polymer system indicates the presence of methylene bridges. Results obtained from the raw SE spectra display an increase in CH vibrations. The data given in Fig. 2A, shows an increase in –OH groups (when all areas are normalised to CH peak emission). These two results provide evidence to support the conclusion that areas 1 and 2 contain a greater density of methylene bridges than area 3.

All three areas show emissions within the SE emission region associated with C–O bonding. C–O bonding in area 3 displays the strongest emission ratios (when all areas are normalised to their respective CH emissions peak) compared to areas 1 and 2. As C–O bonding in phenolics is related to ether bridges (see Fig. 2B), area 3 possesses a large density of ether bridges compared to area 1 and 2. Fig. 2B shows the chemical bond formation of the two common types of crosslinks present within phenolic resin. Fig. 2B(1) depicts the various example structures of methylene bridges formation which is the most common form of crosslink with phenolic resin networks.¹⁵ Fig. 2B(2) depicts the formation of ether bridges which are less commonly found within phenolic resin.

From the SE spectra results it can be assumed that this is consistent with areas 1 & 2 having a greater matrix (areas away

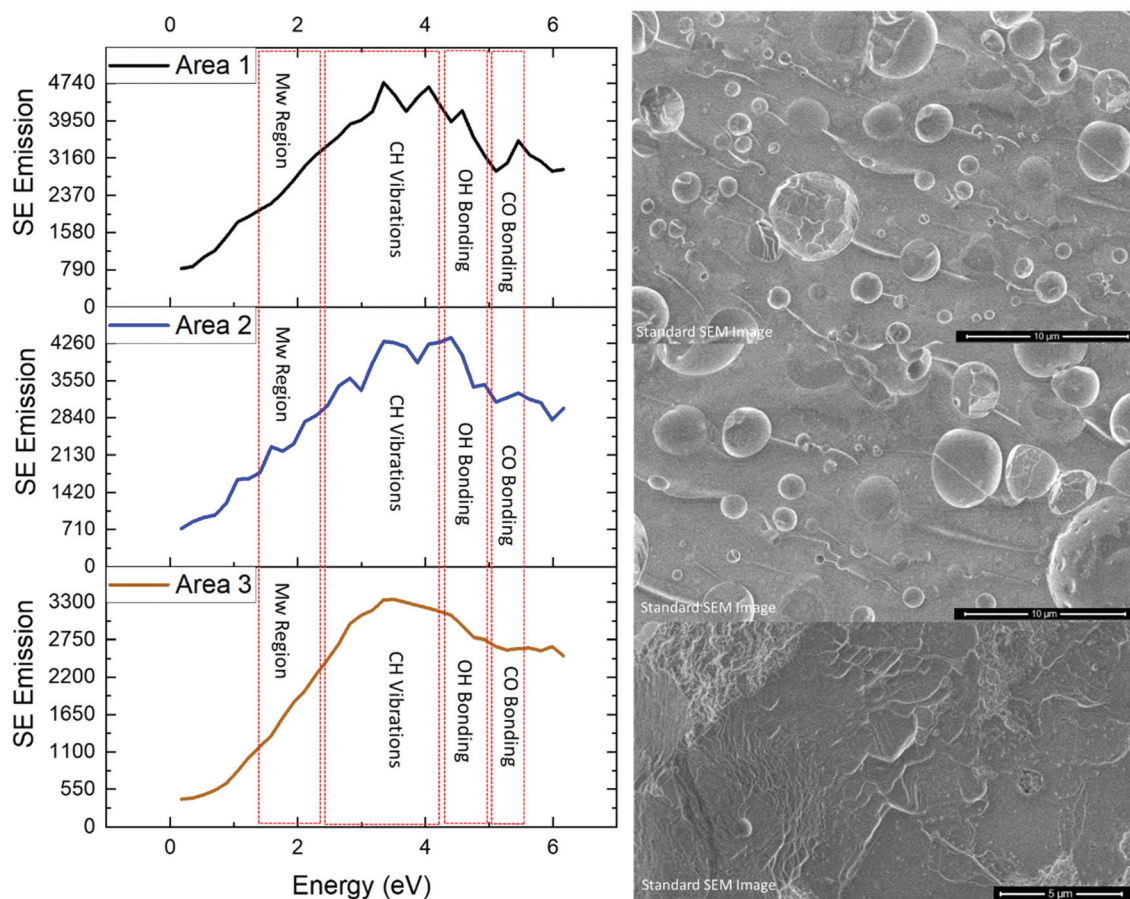


Fig. 1 Secondary electron spectra with accompanying SEM images for PR382 area 1, 2 and 3 highlighting SE regions identified as associated with functional group emissions. Area 1 & 2 HFW = 30 μm whereas area 3 HFW = 25 μm.



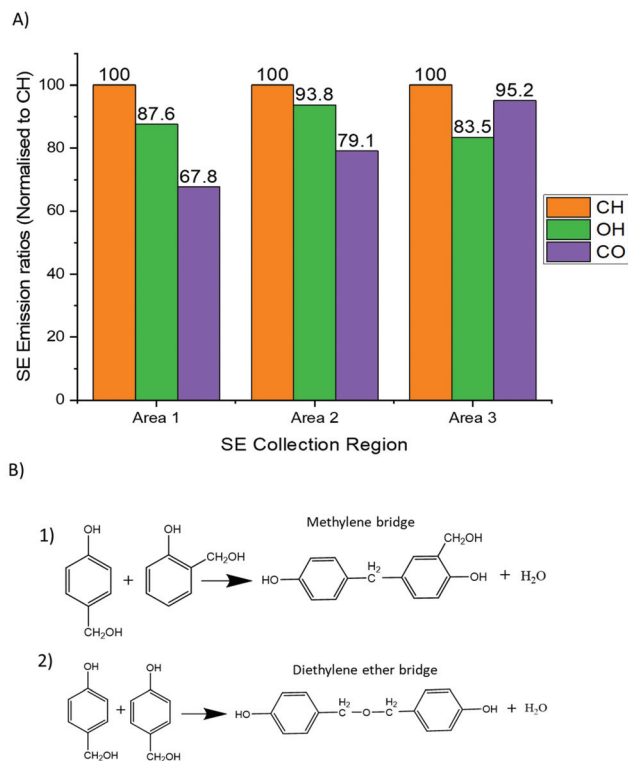


Fig. 2 (A) A graph which shows the ratio of OH and CO functional groups for area 1, 2 and 3 after all area spectra were normalised to their CH emission peaks. (B) Displays the possible cross-linking mechanisms (methylene and ether bridge formation) within phenolic resin.

from voids) concentration in the analysed field of view which will consequently have more (CH_2 , $-\text{OH}$) linked methylene bridges. Thus the SE spectra results show that areas 1 and 2 contain a higher density of methylene bridges than area 3 and also display a greater molecular order SE peak than area 3 compared to area 3. Methylene bridges possess a shorter bridging length when compared to that of ether bridges, which has a greater number of atoms between its phenyl rings. Therefore, phenolic resin with a greater ratio of methylene bridges to ether bridges would present a more ordered structure by virtue of ether bridges having a higher number of rotational degrees of freedom and being inherently flexible (see Fig. 3). The difference in chain length could also explain why there is a higher concentration of $-\text{OH}$ detected as the phenyl rings appear more densely packed.

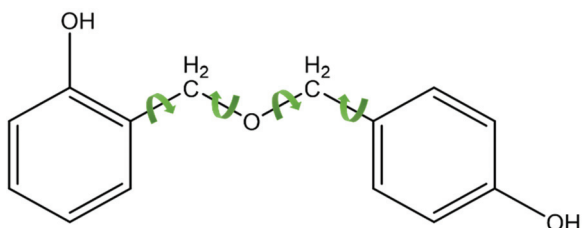


Fig. 3 The rotational degrees of freedom observed in ether bridges.

Various techniques have already shown that phenolic resin contains different ratios of methylene and ether bridges and this study's results above are not novel in that respect. However, by building on SE emission ranges obtained from the resulting SE spectra, it is now possible to use SEHI to map ether and methylene bridge spatial distributions on different length scales as demonstrated in Fig. 4 (and SI1†).

Fig. 4 shows SEHI images overlaid on standard SEM images to show the distribution of CO bonding. While the standard SEM image does not allow to determine the origin of the con-

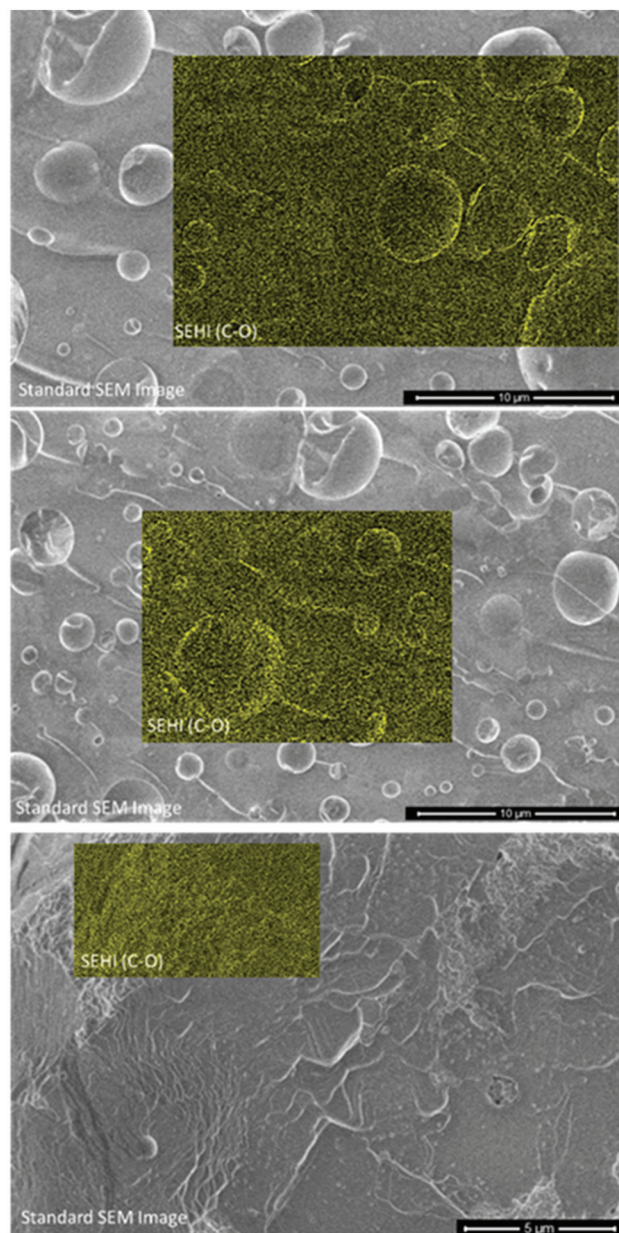


Fig. 4 SEHI images generated from the component analysis of PR382 mapping CO bonding (indicating ether bridge distributions). With the stronger emission intensity showing greater CO bonding. SEHI images are overlaid with grayscale standard SE images (integral over all energy ranges) of PR382.



trast associate with the voids, SEHI data enable component analysis to be performed on image stacks utilising non-negative matrix factorization (nnmf) to isolate components of interest (see ESI 1, 2 & 3†). The nnmf process gives a number of components which are derived in relation to the SE emission peaks of interest. Of particular importance to phenolic resin, nnmf isolated a region around 5–5.5 eV which has previously been shown to be a response to CO bonding.^{16,24} Therefore, this technique provides SEHI with the ability to map where ether bridges exist within the resin. SEHI images observe CO bonding emission to be most prominent around the edges of void sites. The mechanism of how ether bridges form around these voids is a subject for debate. The authors in this instance propose two potential mechanisms to be involved, but future work is required to fully understand this reaction.

One mechanism is based on the curing reaction of the resin itself: the structural inhomogeneity of “water/formaldehyde bubbles” is associated with density fluctuation that is related to crosslink density distributions that have been reported to exist within phenolic resin.²⁵ In this case we propose that the inhomogeneous distribution of crosslinks can cause void trapping. As the water/formaldehyde bubbles form and migrate within the autoclave to the surface of the material, it is postulated that they become trapped by ether bridges developing around the edges of the voids. It has been long established that increasing the F : P molar ratios favours the production of ether bridges.¹⁴ As the void sites predominantly contain water and formaldehyde, both by-products of previous crosslink reactions, it is suggested that void sites have an increased localised F : P ratio. This relationship would explain the ether bridge configuration around void sites as their formation is the preferred crosslink route.¹⁵

A proposed alternative mechanism is associated with the possibility that there is a preferred route for the water/formaldehyde bubbles take when attempting to leave the resin during curing.²⁶ As the phenolic resin cures, the bubbles will leave the material by following a path of least resistance and therefore their migration will follow the least dense regions within the resin (see Fig. 5). Consequently, the voids will be concentrated away from areas of higher density molecular structures (strong methylene bridge content) and towards less dense molecular regions (strong ether bridge content). This is as a result of ether bridges containing a greater number of atoms between the anchoring phenol rings with intramolecular forces known to decrease rapidly with distance. Prior modelling studies have revealed that mass density fluctuations within phenolics are due to the inhomogeneous reactions described previously.²⁷ These studies have observed density variations at the nano-scale but have encountered difficulties modelling at larger length scales. SEHI, being inherently multiscale in analysis, confirms the observed density variations in phenolic resin at the nano-micron scale and also provides evidence that they are dependent on inhomogeneous crosslinking reactions. Fig. S14† supports the proposal that such variation observed in molecular density and crosslinking reactions does translate to large variations being exhibited in the nano-structural hardness of the resins.

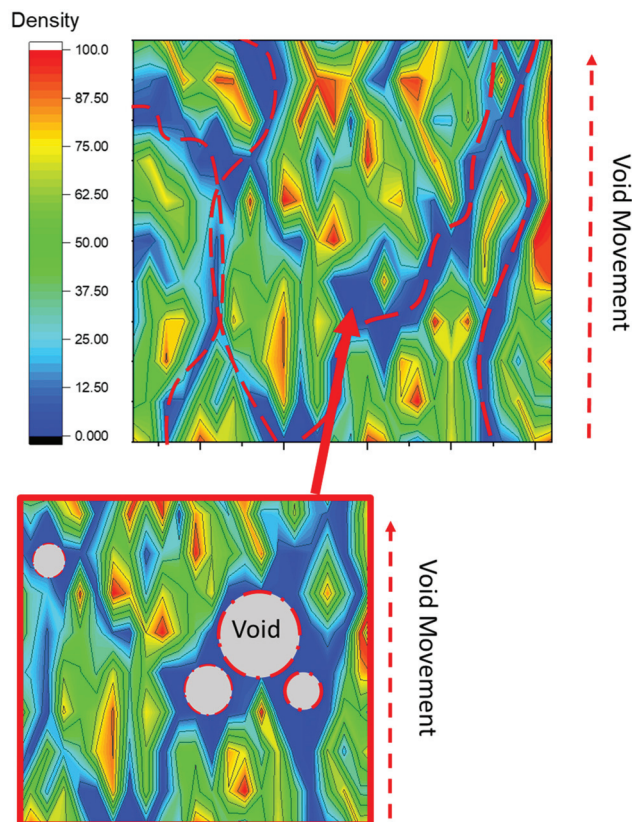


Fig. 5 Water/formaldehyde bubble migration due to material density formation.

Conclusions

The presented SEHI analysis and related SE spectra provide compelling evidence that a greater prevalence of C–O bonding exists in close proximity (~50 nm) to void sites than the typical distribution observed within the matrix. This result can be explained to be the consequence of an increased incidence of ether bridges observed at such void sites. SEHI further revealed local variations in crosslinking and molecular order and functional groups (CH, OH) across the resin. Based on the demonstrated capability, SEHI is considered to be an ideal analysis tool with the capacity to isolate local variations in reactant remnants, such as formaldehyde, within phenolic resin.

Conflicts of interest

The authors declare no conflict of interest.

Acknowledgements

The authors thank EPSRC for funding under SEE MORE: Secondary Electron Emission-Microscopy for Organics with Reliable Engineering Properties (EP/N008065/1), and studentship for N. F. (EP/R513313/1). NF would also like to thank the



Pico-FIB network for travel and collaboration funding. Electron microscopy and analysis was performed in the Sorby Centre for Electron Microscopy at the University of Sheffield.

References

- 1 K. Hirano and M. Asami, Phenolic resins—100years of progress and their future, *React. Funct. Polym.*, 2013, **73**(2), 256.
- 2 Y. Xu, L. Guo, H. Zhang, H. Zhaiab and H. Ren, Research status, industrial application demand and prospects of phenolic resin, *RSC Adv.*, 2019, **50**(9), 28924.
- 3 S. Rapheepraew and E. Vuthichai, Synthesis of poly (siloxane/double-decker silsesquioxane) via dehydrocarbonative condensation reaction and its functionalization, *Polymer*, 2016, **86**, 113.
- 4 T. Holopainen, L. Alvila, J. Rainio and T. Pakkanen, Phenol-Formaldehyde Resol Resins Studied by ¹³C-NMRSpectroscopy, Gel Permeation Chromatography, and Differential Scanning Calorimetry, *J. Appl. Polym. Sci.*, 1997, **66**, 1183.
- 5 N. Gabilondo, M. López, J. A. Ramos, J. M. Echeverría and I. Mondragon, Curing kinetics of amine and sodium hydroxide catalyzed phenol-formaldehyde resins, *J. Therm. Anal. Calorim.*, 2007, **90**(1), 229.
- 6 S. Hamad, N. Farr, T. Fei, N. Shukor, J. Dean, S. Hayes, J. Foreman and C. Rodenburg, Optimizing size and distribution of voids in phenolic resins through the choice of catalyst types, *J. Appl. Polym. Sci.*, 2019, **136**, 48249.
- 7 S. Hamad, N. Stehling, S. Hayes, J. Foreman and C. Rodenburg, Exploiting Plasma Exposed, Natural Surface Nanostructures in Ramie Fibers for Polymer Composite Applications, *Materials*, 2019, **12**(10), 1631.
- 8 S. Q. Liu, P. C. Ning and Z. M. Ding, Research progress of modified phenolic resin, *Thermosetting Resin*, 2016, **31**, 64–70.
- 9 Z. Li, W. Zhou, L. Yang, P. Chen, C. Yan, C. Cai, H. Li, L. Li and Y. Shi, Glass Fiber-Reinforced Phenol Formaldehyde Resin-Based Electrical Insulating Composites Fabricated by Selective Laser Sintering, *Polymers*, 2019, **11**, 135.
- 10 X. M. Nie, Z. P. Gao and F. Q. Yi, Development of Phenolic Resin/Fiberglass Cloth Composite Prepreg Modified by Nitrile-Butadiene Rubber, *Eng. Plast. Appl.*, 2019, **47**, 42.
- 11 W. Solyman, H. Naguib, N. Alian, N. Shaker and U. Kandil, Synthesis and characterization of phenol/formaldehyde nanocomposites: Studying the effect of incorporating reactive rubber nanoparticles or Cloisite-30B nanoclay on the mechanical properties, morphology and thermal stability, *J. Radiat. Res. Appl. Sci.*, 2016, **10**(1), 72–79.
- 12 J. Bouajila, G. Raffin, H. Waton, C. Sanglar and S. Alamerçery, M.F Grenier-Loustalot, Phenolic Resins (II) – Influence of the Chemical Structure of High Molecular Weight Molecules on the Mechanisms of Cross-linking and on the Final Structure of the Resins, *Polym. Polym. Compos.*, 2003, **11**(4), 233–262.
- 13 D. X. Wang, Z. M. Chen, G. X. Zhang, X. C. Liang, B. H. Li, X. Q. Cao and C. Wang, Study on Fast-Curing Phenol-Formaldehyde Resin Adhesive, *Chem. Adhes.*, 2016, **38**, 447.
- 14 P. W. King, R. H. Mitchell and A. R. Westwood, Structural analysis of phenolic resole resins, *J. Appl. Polym. Sci.*, 1974, **18**(4), 1117.
- 15 P. S. Parameswaran and E. T. Thachil, *Int. J. Polym. Mater. Polym. Biomater.*, 2007, **56**, 177.
- 16 N. Farr, S. Pashneh-Tala, N. Stehling, F. Claeysens, N. Green and C. Rodenburg, Characterizing Cross-Linking Within Polymeric Biomaterials in the SEM by Secondary Electron Hyperspectral Imaging, *Macromol. Rapid Commun.*, 2020, **41**, 1900484.
- 17 Q. Wan, K. J. Abrams, R. C. Masters, A. C. S. Talari, I. U. Rehman, F. Claeysens, C. Holland and C. Rodenburg, *Adv. Mater.*, 2017, **29**, 1703510.
- 18 R. C. Masters, A. J. Pearson, T. S. Glen, F.-C. M. Sasam, L. Dapor, Li. A. M. Donald, D. G. Lidzey and C. Rodenburg, Sub-nanometre resolution imaging of polymer–fullerene photovoltaic blends using energy-filtered scanning electron microscopy, *Nat. Commun.*, 2015, **6**, 6928.
- 19 P. S. Kazemian, A. M. Mentink, C. Rodenburg and C. J. Humphreys, Quantitative secondary electron energy filtering in a scanning electron microscope and its applications, *Ultramicroscopy*, 2007, **107**, 140.
- 20 J. Schindelin, I. Arganda-Carreras, E. Frise, V. Kaynig, M. Longair, T. Pietzsch, S. Preibisch, C. Rueden, S. Saalfeld, B. Schmid, J. Y. Tinevez, D. J. White, V. Hartenstein, K. Eliceiri, P. Tomancak and A. Cardona, Fiji: an open-source platform for biological-image analysis, *Nat. Methods*, 2012, **9**, 676.
- 21 N. A. Stehling, R. Masters, Y. Zhou, R. O'Connell, C. Holland, H. Zhang and C. Rodenburg, New perspectives on nano-engineering by secondary electron spectroscopy in the helium ion and scanning electron microscope, *MRS Commun.*, 2018, **8**, 226.
- 22 R. C. Masters, N. Stehling, K. Abrams, V. Kumar, A. Schäfer, D. Lidzey and C. Rodenburg, Mapping Polymer Molecular Order in the SEM with Secondary Electron Hyperspectral Imaging, *Adv. Sci.*, 2019, **6**, 5.
- 23 K. J. Abrams, M. Dapor, N. Stehling, M. Azzolini, S. J. Kyle, J. S. Schäfer, A. Quade, F. Mika, S. Kratky, Z. Pokorna, I. Konvalina, D. Mehta, K. Black and C. Rodenburg, Making Sense of Complex Carbon and Metal/Carbon Systems by Secondary Electron Hyperspectral Imaging, *Adv. Sci.*, 2019, **6**, 19.
- 24 N. Farr, J. Thanarak, J. Schäfer, A. Quade, F. Claeysens, N. Green and C. Rodenburg, Understanding surface modifications induced via Argon Plasma sterilisation through Secondary Electron Hyperspectral Imaging, *Adv. Sci.*, 2020, 2003762.
- 25 Y. Shudo, A. Izumi, K. Hagita, T. Nakao and M. Shibayama, Large-scale molecular dynamics simulation of crosslinked phenolic resins using pseudo-reaction model, *Polymer*, 2016, **103**, 261.
- 26 A. C. Loos and G. S. Springer, Curing of epoxy matrix composites, *J. Compos. Mater.*, 1983, **17**, 135.
- 27 Y. Shudo, A. Izumi, K. Hagita, T. Nakao and M. Shibayama, Structure-mechanical property relationships in crosslinked phenolic resin investigated by molecular dynamics simulation, *Polymer*, 2017, **116**, 506.



Supplementary Information

Identifying and mapping chemical bonding within Phenolic Resin using Secondary Electron Hyperspectral Imaging.

Nicholas TH. Farr^{1,2}, * Sameer F. Hamad,¹ Euan Gray,¹ Christopher M. Magazzeni³, Fodio Longman¹, David Armstrong³, Joel P. Foreman,¹ Frederik Claeysens,¹ Nicola Green,¹² and Cornelia Rodenburg¹

1 Department of Materials Science and Engineering, Sir Robert Hadfield Building, Mappin Street, University of Sheffield, UK.

2. Insigneo Institute for *In Silico* Medicine, The Pam Liversidge Building, Sir Robert Hadfield Building, Mappin Street, Sheffield, UK

3. Department of Materials, University of Oxford, Parks Road, Oxford, UK

1. Additional background

1.A - Background of the interpretation of Secondary electrons

The primary electron beam interacts with atoms within the material by causing electrons to be emitted. These emissions are as a result of a range of physical interactions (2). Figure SI1 shows the interaction volume of a primary electron beam and a range of association emission.

Elastic interactions are those which change the path of the incident electrons in the primary electron beam probe whilst having a negligible effect on their kinetic energy. Inelastic interactions in contrast are those which result in a loss of kinetic energy of the incident electrons (3). High energy electrons that are emitted by an elastic interaction of an incident electron, with the nucleus of the material samples' atoms, are designated as back scattered electrons (BSE). The energy of BSEs is comparable to that of the beam probe's incident electrons. Electrons emitted from the sample at lower energy are categorised as SE. SEs typically display energy voltage of less than 50 eV. Secondary electrons (SE) result from inelastic scattering and are the consequence of either collisions within the electron cloud or by interaction with loosely bound electrons in the material's structure.

The electron beam probe will only interact within a finite interaction volume due to the effect of inelastic interactions. This volume is depended on the primary beam energy. The greater the primary beam energy is the greater volume of sample interaction. This incident beam interaction volume is repressed in figure SI1 with a characteristic 'waterdrop' shape.

SEs are the sample emissions that are associated with SEM images (4). SEs may be emitted from the materials at relatively low kinetic energies, < 10 eV, as a result of potential interaction with electron clouds. The low kinetic energy places a significant limit on the actual escape depth of SEs emitted from a sample, which can often be < 10 nm, as a consequence SE derived images are inherently surface specific. To interpret the images generated by an SEM it is essential to understand how the SE contrast is captured. Selection of an appropriate detector by the user is also dependent on this knowledge.

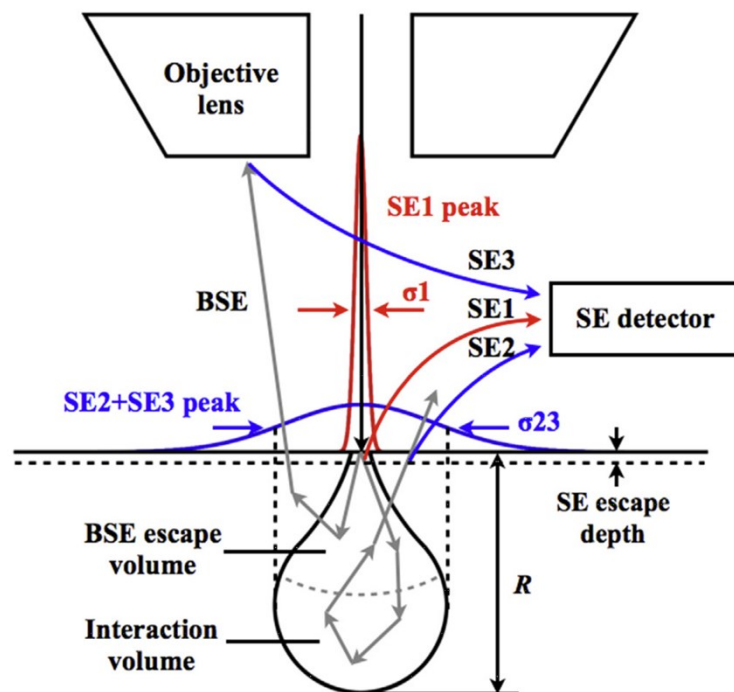


Figure SI 1 – Diagram shows the relative escape depths of SEs and BSEs and their interaction paths prior to detection. Image adapted from (5) with permission from Elsevier. “Schematic of the electrons emitted from a range, R , below the surface of the sample. SE1 is generated from impacted electrons (IE) right after incidence, SE1 have spatially localised information (s_1). Then, IE spread to interaction volume with a size of range R .”

There are a number of different ways that SEs are detected in an SEM (See SI 1), the majority of SEs detected originate as a result of inelastic interactions between the probe incident electrons and the sample (4), in addition to collisions between BSEs and the SEM chamber components after emission from the target sample surface. (This process is depicted in figure SI 1) These different sources of SEs are termed SE1, SE2 and SE3 retrospectively. SEs from each of these difference sources exhibit dissimilar signals types for both resolution and contrast. When undertaking SEM analysis of a polymer’s topographical nanostructure, it is essential to configure the apparatus with a detector which can isolate SE1 from SE2 and SE3. Despite both SE1 and SE2 emissions providing topographical contrast due to their angular distribution and their short escape depth (as shown in Fig2). SE1 emission differs from that of SE2 as a result of their interaction paths, SE2s emissions are generated from BSEs when they pass through the surface, unlike SE1 which are generated

from impacted electrons directly after beam incidence. *SE1* emissions are therefore possess spatially localised information and are suitable for processing into high resolution surface images.

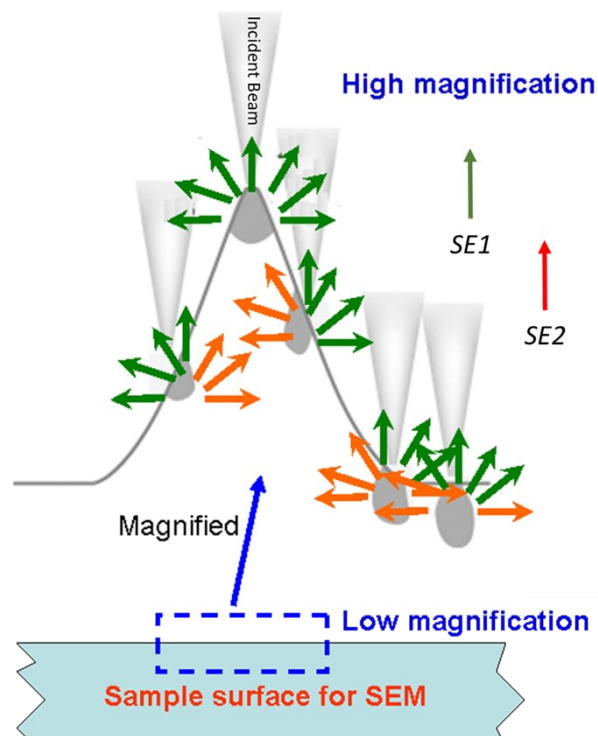


Figure SI 2 –Diagram showing the topographic effect on SEM contrast of *SE1* and *SE2* emissions. Figure amended from “Yougui Liao, Practical Electron Microscopy and Database, (2006), www.globalsino.com/EM/”

1. B- Electron Detectors within an SEM.

Both SE and BSE emissions can each be exploited to extract complementary sets of information from a target sample within an SEM. Modern SEMs are configured to utilise detectors which have the ability to distinguish between these two types of emissions and are capable of filtering either SEs or BSEs from an intermixed sample image signal. As previously highlighted the ability to research surface effects in polymers at the nanoscale level relies primarily on the capture of target images built from *SE1s* emissions. The most common detector used in SE imaging is the Everhart-Thornley detector (ETD). ETDs mix *SE1*, *SE2* and *SE3* emissions, this provides limited resolution with SE images being hard to interpret in respect to their specific SE emissions. Alternatively, the other commonly used SE detector is the Through-lens detector (TLD). The TLD suppresses *SE2* and *SE3* to collect mainly *SE1* emission (6). By virtue of collecting *SE1* emissions the TLD can

provide high resolution surface images, suited perfectly for the use of chemically mapping the nanoscale surface of polymers. The TLD used for this study is depicted in figure SI 3. This TLD step up utilises electrostatic deflectors to enable the detection of SEs when set to a high-resolution immersion mode where target samples are immersed in a magnetic field and the TLD is positioned above the objective lens of the electron column (8).

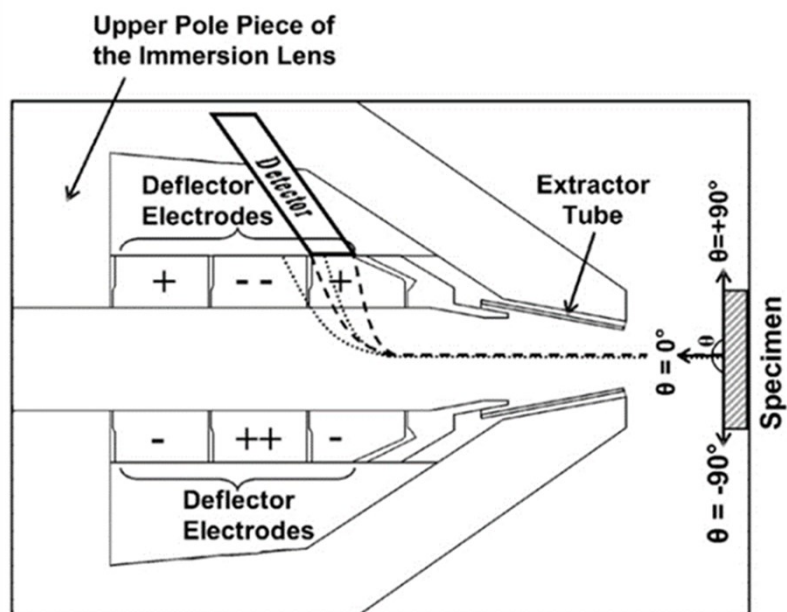


Figure SI 3. Schematics of TLD arrangements in SEMs manufactured by FEI Co. XL-30 design TLD. Adapted from (8) with permission from Elsevier.

Configuration of TLD detectors varies according to both manufactures and actual SEM models. Figure SI 3 illustrates a FEI XL-30 design which is a widely used SEM having a TLD integrated into the incident electron probe consisting of a scintillator detector and a 'deflector' electrode (8). The deflector is installed as a guide to drive SEs towards the detector and is set to a bias of -60V. This bias can be adjusted to collect *SE1* emissions from energy ranges of interest. Additionally, the SEM's pole-piece incorporates a positively biased electrode whose purpose is to help attract SEs within the specimen chamber towards the detector. TLDs predominantly detect *SE1s* which provide the highest spatial resolution information as they are emitted by the target sample through direct interaction with the primary electron beam.

1.C – Information contained in secondary electron spectroscopy (SES)

Electrons emitted from a target sample through probe electron/material interactions within the SES can be detected and displayed by way of spectra constructed according to their measured energy ranges. From the resultant spectra, conclusions can be drawn regarding the samples chemical composition and structure. SES is not a recent development for material characterisation, SES has been investigated since 1947 (9). Over the last few decades, SES has only recently started to flourish through innovations in instrumentation, signal processing and imaging proficiency (10,11,12,13).

The process of developing SE spectra wholly relies on the probe electron – material interactions. SES measures electron emission energies post inelastic sample collisions. SES benefits from employing a low KeV (between 0.5-2 keV) primary electron beam which makes it possible for the SES to collect the spectra of beam sensitive materials. Although, SEs are produced throughout the primary beam interaction depth, only SEs emitted within the SE escape depth can be detected, as SEs emitted at a greater depth will be absorbed by the bulk of the sample material. The SE shallow escape depth raises the issue of surface contamination affecting the spectra results, a problem faced by other surface analysis techniques. However, SES has been shown to have operational characteristics that allow it to overcome substantial surface contamination to produce accurate spectra that are reproducible and reveal characteristics of the underlying material (10, 13). In contrast EELS provides an average measurement over the material samples thickness and does not allow for high resolution surface characterisation. For polymers which require a tailored surface, such as polymer derived biomaterials, the SES form of detailed surface analysis is considered to be an essential perspective due to the fact that established cells react to a biomaterial's surface on the nanoscale level.

Although, SES, EELS and XPS all have strengths as material characterisation methods, the singular ability of SES to support the secondary electron hyperspectral imaging (SEHI) technique is considered particularly advantageous for the analysis of a range of material types. As distinctive SE energy spectra have been collected for many decades (9,12,13) it is often wrongly assumed that SE images show only topographical contrast. However, with recent progress in SE spectra analysis and energy-filtering detection, advances in capability now enable the capture of spectral images from selected distinct SE energy ranges, which studies have shown to carry chemical and functional information [11, 14, 19]. Both SE and BSE emitted at low primary beam energy ranges contain chemical information. Lower energy SEs contains information about valence bands and higher energy SEs (SE2) have been associated to the atomic number of the elements from which they are emitted (13). BSE imaging has demonstrated a capacity to provide chemical contrast images of materials where topographical features are negligible however, SEHI can provide comparable images of materials at significantly enhanced image resolutions (14).

Standard SEM images are compiled from all surface emitted SEs without discrimination of their energy ranges. In contrast, SEHI compiles a series of images based on the specific energy ranges of emitted SEs. SEHI software processes this captured series of energy range images to construct an inclusive SE spectrum for the material.

Figure SI 12 (graphical abstract) displays the process by which information contained in the SEHI spectrum provides the basis for mapping chemical changes within the surface of materials. This capability is predicted to provide new opportunities for researchers to characterise novel polymer materials. The value of the SEHI characterisation technique has successfully been demonstrated in range of applications, varying between the analysis of molecular orientation within organic electronic devices, semi-crystalline polymers chemical mapping and exposing variations in nanostructures that form natural materials (11, 15). SEHI can be summarised as a technique that is responsive to surfaces and is capable on beam sensitive materials of resolving chemical, compositional and structural differences at the nanoscale level. It is proposed that an effective microanalysis tool for nanostructured polymers, results from the integration of the capabilities of a low voltage SEM and those of secondary electron microscopy.

1.D - Modelling secondary electron spectroscopy (SES)

SE emissions captured in electron microscopes has been the subject of an increasing number of studies, using a modelling approach that simulates the production of secondary electron emission from sample materials. Many of these studies have adopted the Monte Carlo approach to simulation modelling. Within a Monte Carlo simulation a statistical probability is assigned to every event, with the probability figure based on first principles and available experimental results. Multiple events are simulated until the process yields a statistically relevant result. Monte Carlo simulation, based on a conductive polymer using experimental data, has revealed that a material's local crystallinity and electron affinity directly influence the SE energy spectrum (16,17).

In addition to polymer analysis, further insightful work has been directed at carbon species analysis. The characteristic SE spectra of sp³ hybridised, sp² hybridised, or hydrocarbon contamination moieties captured using a combination of experimental studies and Monte Carlo based simulation has been published (18, 19). This result has enabled carbon based contamination and deposition induced by the electron beam within a SEM to be identified and mitigated. Through applied modelling simulations, significant advances in the appreciation of time dependence both in secondary electron emission (20) and in the charge dynamics of insulators (21) have been made.

2. Additional Results

2. A – Selecting the Region of Interest (ROI) for Phenolic Resin.

Figure SI 4 shows an example of the process used to select ROIs of phenolic resin samples for SES and SEHI analysis. After having been subject to flexural testing, spectra were collected from the centre of a cross-section area of P382 resin exposed as result of flexural testing (figure SI4 A). The red boxes within the figure show how by increasing the magnification the user can select the length scale of sample area they wish to analyse. The ability to perform multi-length scale analysis is one of the key advantages of using SES and SEHI. The material system is described in detail in Hamad et al (1).

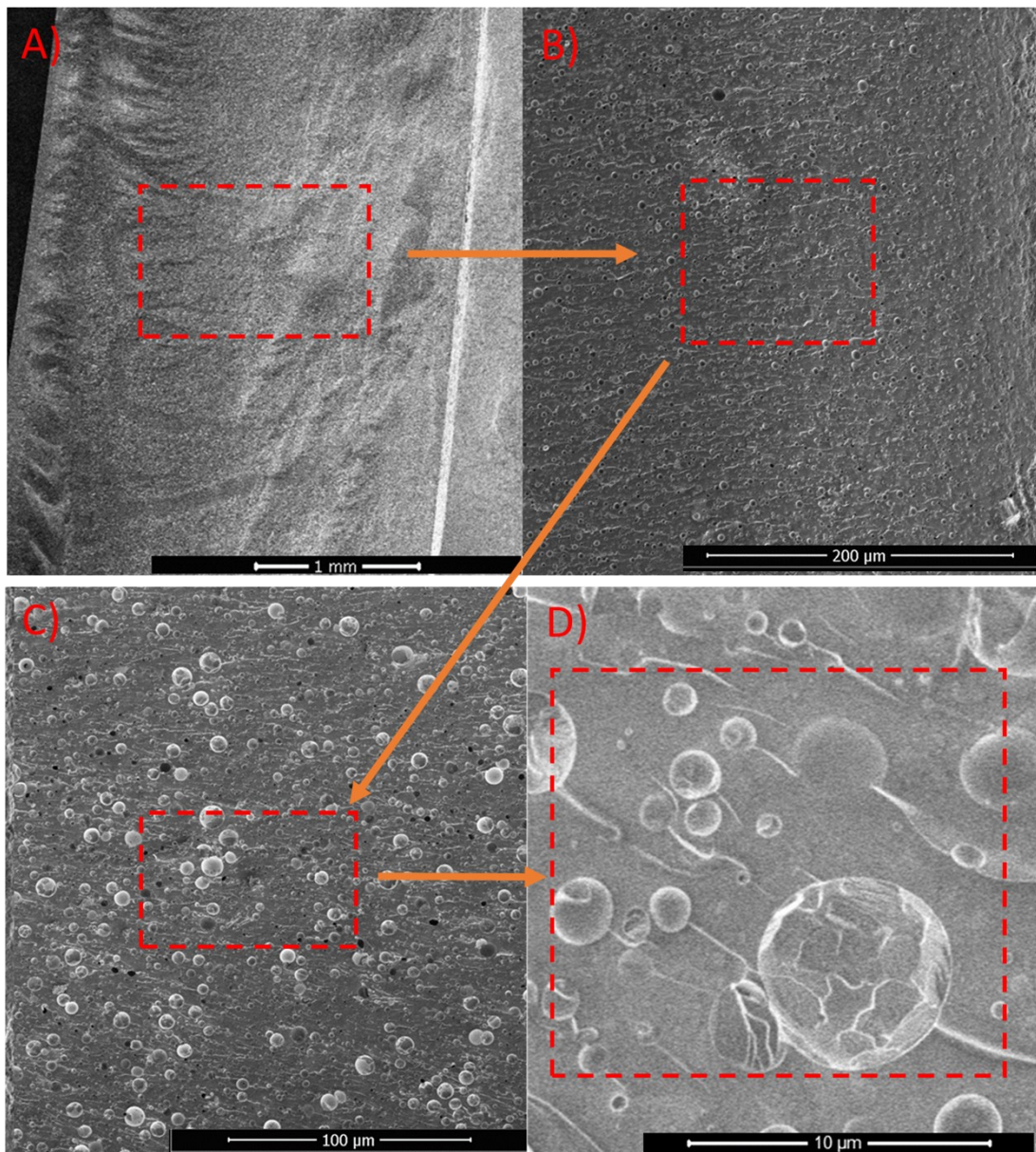


Figure SI 4 – A diagram showing the process of selecting a ROI within Phenolic resin prior to SES and SEHI analysis. Red boxed inserts show the process of enhancing magnification to allow the user to analyse a length scale of interest.

2.B - Secondary electron spectroscopy (SES) analysis of long cure phenolic resin.

Previous work has validated SES's ability to isolate chemical bonding and functional groups in a range of materials (22).

However, this is the first time such analysis has been conducted on phenolic resin. To corroborate the SES results described in the main manuscript an additional phenolic sample was included as a control sample. This control is a phenolic resin sample produced by the application of a long cure cycle, with the same F:P molar ratio as that of the Phenolic 382 used in this publication. The only difference between the two materials is that the control sample's long cure cycle does not employ a fast acting acid catalyst and consequently cures over a longer period of time and produces a void free material.

A comparison between phenolic 382 and a long cured phenolic resin (LCP) has previously been conducted in Hamad et al 2019 (1) study, there it was concluded that although a P832 cure time was substantially shorter than LCP, its flexural strength properties were significantly reduced, 88 MPa and 47 MPa respectively (1). Fourier Transform Infrared Spectroscopy (FTIR) measurements captured in this study showed that there was a reduction in ether bridges formation within phenolic resin cured using a fast action catalyst when compared to that of phenolic resin cured without such an acid catalyst. The paper stated that the more acidic the catalyst, the more the phenol is protonated and therefore the less nucleophilic it is (1). As a result, it is less likely that it will follow the crosslinking mechanism which forms ether bridges. Figure SI 5 displays a spectra comparison of the LCP control sample and the three areas of P382. Here, we observe the results are consistent with those given in the Hamad et al publication. The LCP control sample shows a greater molecular order peak emission (1.4 – 2.3 eV) and increased CH vibrations emissions (2.3 - 4.3 eV) compared to that of the PR832 sample areas. This result is expected as both an increase in crystallinity and methylene bridges (CH_x related) in the LCP sample would indeed create a material with greater flexural strength. A point of interest in the SES data is that the LCP does show more emissions are related to methylene bridge (CH) than ether bridge (CO) formation. This finding is predicted by the chemical crosslinking analysis described above and supports the proposition that an increasing ratio of acid catalyst inclusion would favour methylene bridge formation. When comparing CO functional group emission between LCP and areas of PR382 it is also noticeable that CO bonding is slightly less in LCP. This is also an expected result as even though ether bridges are still present in LCP they are not the anticipated prevailing method of crosslinking within this material.

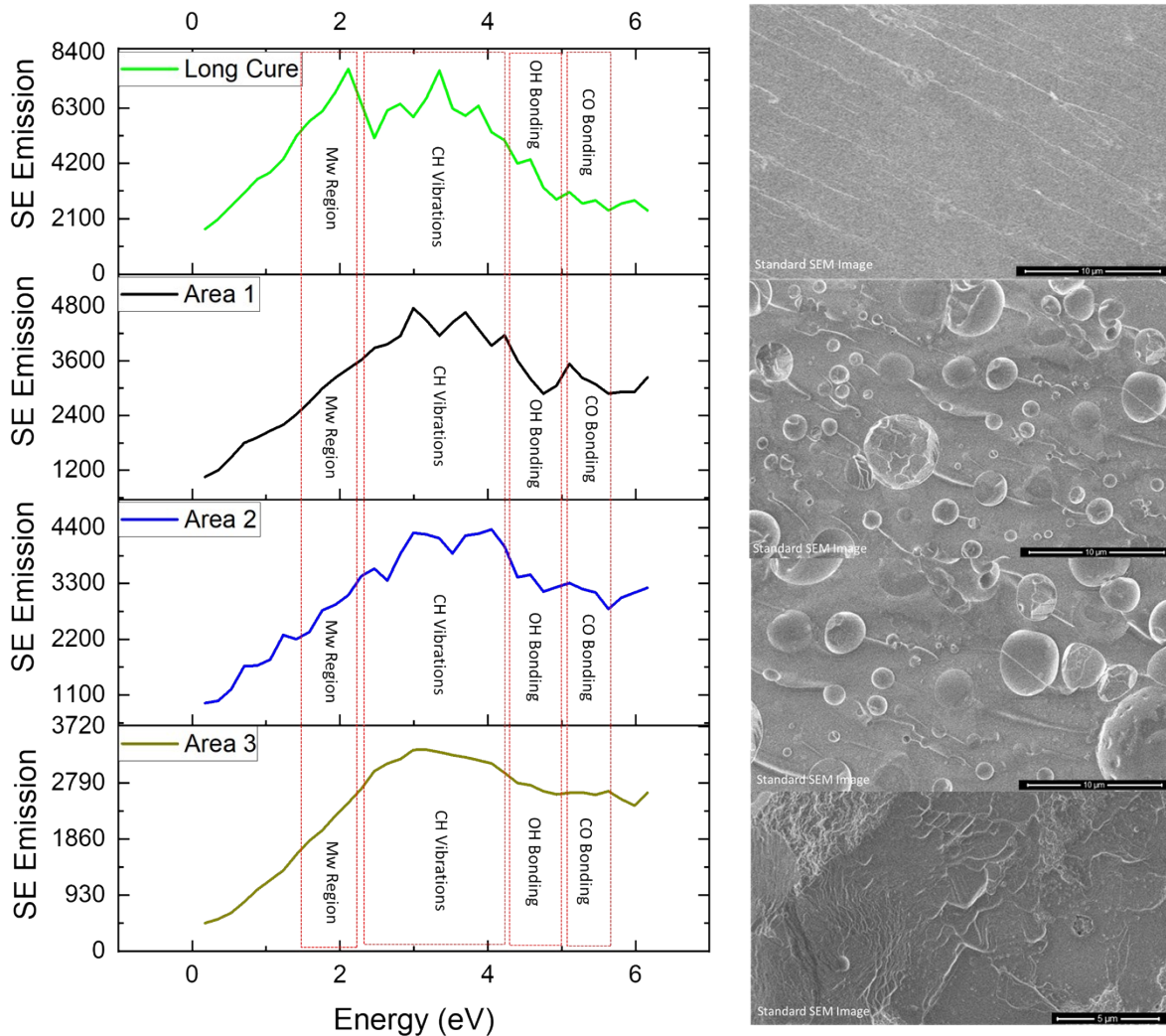


Figure SI 5 - Secondary electron spectra with accompanying SEM images for LCP (long cure) and PR382 Area 1, 2 and 3 highlighting SE regions identified as associated with functional group emissions. Area 1 & 2 HFW = 30 µm whereas Area 3 HFW = 25 µm.

2.C - Secondary electron spectroscopy (SES) energy calibration.

Prior to SE spectra capture it is good practise is to collect test spectra from known sample materials for the purpose of energy range calibration and assessment of the SEM environment conditions for SE collection. By virtue of SES high surface sensitivity it has been shown that surface contamination, often in the form of amorphous carbon, can produce emissions that are captured by SES and distort the resulting target materials spectra. The amorphous carbon can be present within the chamber of the SEM as a consequence of previous use prior to imaging or it can form on the surface of a test material as a product of the e-beam probe. Essential requirements for a control sample are to calibrate the SE energy ranges and also to have the ability through their SE spectra to highlight contamination indicators. For these purposes the authors recommend the use of highly oriented pyrolytic graphite (HOPG) as the energy calibration sample of choice. HOPG is a molecular ordered form of synthetic graphite (23). HOPG offers a calibration spectra, for collection accuracy, by observing background emission

peaks within a materials spectrum. Figure SI 6 gives an example of this calibration process by comparing the spectra of PR382 to that of the calibration HOPG material. With SEHI being shown to be effective in monitoring beam damage (19) the technique can therefore be utilised to avoid beam damage through an appropriate choice of frame integration and short dwell times. This study also evaluated SES's ability to characterise contributions of sp²-like or sp³-like bond types and amorphous hydrogenated carbon on HOPG surfaces (20). In such circumstances, we use HOPG to avoid contamination by regularly plasma cleaning the chamber and then monitoring sp² amorphous carbon build up within the HOPG spectra after prolonged exposure (19).

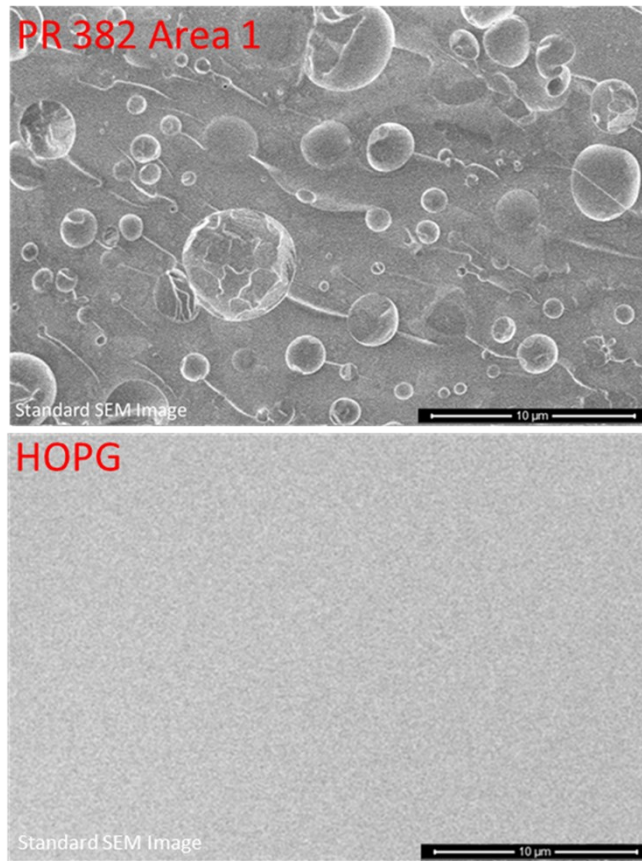
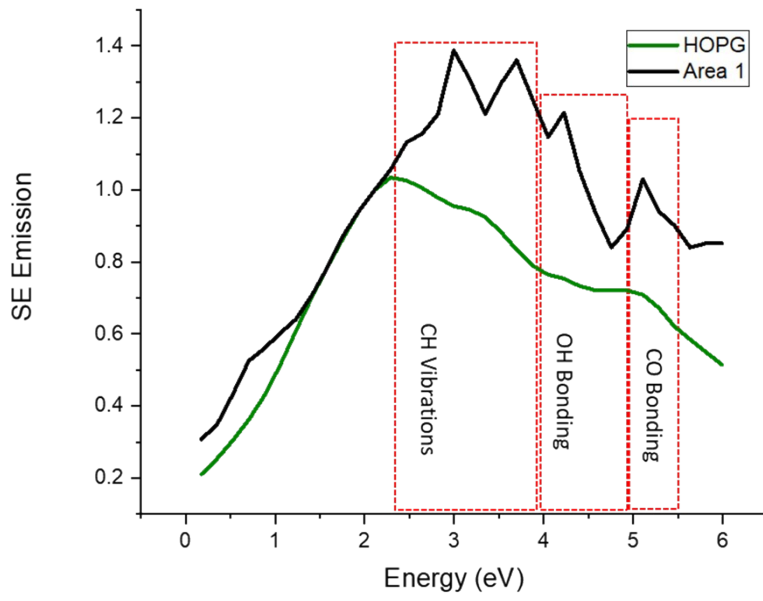


Figure SI 6 - Secondary electron spectra with accompanying SEM images for PR382 and HOPG. Spectra emission normalised to MW peak SE emission range. Spectra highlights SE regions associated with functional group emissions.

2. D - Observing the drying process of Carbon paint using SES.

In this investigation a dynamic experimental approach was designed to demonstrate the capabilities of SES to identify functional group changes over time within a material whilst within an SEM. The material selected for this experiment was a Carbon paint known as “Conductive graphite paint with isopropanol base” (Agar Scientific). Carbon paint is commonly used to attach a material of interest to an aluminium stub prior to SEM imaging. After the material of interest is positioned on the stub, Carbon paint is applied and the user waits for it to dry/set to bind the material to the stub. As the Carbon paint dries, the paint’s isopropanol base evaporates. In this study, carbon paint alone was applied to an aluminium stub and spectra were collected at regular time points as the carbon paint dried. The purpose behind the experiment was twofold; firstly, to analyse how long it takes for the paint to dry, which is useful information to SEM users in general, and secondarily as the paint dries and the isopropanol evaporates off the surface, to monitor the prevalence of functional groups (CO, OH and CH) which are predicted to gradually decrease over time as a consequence. Figure SI 7 displays SES spectra captured during this experiment which corroborate the experimental results with the predicted results. OH and CO functional groups were observed to greatly diminish as the carbon paint dried by the evaporation of isopropanol. After 30 minutes from commencement of the experiment the dried carbon paint, now purely graphite flakes, as expected provided spectra that was markedly similar to that of the HOPG spectra shown in figure SI 6.

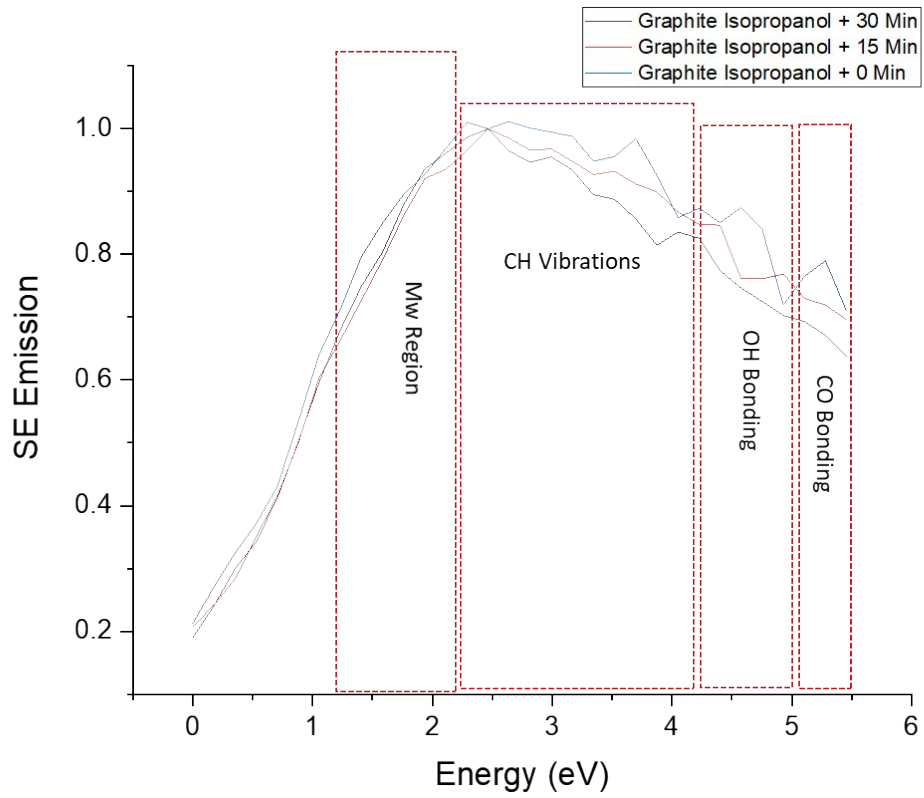


Figure SI 7 - Secondary electron for Graphite flakes in an Isopropanol base taken at different time points. Spectra emission was normalised to MW peak SE emission range. Spectra highlights SE regions associated with functional group emissions.

2. E - CH / CO / OH Mapping of Phenolic Void remnants.

Figure SI 8 displays component analysis of PR382. In this instance non-negative matrix factorisation (nnmf) isolated three major components between 2 – 6 eV; firstly a component around 3.2 eV, highlighted in the text as CH vibrations, a second component peak at 4.5 eV related to CO bonding and lastly a component peak around 5.5 eV related to OH groups. The images displayed in figure SI1 reflect the spatial variation in components 1, 2 and 3 in response to void like macrostructures. These images provide further support for the view that CO bonding is apparent with greater emission within the void sites than when compared to either CH or OH.

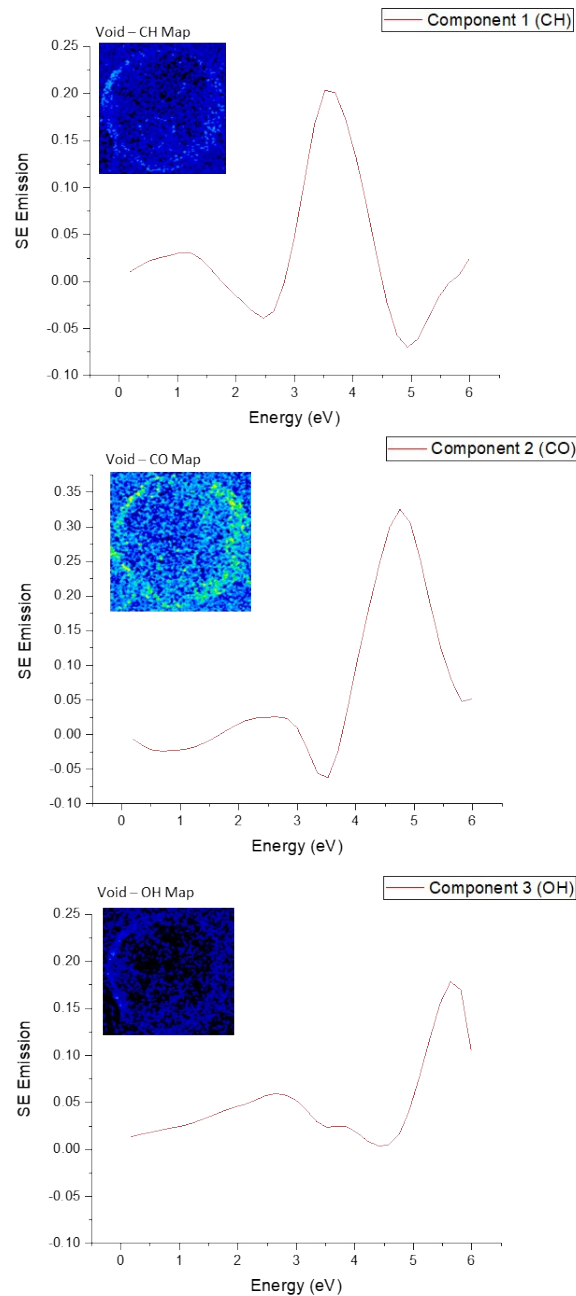


Figure SI 8 - Non negative matrix factorisation (nnmf) multivariate analysis of PR382. Isolating three components: component 1 is associated with CH Vibrations, component 2 is associated with CO bonding and component 3 is associated with OH groups. Each spectrum includes an inset of the resulting void images from nnmf component analysis (HFW = 3 μ m).

2. F - Nanoindentation

Figure SI 9 shows the measured modulus obtained through nanoindentation mapping with a KLA Tencor NanoG200. Using a diamond Berkovich tip at a load of 0.02 mN, corresponding to an average depth of approximately 150 nm, the map was collected with an indent spacing of 0.9 μm . Care must be taken when considering the values reported: the absolute values have been calculated through a proprietary method which has been shown to produce variable data. Furthermore, this dataset is collected with a relatively low load, owing to the requirement to space the indents in close proximity to one another. The capacity of the mapping method to accurately collect data at such loads has not been tested. Finally, the specimen is known to contain scratches throughout the surface. Considering these caveats, the data can be used speculatively to compare the relative modulus from pixel to pixel. In this respect, the variability shown arises from a combination of surface effects and fundamental material behavioural change from the presence of ether bridges.

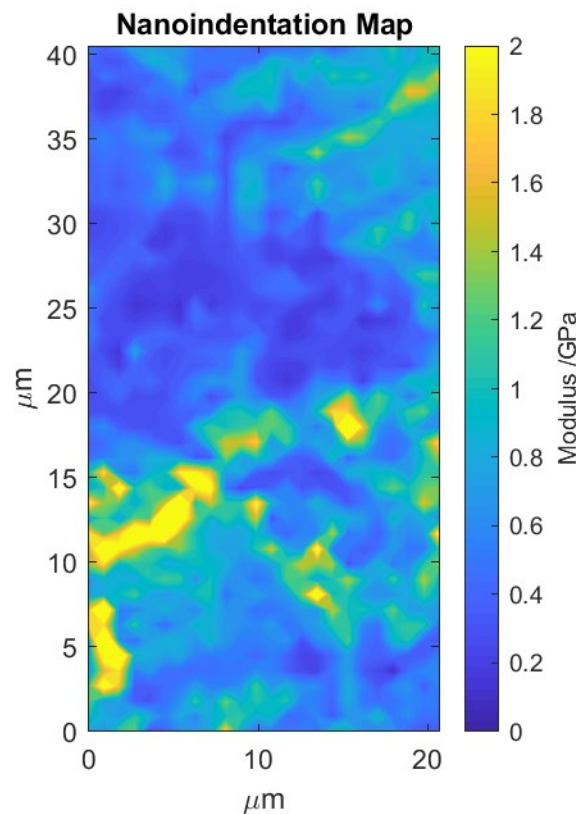


Figure SI 9 – Nanoindentation mapping of Phenolic Resin P382. Nanoindentation modulus measured through nanoindentation mapping with a KLA Tencor NanoG200. Using a diamond Berkovich tip at a load of 0.02 mN, corresponding to an average depth of approximately 150 nm, the map was collected with an indent spacing of 0.9 μm .

3. More detailed methodology background

3.A Selection of suitable component analysis method

An example data set that analysed phenolic resin was used to highlight the selection of the component analysis methodology. In this instance a 5 component analysis was selected for review. Component Analysis is used to determine the spectrum distribution of components in the material. In Fig SI 10, the spectrum plot of five (5) components is shown. Two methods are utilised to compare their performances in the component analysis. Firstly, the Principal Component Analysis (PCA) that aims to reduce the dimensionality of the data (stack of hyperspectral SEHI image) in an interpretable (components) way. It achieves this by preserving the information of the data within the components and clustering positive and negative correlated components together. PCA assumes that the components are a linear combination of features and therefore, concentrates these features within the first component of the data as shown in Fig SI 11. Additionally, we notice large variance axes in the first component, while areas of low variance axes are treated as noise with little information in subsequent components especially in components 3 and 4. The orthogonality assumption of PCA implies that spectrum is only concentrated in the first component of the analysis. On the other hand, the Non-Negative Matrix Factorization (NNMF) method preserves the spatial information of extracted components that corresponds to the structural differences in the components, hence retaining the global structure of the material. It achieves this by allowing only additive (positive) correlated combinations this enables an intuitive representation of the data since each component form a part of the data (see Fig SI10).

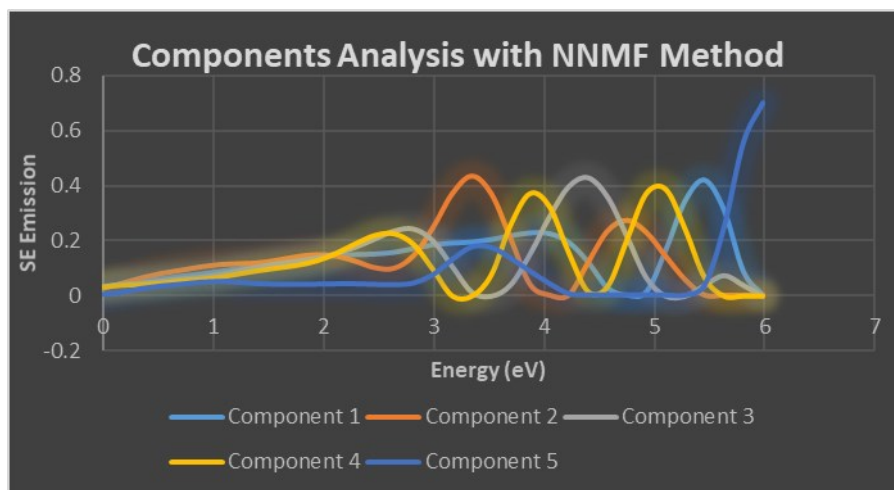


Figure - SI 10 FIVE COMPONENT ANALYSIS USING THE NON-NEGATIVE FACTORIZATION METHOD

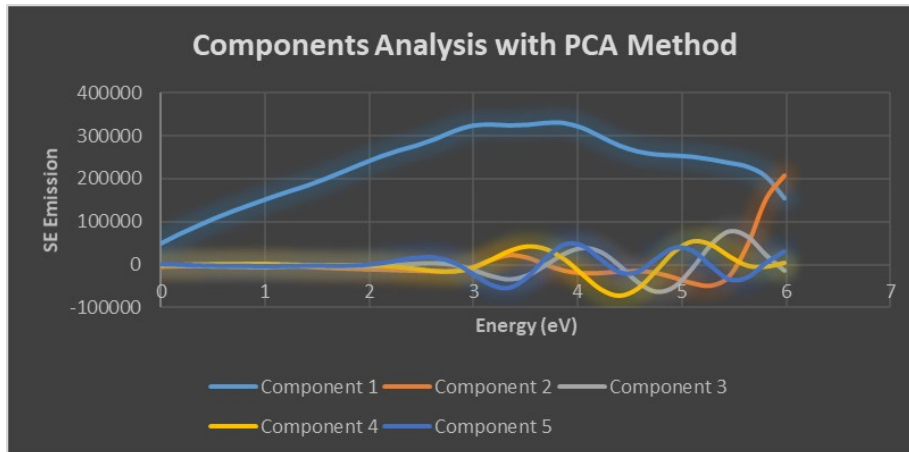


Figure SI 11 - FIVE COMPONENT ANALYSIS USING THE PRINCIPAL COMPONENTS ANALYSIS METHOD

The above analysis shows that the NMF performs better when dealing with SEHI image stacks due to its ability to efficiently extract features that are only positively correlated which ensures that both spatial and structural information are retained. Additionally, this non-negativity nature of NMF improves result interpretation and precision.

4. Graphical Abstract

Figure SI S12 displays the graphical abstract for this publication.

“Secondary Electron Hyperspectral Imaging (SEHI) is an innovative SEM-based analysis tool allowing spatially-resolved chemical analysis beyond elemental composition.”

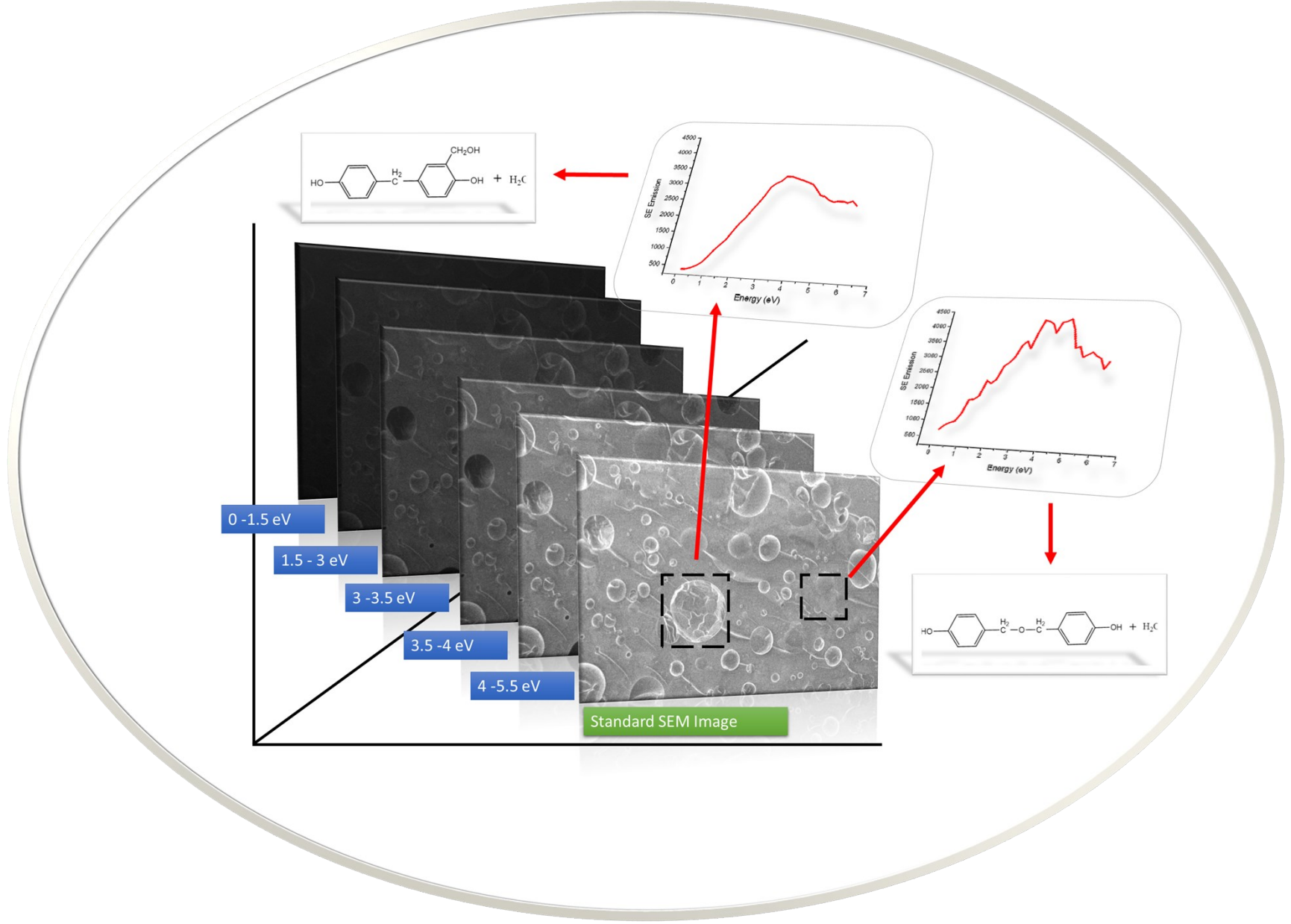


Figure SI 12.

References

1. S. Hamad, N. Farr, T. Fei, N. Shukor, J. Dean, S. Hayes, J. Foreman, C. Rodenburg, Optimizing size and distribution of voids in phenolic resins through the choice of catalyst types. *J. Appl. Polym. Sci.*, 2019, 136, 48249.
2. Z. Wang *Elastic and Inelastic Scattering in Electron Diffraction and Imaging* (Plenum Press, 1995)
3. W. Zhou, R. P. Apkarian, Z. L. Wang, and D. C. Joy, "Fundamentals of Scanning Electron Microscopy," in *Scanning Microscopy for Nanotechnology*, W. Zhou and Z. L. Wang, Eds. New York, NY: Springer New York, 2006, pp. 1–40.
4. Q. Wan "Angle selective backscattered electron contrast in the low-voltage scanning electron microscope: Simulation and experiment for polymers," 2016. *Ultramicroscopy*, vol. 171, pp. 126–138
5. M. Suga, S. Asahina, Y. Sakuda, H. Kazumori, H. Nishiyama, T. Nokuo, V. Alfredsson, T. Kjellman, S. M. Stevens, H. S. Cho, M. Cho, L. Han, S. Che, M. W. Anderson, F. Schüth, H. Deng, O. M. Yaghi, Z. Liu, H. Y. Jeong, A. Stein, K. Sakamoto, R. Ryoo, O. Terasaki. Recent progress in scanning electron microscopy for the characterization of fine structural details of nano materials. 2014. *Progress in Solid State Chemistry*. 42, 1–2.
6. J. Goldstein. *Scanning Electron Microscopy and X-Ray Microanalysis*, 3rd Edition. Springer, 2003.
7. T. Everhart and R. F. M. Thornley. "Wide-band detector for micro-microampere lowenergy electron currents," 1960. *J. Sci. Instrum.*, vol. 37, no. 7, pp. 246–248.
8. P. Kazemian, S. A. M. Mentink, C. Rodenburg and C. J. Humphreys, "Quantitative secondary electron energy filtering in a scanning electron microscope and its applications," *Ultramicroscopy*, vol. 107, no. 2–3, pp. 140–150, 2007.
9. V.R. Kollafh, Zur Energieverteilung der Sekundarelektronen :I. 1947 Mepergebnisse und Diskussion
10. D.C. Joy, M.S. Prasad, and H.M Meyer, III. Experimental secondary electron spectra under SEM conditions. 2004. *Journal of Microscopy*, 215: 77-85.
11. Q. Wan, K. J. Abrams, R. C. Masters, A. C. S. Talari, I. U. Rehman, F. Claeysens, C. Holland, C. Rodenburg, *Adv. Mater.* 2017. 29, 1703510.
12. J. A. Venables, D. R. Batchelor, M. Hanbucken, C. J. Harland and G. W. Jones. *Surface Microscopy with Scanned Electron Beams*. 1986. *Philosophical Transactions of the Royal Society of London. Series A, Mathematical and Physical Sciences*, Vol. 318, No. 1541.
13. A. Khursheed. *Secondary Electron Energy Spectroscopy in the Scanning Electron Microscope*. World Scientific Publishing Co Pte Ltd. ISBN: 9789811227028.
14. V. Kumar, W.L. Schmidt, G. Schileo, R.C. Masters, M. Wong-Stringer, D.C. Sinclair, I.M. Reaney, D. Lidzey and C. Rodenburg: Nanoscale Mapping of Bromide Segregation on the Cross Sections of Complex Hybrid Perovskite Photovoltaic Films Using Secondary Electron Hyperspectral Imaging in a Scanning Electron Microscope. *ACS Omega* 2, 2126 2133 (2017).
15. R. C. Masters, A. J. Pearson, T. S. Glen, F.-C. M. Sasam, L. Dapor, Li. A. M. Donald, D. G. Lidzey, C. Rodenburg, *Nat. Commun.* 2015. 6, 6928
16. M. Dapor, R.C. Masters, I. Ross, D.G. Lidzey, A. Pearson, I. Abril, R. Garcia-Molina, J. Sharp, M. Unčovský, T. Vystavel, F. Mika and C. Rodenburg: "Secondary electron spectra of semicrystalline polymers – A novel polymer characterisation tool?" *J. Electron Spectros. Relat. Phenomena* 222, 95–105 (2018), doi:10.1016/j.elspec.2017.08.001.
17. R.C. Masters, N.A. Stehling, K.J. Abrams, V. Kumar, M. Azzolini, N.M. Pugno, M. Dapor, A. Huber, P. Schäfer, D.G. Lidzey and C. Rodenburg: Mapping Polymer Molecular Order in the SEM with Secondary Electron Hyperspectral Imaging. *Adv. Sci.* (2019).

18. M. Azzolini, T. Morresi, K. Abrams, R. Masters, N. Stehling, C. Rodenburg, N.M. Pugno, S. Taioli and M. Dapor: An Anisotropic Approach for Simulating Electron Transport in Layered Materials: Computational and Experimental Study of Highly Oriented Pyrolytic Graphite, 2018), doi:10.1021/acs.jpcc.8b02256.
19. K.J. Abrams, M. Dapor, N. Stehling, M. Azzolini, S.J. Kyle, J.S. Schäfer, A. Quade, F. Mika, S. Kratky and Z. Pokorna: Making Sense of Complex Carbon and Metal/Carbon Systems by Secondary Electron Hyperspectral Imaging. *Adv. Sci.* 1900719 (2019).
20. C. Li, S.F. Mao and Z.J. Ding: Time-dependent characteristics of secondary electron emission. *J. Appl. Phys.* 125, 24902 (2019), doi:10.1063/1.5080264.
21. C. Li, S.F. Mao, Y.B. Zou, Y.G. Li, P. Zhang, H.M. Li and Z.J. Ding: A Monte Carlo modeling on charging effect for structures with arbitrary geometries. *J. Phys. D: Appl. Phys.* 51 165301 (2018), doi:10.1088/1361-6463/aab2cf.
22. N.Farr et al – Understanding surface modifications induced via Argon Plasma sterilisation through Secondary Electron Hyperspectral Imaging. Accepted at *Adv Sci*. Submitted April 2020.
23. L. C. F. Blackman, A. R. Ubbelohde (1962). "Stress Recrystallization of Graphite". *Proceedings of the Royal Society of London. A*266 (1324): 20–32.

6. Conclusions and Future Work

It is widely accepted that a key enabler for the development of more effective biomaterials for clinical use is the ability of researchers to gain a greater understanding of the chemical, structural and topographical characteristics of the material. To be successful, any newly developed material characterisation technique is expected to offer new insights into one or more of these characteristics, ideally at a range of scales, including the nanoscale. The literature review presented in chapter 2 revealed a “gap” exists in currently available characterisation techniques, where none are capable of providing nanoscale surface chemical mapping of polymers used for TE. The leading requirement for such a technique in respect to biomaterials development is primarily due to the specific relationship between cellular adhesion and the surface properties (< 10 nm) of the material.

In this thesis, to evaluate the potential significance of the SEHI technique an extensive range of novel and advanced characterisation techniques were applied to characterise polymer-derived biomaterials, all of which had previously undergone various surface modification treatments. A wide range of polymers were also selected for analysis to allow for a broad range of polymer systems within which to evaluate SEHI's application, these included: PGS-M, Polycaprolactone (PCL), Nylon, Polypropylene, Polyvinylidene fluoride and Phenolic Resin. The publications presented in this thesis in chapters 3-5

highlight evaluations of the experimental application of SEHI. These publications not only demonstrated the unique capabilities of SEHI in the field of material characterisation but also provided evidence attained from established characterisation techniques (EDX, EELS, XPS, Raman, AFM) to corroborate the finding that SEHI is capable of delivering chemically mapping at the nanoscale. This multiscale approach included the ability to identify and evaluate the chemical functional groups within nano-structural features found at the surface of polymer derived biomaterials.

Two key questions were identified as part of the literature review in chapter 2, regarding the future use of SEHI for the characterisation of polymer derived biomaterials:

- 1) Can SEHI deliver insights into the mechanical properties of a biomaterial?
- 2) Is the captured SE spectra able to identify specific functional groups that play a key role in biomaterials engineering /TE? And if so can SEHI map these functional groups at the nanoscale?

Table 2: summarises the answers to the questions based on the publications presented in chapter 3-5.

<p>Question 1: SEHI deliver insights into the mechanical properties of a biomaterial?</p>	<p>Question 2: Is the captured SE spectra able to identify specific functional groups that play a key role in biomaterials engineering /TE? And if so can SEHI map these functional groups at the nanoscale?</p>
<p>Chapter 3 - Chapter 3 tackled the question by evaluating the efficacy of SES by revealing new insights into the mechanical properties of PGS-M morphology. Chapter 3 was the first publication to show secondary electron spectroscopy (SES) being used to characterise crosslinking in polymer derived biomaterials. Characterisation of three different forms of PGS-M with different crosslinking was successfully conducted. Here SES provided a cross-linking characterisation toolset with crosslinking density and variation captured at a multi-scale level. Prior to this publication the magnitude of crosslinking within a biomaterial could only be inferred through limited analytical techniques with traditional approaches for measuring the extent of crosslinking based on bulk mechanical averaging techniques.</p> <p>SES showed the capacity to overcome these limitations by providing the means to identify the bonding (CHx) associated with crosslinking within PGS-M together with the unique ability to distinguish spatial distributions of this bonding across the polymers surface. This result was the first time SES had been shown to be capable of predicting and evaluating indirectly the mechanical properties of a polymer.</p> <p>Chapter 4 - further progressed the work presented in chapter 3 by modifying the surface of PGS-M using Ar plasma treatment. SEHI data and nanoindentation measurements identified that Ar plasma treatment significantly increased the stiffness of PGS-M samples due to crosslinking. SEHI produced maps of CO bonding, for the first time suggested that surface structures of PGS-M varied locally and can be changed depending on Ar treatment time. SES provided a toolset that delivered crosslinking density and variation at the nanoscale.</p>	<p>Chapter 3 - was the first publication to identify SE emission of a chemical functional group. SES provided the means to identify the bonding (CHx) associated with crosslinking within PGS-M together with the ability to distinguish spatial distributions of this bonding across the polymers surface.</p> <p>Chapter 4 - Furthering chapter 3, the SEHI technique facilitated the capture of a number of key insights into the sample's electron emission properties leading to the identification of their chemical functional groups (C-H, C-O, C-C, O-H). This consequently resulted in the establishment of high resolution chemical imaging. The publication showed for the first time such chemical imaging was capable of being produced using SEHI and also provided evidence of its potential to reveal key insights into the biocompatibility of the biomaterials analysed.</p> <p>The publication focused on characterising the effects on the biomaterial samples of different conditions of Argon Plasma treatment when compared to the known industry standard of Autoclave sterilisation. The experimental process followed during this work exploited a range of analysis techniques, including the pioneering use of SEHI. This was an exciting development for SEHI as it delivered for the first time the ability to isolate functional groups on the surface of biomaterials, in addition to its novel capacity to map them at the nanoscale.</p> <p>The publication presented in chapter 4 also analysed a range of polymers with different functional group distributions. These included; PGS-M, PCL, PCL-M, Nylon 6 and polypropylene. All the materials apart from polypropylene were imaged as a flat (rough) surface and SES/SEHI had no issues imaging or mapping their surfaces chemically. Polypropylene analysis was the first time SES/SEHI mapping had been conducted on a fibre</p>

Chapter 5 – SEHI revealed local variations in crosslinking and molecular order across Phenolic Resin. This was the first time SES or SEHI was applied to thermoset, highly cross-linked networks. Presented SEHI analysis and related SE spectra provided compelling evidence that a greater prevalence of C–O bonding exists in close proximity (~50 nm) to void sites than the typical distribution observed within the matrix. This result can be explained to be the consequence of an increased incidence of ether bridges observed at such void sites. Based on the demonstrated capability, SEHI is considered to be an ideal analysis tool with the capacity to isolate local variations in chemical bonding which have a direct relation to the mechanical properties of phenolic resin.

shaped material with differing surface angles. Despite this challenge SES analysis was successfully performed and reliable mapping data of Polypropylenes surface functional groups distributions was collected.

Chapter 5– Chapter 5 applies the findings from chapters 3 and 4 to a different materials system for further evaluation. SEHI images overlaid on standard SEM images showed for the first time the distribution of CO bonding within Phenolic resin. In this publication SEHI mapped CHx CO and OH functional groups providing a better understanding of the functional group distribution existing around phenolic resin void sites.

Overall the analysis results, based on a wide range of biomaterials, captured by the SEHI toolset combination has made a persuasive argument for establishing the toolset as a highly effective and innovative option for polymer characterisation. It is anticipated that the research published during the completion of this thesis will assist researchers to target and accelerate fresh developments in the search for effective biomaterials by offering new insights into the composition and structure of material systems. The author is confident that the novel advanced characterisation approach provided by SEHI will be of value in the characterisation of multiscale polymers and complex chemical structures undertaken by researchers from many disciplines. It is further considered that the development of advanced polymeric materials, can only be efficiently achieved with the development of correspondingly advanced characterisation techniques.

Future work

At this stage of development, researchers have the option to take the future development and application of SEHI in many different paths, the authors own recommendation would be to consider three different avenues. Firstly, to conduct research directed at further development of the SEHI material characterisation techniques such that they will advance their ability to be applied to a broader range of material systems and also to facilitate SEHI's potential for ground-breaking investigative research within specific materials. As highlighted above, further work is required to help develop SEHI to become a more complete and accessible material characterisation tool. It has been

shown that the SE spectra are reflected from the surface properties of a range of biomaterials, therefore, an appropriate starting point for future investigations in to SE spectroscopy is a larger comparison study employing a wider set of organic biomaterials in combination with conventional methods for probing polymer structures such x-ray photoelectron spectroscopy. Having previously shown in papers published that focus on biomaterials and phenolic resin, the author is particularly interested and indeed excited about the opportunity for SEHI to be used to characterise other polymers and potentially further research into using SEHI to study inorganic material systems. To achieve this a set of reference samples would be required to be selected and undergo bulk SES and SEHI analysis in order to build a database of material signatures.

The second area of interest would be to add to the current body of research evaluating how cells react to polymer surfaces. Currently, a significant constraint of using SEHI to evaluate biomaterials is that of the material is not able to incorporate living cells at the time of imaging. Possessing the ability to take SEHI maps of the behaviour of live cells on material surfaces would be a significant step forward in our ability to observe cell/surface interaction of time periods. Using the SEHI material surface penetration capability could theoretically facilitate the capture of images 'through the cells' and capture local chemical information of the surface structures that the cells adhere too. However, such a novel process would not conventionally be possible as SEM's require samples to be placed within high vacuum conditions which would not sustain cellular life. However, recent advancements have led to the development of a thin barrier layer (TBL) which holds moisture on the surface

of a polymer which protects cells that have been cultured on a biomaterial and allows them to survive for a time period within the SEM's high vacuum conditions. Together with SEHI and this new coating advancement this approach is considered a prime opportunity to showcase the novel and precise material characterisation capabilities possible when the SEHI technique is applied to a polymer system. Additionally, utilising a TBL solution will also offer the opportunity of a step forward for SEHI development by facilitating direct SEM observation of live cells. This development would provide an insightful ability to better understand the interactions between cells and biomaterials at a scale of analysis previously not possible.

The third area of future work would be to consider integrating the SEHI technique with an oxygen plasma FIB-SEM (O-PRFIB) approach to produce a 3D chemically sensitive characterisation ability. This future work could lead to the establishment of a combined toolset that is potentially capable of providing compelling new insights in materials characterisation with the prospect of developing a wide range of more effective materials. An initial assessment study has raised confidence that SEHI and the O-PRFIB have complimentary capabilities and it is feasible that through integration they could develop into a highly effective single instrument to perform enhanced 3D chemically sensitive characterisation which is optimised for biomaterial applications.

7. Supporting Information

Appendix 1.

Selected Conference presentations:

2019

Insigneo Showcase 2019, Sheffield, UK, May 2019, conference poster presentation

Microscience Microscopy Congress 2019, Manchester Central, UK. Abstract accepted for Flash talk and Poster presentation.

Engineering Researcher Symposium, Sheffield, UK 2019. Abstract accepted, poster presented.

Multiscale Innovative Materials and Structures 2019, Salerno, Italy. Abstract and accepted for 20 minute oral presentation.

PicoFIB workshop 2019, UCL London. Abstract and accepted for 20 minute oral presentation.

2020

Nanobrucken 2020, Max Planck Institute, Germany, Abstract and accepted for 20 minute oral presentation.

European Microscopy Congress 2020, Copenhagen, Abstract and accepted for 20 minute oral presentation.

Appendix 2.

Prelude

Prior to the publication of the paper presented in chapter 5, the author of this thesis co-authored the publication “Optimizing size and distribution of voids in phenolic resins through the choice of catalyst types” This publication laid the groundwork for the development of the fast acting resin investigated within chapter 5. In Hamad *et al*, investigation of the chemical bonding present within the newly developed phenolic resin was conducted by bulk chemical averaging methods and did not provide information of the chemical bonding variation existing within the material. This analysis limitation was overcome in the results presented in chapter 5.

“Optimizing size and distribution of voids in phenolic resins through the choice of catalyst types.”

Sameer F. Hamad,(1,2) Nicholas Farr,(1) Teng Fei,(1) Nur F. Shukor,(1) Julian S. Dean,(1) Simon A. Hayes,(3) Joel P. Foreman,(1) Cornelia Rodenburg (1)


1. Department of Materials Science and Engineering, The University of Sheffield, Sheffield S1 3JD, UK
2. College of Engineering, University of Misan, Maysan 62001, Iraq
3. Department of Multidisciplinary Engineering Education, The University of Sheffield, Sheffield S3 7RD,

July 2019 Journal of Applied Polymer Science 136(47):48249

DOI: 10.1002/app.48249

License: CC BY 4.0

Optimizing size and distribution of voids in phenolic resins through the choice of catalyst types

Sameer F. Hamad ^{1,2}, Nicholas Farr,¹ Teng Fei,¹ Nur F. Shukor,¹ Julian S. Dean,¹ Simon A. Hayes,³ Joel P. Foreman,¹ Cornelia Rodenburg¹

¹Department of Materials Science and Engineering, The University of Sheffield, Sheffield S1 3JD, UK

²College of Engineering, University of Misan, Maysan 62001, Iraq

³Department of Multidisciplinary Engineering Education, The University of Sheffield, Sheffield S3 7RD, UK

Correspondence to: S. F. Hamad (E-mail: sfhamad1@sheffield.ac.uk or sfhamad3@gmail.com)

ABSTRACT: Phenolics are widely used for over a century in different industries due to their chemical resistance and thermomechanical properties. However, the presence of voids in phenolic resins has negative effects on the mechanical properties and a conventional approach is to avoid these by utilizing very long cure cycles. Our alternative approach investigates the tailoring of void size and distribution to achieve a better balance between processing time and mechanical properties. Therefore, we produced phenolic resin with a void-free microstructure by a long cure cycle as a reference. To alter the void size and distributions, we utilized different catalysts and a short cure cycle to obtain phenolic resins and test their flexural properties with respect to the reference. We investigated the fracture surfaces of all materials by SEM, FTIR and compared results to finite element modeling that confirmed the effects of different void size and distributions on the mechanical properties. © 2019 The Authors. *Journal of Applied Polymer Science* published by Wiley Periodicals, Inc. *J. Appl. Polym. Sci.* **2019**, *136*, 48249.

KEYWORDS: mechanical properties; microscopy; morphology; porous materials; thermosets

Received 28 April 2019; accepted 2 June 2019

DOI: [10.1002/app.48249](https://doi.org/10.1002/app.48249)

INTRODUCTION

Phenolics or phenol-formaldehyde resins are amongst the oldest thermosetting polymers, with excellent ablative properties, low smoke density, high chemical resistance, and thermal stability.^{1–5} Such resins have been used in a broad range of applications such as molding compounds, thermal insulation materials, coatings, laminates, wood products industry, and structural adhesives,^{6,7} and most of all as light weight foams in aerospace applications.^{8,9} Furthermore, phenolics are also utilized as a matrix material for composite applications in the sport and construction industries due to their capability of withstanding highly corrosive environments.¹⁰ However, it might be seen surprising even nowadays phenolic resins still suffer from the slow crosslinking rate and the high curing temperature.¹¹ Moreover, the mechanical properties of phenolic resins can be compromised by porosity and how to control it to a desired level still poses a scientific and industrial challenge.¹² The reason for this is the long and complex polymerization process together with the generation of water and formaldehyde as by

products. Void-free phenolic parts usually require long heating cycles,¹³ thus not only taking a long time to produce but their production is also energy intensive. Here, we investigate how to minimize any loss in mechanical properties as a consequence of implementing a short curing cycle.

Phenolic resins are produced from the polycondensation reaction of the phenol and formaldehyde. Based on the formaldehyde/phenol molar ratios and curing properties, phenolic resin is characterized into two main categories: novolac and resole resins.^{14–16} Generally, both cured phenolic resin types (novolac and resole) are almost identical in terms of mechanical properties and chemical resistance.¹⁷ Novolacs are synthesized in the presence of an acid catalyst with an excess of phenol and do not react further without a curing agent. Hence, to produce a crosslinked structure of novolac resin, curing agents such as hexamethylenetetramine (HMTA) must be added.¹⁷ However, the resin of interest for liquid molding is resole resin.¹⁶ Resoles are prepared in the presence of an alkaline catalyst with an excess of formaldehyde, producing a soluble and

Additional Supporting Information may be found in the online version of this article.

© 2019 The Authors. *Journal of Applied Polymer Science* published by Wiley Periodicals, Inc.

This is an open access article under the terms of the Creative Commons Attribution License, which permits use, distribution and reproduction in any medium, provided the original work is properly cited.

fusible prepolymer. Resole structures contain reactive hydroxymethyl groups and by heating, a crosslinked structure can be produced.¹⁷

During the crosslinking of the phenol-formaldehyde resin, the release of the by-products becomes very difficult as the resin viscosity rises.¹⁸ Consequently, the presence of these by-products in the cured resin can lead to porosity in the form of macro¹³ or microvoids (8–10 μm in size),¹⁶ which adversely affects the mechanical properties of the final cured resin.¹⁶ However, it has been reported that phenolic resin with void-free microstructures could be produced if the gelation time is kept long enough for the water vapor to be released.^{13,19} This approach requires a very long heat cure cycle, which is not favorable for most industries due to time and energy consumption issues. Therefore, there have been many attempts to accelerate the crosslinking rate of the phenolic resins with the use of different curing agents^{20–23} but in each case, the formation of voids cannot be avoided.

No existing approaches allow void-free microstructures to be achieved with a short cure cycle, therefore, a novel approach to optimize the microvoids size and distribution in a fast curing process for better mechanical properties at minimum processing time is proposed as an alternative. This investigation is inspired by the observation that in phenolic foams with deliberately high void volumes, the void diameter and distribution do affect the mechanical properties in a way that is not predicted by any current models.²⁴ Not only the void volume fraction but void diameter and void distribution were empirically found to be of importance in determining the final mechanical properties. However, the void size distributions (100–450 μm) obtained in phenolic foams²⁵ are significantly larger than those in phenolics intended as bulk materials or as matrix for composite materials. For the latter group of materials, few studies have considered the effects of the void size and distribution on the final mechanical properties of the cured phenolic resins.²⁶ Most studies have focused on the investigation of the effects of formaldehyde/phenol (F/P) molar ratios,^{27–29} reaction conditions (temperature and time),²⁶ degree of condensation,³⁰ catalyst concentrations,²⁶ and catalyst type³¹ on the final properties of the cured resins. Here, we investigate the possibility of changing the catalyst type to tailor void size and distributions in order to enable fast resin curing, while minimizing the effect of voids on the mechanical properties in comparison to the reference sample.

The objective of this study is to investigate the optimum void size and diameter distribution as well as the spatial distribution of the voids in the phenolic produced in a fast curing process and compare their mechanical properties to a void-free reference phenolic. To this end a cross-linked resole phenolic resin material was produced using a long cure cycle (4 days) without the use of a catalyst. A slow action acid catalyst (Phencat 382) and a fast action acid catalyst (Phencat 10) were then utilized to produce two phenolic resin samples types with varying void sizes and distributions and mechanical properties (strength and modulus obtained from bending tests). To visualize and quantify detailed void structures, diameters and distributions, low voltage scanning electron microscopy (LV-SEM) was used to image the fractured surface of the above three types of cured phenolic resin. The latter enables the observation of highly localized variation in chemistry and crack behavior. To account for the effects introduced by the variation of average chemical composition all of the cured phenolic resins were subject to analysis by Fourier transform infrared (FTIR).

EXPERIMENTAL

Materials

In this study, a resole commercial phenolic resin called Cellobond J2027X was used (kindly supplied by Caleb Technical Products Ltd., UK). This kind of resin is usually available as a water-based controlled-viscosity resin, which can be cured either with the application of heat only (long cure cycle) or at lower temperature (60°C), short cure cycle (3 h), with the use of a strong acid catalyst.¹⁶ It is suitable for the fabrication of fiber composites by hand layup and resin transfer molding.³² Two types of catalyst (Cellobond Phencat 382 and Cellobond Phencat 10) supplied by the same company (Caleb Technical Products Ltd., UK) were used in this study. Phencat 382 is a relatively slow action acid catalyst (working life 4 h), which is activated at low temperature, typically 60–80 °C.¹⁶ It is an acid-based catalyst consisting of phosphoric acid, C3-9-alkyl esters (75–90%), and phosphoric acid (10–25%) by weight. Phencat 10 is a general purpose catalyst for processes such as contact molding giving working life of about 20 min. It is a composition consists of p-toluenesulphonic acid (35–50%) and phosphoric acid (10–25%) by weight.

Curing Process of Commercial Resole Phenolic Resin

Two different curing schedules were used to cure the resole phenolic resin:

- 1-. Long cure cycle, the as received resole phenolic resin was poured into a PTFE mold and then placed in an autoclave to be cured using the cure cycle as shown in Figure 1.
- 2-. Short cure cycle, the resole phenolic resin was first mixed with either slow action acid catalyst (phencat 382), or fast action acid catalyst (phencat 10), and then poured into the PTFE mold to be placed in an autoclave using a short cure cycle as shown in Table I. The catalyst ratio was maintained at 5 wt% of the resin for all samples.

Characterization

Scanning Electron Microscopy SEM. Scanning electron microscopy (FEI Nova Nano SEM 450) was used for the morphology observation of the fracture surface of the flexural strength samples. Unlike standard SEM analysis, no conductive coating was deposited onto the samples. Therefore, a low accelerating voltage (1 KV) was used to avoid sample surface charging and damage with typical vacuum pressure of 10^{-5} mbar, and a working distance of about 4 mm. Secondary electron images were collected using either an Everhart–Thornley Detector (ETD) for low magnification images or a Through Lens Detector (TLD) to obtain high magnification images.

Fourier Transform Infrared Spectroscopy. The chemical composition of all cured phenolic resins was investigated using a PerkinElmer Frontier spectrometer. To prepare the FTIR sample pellet, 2 mg of sample powder (ground from the bulk sample) was diluted with 300 mg of spectroscopic grade KBr. The test was performed at room temperature ($22 \pm 3^\circ\text{C}$) with a wavenumber range between 4000 and 600 cm^{-1} , and the average of scan repetitions was 32 scans for each sample at 2 cm^{-1} of resolution. Before loading the sample, a background spectrum was taken as a control.

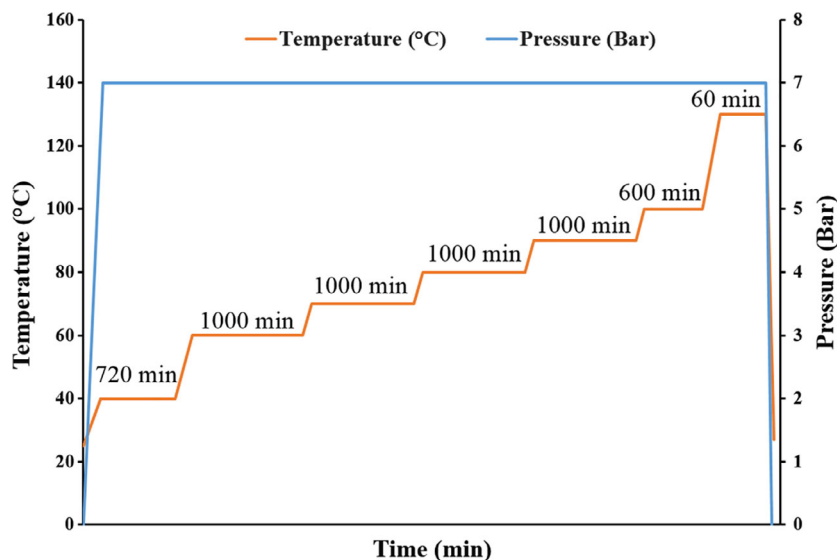


Figure 1. Long cure cycle used to cure phenolic resin without any catalyst. The heating ramp rate and pressure ramp rate were 2°C/min and 0.3 Bar/min, respectively. [Color figure can be viewed at wileyonlinelibrary.com]

Flexural Test. The flexural properties (strength and modulus) of all specimens were determined using a Lloyd TA500 tensometer. The test was performed according to the ASTM D790 (standard test methods for flexural properties of unreinforced and reinforced plastics and electrical insulating materials) with a span to sample thickness ratio of 16. Crosshead speeds of all tests were 2.0 mm/min. The tests were performed at room temperature ($22 \pm 3^\circ\text{C}$).

The ultimate bending results of each type of phenolic resin were calculated as an average of seven specimens per test condition. The flexural modulus was determined from the following formula:

$$E = \frac{L^3 F}{4 w h^3 d} \quad (1)$$

Where E is the modulus of elasticity in bending (MPa), L is the support span (mm), F is the peak load (N), w is the width of the sample (mm), h is the thickness (mm), and d is the sample deflection (mm).

RESULTS AND DISCUSSION

Fracture Surface Characterization

The fracture surfaces obtained by the bending test of the three types of cured phenolic resin were observed by LV-SEM and their micrographs are shown in Figure 2. A homogenous fracture

surface without any micron-sized voids was observed for the reference sample cured without catalyst, using the long cure cycle (Figure 1), as shown in Figure 2(a). A higher magnification image [Figure 2(b)] reveals the presence of a large number of bright nanostructures with diameters well below 100 nm. Their dimensions are consistent with previous electron microscopy studies of replicas of fractured phenolic resin surfaces.³³ These structures were interpreted as localized areas of increased crosslinking density³³ but the observed contrast would have been consistent with voids too. A few such bright nanostructures can be seen also in at the fracture surface of the specimens prepared with the slow action catalyst as shown in Figure 2(c,d). However, the latter fracture surfaces also show clear evidence of voids with diameters that reach from hundreds of nanometres to several micrometers. This is more easily seen in the diameter distribution histograms in Figure 3(a), which was derived from the binary images [Figure 4(a)]. Likewise, we present SEM images of the fracture surfaces obtained from materials produced with a fast action catalyst in Figure 2(e,f) and the respective diameter distribution histogram in Figure 3(b). The histogram was derived from the binary images presented in in Figure 4(b). The histogram [Figure 3(b)] shows clearly that the overwhelming majority of structures is of submicron size, with an average diameter of $0.52 \pm 0.15 \mu\text{m}$, while the SEM images demonstrates the dense and homogenous coverage [Figure 2 (f)] of the fracture surface with spherical features.

Table I. Short Cure Cycle Used to Cure Phenolic Resin With the Addition of Catalyst

Temperature (°C)	Temperature ramp rate (°C/min)	Pressure (Bar)	Pressure ramp rate (Bar/min)	Dwell time (min)
80	2.00	7.00	0.30	180
130	2.00	7.00	0.00	60
27	2.00	0.00	0.20	0.00

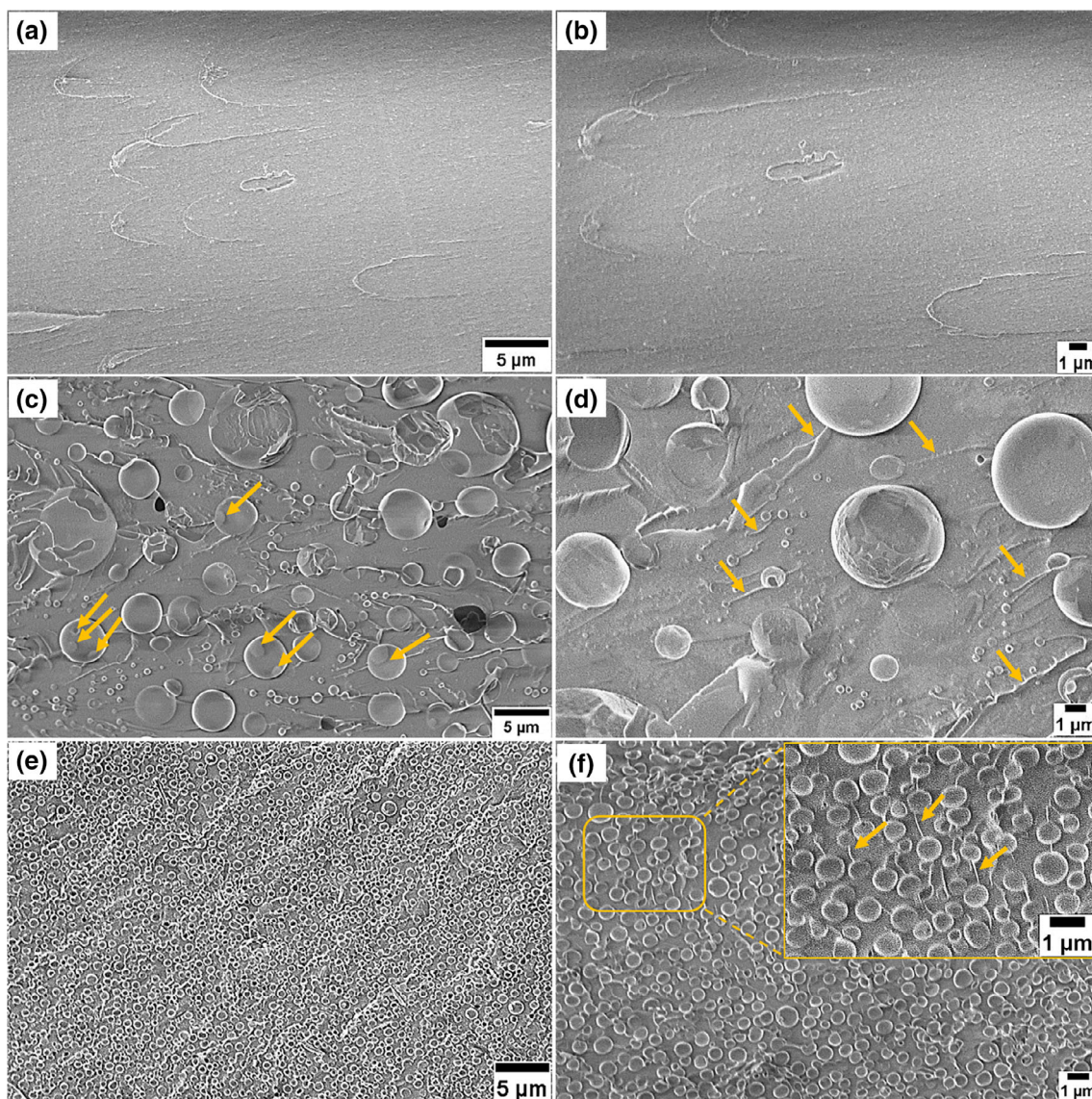


Figure 2. LV-SEM micrographs of the fracture surface of the three types of cured phenolic resins, (a) low and (b) high magnification images of phenolic resin cured using long cure cycle without added catalyst, (c) low and (d) high magnification images of phenolic resin cured with the addition of slow action catalyst (phencat 382), and (e) low and (f) high magnification images of phenolic resin cured with the addition of fast action catalyst (phencat 10). Arrows in (c) indicate the bubbles coalescence. Arrows in (d) and (f) (insert micrograph) indicate the cracks. [Color figure can be viewed at wileyonlinelibrary.com]

To understand the origin of the patterns is worth noting that a combination of small-angle neutron scattering (SANS) and small-angle X-ray scattering (SAXS) experiment on phenolic resins revealed that rough interfaces between voids and phenolic matrix with a fractal dimensions ~ 2.46 to 2.6 exist.³⁴ This fractal dimension is consistent with the existence of Apollonian arrangement for which a fractal dimensions of 2.4739465 was established.³⁵ Apollonian packing is found and used in the controlled preparation of ordered porous films exploiting Breath Figures, to produce so called Breath Figure arrays (BFA).³⁶ In BFA fabrication, the irregular pore arrays are observed if water droplet can coalesce, while homogenous pore arrays when the coalesce of water droplets can be prevented.

Therefore, all of the observations in Figure 2 can be understood in terms of time available before the gel point is reached. If this is long enough for the release of the water vapor before the start of

crosslinking in the resin structure,¹⁹ the formation of voids can be prevented as is the case in the reference material [Figure 2(a)]. In contrast, with the use of catalysts, the crosslinking rate of the phenol-formaldehyde resins is relatively fast. As the amount of water in the resin increased during the reaction, molecular clusters can form that then nucleate when the saturation level at a given temperature and pressure is locally exceeded.¹² This leads to phase-separation and produces water domains.³² With the fast action catalyst [Figure 2(e,f)], the crosslinking rate is very fast (only 20 min working life according to the technical data sheet), and the gelation time is very short. Therefore, the trapped water, present as a result of the complex polymerization process including the release of formaldehyde and water as by-products,³⁷ will not be able to be released or diffuse, resulting in a homogenous distribution of voids with the very narrow size distribution as seen in

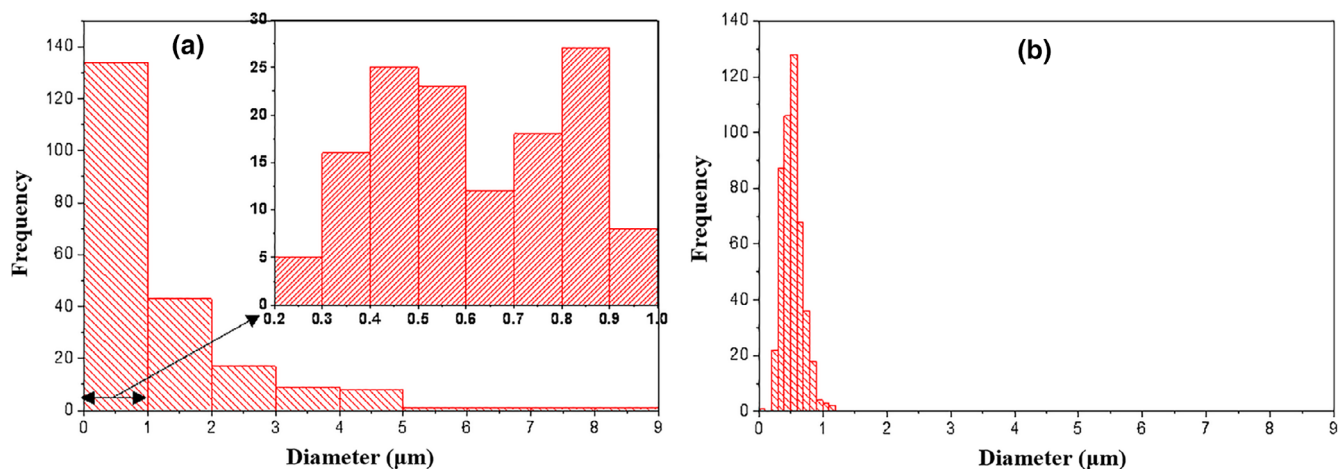


Figure 3. Histogram of voids diameter distribution: (a) phenolic resin cured with a slow action catalyst (phencat 382), and (b) phenolic resin cured with a fast action catalyst (phencat 10). [Color figure can be viewed at wileyonlinelibrary.com]

Figure 3(b). In contrast, with the use of a slow action catalyst [material in Figure 2(c,d)], the cross linking rate is slower (4 h working life according to the technical data sheet), and the gelation time is longer. Therefore, the generated water can move and coalesce leading to the very broad size distribution of voids, as well as a wide variation in distances between voids. Larger voids tend to be surrounded by void-free zones as can be seen in the binary image and distance map in Figure 4(a). The distance between small voids in Figure 4(a) is similar to that found in the distance map obtained from the material made by the fast action catalyst [Figure 4(b)]. However, the distance to larger voids in Figure 4(a) is substantially larger than the distance in Figure 4(b).

The above is also reflected in Figure 4(c), which compares the distances between voids in the materials made using slow and

fast action catalysts, respectively. While for the slow action catalysts, distances between voids can exceed 4 μm , the use of fast action catalyst results in distances between voids $<1.5 \mu\text{m}$. This difference is likely to play a critical role with regards to the mechanical properties, as the voids do seem to effect crack initiation and growth as evidenced by Figure 2(d,f) (indicated by arrows). Both figures contain the evidence of cracks (wide due to the edge effect). In the material produced from the slow action catalyst [Figure 2(d)] fewer but longer cracks are observed than in the material made with the fast action catalyst [Figure 2(f) (insert micrograph)]. The longest cracks in Figure 2(d) are found to propagate in the void-free zones with no clear termination point, while all of the cracks visible in Figure 2(f) (insert micrograph) are terminated at both ends by voids.

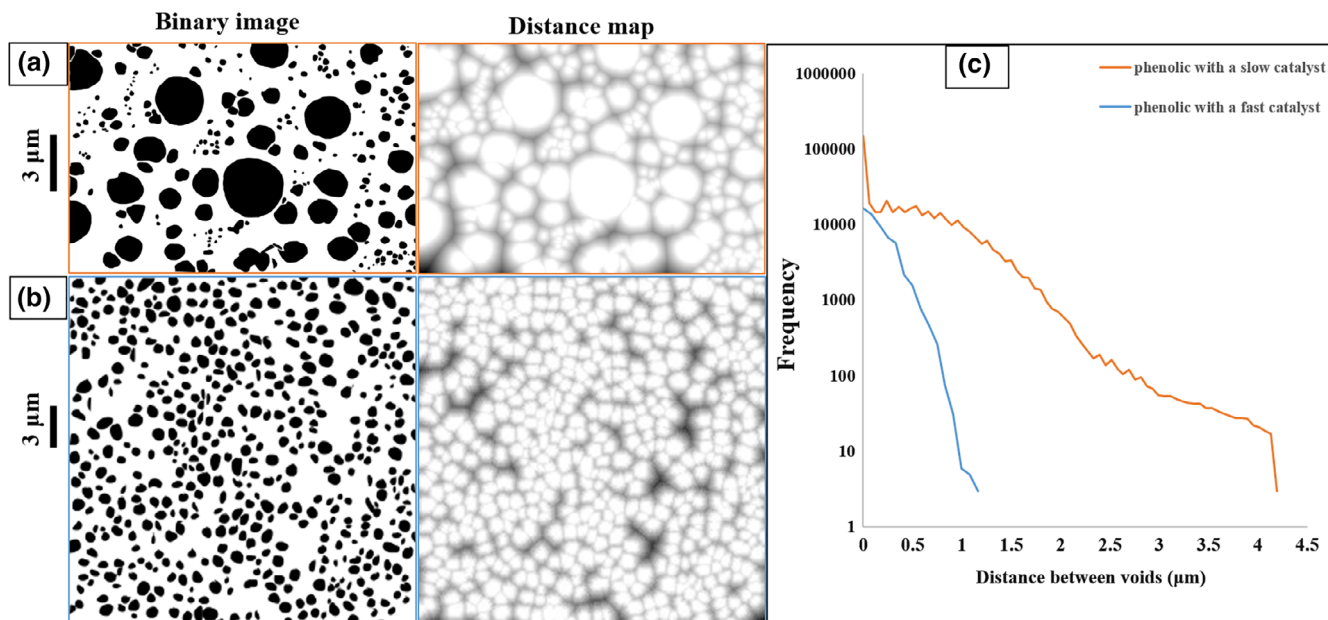


Figure 4. Voids analysis in phenolic resins cured with (a) a slow action catalyst, and (b) a fast action acid catalyst. (c) Histogram of intervoids distance for the images presented in (a) and (b). Image processing was performed using Fiji software.³⁸ [Color figure can be viewed at wileyonlinelibrary.com]

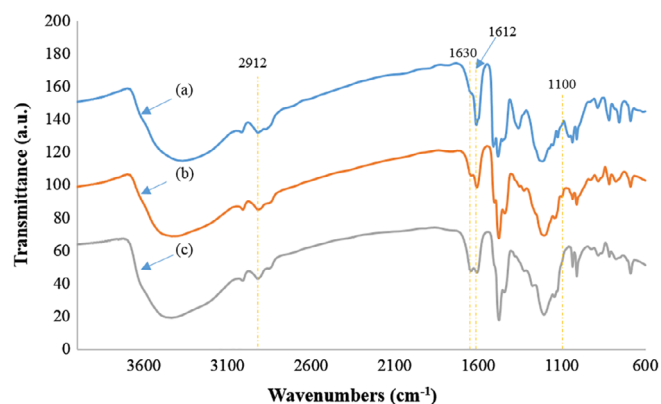


Figure 5. The IR spectrum of phenol/formaldehyde resin cured (a) without catalyst, (b) with a slow action catalyst (Phencat 382), and (c) with a fast action catalyst (Phencat 10). [Color figure can be viewed at wileyonlinelibrary.com]

Further differences between the materials made using slow and fast action catalysts, respectively, is in the volume fraction taken up by the voids structures. We can only measure area fractions from the 2D SEM images (28% in materials from fast action catalyst & 33% in materials using slow action catalyst). However, the volume fraction is only directly proportional to the area fraction if the sectioning plane intersects the structural features at random. As are sections are produced by fracture the later condition is not necessarily fulfilled here, because as seen in Figure 2(d)

(indicated by arrows) wide cracks are seen to run along the larger voids. While all of the above will affect the mechanical properties (see sections 3.3 and 3.4 for full details), differences in chemistry as a result of using the different catalysts could also be responsible for the differences in mechanical properties.

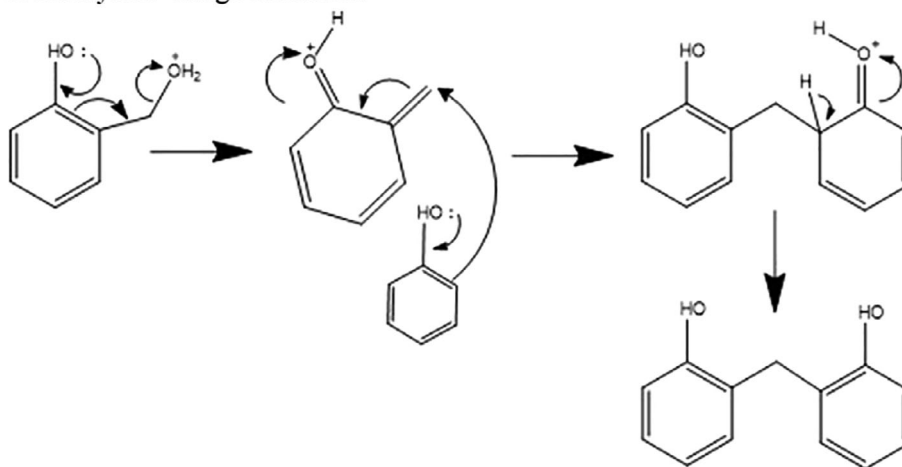
The Chemical Composition Analysis

Results of FT-IR measurements are presented in Figure 5 in order to enable component identification of the products produced by the condensation reaction of phenol and formaldehyde. The standard peak positions³⁹ and the observed peaks of the resole phenol/formaldehyde resins are assigned in Supporting Information (Supporting Information Table S1).

It was expected that both catalysts used would be observable through two clear absorption bands; one band at 1650 cm^{-1} , noted for hydrated phosphates P—OH and corresponding to O—H stretching and O—H deformation vibrations and second band between 1300 and 900 cm^{-1} that is characteristic of P—O and C—O vibrations.⁴⁰ In this reaction, these absorption bands cannot be independently isolated as both bands coincide with the phenolic resin bands at 1594 cm^{-1} , corresponding to the absorption of C=C of phenyl rings, and bands 1100 cm^{-1} , which are the characteristic of the C—H flexural of phenyl rings.

Two bands observed at 1630 cm^{-1} and 1612 cm^{-1} are of particular interest. The first band was noted as the C = O stretch

1. Methylene bridge formation



2. Ether bridge formation

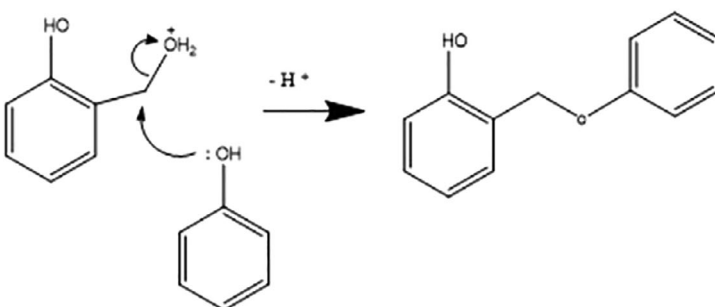


Figure 6. Two possible reactions of phenol/formaldehyde resin with acid catalyst.

Table II. Flexural Properties of The Three Types of Cured Phenolic Resins

Sample	Flexural strength (MPa)	STDEV	Flexural modulus (GPa)	STDEV	Deflection (mm)	STDEV
Phenolic without catalyst	88	18	3.2	0.28	1.2	0.25
Phenolic with slow action catalyst (382)	47	8	2.0	0.25	0.99	0.11
Phenolic with fast action catalyst (10)	68	12	2.3	0.43	1.2	0.25

(overlapped with OH scissors of water), which is the characteristic of unreacted formaldehyde. This first band has higher intensity when the materials is made using a catalyst with a short cure cycle when compared to phenolic cured without a catalyst using long cure cycle. This absorption band can be interpreted in either of the two ways: firstly, the resins formed using a catalyst might have a slightly reduced cross linking density or secondly, and more likely, the acid catalyst pushes the equilibrium of the two-step reaction toward the second step of the polymerization of phenolic resin. Either interpretation results in less formaldehyde being used in the initial reaction and thus leads to the presence of unreacted formaldehyde. The latter is more likely because it is observable that the phenolic resin cured with a fast action acid catalyst showed a stronger 1630 cm^{-1} band when compared to that of phenolic resin cured with a slow action acid catalyst. This result would be expected as the fast catalyst is the more acidic.

An interesting feature is the absorption band present at 1612 cm^{-1} . This absorption band displays a greater intensity in the case of phenolic resin cured without catalyst than that of either catalyst. The band is caused by the $\text{C}=\text{C}$ aromatic ring within a functional group of phenol-formaldehyde resin. This is the product of the first step reaction of phenol and formaldehyde and therefore is consistent with the premise that the acid catalyst is slowing down the formation of this product.

Two interesting bands were also noted at 2912 cm^{-1} and 1100 cm^{-1} , these bands are attributed to methylene and ether bridges, respectively.³⁹ Changes in the two bands values were observed

between the two catalysts. These changes are expected to originate from the differences of the phenol-bonding mechanism. It was noted that there was a reduction of ether bridges within phenolic resin cured with a fast action catalyst when compared to that of phenolic resin cured with a slow action catalyst and a consequential increase in methylene bridges in phenolic cured with fast catalyst when compared to that of phenolic cured with slow catalyst. The more acidic the catalyst, the more that the phenol is protonated and therefore the less nucleophilic it is. As a result, it is less likely that it will follow a second mechanism and form ether bridges (see Figure 6). The results observed point to an increased likelihood that the first mechanism is the correct one. If so, the more acidic catalyst (fast action catalyst) will promote the formation of methylene bridges within the phenolic. Methylene bridges have a greater bond strength than that of ether bridges.⁴¹ This can result in different mechanical properties of the phenolic due to more methylene bridges (see section 3.3).

Flexural Strength and Modulus

The flexural properties of the three types of cured phenolic resins were determined and are presented in Table II. It can be seen that the phenolic resin cured without a catalyst, using a long cure cycle (almost 4 days), has the highest average values of flexural strength ($88 \pm 18\text{ MPa}$) and modulus ($3.2 \pm 0.28\text{ GPa}$) in comparison to those of phenolic resins cured with catalysts. This is expected and can be explained in part by the reduced area of phenolic resin due to the presence of voids when prepared with catalysts. With the use of a slow action catalyst, the flexural strength and modulus of the cured phenolic resin were decreased

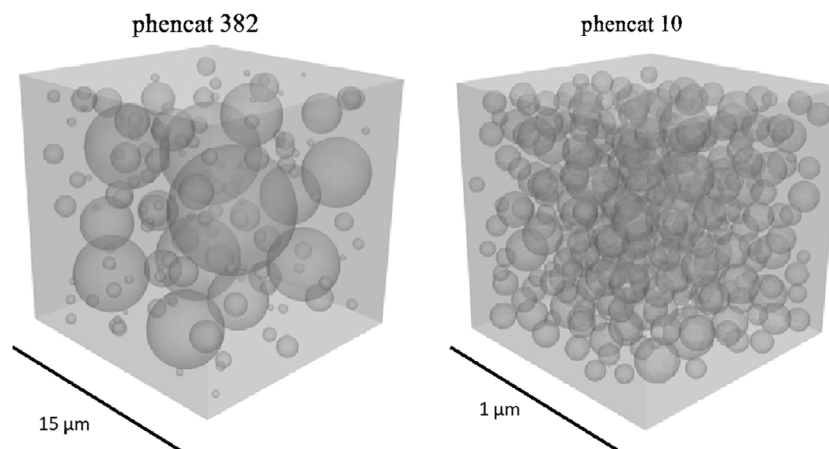


Figure 7. The microstructural representations of phenolic resin cured with a slow action catalyst (Phencat 382) (~150 individual microvoids) and a fast action catalyst (Phencat 10) (~300 individual microvoids). Each model has an overall solid density of 70%.

to 47 ± 8 MPa and 2.0 ± 0.25 GPa, respectively. The presence of the voids in the cured resin increases the pressure on the surrounding resin and also they act as stress concentrators rendering the material more fragile.^{42,43} When the sample is subjected to a load, stress and strain concentrations will be generated around the voids causing a local plastic deformation. Then with increasing load, cracks will be initiated and grow in the voids-free resin zones, with the resultant reduction in the resin strength.^{44,45} Such cracks were clearly observed by SEM image as shown in Figure 2(d).

However, it is important to point out that the average values of the flexural strength (68 ± 12 MPa) and the flexural modulus (2.3 ± 0.43 GPa) of the phenolic resin cured with a fast action catalyst were higher than those of phenolic resin cured with a slow action catalyst. Moreover, some of the tested samples from

the phenolic resin cured with a fast action catalyst showed very close or even the same flexural strength values as some of phenolic resin cured without a catalyst (see Supporting Information Table S3 and Figure S1). By taking into account the void volume fraction, it has been noted that the flexural strength of the phenolic resin cured with a fast action catalyst was similar to the flexural strength of the reference sample (cured without catalyst). Whereas in the case of using a slow action catalyst, the flexural strength remains lower than that of reference and fast action cured samples.

Therefore, the differences in the flexural properties between the two phenolic resins (cured with either slow or fast action catalyst) can be attributed to both the structural and chemical changes presented in this article. In terms of the chemical changes, it is possible that the presence of high prevalence methylene bridges

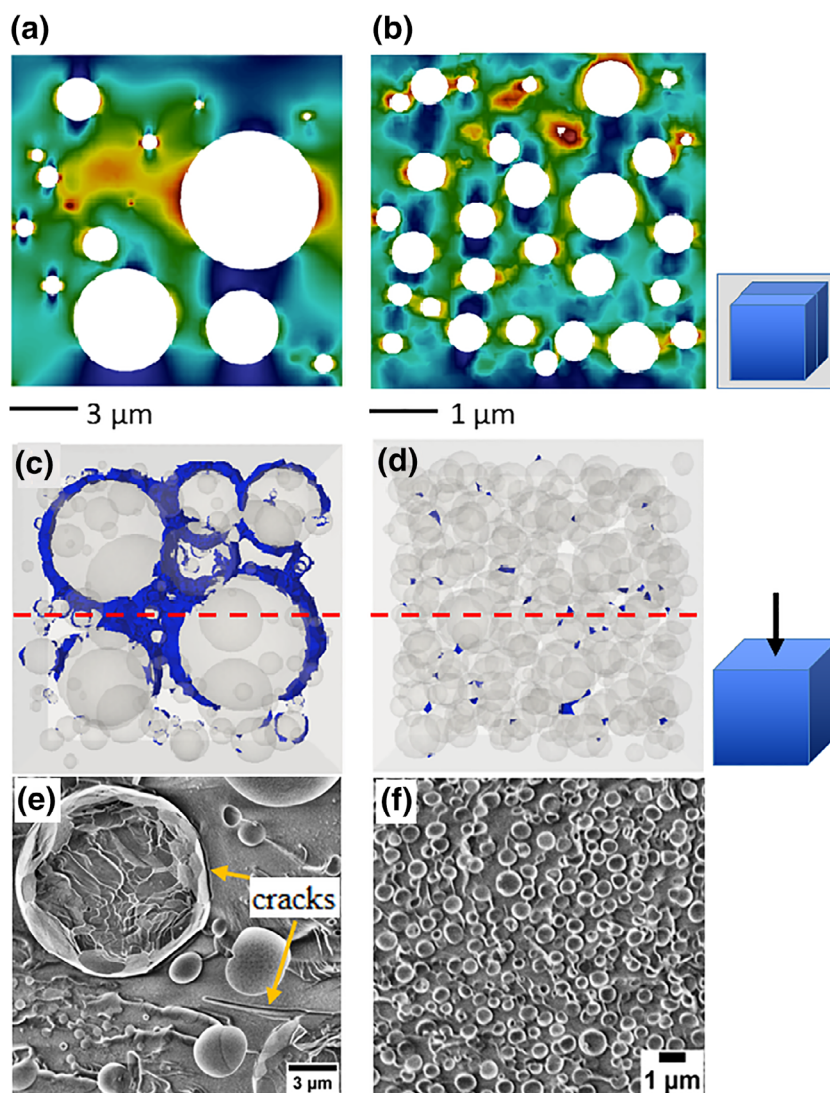


Figure 8. The comparison of the stress distribution in models that represent phenolic resin cured with a slow action catalyst (phenocat 382) (a,c) and phenolic resin cured with a fast action catalyst (phenocat 10) (b,d). The resulting von-Mises stress is plotted (a,b) as a cross section of the cube. Red indicates a stress of 88 MPa, while blue indicates a minimum stress of 0. Parts (c) and (d) are top down views of the model highlight only the top 20% of stresses (70–88 MPa) within the system. The red-dashed line indicates the cross section seen in parts (a) and (b). Parts (e) and (f) are the SEM micrographs of the fracture surface of the phenolic cured with slow action catalyst and fast action catalyst, respectively. The small images to the right of the figure highlight the direction of the image seen. [Color figure can be viewed at wileyonlinelibrary.com]

in the case of using a fast action catalyst (as discussed within FTIR analysis in section 3.2) could potentially improve the flexural properties of the cured resin. But more significantly, it can be confirmed that the increase in the flexural properties in the case of using fast action catalyst were due to the void size and distribution in the cured resin. For instance, in phenolic foams, it has been found that the cell size and cell distribution have significant effects on the final mechanical properties of the foam. Smaller and more uniform cell size in the final cured foam will potentially improve the mechanical properties.²⁴ Similarly, in this study, the LV-SEM micrograph and image analysis of the fracture surface of the phenolic resin cured with a fast action catalyst shows small and uniform void diameter distribution, whereas a non-uniform void diameter distribution was observed in the case of using slow action catalyst (see section 3.1).

To understand this further, it was thus confirmed that the void diameter distribution plays a major role in the crack initiation and propagation. Small cracks terminated at both ends by voids were observed in the fracture surface of phenolic resin cured with a fast action catalyst. It was assumed that the small and uniform distances between the small voids can help to prevent the crack propagation in the void-free resin. This is in contrast, to the cracks in the case of using a slow action catalyst was fewer and longer cracks exist, which are seen by SEM in Figure 2(d) to propagate in the void-free area and also along the large voids. Moreover, the long boundary between the void-free area and the large voids is also expected to accelerate the crack growth and hence the early sample failure. All the above were further confirmed by the model in section 3.4.

Finite Element Modeling

To study the effect of the void size and distribution of phenolic resin cured with slow and fast action catalyst has upon the stress concentration and ultimately the failure strength of the resins, we employ a simplistic finite element model. Experimental void sizes calculated in Figure 3 are directly implemented into a finite element model using an approach previously used to study the effect of electric field enhancement in electro-ceramic materials.⁴⁶ Treating the voids as hard spheres, the lists of diameters are randomized and then sequentially positioned randomly into a cube. This process continues until the effective density of the solid is reduced to 70% (assuming both materials have the same voids area fraction [30%] for simplification). These spheres are then subtracted from the solid cube to form the semidense structure replicated the two materials. Due to the differences in size and number of voids for each system (as already seen in SEM images [section 3.1]), the size of the cube is modified to save computation time. Hence, to create models for phenolic resin cured with a fast action catalyst requires approximately 300 voids in a cube of $5\mu\text{m}^3$, while for phenolic resin cured with a slow action catalyst, approximately 150 voids in a cube of $15\mu\text{m}^3$ are need to generate a 70% dense solid. An example for each model can be seen in Figure 7.

The models are then imported into COMSOL⁴⁷ and solved using the structural module. We assume the resin Young's modulus is 3.2 GPa with a Poisson's ratio of 0.3.⁴⁸ The model assumes the resin is entirely elastic and isotropic. Due to the simplicity in performing the model with the tensile load instead of the bending load, we apply a tensile load of 21 MPa on the top surface as a

reference. This value is chosen as it generates a maximum stress in both samples of approximately 88 MPa, the failure point of the microvoid-free sample. The bottom surface was restricted in movement within plane and a single node in the center of the surface fixed rigidly in all dimensions to not overly constrain the system. Symmetry was employed on the other four surfaces to replicate a central region of "bulk"-like material. The model was then discretised with over two-million tetrahedron elements, ensuring convergence of the results. Figure 8 shows von-Mises stress, highlight in red, the points at which failure may begin. In Figure 8(a), it can be seen that the representation of phenolic resin cured with a slow action catalyst (phencat 382) generates significant stresses between the large voids (over 70 MPa), which extends over a few micrometers in length. This is in comparison to phenolic resin cured with a fast action catalyst (phencat 10) where stresses are as great but highly localized between the small particles and typically restricted to less than 1 μm in length due to the proximity of the voids [Figure 8(b)]. To highlight this further, we plot only the stresses greater than 70 MPa in Figure 8(c,d) as a top-down view. It is clearly visible that for phenolic resin cured with a slow action catalyst high stresses are located around the circumference of larger voids in relation to the applied stress [Figure 8(c)] and extend through the system to other large voids. The same high stresses in phenolic resin cured with a fast action catalyst are only found between two closely placed voids [Figure 8(d)]. If the yield strength of the material is considered to be the point at which a crack would form and spread, it is clear that for phenolic resin cured with a fast action catalyst, these cracks would be between neighboring voids, traveling less than 1 μm . Conversely, for phenolic resin cured with a slow action catalyst, due to the increased distance between voids, the crack could propagate much further, and as such reach a critical point for fracture earlier. This is clearly consistency with the SEM micrographs shown in Figure 8(e,f) and also in good agreement with the flexural property results in section 3.3 (Table II).

CONCLUSIONS

LV-SEM combined with the finite element modeling suggests that the size and spatial distribution of the voids in the cured phenolic resin are of great importance in determining the final mechanical properties of the resin. While the conventional approach in phenolic resins is to minimize or to avoid the void content in the cured resin, here we show that for the similar void content, achieving a homogenous void distribution is critical. More attention should be paid to the engineering of voids size and distribution. With the use of fast action catalyst in curing the resole phenolic resins, a better balance between the properties and cure cycle could be achieved.

ACKNOWLEDGMENTS

Sameer F. Hamad gratefully acknowledges the Iraqi Ministry of Higher Education and Scientific Research and its representative in the UK, the Iraqi Cultural Attaché for the financial support. C. Rodenburg thanks the Engineering and Physical Sciences Research Council (EPSRC) for funding under EP/N008065/1. Nicholas Farr thanks EPSRC for funding of his doctoral training studentship. Joel P. Foreman thanks Peter Willson at Caleb Technical Products for providing the resin.

REFERENCES

1. Wang, J.; Zhang, Y. F. *Polym. - Plast. Technol. Eng.* **2012**, *51*, 1213.
2. Ratna, D.; Karger Kocsis, J. *J. Appl. Polym. Sci.* **2013**, *127*, 4039.
3. Wang, J.; Jiang, H.; Jiang, N. *Thermochim. Acta.* **2009**, *496*, 136.
4. Budiono, H. S.; Surojo, E.; Muhayat, N.; Raharjo, W. W. *MATEC Web Conf.* **2018**, *159*, 1.
5. Der Wu, H.; Lee, M. S.; Wu, Y. D.; Su, Y. F.; Ma, C. C. M. *J. Appl. Polym. Sci.* **1996**, *62*, 227.
6. Alkan, Ü. B.; Kızılcan, N. *Procedia - Soc. Behav. Sci.* **2015**, *195*, 2067.
7. Zhang, Y.; Shen, S.; Liu, Y. *Polym. Degrad. Stab.* **2013**, *98*, 514.
8. Niu, M.; Wang, G. *Cell. Polym.* **2013**, *32*, 155.
9. Yu, Y.; Wang, Y.; Xu, P.; Chang, J. *Materials (Basel)*. **2018**, *11*, 2228.
10. Asim, M.; Saba, N.; Jawaid, M.; Nasir, M.; Pervaiz, M.; Alothman, O. Y. *Curr. Anal. Chem.* **2018**, *14*, 1.
11. Li, J.; Zhu, W.; Zhang, J.; Zhang, S.; Gao, Q.; Li, J.; Zhang, W. *J. Appl. Polym. Sci.* **2019**, *136*, 1.
12. Pupin, C.; Ross, A.; Dubois, C.; Rietsch, J.; Ruiz, E. *Compos. Part A.* **2017**, *100*, 294.
13. Natali, M.; Kenny, J.; Torre, L. *Compos. Sci. Technol.* **2010**, *70*, 571.
14. Sulaiman, S.; Yunus, R.; Ibrahim, N. A.; Rezaei, F. *J. Eng. Sci. Technol.* **2008**, *3*, 79.
15. Manikandan, G. N.; Bogeshwaran, K. *ChemTech Res.* **2016**, *9*, 30.
16. Singh, K. P.; Palmese, G. R. *J. Appl. Polym. Sci.* **2004**, *91*, 3096.
17. De Medeiros, E. S.; Agnelli, A. M.; Joseph, K.; De Carvalho, L. H. *J. Appl. Polym. Sci.* **2003**, *90*, 1678.
18. Parameswaran, P. S.; Bhuvaneswary, M. G.; Thachil, E. T. *J. Appl. Polym. Sci.* **2009**, *113*, 802.
19. Kaynak, C.; Tasan, C. C. *Eur. Polym. J.* **2006**, *42*, 1908.
20. He, L.; Han, R.; Zhang, Y. *J. Adhes. Sci. Technol.* **2009**, *23*, 1639.
21. Park, B. D.; Riedl, B.; Hsu, E. W.; Shields, J. *Polymer (Guildf)*. **1999**, *40*, 1689.
22. Singh, A.; S. Aggrawal; D. Lal. *Def. Sci. J.* **2019**, *69*, 46–52.
23. Aierbe, G. A.; Echeverria, J. M.; Martin, M. D.; Mondragon, I. *Polymer (Guildf)*. **1998**, *39*, 3467.
24. Mougel, C.; Garnier, T.; Cassagnau, P.; Sintes-Zydowicz, N. *Polymer (Guildf)*. **2019**, *164*, 86.
25. Li, Q.; Chen, L.; Li, X.; Zhang, J.; Zheng, K.; Zhang, X.; Tian, X. *J. Appl. Polym. Sci.* **2016**, *133*, 1.
26. Wolfrum, J.; G. W. Ehrenstein. *J. Appl. Polym. Sci.* **1999**, *74*, 3173.
27. Astarloa Aierbe, G.; Echeverría, J. M.; Martin, M. D.; Etxeberria, A. M.; Mondragon, I. *Polymer (Guildf)*. **2000**, *41*, 6797.
28. Lin, C. C.; Teng, H. *Ind. Eng. Chem. Res.* **2002**, *41*, 1986.
29. Hu, X.-M.; Zhao, Y.-Y.; Cheng, W.-M. *Polym. Compos.* **2015**, *36*, 1531.
30. Monni, J.; Alvila, L.; Pakkanen, T. T. *Ind. Eng. Chem. Res.* **2007**, *46*, 6916.
31. Loustalot, M. F. G.; Larroque, S.; Grande, D.; Grenier, P. *Polymer (Guildf)*. **1996**, *37*, 1363.
32. St. John, N. A.; Brown, J. R. *Compos. Part A Appl. Sci. Manuf.* **1998**, *29*, 939.
33. Spurr, R. A.; Erath, E. H.; Myers, H.; Pease, D. C. *Ind. Eng. Chem.* **1957**, *49*, 1839.
34. Izumi, A.; Nakao, T.; Iwase, H.; Shibayama, M. *Soft Matter.* **2012**, *8*, 8438.
35. Borkovec, M.; Paris, W. D. E. *Appear. Fractals.* **1994**, *2*, 521.
36. Zhang, A.; Bai, H.; Li, L. *Chem. Rev.* **2015**, *115*, 9801.
37. Ku, H. S. L.; Cardona, F.; Trada, M.; Vigier, G. *J. Appl. Polym. Sci.* **2009**, *114*, 1927.
38. Schindelin, J.; Arganda-Carreras, E.; Frise, I.; Kaynig, V.; Longair, M.; Pietzsch, T.; Preibisch, S.; Rueden, C.; Saalfeld, S.; Schmid, B.; Tinevez, J.-Y.; White, D. J.; Hartenstein, V.; Eliceiri, K.; Tomancak, P.; Cardona, A. *Nat. Methods.* **2012**, *9*, 1.
39. Poljanšek, I.; Krajnc, M. *Acta Chim. Slov.* **2005**, *52*, 238.
40. Jähnigen, S.; Brendler, E.; Böhme, U.; Heide, G.; Kroke, E. *New J. Chem.* **2014**, *38*, 744.
41. Parameswaran, P. S.; Thachil, E. T. *Int. J. Polym. Mater. Polym. Biomater.* **2007**, *56*, 177.
42. Brown, J.; Mathys, Z. *J. Mater. Sci.* **1997**, *32*, 2599.
43. Feih, S.; Mathys, Z.; Mathys, G.; Gibson, A. G.; Robinson, M.; Mouritz, A. P. *Polym. Degrad. Stab.* **2008**, *93*, 376.
44. Aratama, S.; Hashizume, R.; Takenaka, K.; Koga, K.; Tsumura, Y.; Miyake, T.; Nishikawa, M.; Hojo, M. *Adv. Compos. Mater.* **2016**, *3046*, 1.
45. Paskaramoorthy, R.; Bugarin, S.; Reid, R. G. *Int. J. Solids Struct.* **2011**, *48*, 2255.
46. Dale, G.; Strawhorne, M.; Sinclair, D. C.; Dean, J. S. *J. Am. Ceram. Soc.* **2018**, *101*, 1211.
47. COMSOL. Multiphysics® Modeling Software. <https://uk.comsol.com/> (accessed 18 April 2019).
48. Arnold, S. M.; Murthy, P. L.; Bednarczyk, B. A.; Lawson, J. W.; Monk, J. D. *NASA Tech. Memo.* **2016**, *219124*, 1.